

# Combination of dielectrophoretic and hydrodynamic traps for the controlled contact between cells or beads and application to adhesion assays

Présentée le 3 mars 2023

Faculté des sciences et techniques de l'ingénieur  
Laboratoire de microsystemes 4  
Programme doctoral en microsystemes et microélectronique

pour l'obtention du grade de Docteur ès Sciences

par

## Clémentine Sophie Sarah LIPP

Acceptée sur proposition du jury

Dr G. Boero, président du jury  
Prof. Ph. Renaud, Dr A. Bertsch, directeurs de thèse  
Prof. B. Le Pioufle, rapporteur  
Prof. B. Pruitt, rapporteuse  
Prof. G. Villanueva, rapporteur



"What do you think success is?" asked the boy.

"To be kind." said the mole.

Charlie Mackesy, *The Boy, the Mole, the Fox and the Horse*

To the students who participated to this work.

# Acknowledgements

This thesis was an exceptional journey from both a scientific and personal perspective. I cannot count the number of times I felt I was not able to bring this work to the finish line. It would not have been what it is today without the help and contributions of many people I would like to acknowledge.

I would like to express my gratitude to Philippe Renaud for his wise guidance, his precious advice and for his kindness. Many thanks as well to Arnaud Bertsch for his criticism that greatly helped me improve this work, for the countless hours he spent correcting my scribbles and for challenging my ideas and beliefs. I thank the Jury members Beth Pruitt, Bruno Le Pioufle, Guillermo Villanueva and Giovanni Boero for spending time reading this thesis and providing their expertise and feedback, but also for the very interesting discussions they brought.

This thesis was done in the frame of a joint project between Switzerland and France and was performed in close collaboration with the AS2M department of the FEMTO-ST institute and the UMR RIGHT department of the EFS institute both in Besançon, France. Discussion with both institutes were held during the whole development phase of the chip and the lifetime measurement experiments with T-cells and cancer cells were done during a stay at EFS. I would like to thank the FEMTO-ST collaborators who participated to the project: Aude Bolo-pion, Laure Koebel, Hugo Daguerre, Alexis Lefevre and Michaël Gauthier. I especially thank Aude Bolo-pion for the support she gave me and for the warm welcome in Besançon and for providing feedback on the manuscript until the last minute. I thank Laure Koebel for the technical support without which not half of the experiments could have been done and for spending countless hours in the dark and with the noise of the compressor waiting for a cell to arrive in the chip. Many thanks also for all the discussions and activities we had together which made my stay in Besançon memorable.

I did not have many notions of biology when I started this project and I would like to thank EFS members Romain Loyon and Laurie Spohner for their patience and tenacity in explaining

me why cells are more complicated than beads, need to be considered more carefully, and all the subtleties of the biological goal of the project. Also thank you for never doubting the capability of the tool we were building and for their motivation to drive this project to the application. Many thanks as well to Christophe Borg and Jean-René Pallandre for welcoming me at the EFS.

During this work I had the chance to work with master students for summer and semester projects and I would like to thank every one of them for their contribution to this project. Working with you was what I enjoyed the most in this adventure, I learned so much from you and this thesis is therefore dedicated to you: Lancelot Barthe, Arthur Jaccottet, Tristan Tarasi, Kevin Uning, Guillaume Grosjean, Sylvain E-Khoury, Albane Legrand, Théo Nass, Aviv Huttner, Théo Mayer and Audrey Jacquillat.

To all the LMIS4 member, thank you for providing this particular workspace where I learned and laughed so much. A special thank you to Jonathan who spent time putting me up to speed on lab know-how, dielectrophoresis, the art of presentation and networking. Many thanks to Margaux for spending time teaching me proper biological work and for her patience with my countless questions about cells, but as well for the precious advice and discussions about work or non work related topics and for the example you represent. Many thanks to Benoît who convinced me that research could be fun and was worth the struggle, I cannot stress enough how much I owe you for that. To Seb thank you for relentlessly convincing me to go climbing, for the countless pieces of advice and for being "le pillier de labo" during these years.

To my office mates Nadya, Joan, Miguel and Ludo, thanks for sharing (or not) crazy cat people vibes, for providing coffees and taking care of the worms. To Joan Edward Kaylee André, your presence made this adventure so much easier and I thank you for supporting my need to discuss stupid topics in the office and for hiding pictures in my desk. Many thanks to Nicolas Lafayette for motivating me to go running, swimming or climbing and for sharing the passion for stupid videos. Jiande thank you for introducing me to swimming and for sharing the fun and struggles of the PhD journey in the office and during writing nights. I thank you Evgenii for being always up for some extra work activities and for your kindness. Matin thank you for your openness, it was always a pleasure discussing cultural and religion topics with you. Daniel many thanks for the super interesting and fun discussion on the different models, I could always count on you to help me understand and model any physical phenomenon.

Thanks to Luca and Albert for bringing fun and mustache to the lab. To the Arcoscreen team, Thamani, Gherici, and Nora it was a real pleasure to share the lab space with you and to chat at any time around the lab about any topic. Thamani many thanks for the precious help with calcium imaging, but also for being able to count on you for anything. Thanks as well to the Parithera team Antoine and Weida for providing insight to the startup world and sharing

coffees.

To all the CMi team a huge thank you for running this amazing place that are the cleanrooms. Running behind the machines we break and relentlessly answering users questions must not be an easy task, but your work makes possible to bring to reality all these ideas. A huge thank you to Philippe Flückiger, PAM, Cyrille Hibert, Joffrey Pernollet, Rémy Juttin, Didier Bouvet, Blaise Cuénod, Giovanni Monteduro, Niccolò Piacentini, Julien Dorsaz, Manuel Pillon, Zdenek Benes, Makhlad Chahid, Miguel Marmelo, Adrien Toros, Vivigan Sinnathamby, Giancarlo Corradini, Guy-François Clerc, Erwann Imhof, Gatera Kumuntu, Céline Cornaz, Marie-Noëlle Verhar and all the others.

Aux microtech vous avez rendu ces années d'études des plus mémorables, entre révisions intenses et fêtes à la paroisse. Aujourd'hui le groupe a grandi en une bande de copains des séjours à la mine. Toujours prêts à partager des moments magiques et pleins de folies entre sport, discussions et fêtes, vous êtes un socle et une grande ressource. Si je suis convaincue d'avoir des amis pour la vie, c'est bien vous.

Cap'tain, t'as beau être loin tes appels sont toujours des shots de positivité qui me boostent pour un nouveau tour. Merci à Caro pour avoir toujours été disponible pour écouter mes soucis peu importe l'heure, et merci à Corinne pour m'avoir permis de structurer mes pensées et mes émotions sans quoi j'aurais probablement abandonné à mi-chemin. Et à tous les autres qui ne rentrent pas dans une catégorie mais qui comptent tout autant, Lisa, Vicky, Pierre, Alexandre, Lynn, Dara, Anaëlle et à tous les autres que j'ai oublié, merci!

A toute ma famille merci d'être toujours là et de représenter cette structure, cette constante dans ma vie. "Famille signifie que personne n'est ni abandonné ni oublié" est ce que vous m'avez appris à travers toutes ces années. A mes grand-papa et Vincent aussi, vous avez été des exemples pour moi et vous me manquez beaucoup.

"Tu crois qu'un jour on aura plus rien à se raconter?" je t'avais demandé il y a quelques années, aujourd'hui je n'ai plus aucun doute. Niccolò merci pour avoir été là chaque jour, dans le meilleur et dans le pire et sans jamais flancher. Encore plus important que les infinies discussions qu'on peut avoir sur des sujets scientifiques, tu sais toujours comment me faire rire ou comment me calmer, comme un port dans les eaux agitées.

Last but not least, j'aimerais remercier mes parents, ma soeur et mon frère pour leur soutien durant cette période. Si ce n'est ni le voyage ni la destination qui comptent, c'est bien la compagnie. Merci aussi d'avoir supporté ma détermination à vouloir vous faire comprendre ce que je faisais, quitte à y passer des heures. J'ai toujours pu compter sur vous et sur notre complicité pour avancer. Papa, Maman, Mad et Gus, c'est grâce à vous que j'ai pu aboutir ce travail!

To all of you, a huge thank you!

*Lausanne, le 9 Janvier 2023*

Clémentine Lipp

# Abstract

Multicellular organisms require very well organized and finely balanced cell-cell communication, adhesion, coordination and programmed cell death to ensure the organisms homeostasis. These functions rely on specialized receptors placed at the cells membrane whose binding to their ligand triggers a defined response. Receptor-ligand interactions thus not only maintain the cells physically adhered to one another, but also enable communication to ensure proper organism function. Malfunction of the receptors to properly trigger the appropriate response leads to imbalances in the organism and failure to exert specific functions. Our understanding of these pathologies thus relies on the capacity to study such interactions. However, the tools currently capable of placing two micro-sized objects such as beads or cells in contact for a controlled amount of time and probe their state of adhesion are cumbersome, require highly skilled staff and are low throughput. Additionally, controlled contact between cells is of specific interest for cell-based cancer immunotherapies. Indeed the process of selecting patient T-cells with high antitumor activity is currently a long and very expensive process, limiting the generalization of such approach despite their proven efficacy. In this context, a tool able to reliably pair T-lymphocytes with antigen presenting cells or tumor cells and rapidly assess the specificity of the interaction could simplify the long process of T-cell selection and facilitate in the long term the access to this kind of therapy.

This thesis tackles these challenges by developing a microfluidic tool combining two means for the controlled trapping of micro-sized objects such as beads or cells to control their physical contact in flow conditions and probe their state of adhesion. Because the forces derive from a different phenomenon for each object, the effects are orthogonal and allow an independent manipulation of the two micro-sized particles.

The first part of the thesis describes a novel method for the hydrodynamic trapping of beads and cells relying on superimposed levels of microfluidic channels interconnected by microfluidic vias. This type of hydrodynamic traps enables the immobilization of objects without



influencing neighboring objects. This method is a cornerstone of the chip as the controlled contact between two objects and the assessment of their state of adhesion can only be reliable when forces acting on them do not have intercrossed effects. A novel microfabrication process was developed to fabricate 3D channels in a totally transparent substrate. The trapping mechanism of cells is first characterized in single traps to define the frame of operation that ensures that no damage is done to the cells. The trapping of beads and cells and their arrangement in large arrays of traps is then shown to demonstrate the capabilities of the method.

Second, a design of coplanar electrodes creating a three dimensional dielectrophoretic force field directing to a single point against the flow is proposed. The DEP traps are used in combination with a DEP based deviation system to control the number of objects directed to the traps. The device is used to demonstrate single object trapping and the creation of aggregates composed of a controlled number of cells from two populations.

Finally, the two trapping means are combined to provide a device capable of performing in flow cell-cell and cell-bead interaction with time of contact between the two objects controlled down to the second resolution. The functionality of the tool is then validated by performing an adhesion frequency assay with fibroblasts cells and fibronectin coated beads. The extracted binding kinetics parameters are compared to literature showing good agreement with previously reported values. The potential of such a tool in immunotherapy applications is demonstrated by pairing human T-cell clones with cancer cells. The lifetime of the pairs is measured and the effect of TCR-pMHC bonds on the latter is demonstrated. A measurement of cellular avidity based on the lifetime of the pairs is then proposed by assigning a pair lumped off-rate as metric. The characteristics of the device are finally discussed as well as future developments and perspectives.

The developed device and method pave the way to faster devices for high-throughput T-cell screening and applications in adoptive cell therapies.

Key words: Microfluidics, hydrodynamic traps, dielectrophoretic traps, cell-cell contact, receptor-ligand interaction

# Résumé

Les organismes multicellulaires requièrent une régulation très fine dans leur communication inter-cellulaire, adhésion, coordination et mort programmée pour assurer l'homéostasie de l'organisme. Ces fonctions sont assurées par des récepteurs spécialisés placés dans la membrane cellulaire, récepteurs dont la liaison à leur ligand déclenche une fonction cellulaire définie. En effet, les liaisons récepteur-ligand assurent non seulement l'adhésion physique inter-cellulaires ou cellule-matrice, mais permettent aussi le transfert d'information. Des récepteurs défaillants, ne déclenchant pas la réponse appropriée, mettent en péril la capacité de l'organisme à fonctionner. Notre compréhension des pathologies occasionnées par de tels dysfonctionnements dépend donc de notre capacité à étudier les interactions récepteur-ligand. Cependant, les outils actuellement disponibles, capables de mettre en contact deux objets micrométriques pendant une durée contrôlée puis d'évaluer leur état d'adhésion sont encombrants, très lents et leur utilisation requiert du personnel spécialisé. L'interaction contrôlée entre deux cellules est particulièrement intéressante dans le domaine de l'immunothérapie. En effet le procédé de sélection de cellules T avec une haute activité antitumorale reste pour le moment très long et coûteux, limitant l'accès à ce genre de thérapie malgré leur efficacité prouvée. Dans ce contexte, un outil permettant de mettre en contact des cellules T avec des cellules cancéreuses de manière fiable et capable d'évaluer la spécificité de l'interaction pourrait simplifier le long processus de sélection de cellules T et faciliter l'accès à de telles thérapies sur le long terme.

Afin d'attaquer cette problématique, ce travail propose un outil microfluidique qui combine deux moyens de piégeage d'objets micrométriques, comme des billes ou des cellules, et capable de contrôler leur contact physique et d'évaluer leur adhésion. Comme les méthodes de piégeage utilisées dans cet outil dérivent de phénomènes physiques distincts, leurs effets sont orthogonaux et permettent une manipulation indépendante des deux objets.

La première partie de cette thèse décrit une nouvelle méthode pour le piégeage hydrodynamique de billes et de cellules, basée sur deux niveaux superposés de canaux microfluidiques et interconnectés par des via microfluidiques. Ce type de pièges hydrodynamiques permet l'immobilisation d'objets sans que l'effet utilisé pour le piégeage n'influence pour autant les objets environnants. Cette méthode est une pierre angulaire de l'outil développé car l'évaluation de l'adhésion entre deux objets ne peut être fiable que lorsque les méthodes de piégeries n'ont pas d'effets entrecroisés. Un nouveau procédé de microfabrication a donc été développé afin de fabriquer des canaux tridimensionnels dans un substrat totalement transparent. Le mécanisme de piégeage des cellules est tout d'abord caractérisé dans des pièges uniques afin de définir le cadre d'opération qui garantit la manipulation de cellules sans les endommager. Le piégeage et l'arrangement de billes et de cellules dans de grandes matrices de pièges est aussi présenté afin de démontrer les capacités du système.

De plus, une forme d'électrodes coplanaires est proposée permettant de créer un champ diélectrophorétique tridimensionnel dirigé vers un seul point contre le flux. Ces pièges DEP sont utilisés en combinaison avec un système de déviation afin de contrôler le nombre d'éléments par piège. Le piégeage d'objets uniques ainsi que la création d'agrégats de cellules de composition contrôlée issus de deux populations de cellules distinctes sont démontrés.

Finalement, les deux mécanismes de piégeage sont combinés afin de fournir un dispositif capable d'effectuer l'interaction cellule-cellule et bille-cellule avec une résolution dans le temps de contact d'une seconde. La fonctionnalité de l'outil est validée par un test de fréquence d'adhésion entre des fibroblastes et des billes couvertes de fibronectine. Les paramètres de cinétique d'adhésion sont extraits de ce test et comparés à la littérature, démontrant un bon accord avec les valeurs précédemment rapportées. Le potentiel du dispositif pour des applications d'immunothérapie est démontré par la mise en contact de cellules T et de cellules cancéreuses. La durée de vie des paires est mesurée et l'effet des liens TCR-pMHC sur cette dernière est démontré. Une mesure de l'avidité basée sur la vitesse de dissociation des paires est également proposée. Finalement, les caractéristiques du dispositif ainsi que les futurs développements et perspectives sont discutés.

Le dispositif et la méthode proposés définissent une base de travail pour réaliser des dispositifs plus rapides et plus performants capables de sélectionner des cellules T pour des applications de thérapies adoptives.

Mots clefs : Microfluidique, pièges hydrodynamiques, pièges diélectrophorétiques, contact cellule-cellule, interaction récepteur-ligand

# Contents

<b>Acknowledgements</b>	<b>i</b>
<b>Abstract (English/Français)</b>	<b>v</b>
<b>List of figures</b>	<b>xiii</b>
<b>List of tables</b>	<b>xvii</b>
<b>1 Introduction</b>	<b>1</b>
1.1 Transmembrane receptor-ligand interaction . . . . .	2
1.1.1 Binding kinetics . . . . .	2
1.1.2 Early downstream signalling molecules . . . . .	6
1.1.3 Late molecule production and cell behaviour . . . . .	7
1.2 Characterizing cell-cell adhesion in immunotherapy . . . . .	7
1.3 Tools for the controlled contact between two objects . . . . .	8
1.3.1 Single cell approaches . . . . .	9
1.4 Microfluidics for the controlled contact between two objects . . . . .	10
1.4.1 Compartmentalization . . . . .	11
1.4.2 Dynamic contact . . . . .	13
1.5 Microfluidics combined with other forces for the controlled contact between two objects . . . . .	13
1.6 Scope of the thesis . . . . .	16
<b>2 Planar hydrodynamic traps and buried channels</b>	<b>17</b>
2.1 Standard hydrodynamic trapping principles . . . . .	17
2.2 Strategy . . . . .	19
2.3 Fabrication process literature . . . . .	20
2.4 Fabrication . . . . .	22
2.4.1 Process description . . . . .	22
2.4.2 Process discussion . . . . .	22
2.4.3 Design rules . . . . .	24
2.5 Principle of operation . . . . .	25

2.6	Holding forces: 2D modeling and calculation . . . . .	27
2.7	Materials and methods . . . . .	31
2.8	Characterization of single cell trapping . . . . .	31
2.9	Hydrodynamic trapping of beads in large arrays . . . . .	35
2.10	Hydrodynamic trapping of cells in arrays . . . . .	37
2.10.1	Mammalian cells . . . . .	37
2.10.2	Algae cells . . . . .	39
2.11	Selective trapping . . . . .	40
2.12	Discussion . . . . .	42
2.13	Other applications . . . . .	45
2.13.1	Configuration modalities . . . . .	46
2.13.2	Application . . . . .	47
2.13.3	Flow control strategies . . . . .	49
2.14	Conclusion . . . . .	50
<b>3</b>	<b>Array of dielectrophoretic traps</b>	<b>53</b>
3.1	Motivation and literature . . . . .	54
3.2	Requirements . . . . .	54
3.3	Review of electrode configuration . . . . .	55
3.4	Consideration for the manipulation of cells with DEP . . . . .	57
3.5	Dielectrophoresis for the creation of multicellular aggregates . . . . .	58
3.6	Materials and methods . . . . .	59
3.6.1	Microfabrication . . . . .	59
3.6.2	Materials . . . . .	61
3.6.3	Cell culture . . . . .	61
3.6.4	Chip operation . . . . .	61
3.6.5	COMSOL simulations . . . . .	62
3.7	Concept . . . . .	62
3.7.1	Deviation system . . . . .	63
3.7.2	Counter electrode configuration and simulations . . . . .	65
3.8	Single object trapping . . . . .	67
3.8.1	Bead trapping efficiency . . . . .	67
3.8.2	Single cell trapping . . . . .	70
3.9	Multiple cell trapping . . . . .	71
3.9.1	Scaling rules . . . . .	71
3.9.2	Formation of aggregates of controlled size and composition . . . . .	74
3.10	Conclusion . . . . .	75

<b>4 Combined trapping</b>	<b>77</b>
4.1 Concept . . . . .	77
4.2 Workflow . . . . .	78
4.3 Materials and methods . . . . .	79
4.3.1 Fabrication . . . . .	79
4.3.2 Chip preparation and setup . . . . .	83
4.3.3 Cell culture and preparation . . . . .	84
4.3.4 Medium compatibility . . . . .	85
4.4 Experimental validation of the concept . . . . .	85
4.5 Application to Fibronectin-Fibroblast interaction . . . . .	87
4.6 Application to T-cell-cancer cell interaction . . . . .	89
4.6.1 Medium compatibility . . . . .	89
4.6.2 Results . . . . .	92
4.7 Application to CAR-T cell-cancer cell interaction . . . . .	95
4.7.1 Results . . . . .	95
4.8 Analysis of forces . . . . .	96
4.9 Discussion . . . . .	100
4.10 Conclusion . . . . .	101
<b>5 Perspective and conclusions</b>	<b>103</b>
5.1 Summary . . . . .	103
5.2 Perspective . . . . .	105
5.2.1 Future technological developments . . . . .	106
5.2.2 Other applications . . . . .	108
<b>A Transition pressure</b>	<b>111</b>
<b>B Flow perfusion</b>	<b>113</b>
<b>C Contact between two cells using standard hydrodynamic traps</b>	<b>115</b>
<b>D Aperture-controlled fabrication of all-dielectric structural color pixels</b>	<b>121</b>
D.1 Abstract . . . . .	121
D.2 Introduction . . . . .	122
D.3 Results . . . . .	123
D.3.1 Fabrication . . . . .	123
D.3.2 Cross-section characterization . . . . .	126
D.3.3 Physical modeling . . . . .	127
D.3.4 Validation of reflectance spectra and color appearance . . . . .	128
D.3.5 Color palette . . . . .	131
D.4 Conclusion . . . . .	133

D.5 Materials and methods . . . . .	135
D.5.1 Fabrication . . . . .	135
D.5.2 Reflectance spectrum measurements . . . . .	136
D.5.3 Miscellaneous . . . . .	137
<b>Bibliography</b>	<b>139</b>
<b>Acronyms</b>	<b>157</b>
<b>Curriculum Vitae</b>	<b>159</b>

# List of Figures

1.1	Schematic representation of the effect of a transmembrane receptor binding to its associated ligand. . . . .	3
1.2	Representation of the energy landscape along the distance separating the receptor and the ligand. . . . .	4
1.3	<b>a</b> Evolution of the lifetime of a bond as a function of the disruptive force for catch bonds and slip bonds. <b>b</b> Extraction of the off-rate parameter from lifetime and probability of adhesion measurement . . . . .	5
1.4	Process of adoptive cell therapy based on the interaction between antigen presenting cells (antigen presenting cell (APC)s) engineered to express peptides resulting from somatic mutation with T-cells. Figure from (Rosenberg & Restifo, 2015) . . . . .	8
1.5	Illustration of the tools for the analysis of receptor ligands interactions <b>a</b> with SPR in a 2D configuration <b>b</b> using AFM (2D) <b>c</b> using the DPA 2D method <b>d</b> using OT (2D) method. Reprinted with permission from (Ungai-Salanki et al., 2019). Copyright 2019 Elsevier. . . . .	9
1.6	Examples of compartmentalization strategies for the contact between objects.	12
1.7	Examples of dynamic contact strategies. . . . .	14
1.8	Example of devices using DEP for the controlled contact between two objects. .	15
2.1	Example of standard "contact based" hydrodynamic trapping principles. . . . .	18
2.2	Process for the fabrication of the chips. . . . .	23
2.3	<b>a</b> SEM picture of an access hole cross section showing the Al <sub>2</sub> O <sub>3</sub> mask sandwiched between the LTO layers and the sealing of the access hole. <b>b</b> SEM image of a planar hydrodynamic trap cross section made using FIB etching. The sloped profile of the trap is visible together with the buried channel underneath. . . . .	23
2.4	Bright-field picture of a buried channel connecting a single trap in the main PDMS channel on the left to the PDMS control channel on the right. . . . .	25
2.5	Scheme showing the different modes of operation. . . . .	27
2.6	Representation of the 2D simulation model for the analysis of the different forces acting on a trapped bead of radius $R$ in a trap of dimension $G$ . . . . .	28



2.7	<b>a</b> Representation of the pressure and shear stress at each mesh node on the COMOSL model with the colour indicating the pressure value in the channel. <b>b</b> Analysis of the simulated data using MATLAB: Pressure and shear forces are represented at each mesh node with respective generated moment. The positive moments maintain the bead in the trap whereas negative moments induce rotation of the bead outside of the trap. . . . .	29
2.8	Sum of moments of different sources as a function of control pressure $P_c$ for an inlet pressure of 10000 Pa, a bead diameter of 5 $\mu\text{m}$ and a trap width of 2 $\mu\text{m}$ . <b>a</b> Generic view. <b>b</b> Zoom in view of the pressures at which the moment switch from positive to negative. . . . .	30
2.9	Brightfield pictures showing a sequence of trapping and releasing of a Colo205 cell in a single trap. . . . .	32
2.10	Fluorescent pictures of the different cells outcomes when trapped. . . . .	33
2.11	Characterization of single cell trapping in different hydrodynamic trap diameters and pressure conditions. . . . .	34
2.12	Characterization of bead trapping in large arrays of traps. . . . .	37
2.13	Fluorescent picture showing the successful trapping of 24 Colo205 cells stained with calcein AM in an array of 25 traps. The pressures are set so that the difference of pressure $\Delta P_p$ endured by the cells is always under the pressure threshold for membrane rupture. . . . .	39
2.14	Sequence of brightfield pictures showing an empty array ( <b>a</b> ), the trapping of <i>Chlorella</i> cells ( <b>b</b> ), the array of traps filled with <i>Chlorella</i> cells ( <b>c</b> ) and the release of the cells ( <b>c</b> ). The array is composed of 921 traps. . . . .	40
2.15	<b>a</b> Schematic representation of the device used for the selective trapping of beads with two inlets and three lines of interconnected traps controlled by individual control channels. <b>b</b> Brightfield picture of the trapping chamber. . . . .	41
2.16	Superposition of fluorescent pictures taken in the orange and green channels showing the sequential loading of the traps and demonstrating the selective trapping capability of the planar hydrodynamic trapping approach. . . . .	42
2.17	Timelapse image of three cells flowing around the ones immobilized in an array of traps in a "roll-over" manner showing the potential of the device to be used for interaction studies. The cells flowing in the channel are coloured in red by image processing for a better visualization. . . . .	45
2.18	Examples of configuration modalities achievable with the buried channel process.	46
2.19	Example of applications using the buried channel technology. . . . .	47
2.20	Example of flow control strategies. . . . .	50

3.1	Different electrode configurations for generation of a non-uniform electric field used in DEP actuated particles manipulation. The voltage is applied to the electrodes colored in black and the counter electrode is colored in pink. . . . .	55
3.2	Fabrication of coplanar configuration chips. . . . .	59
3.3	Fabrication of facing configuration chips. . . . .	60
3.4	Deviation system, electrodes design and configuration. . . . .	63
3.5	COMSOL simulation along a $xz$ plane in the center of the trap for both configurations. . . . .	64
3.6	3D COMSOL simulation representing the iso-surfaces of the electric field squared $E^2$ for both configurations. . . . .	66
3.7	Characterization of the trapping efficiency. . . . .	68
3.8	Characterization of electroporation. . . . .	72
3.9	Effect of the geometry and channel height on the three dimensional trapping behaviour of coplanar electrodes. . . . .	73
3.10	Proof of concept of the ability of the presented system to create aggregates of controlled size and composition. . . . .	74
4.1	Schematic representation of the microfluidic chip and workflow. . . . .	79
4.2	Processes for the fabrication of chips comprising buried channels and structured electrodes in their vicinity. . . . .	81
4.3	SEM pictures of the fabricated traps. . . . .	82
4.4	Layout of the chips. . . . .	82
4.5	Picture of the experimental setup. . . . .	83
4.6	Pictures of the chip. . . . .	84
4.7	Pictures of the fabricated chips and timelapse image of an interaction. . . . .	86
4.8	Timelapse image of an interaction between four NIH-3T3 cells (highlighted in green by image processing) as DMPs and fibronectin coated beads as HTPs put in contact during 30 seconds. Half of the cells stayed attached to the beads after the forced contact. . . . .	87
4.9	Adhesion assay between fibronectin coated beads and integrin expressing cells. . . . .	89
4.10	Intracellular IFN- $\gamma$ and TNF- $\alpha$ content after 5 h co-incubation of T-cell clones with specific peptide in different media. . . . .	90
4.11	Viability of Colo205 and CD8 T-cells at different stages of immersion in specific medium. . . . .	91
4.12	T cell viability at different stages of immersion in different media. . . . .	91
4.13	Optical microscope picture of a T-cell in contact with a cancer cell after the forced contact spontaneously adhering. . . . .	92

4.14	Pair lifetime measurements after 22 seconds of forced contact between Colo205 and T-cell clones in the case where the Colo205 cells were pulsed (specific) and non pulsed (non specific) with the TCRs cognate peptide. . . . .	93
4.15	Experimental $\ln(P_i(t))$ taken as the natural logarithm of the number of events with a lifetime longer than the $x$ axis as a function of time. The slope of the linear fit represents the lumped off-rate of the pairs. . . . .	94
4.16	Sequence of the interaction between a HER2 expressing SKOV-3 cell and a CAR expressing B3Z cell . . . . .	96
4.17	Simulation used to estimate the drag and dielectrophoresis force acting on the DMPs. . . . .	98
5.1	Proposition of a 2nd generation device free from the need for a deviation system.	107
A.1	Pressure $P_c$ at which the moments of different sources are null, called transition pressure, as a function of trap width for an inlet pressure of 10000 Pa, a bead diameter of 8 $\mu\text{m}$ . . . . .	111
B.1	Timelapse images illustrating the focusing capability of the buried channels. . .	114
C.1	Layout of the device for the controlled contact between two objects using DEP and standard hydrodynamic traps made from PDMS. The electrode layer is displayed in green and the PDMS layer in yellow. . . . .	116
C.2	Result of the 3D simulation of the device with isosurface of the electric field displayed in grey. The direction of the $z$ component of the nDEP force is shown in red for the external and internal part of the structure. . . . .	117
C.3	Timelapse image of the trajectory of cells flowing in the device. . . . .	117
C.4	Timelapse image of the forced contact between two cells. . . . .	119
D.1	Concept of the aperture-controlled thin film stack for interference-based colors.	124
D.2	Process for the fabrication of the structures and characterization of the thicknesses.	125
D.3	Modelled color appearance and reflectance spectra. . . . .	130
D.4	Simulated and measured reflectance spectra. . . . .	131
D.5	Layout for the colour palette structures. . . . .	132
D.6	Colors palettes fabricated using different mask and substrate materials. . . . .	134
D.7	Large scale colorful fabricated using individually colored pixels. . . . .	135

# List of Tables

2.1	Description of the parameters for the sequential filling of three lines of traps with green and orange fluorescent beads using individual pressure control channels and two inlets. The pressures are in mbar. . . . .	41
4.1	Forces acting on the DMPs for polystyrene bead and the T-cell with respective radius . . . . .	99



# 1 Introduction

Multicellularity arose first 3-3.5 billion years ago and occurred 25 times independently throughout the evolution. Only six occurrences however lead to complex organisms to form plants, animals, fungi, red, green and brown algae groups (Grosberg & Strathmann, 2007). Multicellular organisms can benefit from the advantages of having a large size without suffering the disadvantages of small surface to volume ratios. It allows to bypass the intrinsic limitations of small surface to volume ratio such as diffusion (Kaiser, 2001) while benefiting from functions of increased complexity. They nevertheless require very well organized and finely balanced cell-cell communication, adhesion, coordination and programmed cell death to ensure the organisms fitness. These functions rely on specialized receptors placed at the cells membrane whose binding to their cognate ligand triggers a defined function. Thus receptor-ligand interaction is a cornerstone of multicellularity, not only maintaining the cells physically adhered together, but also enabling communication to ensure function and organism homeostasis. Malfunction of these receptors to properly trigger the appropriate response leads to imbalances in the organism and failure to exert specific functions. Our understanding of these pathologies thus relies on the capacity to study such interactions. Cancer is a well known example of cells failing to cooperate with their organism and has been observed in all groups of multicellular organisms. Some researchers found evidence that cancer is associated with a silencing of genes linked to multicellularity (Pennisi, 2018), favouring a selfish behaviour to take advantage of the host organism to proliferate.

Endocrine, or long distance communication relies on the transfer of molecules from one cell to another via the bloodstream. The ligand molecules, in that case hormones, are therefore broadcast to the entire body without specificity and ensure communication between different parts of the body such as organs. Medium range or paracrine signalling is defined when molecules diffuse locally from the secretory cell to neighbouring cells. The binding between a receptor and a surface-bound ligand is part of the contact-dependent signalling and as its name suggests requires the close contact between the two surfaces. Contact-based

signalling is mainly ensured by transmembrane cell receptors that are not only responsible for transferring information, but are also capable of physically maintaining two cells adhered to one another (Alberts, 2010). Transmembrane proteins are divided into four main families: integrins, selectins, cadherins and the immunoglobulin superfamily (Aplin et al., 1998). While integrins typically bind to proteins of the extracellular matrix such as collagen, fibronectin or vitronectin, the other families bind to ligands present on other cell membranes.

## 1.1 Transmembrane receptor-ligand interaction

Transmembrane receptors are complex proteins typically comprising three different domains. The extracellular domain comprises the receptor binding part that specifically attaches to the ligand. The membrane domain is hydrophilic and ensures the anchoring of the receptor in the phospholipid bilayer membrane and the intracellular domain triggers the intracellular signalling. A representation of a transmembrane receptor and the different domains is provided in the inset of Figure 1.1. The cascade of events triggered by the binding of a ligand to a receptor is illustrated in Figure 1.1 (Alberts, 2010). The receptor transduces a binding event into a change of conformation of the intracellular domain. This triggers a cascade of downstream signalling inside the cell, called a signal transduction pathway. This cascade results in the migration of a transcription factor to the nucleus and the expression of the associated gene, which defines the cell response to the stimulus, such as migration, differentiation, division, secretion, morphological changes or apoptosis. Characterization of receptor-ligand interactions is thus necessary to understand how they define the underlying biologic processes and understand the associated pathologies. We can identify three main strategies to characterize and measure receptor-ligand interactions, ranging from the early events to later effects. The first method consists in characterizing the very first events of receptor-ligand binding by measuring their binding kinetics parameters. The second strategy relies on measuring the early downstream signalling molecules inside the cell. The third one is based on the characterization of the cell reaction to the binding by measuring late events of molecules production and cell behaviour.

### 1.1.1 Binding kinetics

Receptor-ligand binding parameters comprise the on-rate ( $k_{on}$ ) which describes how fast the complex forms, the off-rate ( $k_{off}$ ), or how long the bond lasts. The dissociation constant ( $K_D = k_{off}/k_{on}$ ) represents the concentration of ligand necessary for half of the receptor to be occupied at equilibrium. The association constant  $K_A$  is defined as the inverse of  $K_D$  and both terms are routinely used to describe kinetics. The overall equilibrium equation describing the

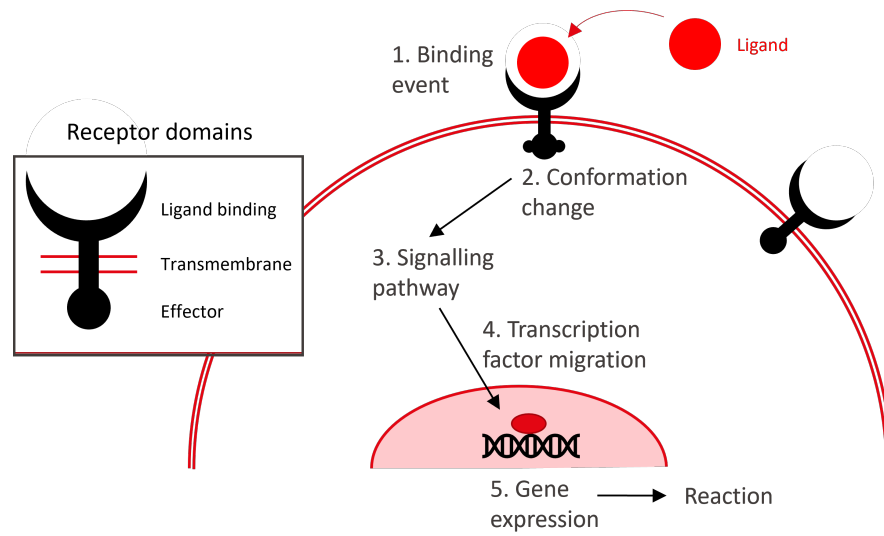


Figure 1.1: Schematic representation of the effect of a transmembrane receptor binding to its associated ligand. A conformation change occurs in the intracellular domain upon recognition of the ligand by the binding site which triggers an intracellular signalling cascade. This latter results in the migration of a transcription factor to the nucleus and expression of the associated gene(s) that defines the cellular response to the stimulus. The inset shows the different domains of a generic transmembrane receptor.

relation between ligand  $L$ , receptor  $R$  and receptor-ligand complex  $RL$  concentration is the following:



These values are typically obtained from so called 3D methods, that are defined by the use of ligand and/or receptor in suspension for the kinetics measurement. 3D methods are valid to model paracrine and endocrine signalling, but display two major obstacles to correctly represent *in-vivo* behaviour in the case of contact-based signalling. First the binding kinetics are measured in a force free system which does not represent the dynamic reality. Secondly, one of the compounds is in solution which adds an orientation component to the equation that is not present when the receptor and ligand are both anchored to surfaces. 2D methods on another hand consider ligands and receptors anchored to surfaces and provide better models for the characterisation of contact-based signalling (B. Liu et al., 2015).

### Effect of a force

First-order forward and backward kinetics are described by a single energy barrier in the potential landscape along the distance between the receptor and the ligand as represented in Figure 1.2. A slip bond describes a type of bond whose energy barrier decreases upon



application of a disruptive force and its result on the energy landscape is shown by the blue line in Figure 1.2 and 1.3a. (Bell, 1978) proposed that lowering this energy barrier results in an increase in the dissociation rate following equation 1.2.

$$k_{off} = k^0 \exp(F/F_b) \quad (1.2)$$

In this model,  $k^0$  is the off-rate under zero force,  $F_b$  is the force necessary to lower the energy barrier by one unit of thermal energy  $k_b T$  with  $k_b$  the Boltzmann constant and  $T$  the absolute temperature. This was later experimentally verified for numerous receptor-ligand complexes. Other types of bonds were discovered such as the catch bond, whose off-rate decreases under

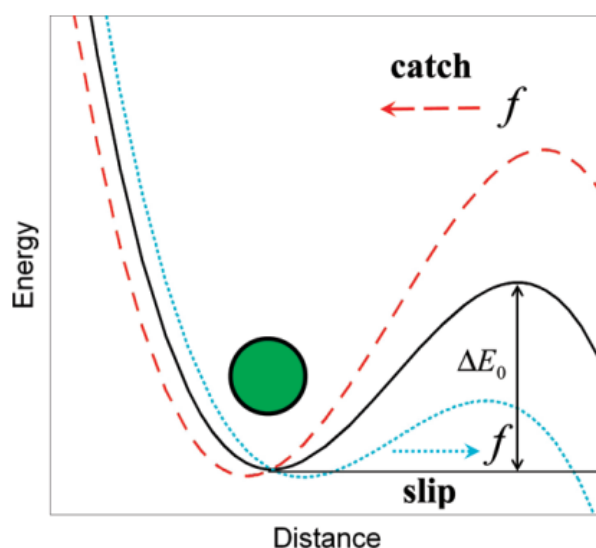


Figure 1.2: Representation of the energy landscape along the distance separating the receptor and the ligand. The effect of a disruptive force is represented for catch bonds in red and slip bonds in blue. Reprinted with permission from (Prezhdo & Pereverzev, 2009). Copyright 2009 American Chemical Society.

increasing force as represented by the red line in Figure 1.2 and 1.3a. Known example of catch bonds include integrins and E-cadherins (Kong et al., 2009). The lifetime of an ideal bond is not affected by a change in the force applied to it (B. Liu et al., 2015).

## Model

The equations presented in this section can be derived assuming that a species of either receptor or ligand outnumbers the other. This scenario neglects the depletion of the species in excess upon formation of bonds. For a controlled contact time  $t$  between the two surfaces and given the surface density of the most abundant species  $m_{max}$  and the least abundant  $m_{min}$ ,

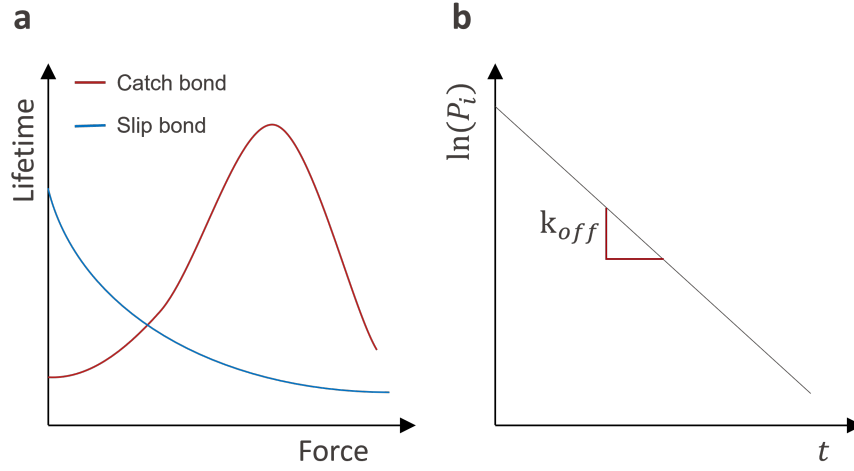


Figure 1.3: **a** Evolution of the lifetime of a bond as a function of the disruptive force for catch bonds and slip bonds. **b** Extraction of the off-rate parameter from lifetime and probability of adhesion measurement

the probability of formation of a bond is given by the following equation (Chesla et al., 1998):

$$p(t) = \frac{m_{max}k_{on}}{m_{max}k_{off} + k_{on}} [1 - \exp(-(m_{max}k_{on} + k_{off})t)] \quad (1.3)$$

With  $A_c$  the effective contact area, the probability of forming  $n$  bonds out of the maximum possible bonds formed  $A_c m_{min}$  is given by the binomial distribution:

$$p_n = \binom{A_c m_{min}}{n} (p(t))^n [1 - p(t)]^{A_c m_{min} - n} \quad (1.4)$$

Given the  $n_{min}$  minimum number of bonds necessary to withstand the disruptive force applied to test an adhesion between the two surfaces, the probability  $P_a$  of observing an adhesion event as a function of contact duration is expressed as:

$$P_a = 1 - \sum_{C=0}^{n_{min}-1} P_C(t) \quad (1.5)$$

To obtain the binding kinetics parameter and characterize a bond, two objects are put in contact during a controlled duration. Once the duration is elapsed, the two objects are pulled apart using a disruptive force and the adhesion state, adhered or non adhered is observed. The measure is made repeatedly and the probability of adhesion is approximated by the frequency of observed adhesion. A fit of the frequency of adhesion as a function of contact duration following equation 1.5 is made to obtain the parameters of interest (Chesla et al., 1998).

In the specific case where the surface densities of the entities are low enough to ensure that

single bonds are formed after the contact, the off-rate can be directly deduced from the measurements of the lifetimes of the complex. Indeed the probability  $P_i$  of a bond formed at time  $t = 0$  to remain intact at time  $t$  is defined by:

$$P_i(t) = \exp(-k_{off} t) \quad (1.6)$$

The probability  $P_i(t)$  is approximated by the number of events with a lifetime larger than  $t$ . The slope of the linear fit of  $\log_{10}(P_i)$  then directly provides access to a measure of  $k_{off}$  (W. Chen et al., 2008) as illustrated in Figure 1.3b.

### 1.1.2 Early downstream signalling molecules

Downstream signalling pathways comprise many molecules and are highly complex. Rather than a straight cascade, it includes a network with many branches while branches generated by different receptors can be identical and overlap. These pathways include different proteins and smaller molecules, called second messengers. Second messengers diffuse quickly in the cells and are thus ideal when fast signalling is required, even though they are less specific. Calcium ions  $\text{Ca}^{2+}$  are a type of second messenger that are stored in the endoplasmic reticulum compartment. They can be released in the cytoplasm via the activation of ion channels to further transmit a signal and are important in processes such as muscle contraction or neuronal transmission. Proteins convey a signal via allosteric regulation, in which the binding of a molecule induces a change in the protein conformation. An example is protein phosphorylation by a protein kinase, or by exchanging one of its guanosine triphosphate (GTP) for a guanosine diphosphate (GDP). Many phosphorylated proteins are protein kinases themselves, that generate a cascade of phosphorylation events. Signalling pathway often results in the migration of a transcription factor to the nucleus and the transcription of the associated gene. (Alberts, 2010).

Different methods exist to study the signalling pathways, most of them relying on fluorescent markers (Jeknic et al., 2019). Most traditional methods such as western blot and immunocytochemistry require either cell lysis or cell fixation and have a poor temporal resolution. Furthermore, these methods cannot be used for longitudinal analysis of cell behaviour. An example of dynamic live-cell method consists in tagging a transcription factor and following its localisation. With this method, a translocation to the nucleus indicates an activation of the associated pathway (Cai et al., 2008; Paek et al., 2016). Kinase activity can be measured using kinase transcription reporter (KTR), which are engineered fluorescent protein constructs that translocate to the nucleus after their phosphorylation by a specific kinase. Thus the intensity of the fluorescence of the nucleus is an indicator of the general activity of this specific targeted kinase in the cell (Kudo et al., 2017). Kinase, protease and phosphatase activity can also be located within the cell using Förster resonance energy transfer (FRET). FRET mechanism is

based on the transfer of energy from a donor fluorophore to an acceptor fluorophore. The light emission from the acceptor is extremely sensitive to the spatial proximity of the donor. FRET reporters are protein constructs with tagged acceptor and donors. A change in the protein conformation upon modification by a specific molecule changes the distance between the acceptor and donor fluorophores. The activity of the molecule can be characterized by a modification in fluorescence emission of the acceptor fluorophore with high spatial and temporal resolution (Hellwig et al., 2008; Zhang et al., 2001). The cytosolic concentration of second messengers like calcium can be imaged via fluorescent reporters, whose emission intensity is increased upon binding of calcium ions (Gee et al., 2000; Hideharu & Haruo, 1994).

### 1.1.3 Late molecule production and cell behaviour

After translocation of the transcription factor to the nucleus and transcription of the associated gene, different methods can be used to assess cell response to the stimulus. Transcriptomics relies on the analysis of the produced ribonucleic acid (RNA) and its changes associated with the stimulus (Kulkarni et al., 2019). After RNA translation, the produced protein can be analyzed and quantified using enzyme linked immunosorbent assay (ELISA) (Tighe et al., 2015), ELISPOT (Kalyuzhny & Kalyuzhny, 2005) or immunoassays methods (Wu, 2006). In turn, optical microscopy methods can be used to assess morphological changes, migration, differentiation or cell death following an interaction stimulus.

## 1.2 Characterizing cell-cell adhesion in immunotherapy

There is a growing interest for cell based therapies because of their curing potential of various diseases. This type of therapy consists in injecting cells selected or engineered for their curing potential to the patients (Heathman et al., 2015). In particular, adoptive cell transfer (ACT) is a promising personalized approach for cancer treatment which consists in administrating activated autologous or allogenic T-lymphocytes with anti-tumor activity to the patient (Garber, 2018). A first approach of ACT uses T-lymphocytes which are genetically engineered to express T-cell receptor (TCR) or chimeric antigen receptor (CAR) with high affinity to the tumor antigens. The challenge consists in finding the right antigen to target because aiming at an overexpressed antigen can be dangerous as it can drive off-target recognition of normal tissues and toxicity. Targetting neoantigens is a safer approach, as these antigens result from somatic mutations in the tumor genome and are specific by definition. However, this specificity also implies a highly personalized therapy to identify the mutations in the genome that code peptides expressed by the major histocompatibility complex (MHC), for which there is currently no reliable predictive algorithm (Garber, 2018). The identification and

selection of the corresponding T-cells is currently made by co-culturing APC engineered to express the peptides resulting from the mutation with autologous T-cells as shown in Figure 1.4. This process is not only time consuming but also very expensive, thus limiting the generalization of such approach despite their proven efficacy (Rosenberg & Restifo, 2015). Another approach consists in isolating tumor infiltrated lymphocyte (TIL)s that are T-cells found at the tumour site and presenting a large proportion of tumor specific TCR. These cells are however exhausted and do not trigger an effective immune response (Jiang et al., 2015). The T-cells are thus stimulated, isolated after co-culture with tumor cells to test for specificity and expanded before re-injection in the patient for treatment (Rosenberg & Restifo, 2015).

In this context, a tool that allows researchers to reliably pair T-lymphocytes with APCs or tumor cells and rapidly assess the specificity of the interaction could simplify the long process of co-culture, facilitate in the long term the access to this kind of therapy and reduce its cost.

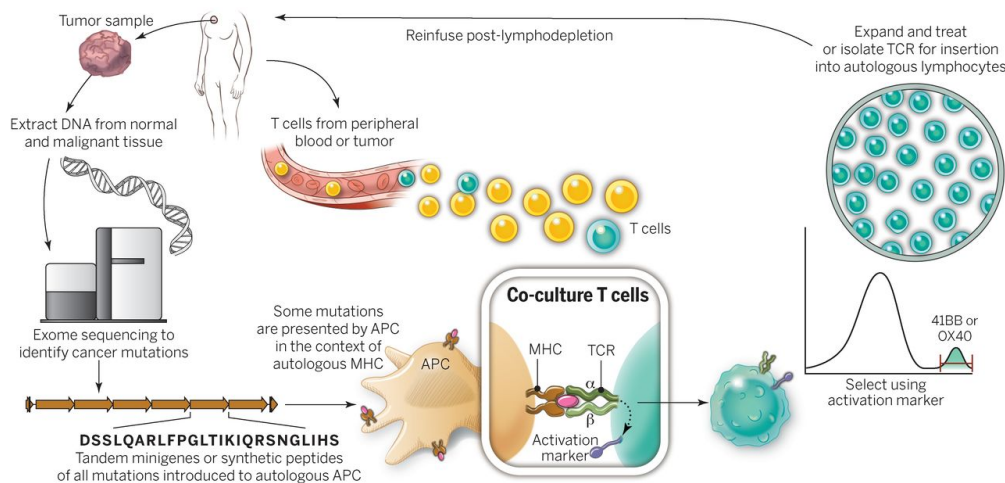


Figure 1.4: Process of adoptive cell therapy based on the interaction between antigen presenting cells (APCs) engineered to express peptides resulting from somatic mutation with T-cells. Figure from (Rosenberg & Restifo, 2015)

### 1.3 Tools for the controlled contact between two objects

3D methods are still widely used as a model to characterize 2D *in vivo* configurations because of their ease of access. They comprise the widely used surface plasmon resonance (SPR) method, in which light reflected from a surface coated with a receptor is sensitive to the quantity of ligand bound to it as illustrated in Figure 1.5a. Dynamics of binding and debinding are analyzed to extract binding kinetics parameters (Pattnaik, 2005). This cell-free system is fast and easy, but it is argued that it does not properly reflect contact-based signalling situations because of the reasons discussed above (B. Liu et al., 2015).

Numerous tools were developed to characterize the interaction between transmembrane

receptors and their ligands in a 2D configuration. Bulk methods comprise centrifugation (Angres et al., 1996), flip-chip (Carmona-Fontaine et al., 2011) and acoustic force (Yerbury, 2022) methods which are interesting when analyzing cell populations and when time resolution is not critical (larger than a minute).

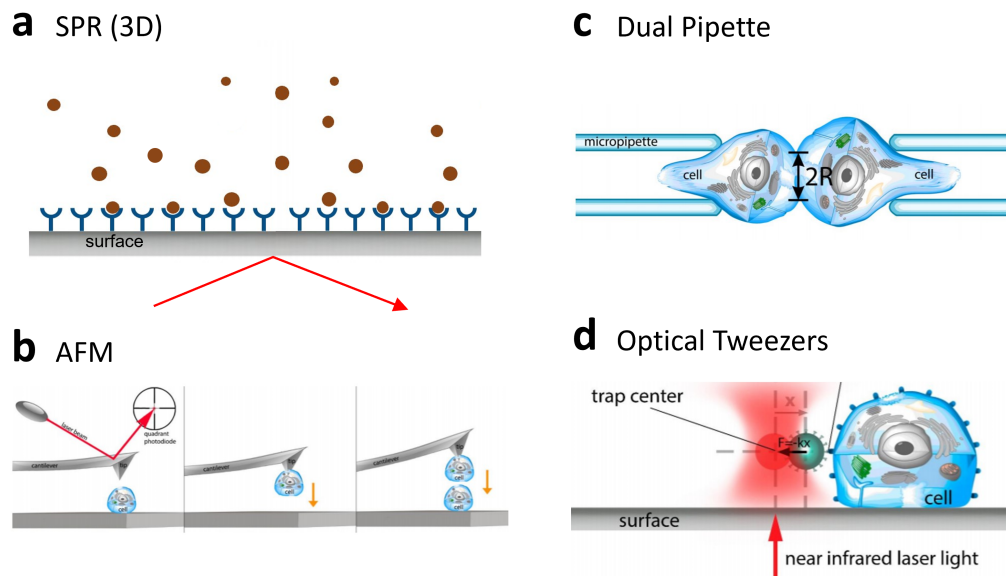


Figure 1.5: Illustration of the tools for the analysis of receptor ligands interactions **a** with SPR in a 2D configuration **b** using AFM (2D) **c** using the DPA 2D method **d** using OT (2D) method. Reprinted with permission from (Ungai-Salanki et al., 2019). Copyright 2019 Elsevier.

### 1.3.1 Single cell approaches

Even though cells share the same genetic material, expression of their genes varies not only upon cell type but also within a cell population and define shape, function and activity. For example the heterogeneous nature of tumor cells is well known and is responsible for cancer drug resistance, recurrence and formation of metastasis. The 2D single-cell analysis tools described below emerged as a solution to unveil heterogeneity in a cell population and some examples of these tools are illustrated in Figure 1.5**b-d**. Atomic force microscopy (AFM) is a precision tool of choice to measure the force characteristics of a bond. The principle of this assay is represented in Figure 1.5**b**. With this approach a cell is picked and attached to the tip of a soft microfabricated cantilever using either surface functionalization (Helenius et al., 2008) or embedded fluidic system (Potthoff et al., 2012) and used to contact another cell adhered to a substrate. The time of contact can be controlled before probing the adhesion state and measuring the force resistance of the formed bond(s) through the deformation of

the cantilever. Single bond detachment can be resolved thanks to the high force sensitivity of the probe.

Alternatively, the dual pipette assay (DPA) makes use of two micropipettes to attach one cell per pipette by suction as shown in Figure 1.5c. The pipettes can then be guided using micromanipulators coupled to high resolution high speed imaging to probe the adhesion state as a function of time of contact (Chesla et al., 1998). Variations of this method comprise the adhesion of a red blood cell coated with the ligand to one of the cells. Indeed red blood cells are soft and a precise force measurement of the bond can be deduced from their deformation. Alternatively, a bead coated with the ligand can be attached to an aspirated red blood cell and put in contact with the receptor presenting cell attached to the other pipette. In that case, the thermal fluctuations of the bead are measurable because of the high deformability of the red blood cells and indicate the adhesion state of the pair (W. Chen et al., 2008). It is then possible to directly measure  $k_{on}$  and  $k_{off}$  from the adhesion state timeline.

Optical tweezers (OT) are another tool that makes the precise manipulation of objects possible thanks to the attraction of particles towards the waist of a highly focused laser beam as shown in Figure 1.5d. OT are then able to both push an object trapped in the waist towards a cell adhered to a surface as well as pull on it with known force to probe the adhesion state and force of adhesion (Thoumine et al., 2000).

Some work used a combination of the different methods for the characterization of contacts (Ounkomol et al., 2010; Qian et al., 2004).

AFM, DPA and OT rely on a very soft spring linked to one of the cells to push and pull it to and from another cell to allow a controlled force and time of interaction. They are thus highly precise but provide a very low throughput and require highly skilled staff to perform the assay. Comprehensive reviews on the subject are provided by Johnson and Harley, 2011; Kashef and Franz, 2015; Ungai-Salanki et al., 2019; H. Wang et al., 2022. There is therefore a need for other methods capable of regulating the contact between micro-sized objects and probing their adhesion state. In fact, microtechnologies provide methods capable of manipulating micro-sized object with high precision and will be discussed in the next section.

## 1.4 Microfluidics for the controlled contact between two objects

The semiconductor industry seek for always smaller transistors and more powerful computers is the main drive for the development of new microfabrication technologies (Mollick, 2006). Consolidated microfabrication processes have later benefited other fields, ranging from the development of microelectromechanical systems to many other ones. Among them stands microfluidics, which handles fluids using channels with micrometer characteristic dimensions. Biology understood the potential of these methods for the precise manipulation of single cells by means of structures in their very same order of magnitude. When used to handle a

living suspensions in microchannels, microfluidic can perform different functions such as the immobilization in arrays using obstacles (Di Carlo et al., 2006), filtering by size (Yamada & Seki, 2005), exposure to concentration gradients of drugs (X. Liu et al., 2021), or encapsulation in micro-droplets separated by oil phase (Sarkar, 2015). Micro-scale operation not only has the advantage of requiring low reagents volume, but more importantly provides a fine control over the environment that allows to mimic *in vivo* conditions.

The different strategies used to place objects in close contact using microfluidics are reviewed here. Because the main drive for developing these strategies comes from immunotherapy applications, most of the examples presented use related cells or particles such as immune cells, cancer cells, APC or antibody coated beads. Comprehensive reviews on cell-cell pairing in microfluidic chips are provided by He and Hsu, 2021; Pang et al., 2021.

### 1.4.1 Compartmentalization

A first category of strategy relies on the compartmentalization of the particles in separate environments. This strategy implies that the readout for a receptor-ligand binding event is either obtained from downstream signalling or from cell behaviour. Indeed the method infers that the adhesion state cannot be probed by pulling apart the two objects. The challenge resides in the control of the loading of the compartment to obtain heterogeneous cell content and the compartmentalization of cells can rely either on an open configuration or on closed configuration. The closed configuration consists in obstacles placed in a microchannel to form cages. The control over the content of the cages was tackled by using deformation or sedimentation as loading mechanism. These works characterized the interaction by measuring the killing efficiency of target cells, dynamics of calcium release in immune cells or engulfment (Dura et al., 2015; Dura et al., 2016; Fan et al., 2021; Jang et al., 2015; Y. Li et al., 2017).

Another possibility to achieve precise positioning of particles includes the use of microwells together with sedimentation in open configuration. A cell suspension is placed on a substrate patterned with an array of wells of specific diameter and depth. With this approach the cells are left to sediment and subsequently washed to leave only the desired number of cells per well (Rettig & Folch, 2005). A very complete work presented by Y. Zhou et al. (2020) relies on microwells of tailored sizes with a hierarchical loading to capture particles of different sizes in a controlled manner. Such a device was used to pair a T-cell with a cancer cell and a capture antibody coated bead. This latter was used together with a fluorescent reporter to measure the cytokine production of the T-cells upon contact with the cancer cells. The T-cell movements were also tracked and the target cell killing efficacy measured for correlation with cytokines production. The measurements were done with cancer cells presenting different peptides to assess the specificity of the TCR to them.



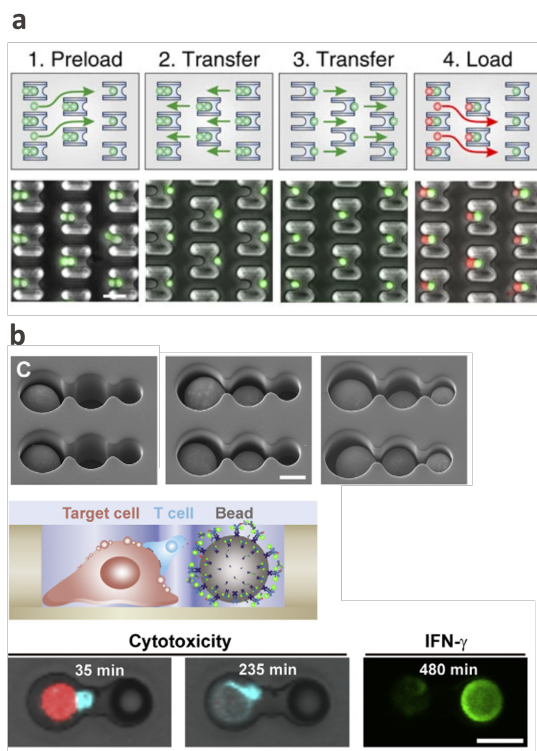


Figure 1.6: Examples of compartmentalization strategies for the contact between objects. **a** Example of closed configuration: two cells of different types are brought in closed contact in cages placed in a microfluidic channel thanks to a loading strategy as proposed by Dura et al. (2015). The fluorescent monitoring of intracellular calcium content was used to profile T-cells reaction upon contact to T-cell activator molecules. Reprinted with permission from (Dura et al., 2015). Copyright 2015 Springer Nature. **b** Example of open configuration: microwells of different sizes allow the precise loading of objects of corresponding diameter as developed by Y. Zhou et al. (2020). The system was used to load a T-cell, a cancer cell and a capture antibody coated bead for the analysis of cytokines production upon presentation of different peptides. Reprinted with permission from (Y. Zhou et al., 2020). Copyright 2020 Elsevier.

Droplets separated by oil phases are another mean of compartmentalizing cells that was used by different studies to assess cell-cell interaction by measuring parameters such as calcium signalling dynamics (Sarkar, 2015), cytotoxicity (Antona et al., 2020) or activation state (Segaliny et al., 2018). These methods are very gentle with the cells and provide them an environment close to physiological. They are thus well adapted for longitudinal analysis of early downstream molecules, late molecule production and cell behaviour upon contact to another cell. However they lack the possibility to perform serial cell interrogation and binding kinetics analysis.

### 1.4.2 Dynamic contact

Systems for the probing of dynamic and serial cell-cell and cell-bead interaction were developed in microfluidic chips. The methods starts by immobilizing the first type of object using either monolayer adhesion (Ashby et al., 2022; Moura Rosa et al., 2016), hydrodynamic traps (M. Duchamp et al., 2019; Stockslager et al., 2017) or hydrodynamic traps combined with sedimentation (Ide et al., 2020). The second type of cell is flown on top of the first objects and reduction in speed upon contact between the two objects, resistance to flow drag force, pair lifetime or calcium signaling is monitored to characterize the interaction. These systems are powerful tools to probe receptor-ligand interactions at higher throughput than the macro methods presented above and allow the measurement of  $k_{off}$  (M. Duchamp et al., 2019). However they are limited in the a possibility to control contact time between the two objects, which can be critical when the pairs need a minimum encounter time for binding such as the TCR-peptide major histocompatibility complex (pMHC) bond (M. C. M. Duchamp, 2020; Limozin et al., 2019).

## 1.5 Microfluidics combined with other forces for the controlled contact between two objects

While they were established for the structuring of silicon, microfabrication technologies were expanded to a variety of materials to meet the needs of other fields of research and industry. Fabrication processes were thus adapted to dielectrics, metals, semiconductors and magnetic material and the structuring of these materials opened the possibility of using different phenomenon such as magnetics (Ko et al., 2001), dielectrophoresis (Demierre et al., 2007), piezoelectricity (Maillard et al., 2021), piezoresistivity (Barlian et al., 2009), acoustics (Guo et al., 2014), thermics (Vigolo et al., 2010) or optics (Thoumine et al., 2000). A significant advantage of microtechnologies is thus the possibility to integrate multiple functions on a microfluidic chip for cells manipulation such as the electrical characterization, separation based on size or other physical properties, filtering, selective release or controlled exposure to medium. These features were naturally used to create devices capable of performing the controlled contact between two objects. For example, acoustic tweezers were also used to form homotypic pairs of cells and assess the formation of gap junctional coupling via the transport of fluorophore between contacting cells (Guo et al., 2014).

Dielectrophoresis (DEP) in particular is a force based on the non-uniformity of an electric-field that impacts a polarizable particle. The electric field is created by electrodes and its associated force can be switched on and off or modulated by the voltage applied to them. These capabilities make this force a method of choice for the versatile manipulation of cells

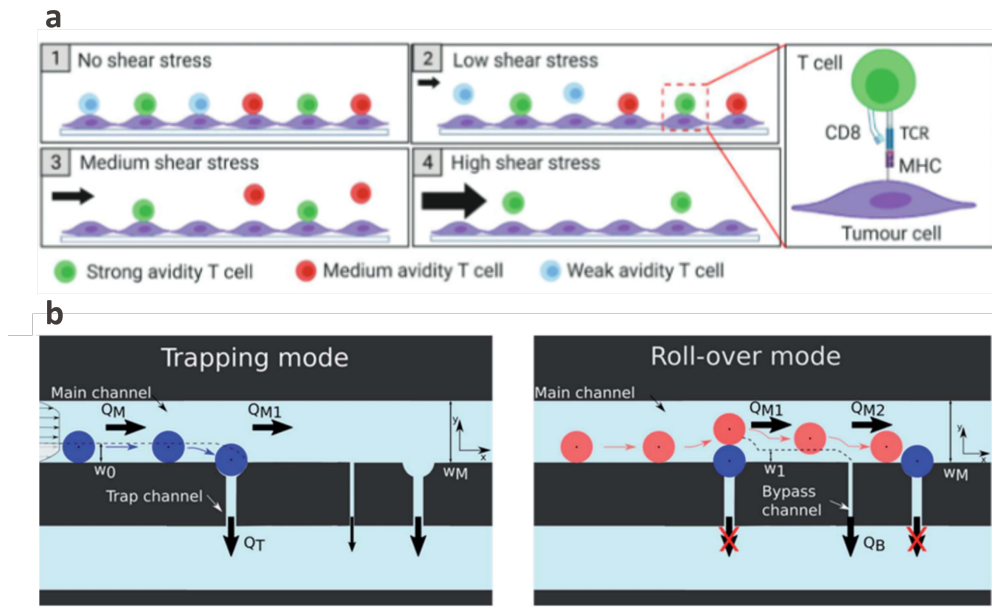


Figure 1.7: Examples of dynamic contact strategies. **a** Ashby et al. (2022) presented a device used for the contact between T-cells and APCs. The APCs are left to adhere on the substrate of a microfluidic channel. Then the T-cells are introduced and left to sediment for around 5 min, before washing by increasing flow rates and the adhesion is characterized by the flow rate at detachment. Reprinted with permission from (Ashby et al., 2022). Copyright 2022 John Wiley and Sons. **b** A microfluidic chip comprising hydrodynamic traps and bypass channels was developed by M. Duchamp et al. (2019) for the controlled contact between two objects. The first type of object is immobilized in the hydrodynamic traps and the second type of objects is brought in contact in flow conditions using a roll-over mechanism.

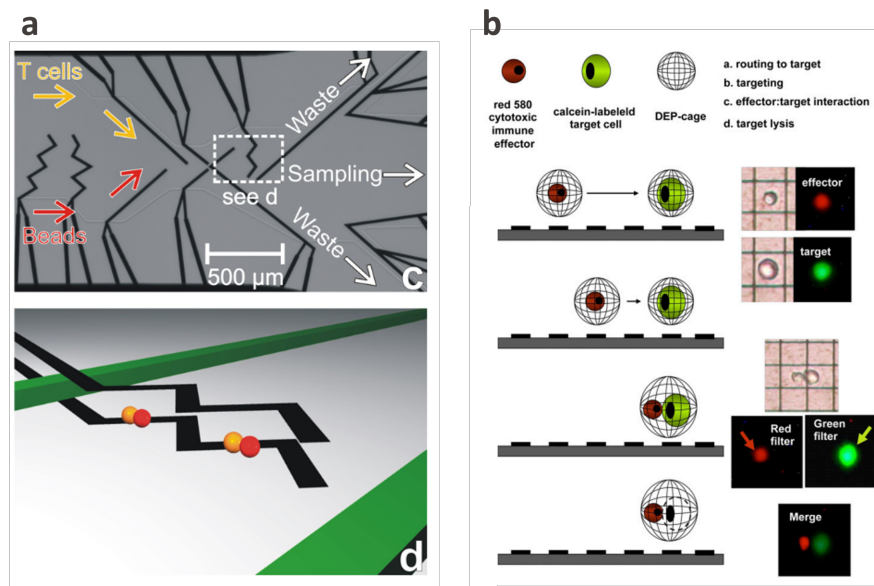


Figure 1.8: Example of devices using DEP for the controlled contact between two objects. Kirschbaum et al. (2008) used a DEP actuated deviation system and DEP cages in flow conditions in a microfluidic channel to place T-cells in contact with antigen presenting beads. Reprinted with permission from (Kirschbaum et al., 2008). Copyright 2008 Elsevier. **b** A CMOS actuated manipulation by DEP cages was developed by Abonnenc et al. (2013) to bring two cells in a common cage. Reprinted with permission from (Abonnenc et al., 2013). Copyright 2013 AAI.

and of special interest for the controlled contact between micro-sized objects. The literature associated to the use of DEP to pair objects is hereafter reviewed.

Kirschbaum et al. (2008) used dielectrophoresis based traps in a microfluidic channel to pair T-cells with beads presenting the T-cell activator antibodies anti-CD3 and anti-CD28. The early signs of interaction were analyzed through the physical adhesion of the pair once the forced contact was released and the objects dragged by the fluid. The activation of the T-cells was also assessed through the expression of activation marker CD69 at their surface after 16-24 h. This system was further improved by computer vision control to automatize the pairing process (Godino et al., 2019).

Alternatively, a CMOS based array of electrodes able to generate dielectrophoretic cages and displace object on a grid was used by Abonnenc et al. (2013) to pair immune and cancer cells. The cytotoxic activity of the immune cells was assessed by monitoring the fluorescent calcium content of the target cells. A hybrid method was proposed by Lu et al. (2015) to form heterotypic pairs of cells using a combination of hydrodynamic and dielectrophoretic trapping. The chip was however not developed in the goal of analyzing cell-cell interaction but to electrofuse the two cells to form hybridoma.

## 1.6 Scope of the thesis

Many approaches, both macro and micro sized, were developed to probe cell-cell interactions while implementing different readout strategies. However a trade-off between time and force resolution and throughput still has to be made when choosing the right method to probe an interaction. Efforts in microtechnologies were made to satisfy both criteria, but there is still a lack of microfluidic methods capable of controlling the time of contact between the two objects to probe their interaction. Previous efforts were limited because they utilized the same force manipulation methods for both cells in a pair.

In this context, this thesis proposes a microfluidic tool to control cell-cell contact using forces deriving from a different phenomenon for each cell. The effects are thus orthogonal and allow an independent manipulation of the two objects. Therefore a chip based on hydrodynamics and dielectrophoresis derived forces is proposed to provide a chip with bi-modal handling of two objects for the controlled contact between them.

First a novel method for the hydrodynamic trapping of beads and cells is proposed in chapter 2 as an alternative to the standard methods. This new trapping feature is developed to overcome the intrinsic limitations of standard traps which are critical for cell-cell interaction. The fabrication process is detailed and the method is characterized for the trapping of beads and cells. Then the development of efficient traps based on dielectrophoresis is presented in chapter 3 and a dielectrophoresis-actuated control system is proposed to achieve single cell resolution. The systems capability is demonstrated via the formation of heterotypic aggregates of cell of controlled size and composition. Finally, the two methods are combined in chapter 4 to control the time of contact between two objects as well as to probe their adhesion. An adhesion frequency assay is performed between fibroblasts and fibronectin coated beads and compared to literature to validate the device. As a proof of concept for the application of the device to immunotherapy, T-cells are put in contact with cancer cells and their avidity measured through the pairs lifetime. The work is summarized in chapter 5 that also discusses the future perspectives. The appendices A to C provide supplementary information to the main text and appendix D details an analysis of the structural colors emerging from the buried channels fabricated using the process reported in chapter 2.

## 2 Planar hydrodynamic traps and buried channels

**This thesis chapter is adapted from the recently published article:** C. Lipp, K. Uning, J. Cottet, D. Migliozi, A. Bertsch and P. Renaud, “Planar hydrodynamic traps and buried channels for bead and cell trapping and releasing”, *Lab on a Chip*, vol. 21 p. 3686-3694, 2021.

This chapter describes the development and characterization of planar hydrodynamic traps and buried channels for the immobilization of objects in a microfluidic channel. It covers the fabrication process, design, operation principle and application to beads and cells trapping.

### 2.1 Standard hydrodynamic trapping principles

Hydrodynamic trapping defines the use of flow-derived forces to precisely position and immobilize an object suspended in a solution. A specific family of hydrodynamic trapping called "contact-based trapping" consists in placing obstacles smaller than the object of interest in its path. The flow shear or pressure derived forces maintain the object against the obstacle and are counter-balanced by the normal forces generated by the obstacle. In the very large portion of the contact based hydrodynamic trapping, the flow shear force maintains the object in contact with the obstacle, which implies flow leaking around the trapped object and passing through the trap. One can mention two standard configurations of contact based hydrodynamic trapping: the pachinko and the serpentine array. The pachinko array is composed of a large flow chamber paved with obstacles in such a manner that the incoming particles have a large probability of encountering an obstacle. The obstacles are typically composed of two pillars of various shape separated by a distance tailored to the object of interest (Figure 2.1 c), or composed of a C-shaped obstacle left with a thin horizontal gap for the fluid to drag and maintain objects in the trap (Di Carlo et al., 2006) as illustrated in Figure 2.1 b. In the former option, the height of the channel depends on the particle size to ensure single object trapping. In the latter, one object occludes the gap and excludes other objects trapping once

filled independently of particle size.

Alternatively, the serpentine array is composed of a single long channel which repetitively splits in two paths. One of the paths has a small hydraulic resistance and comprises a restriction that forms the trap. The other path is called the "bypass" channel and is longer than the first path and of constant width, which generates a larger hydraulic resistance. The first device of this kind presented by W.-H. Tan and Takeuchi (2007) is illustrated in Figure 2.1 a. The particles arriving at the intersection have a larger probability of going to the trap than to the bypass. It is trapped in the restriction, increasing at the same time its resistance and blocking the path for the next particles that will continue their path until they encounter a free trap. The channel height is limited by the particle size as a trapped particle will not obstruct enough surface of the traps cross section for channel much larger than the particles and will induce multiple particles trapping.

Both types of hydrodynamic traps are passive, in the sense that the trapping happens as soon as liquid with particles flow in the channel. The selective release is possible using an external laser locally heating and generating bubbles (W.-H. Tan & Takeuchi, 2007).

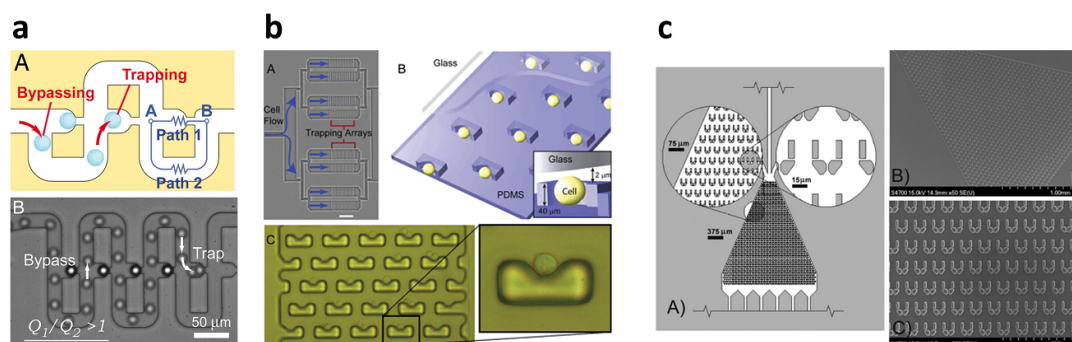


Figure 2.1: Example of standard "contact based" hydrodynamic trapping principles. **a** The serpentine array is composed of a channel regularly split in two branches, one of lower hydrodynamic resistance and comprising a restriction to form a trap. (W.-H. Tan & Takeuchi, 2007), Copyright (2017) National Academy of Sciences. **b** Pachinko type array formed by C-shaped obstacles comprising a thin horizontal gap to allow flow leaks around the trapped object (Di Carlo et al., 2006). Reprinted with permission from (Di Carlo et al., 2006). Copyright 2006 ROYAL SOCIETY OF CHEMISTRY. **c** Pachinko type array formed by obstacles with thin vertical gaps smaller than the object of interest for the flow to pass around and maintain the trapped object (Wlodkowic et al., 2009). Reprinted with permission from (Wlodkowic et al., 2009). Copyright 2009 American Chemical Society.

## 2.2 Strategy

The requirements for the development of hydrodynamic traps combined with dielectrophoretic traps for the controlled interaction between two objects were the following:

1. The hydrodynamic traps should be able to trap cells and beads without causing damage to them.
2. The trap diameter should be smaller than a typical cell, *i.e.*  $< 10 \mu\text{m}$ .
3. The hydrodynamic traps should minimize their influence on the shape of the electric field used for the subsequent DEP trapping.
4. The fabrication method should allow the integration of microfabricated electrodes around the trapped cell for the generation of the electric field used for DEP manipulation of the second object.
5. The hydrodynamically trapped object should have a maximum of its surface available to be in contact with other objects.
6. The force maintaining the first object in the hydrodynamic trap should not have an effect on the second object, meant to be manipulated by DEP.
7. The chips should be fully transparent for compatibility with manipulation under standard inverted microscopes.

Because the main force maintaining the objects in the traps of the standard configurations described above derives from flow leak shear stress, these configurations do not fill the requirement number 4. Furthermore, requirements number 3 and 5 are difficult to satisfy due to nature of the obstacle of the standard configurations.

Based on these criteria, an alternative hydrodynamic trapping principle for single beads and cells can be proposed. It relies on two superimposed levels of microchannels, interconnected by round microfluidic vias smaller than the particle of interest. As the hydrodynamic flow resistance rules the way liquid flows in the channels, particles lying in the streamlines passing inside the vias will be stopped due to their size and will generate an infinite fluidic resistance, virtually cancelling the lower hydrodynamic path. Once a particle is trapped, it is immobilized in the top channel thanks to the difference of pressure at its interface, without any material surrounding it and with maximal surface exposed for interactions with other particles or for biological assays.

These planar hydrodynamic traps can be dynamically switched between different modes of operation by simply tuning the pressure at the outlet of the microfluidic buried level, controlling the magnitude and direction of the flow inside the buried channel layer.



## 2.3 Fabrication process literature

The processes capable of fabricating planar hydrodynamic traps as described above are reviewed.

### Membrane with pores

Kimura et al. (2011) used a commercially available perforated membrane by alkaline etching to yield 5-8  $\mu\text{m}$  slanted pores in a 25  $\mu\text{m}$  thick polyimide sheet. The sheet was sandwiched between two chamber with immersed electrodes and the group used sedimentation assisted by DEP to trap the cells in the orifices for electrofusion applications. The geometry of structures fabricated with this accessible process is however not tunable. Moreover subsequent integration of electrodes in the vicinity of the pores would be difficult.

### Deep etching in silicon

Nagai et al. (2015) presented a process for the fabrication of hollow microprobe array for pick-and-place manipulation of cells. The use of deep reactive ion etching (DRIE) allows to create pores through the wafer whose dimensions are then reduced to adapt to the cells by deposition of  $\text{SiO}_2$ . The pressure control is ensured by a polydimethylsiloxane (PDMS) channel bonded on the backside. This elegant process is nonetheless not feasible on a transparent glass substrate since high aspect ratios etch processes equivalent to DRIE are not easily achievable for that material.

### Layers of laminated photosensitive films

Cao et al. (2021) used stacks of photosensitive laminated SU-8 films together with PDMS channels to create 3D structures of channels comprising a round trap connected to an underneath suction channel. The system was combined with electrodes on top and at the bottom of the trap to characterize the impedance of immobilized object. Using a stack of dry films photoresist is a versatile microfabrication process but has the disadvantage of comprising many photolithography steps. Furthermore, 3-5  $\mu\text{m}$  diameter resolution necessary to trap cells can be difficult to achieve while ensuring materials biocompatibility.

### Laser modification

A 3D glass patterning method was reported that uses a femtosecond laser to locally change the structure of a glass substrate. The illumination of the substrate operates a change of refractive index and etch rate at the focal point: the etch rate in a 5 % diluted hydrofluoric acid (HF) solution is indeed reported to be 5  $\mu\text{m}/\text{min}$  for the exposed glass whereas the etch rate of unexposed glass is of 3 $\mu\text{m}/\text{hour}$ (Bellouard et al., 2004). Thanks to the nonlinear light-matter interaction, structures smaller than the wavelength of the laser can be fabricated. Precisely controlling the position of the substrate thus allows a 3D writing of the substrate to create

complex and suspended structures after selective etching (Bellouard et al., 2012). The company FEMTOprint SA claims to be able to generate structures with a resolution lower than 1  $\mu\text{m}$  with a surface roughness  $R_a < 100 \text{ nm}$  using this technique (2022). This process is highly versatile as the only limit in structures fabrication is the resolution and accessibility of the etchant in the 3D structures. Fabrication of the structures is however a service made by the FEMTOprint SA company and the turnover between designs can be long and the total cost important.

### **Buried channel**

The buried channel method was first presented by Kaplan et al. (1994) and involves bulk micromachining techniques. In the original version, a thin poly crystalline silicon (poly-Si) film is first deposited on top of a quartz substrate and subsequently patterned. The pattern contains two type of features: the access holes are small in dimension and define the channel path while the inlet and outlet are larger in size and will remain open to connect the buried channel. The substrate is selectively and anisotropically etched using HF to form the buried channel. The poly-Si is then fully oxidized which renders the chips fully transparent and reduces the dimension of the access holes. In order to complete the sealing of the access holes for a totally watertight channel, an additional silicon oxide layer is deposited using low pressure chemical vapor deposition (LPCVD). This process has the advantage of requiring a single photolithography step for the self-alignment of the buried channels and inlet and outlet layers. The dimensions of the inlets and outlets are defined by photolithography and are thus limited by light diffraction with standard equipment, but can be further reduced by the last thin film deposition which is a significant advantage for the fabrication of sub-cellular size traps. The channel size and path are defined by underetch dimension and access hole positioning. The authors used this fabrication process to demonstrate the electroosmotic pumping of liquid in capillaries. The concept of thin film deposition and patterning followed by selective underetching and sealing by a thin film deposition was then derived in silicon substrate with various etchant and thin film materials (J. Chen & Wise, 1997; Dijkstra et al., 2008; Holm et al., 1997; Rasmussen et al., 2001; Vieider et al., 1997). Moreover this process is compatible with the subsequent micropatterning of electrodes around the traps.

Based on this review, the buried channel technology was selected to create planar hydrodynamic traps connected to buried channels. Indeed the process is also compatible with the bonding of a top fluidic layer of PDMS on top of the substrate. Their fabrication is described in the following section.

## 2.4 Fabrication

### 2.4.1 Process description

The process to fabricate two superimposed levels of channels interconnected by planar hydrodynamic traps is illustrated in Figure 2.2 and starts with the deposition of 500 nm  $\text{Al}_2\text{O}_3$  on a fused silica 4" wafer by sputtering methods (Spider 600, Pfeiffer). A 750 nm thick photoresist layer (AZ ECI 3007, MicroChemicals) was spincoated and developed using an automated coater and developer (ACS200 GEN3, Süss) and exposed using direct writing methods (MLA150, Heidelberg Instruments). The pattern comprises 1  $\mu\text{m}$  access holes used to define the fluidic path of the buried channels and larger patterns that function as fluidic vias. The pattern is transferred to the  $\text{Al}_2\text{O}_3$  layer using ion beam etching (Nexus IBE350, Veeco) and the photoresist is stripped using an oxygen plasma (GiGAbatch, PVA Tepla) (step 1a). The substrate is selectively underetched using 3 pulses of 10 min exposition to vapour HF (uEtch, SPTS) which leads to  $\sim 5.5 \mu\text{m}$  lateral etching. The access holes are placed in such a way that the under-etching of neighbouring access holes coalesce and create a continuous channel (step 1b). The access holes are then sealed by a deposition of 2.5  $\mu\text{m}$  of low temperature oxide (LTO) doped with boron and phosphorus glass (Centrotherm furnace) (step 1c). The top fluidic layer is made by casting PDMS on a silicon mold fabricated by deep reactive ion etching (DRIE) (AMS200, Alcatel). The PDMS is cured, punched, aligned and permanently bonded to the buried channels using a method described previously (Cottet et al., 2017).

### 2.4.2 Process discussion

As described above, the process to fabricate buried channel necessitates the patterning of access holes, inlets and outlets in a thin film with large etch selectivity with respect to the substrate on which it is deposited, while both materials need a low light absorbance in the visible range. The process proposed by (Kaplan et al., 1994) fulfils all these criteria, but was further improved. Indeed the thermal oxidation of the poly-Si layer is a step that both lengthen the process and causes deformation of the membrane due to the high stress induced by the thermal oxidation. We thus chose to deposit 500 nm of sputtered aluminum oxide  $\text{Al}_2\text{O}_3$ . Both materials are transparent in the visible range and fused silica is etched in a vapor phase of HF while  $\text{Al}_2\text{O}_3$ , even in amorphous phase, is totally unaffected (Bakke et al., 2005). Vapor HF is an etching method of choice when structures are sensitive to stiction as all by products are eliminated in a gas phase and the process does not need any rinsing and drying steps.

Typical solutions for the wet etching of  $\text{Al}_2\text{O}_3$  comprise phosphoric acid  $\text{H}_3\text{PO}_4$  (B. Zhou & Ramirez, 1996), buffered HF (BHF), KOH or piranha solution (Williams et al., 2003). The wet etching is however isotropic which requires a fine control over the etch rate to obtain the desired dimension and implies the manipulation of wet chemistry. Alumina can also

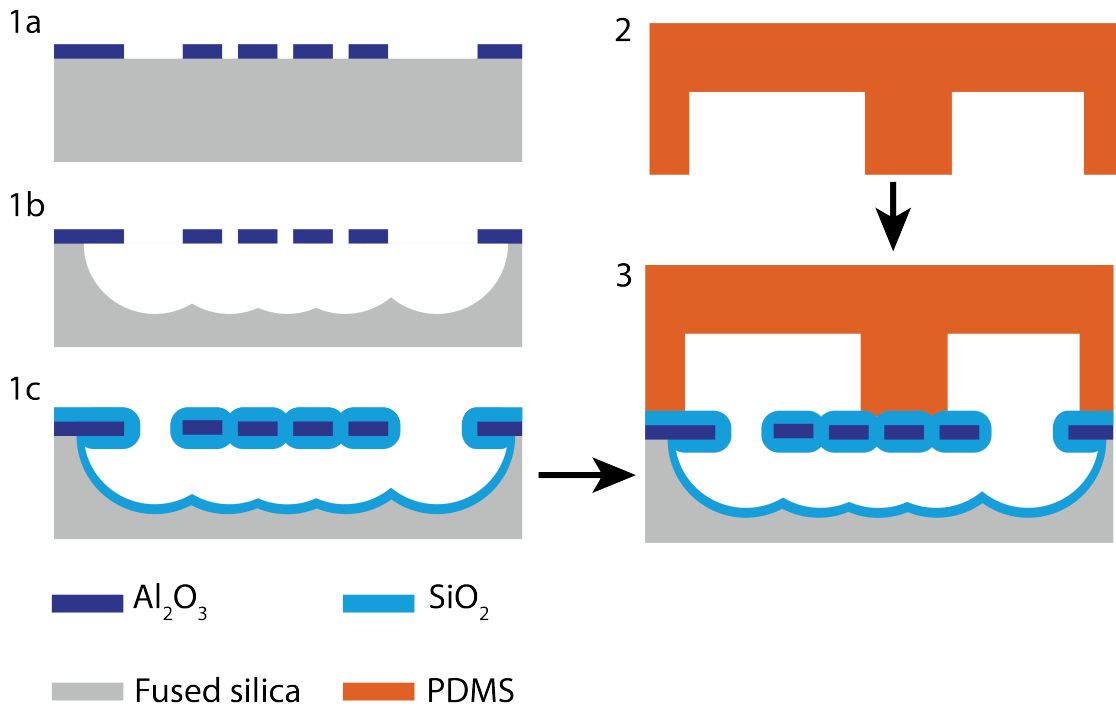


Figure 2.2: Process for the fabrication of the chips. 1a) Deposition and patterning of a thin  $\text{Al}_2\text{O}_3$  layer on a fused silica substrate. The pattern comprises access holes of small dimension and larger features 1b) The substrate is selectively under-etched using HF in vapour phase. The under-etch merge to create a continuous channel. 1c) A thin  $\text{SiO}_2$  deposition seals the access holes and creates buried channels connected by microfluidic vias. 2) PDMS is cast on a silicon mold and inlets and outlets are punched. 3) The two fluidic layers are aligned and permanently bonded to create two superimposed layers of microfluidic channels interconnected by microfluidic vias.

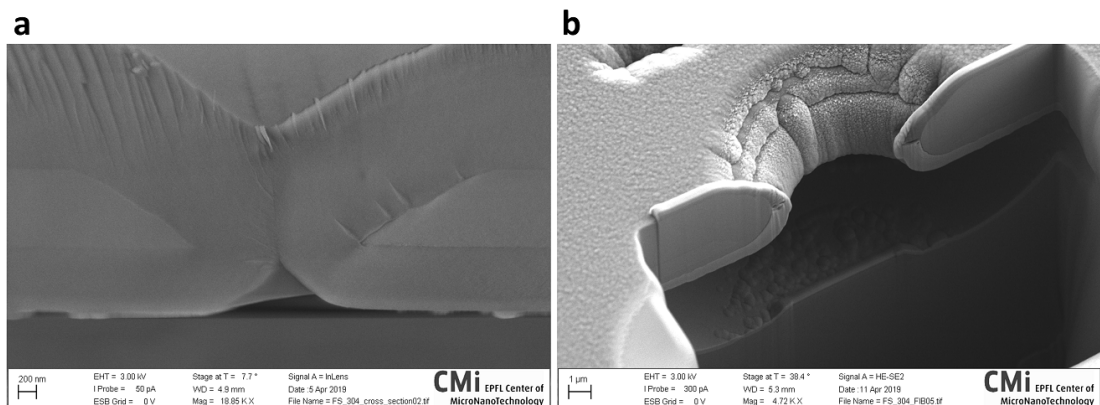


Figure 2.3: **a** SEM picture of an access hole cross section showing the  $\text{Al}_2\text{O}_3$  mask sandwiched between the LTO layers and the sealing of the access hole. **b** SEM image of a planar hydrodynamic trap cross section made using FIB etching. The sloped profile of the trap is visible together with the buried channel underneath.

be etched by plasma with gases combining argon with either chlorine, bromine or fluorine chemistry. The selectivity however is very low for photoresist masks and demands the use of a hard mask which complicates the process. In comparison, ion beam etching (IBE) offers a good directionality in the etching while having a selectivity of  $\sim 1:1$  with the photoresist mask and was thus chosen as the  $\text{Al}_2\text{O}_3$  etch method.

Another option for the fabrication of planar hydrodynamic traps is to use low stress silicon nitride as a thin film instead of  $\text{Al}_2\text{O}_3$ . Indeed while silicon nitride is affected by HF in vapour phase, its etch rate in liquid HF is very low compared to glass (Williams et al., 2003). Furthermore, silicon nitride is easily etched and with good photoresist selectivity by inductively coupled plasma etching with fluorine chemistry (Williams et al., 2003). This process was not selected because it would complicate the fabrication and requires the manual operation of HF, but was used for the fabrication of structural colors detailed in appendix D

### 2.4.3 Design rules

To obtain a trap of diameter  $d$  after the  $2.5\ \mu\text{m}$  LTO deposition, we experimentally found that a diameter of  $d+2\ \mu\text{m}$  should be designed and etched in the  $\text{Al}_2\text{O}_3$  layer. The final deposition of LTO induces a gradient of stress that deforms the membrane which would break during the dicing step for dimensions above  $200\ \mu\text{m}$ . To overcome that problem, regions without access holes were designed periodically on the membrane, leaving the substrate protected below those regions and creating pillars that sustain the membrane. Using this design, membranes with dimensions of  $300 \times 400\ \mu\text{m}^2$  were successfully fabricated. The depth of the channel is defined by the etching time and is uniform across the wafer. Its width however is determined by the design of the access holes and can be chosen arbitrarily. The minimum width however is restricted to twice that of the depth plus the access hole diameter due to the isotropic nature of the etching. The distance between two neighboring access holes should be larger than the depth of the isotropic etch of the fused silica to obtain a continuous channel. The closer the access holes are to each other, the more uniform is the topography of the buried channel but the weaker is the suspended mechanical structure. This distance was chosen to be equal to the etch depth,  $5\ \mu\text{m}$  in this study as a trade-off between topography and mechanical resistance.

## 2.5 Principle of operation

Figure 2.4 shows a brightfield view of a buried channel and trap connecting two PDMS channels. An orange filter is superimposed to the image and indicates the regions where the PDMS is bonded to the substrate. The control channel on the right is short and wide in order to minimize its fluidic resistance and is connected to the pressure control  $P_c$ , while beads or cells flow in the left PDMS channel from the top to the bottom under the effect of the inlet pressure  $P_{in}$ . The top inset shows a SEM picture of a trap, whose diameter is smaller than the dimension of the particle to be trapped.  $P_c$  is the control pressure and  $P_{in}$  the inlet pressure,  $Q_{in}$  is the flow upstream of the trap and  $Q_{bc}$  is the flow inside the buried channel. The chip presented here can be operated in four different modes presented in Figure 2.5.

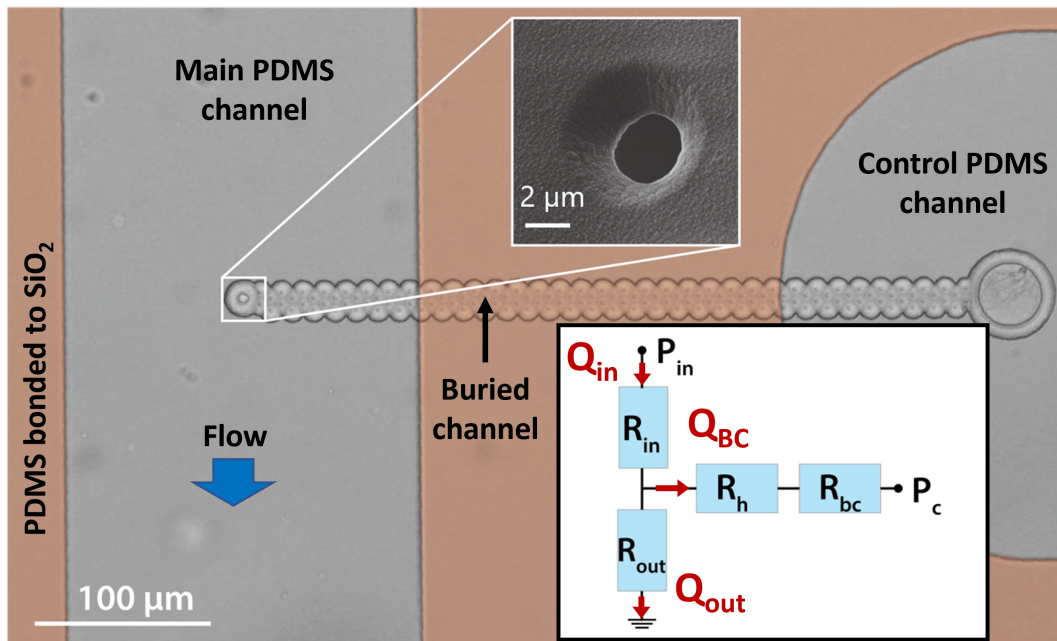


Figure 2.4: Bright-field picture of a buried channel connecting a single trap in the main PDMS channel on the left to the PDMS control channel on the right. An orange filter is added where the PDMS is bonded to the glass. The top inset shows a SEM picture of a trap and the bottom inset shows the equivalent electric circuit where  $P_{in}$  is the inlet pressure,  $R_{in}$  is the resistance of the main PDMS channel upstream of the trap,  $R_{out}$  is the resistance of the main PDMS channel downstream of the trap,  $R_h$  is the resistance of a trap,  $R_{bc}$  is the resistance of the buried channel and  $P_c$  is the pressure imposed to the control channel

In order to model the behaviour of the chip, we assumed a non-compressible Newtonian fluid and used the Hagen-Poiseuille law  $\Delta P = R_{hyd}Q$  (Bruus, 2011), where  $\Delta P$  is the difference of pressure across a channel of fluidic resistance  $R_{hyd}$  in which a flow  $Q$  is present, and used the electric-hydraulic circuit equivalence (Oh et al., 2012) to model the behaviour of the chip. The

equivalent circuit is represented in the bottom inset of Figure 2.4 with  $R_{in}$  the resistance of the PDMS channel upstream of the trap,  $R_{out}$  the resistance of the PDMS channel downstream of the trap,  $R_h$  the resistance of a trap,  $R_{bc}$  the resistance of the buried channel,  $P_{in}$  the inlet pressure and  $P_c$  the control pressure. We used these values to determine the conditions to operate in each of the four modes that are illustrated in Figure 2.5:

### Idle mode

In the idle mode,  $P_c$  is set such that there is no flow in the buried channel ( $Q_{bc} = 0$ ). The particles behave as if no trap or buried path was present.

$$P_{c,idle} = P_{in} \frac{R_{out}}{R_{in} + R_{out}} \quad (2.1)$$

### Trapping mode, empty

To trap a particle, the control pressure is set to a value smaller than the idle control pressure ( $P_c < P_{c,idle}$ ), resulting in a net flow in the buried channel from the main channel towards the control channel ( $Q_{bc} > 0$ ). Particles in the flow lines passing inside the buried path are directed towards the trap.

### Trapping mode, full

A particle is trapped, sealing the buried path and stopping the flow in the buried channel ( $Q_{bc}=0$ ). The main channel behaves as in the idle mode and a pressure difference across the trapped particle  $\Delta P_p$  maintains it in the trap:

$$\Delta P_p = P_{in} \frac{R_{out}}{R_{in} + R_{out}} - P_c \quad (2.2)$$

### Release mode

To release a trapped particle, the control pressure is larger than the idle control pressure ( $P_c > P_{c,idle}$ ), resulting in a net flow in the buried channel from the control channel towards the main channel ( $Q_{bc} < 0$ ). The particle is pushed away from the trap.

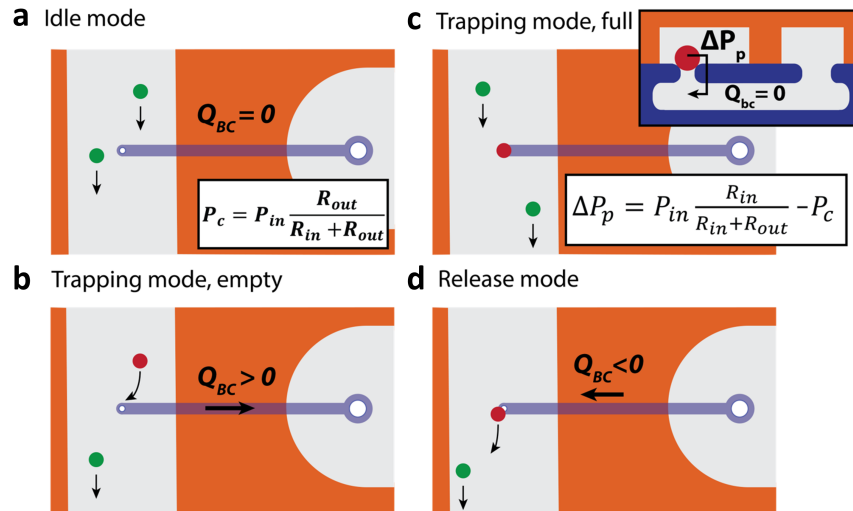


Figure 2.5: Scheme showing the different modes of operation. **Idle mode:**  $P_c$  is set to obtain a null flow in the buried channel and the flow in the main channel behaves as if no trap was present. **Trapping mode, empty:** Part of the main channel fluid is directed toward the buried path. The particles lying in the streamlines going to the buried path are deviated towards the trap. **Trapping mode, full:** a particle is trapped and there is no fluid flow in the buried channel. The particle is immobilized by the difference of pressure at its interface  $\Delta P_p$ . **Release mode:** The control pressure  $P_c$  is increased to reverse the flow in the buried path, the trapped particle is pushed away from the trap.

## 2.6 Holding forces: 2D modeling and calculation

In an effort to understand the role of the different forces implied in the trapping of beads with these novel hydrodynamic traps, a 2D finite element model was developed using COMSOL Multiphysics. Indeed the sealing between a supposedly undeformable immobilized bead and the trap is never perfect. The difference of pressure between the top and the bottom of the trap thus induces flow leaks around the bead that apply a shear force on the bead. The criteria chosen to determine whether the bead stays trapped or leaves the trap is the sum of moment at the downstream bead contact point with the surface generated by the different forces: a positive moment maintains the bead in the trap and a negative moment induces rotation of the bead outside of the trap. This point is marked as "A" in Figure 2.6 b. The forces acting on the bead considered for this study are pressure induced forces and drag shear forces with shear forces directed parallel to the bead surface and pressure forces perpendicular. A parametric study was conducted to understand the influence of trap dimension and bead diameter on the pressure control at which the bead leaves the trap.



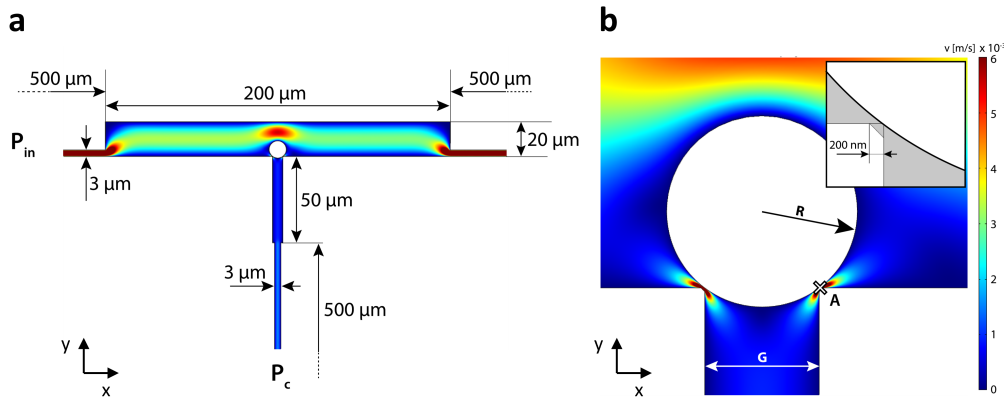


Figure 2.6: Representation of the 2D simulation model for the analysis of the different forces acting on a trapped bead of radius  $R$  in a trap of dimension  $G$ . The colour is the flow velocity magnitude for an inlet pressure of 10000 Pa. **a** General view of the model. **b** Zoomed in view of the model, the inset illustrates the 200 nm cut off the corners of the trap to include leaks in the model.

The 2D model depicted in Figure 2.6 a comprises resistance channels of 500  $\mu\text{m}$  length and 3  $\mu\text{m}$  in height at the inlet, outlet and control channel. The trapping chamber is at the intersection between the inlet and control channels and is 200  $\mu\text{m}$  in length and 20  $\mu\text{m}$  in height. The trapped bead is represented by a solid circle of radius  $R$  and stands on a trap of width  $G$ . The leaks around the trapped bead are included by cutting off the contact corner between the bead and the trap by 200 nm as represented in the inset of Figure 2.6 b. The inlet pressure is fixed to 10000 Pa and that of the outlet to 0. COMSOL simulations with parametric sweeps in  $R$ ,  $G$  and  $P_c$  were generated using the LiveLink for MATLAB. The pressure and shear stress are represented by the colored arrows in Figure 2.7 a and are exported for each mesh node on the perimeter of the bead. The exported data is analyzed in MATLAB and the values of pressure and shear stress are multiplied by the corresponding mesh segment length to obtain the exerted force at a given mesh node. The moment generated as of point A by these forces are calculated and represented in Figure 2.7 b. The forces are represented in the  $x - y$  plane and the moment induced by these forces represented out of the plane, a positive moment contributing to keeping the bead in the trap and a negative moment contributing to the rolling of the bead out of the trap.

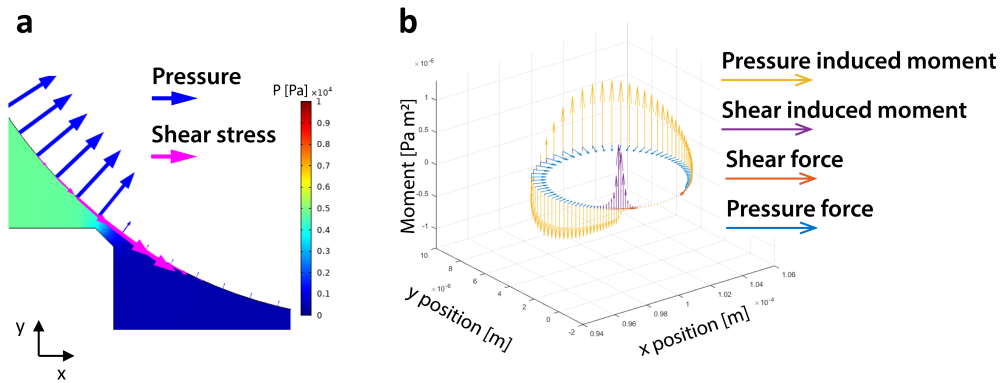


Figure 2.7: **a** Representation of the pressure and shear stress at each mesh node on the COMOSL model with the colour indicating the pressure value in the channel. **b** Analysis of the simulated data using MATLAB: Pressure and shear forces are represented at each mesh node with respective generated moment. The positive moments maintain the bead in the trap whereas negative moments induce rotation of the bead outside of the trap.

We distinguish three sources of moment:

- **Shear leaks**  $M_{SL}$  is the sum of the moments generated by the shear forces in the region where the bead contacts the trap due to liquid flowing towards the control channel.
- **Shear main**  $M_{SM}$  is the sum of the moments generated by shear forces due to liquid flowing towards the outlet.
- **Pressure**  $M_P$  is the sum of the moments generated by pressure forces.

We also define the summed moments:

- **Shear total**  $M_{SM}$  is the total moment generated by shear forces.
- **Total**  $M_{tot}$  is the total moment generated by all the considered forces.

Figure 2.8 represents the sum of the moments of different sources as a function of  $P_c$  for a bead diameter of  $5 \mu\text{m}$  in a trap of  $2 \mu\text{m}$  width. As expected, the shear main moment varies very little across the range of  $P_c$  and is always negative, dragging the bead out of the trap. The shear leak and pressure moments are positive at low  $P_c$  and transition to negative as  $P_c$  increases. The shear leaks and shear main moments magnitude were found to be two orders of magnitude lower than the pressure moment at  $P_c = 0$ . The pressure at which the shear leaks moment is null, hereafter called transition pressure, is found at exactly half of the inlet pressure

because it is the pressure at which the pressure under the bead matches the pressure above the bead nullifying the leak flow. The transition pressure of the pressure-induced moment is found a slightly lower than half of the inlet pressure. This is because of the pressure drop in the main channel from upstream to downstream of the bead, increasing the contribution of the upstream pressure with negative moment illustrated in Figure 2.7 b. This is an artifact of the 2D modeling because the presence of the bead creates a restriction in the channel that generates a larger flow above the bead and a pressure drop across it. Indeed in the 3D model the flow would pass around the bead and the pressure drop across the bead would be negligible. This artifact is also observed for the shear main moment whose contribution is increased by the restriction on top of the bead. However the total pressure transition shifts only of 1.5% compared to half of  $P_{in}$  and the leaks are found to play only a small contribution in the total moment. Appendix A describes the transition pressure of the different moments as a function of trap diameter for a bead diameter of  $8\ \mu\text{m}$  and brings to the conclusion of pressure being the main force responsible in the trapping of the beads.

It was concluded from this study that the main force maintaining beads in a planar hydrodynamic trap is the difference of pressure built across them. Indeed the larger impact of the shear stress in the main channel for larger beads was understood to be an artifact of the 2D simulation and the shear stress arising from the leaks was found to be insignificant. The only impact of the leaks was found to increase the effective pressure underneath the bead because of the pressure drop in the control channel.

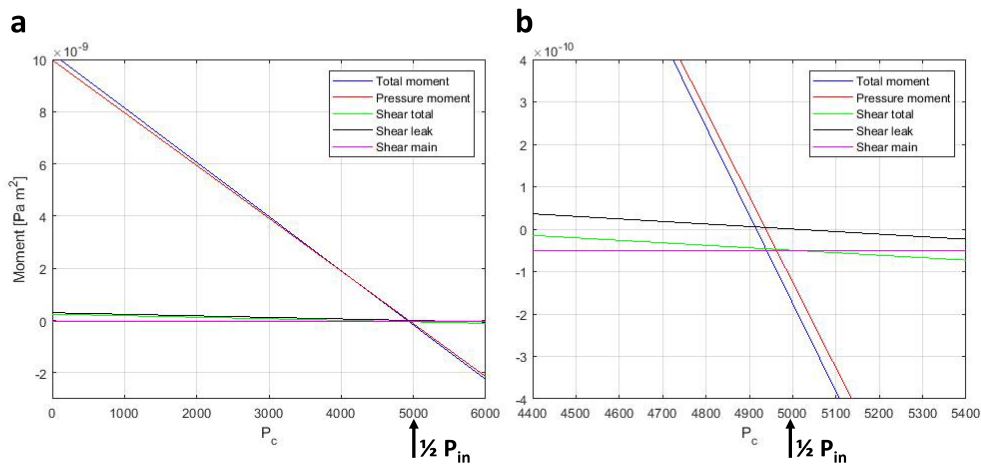


Figure 2.8: Sum of moments of different sources as a function of control pressure  $P_c$  for an inlet pressure of 10000 Pa, a bead diameter of  $5\ \mu\text{m}$  and a trap width of  $2\ \mu\text{m}$ . **a** Generic view. **b** Zoom in view of the pressures at which the moment switch from positive to negative.

## 2.7 Materials and methods

### Mammalian cells culture and preparation

The semi-adherent cell line Colo205 (ATCC) was cultured in RPMI 1640 supplemented with 10% fetal bovine serum (FBS) and 1% penicillin–streptomycin at 37 °C in a 5% CO<sub>2</sub> atmosphere. Cell staining was performed by incubating the adherent part of the cell population for 1 h in RPMI with 1 μM calcein AM (Calbiochem). The supernatant was removed and the cells were washed with phosphate-buffered saline (PBS), detached using trypsin and centrifuged at 1200 rpm for 2 minutes. The cells were resuspended in PBS containing 1 mM EDTA and 1% bovine serum albumin (BSA) at a concentration of  $1 \cdot 10^6$  cells/ml and passed through a 40 μm cell strainer for the experiment. All the reagents are from Gibco unless specified. The distribution in the cell diameter was measured using an image analysis method on 260 cells. The mean diameter was 16.9 μm with a standard deviation of 3.1 μm.

### Algae cells culture and preparation

*Chlorella vulgaris* cells were cultured at room temperature under continuous ambient light in Tris-Acetate-Phosphate (TAP) medium at pH 7. The cells were suspended at a concentration of  $1 \cdot 10^6$  cells/ml in TAP buffer and passed through a 40 μm cell strainer for the experiments.

### Microfluidic setup and chip preparation

The PDMS chip was degassed in a desiccator for 30 minutes prior to the experiment to avoid formation of bubbles, and primed with Pierce protein-free (PBS) blocking buffer for 1h to prevent proteins, beads and cells from adhering to the surfaces. The cells or beads were placed in a chromatography vial connected to the punched PDMS with 360 μm outer diameter tubing for tight sealing. Pressure was applied to the vial using Fluigent Flow-EZ pressure controllers. The chip was mounted on the stage of a Leica DMI3000 B inverted microscope and observed using a uEye (IDS) camera.

### Polystyrene beads

For the trapping of beads in large arrays, 5 μm diameter polystyrene beads were purchased from Sigma-Aldrich and suspended in deionized (DI) water containing 0.1% TWEEN 20 (Sigma-Aldrich) at a concentration of  $5 \cdot 10^5$  beads/ml. For the selective trapping experiment, 8 μm diameter green and orange fluorescent Fluorophorex polystyrene beads were purchased from Phosphorex Inc. and resuspended at a concentration of  $5 \cdot 10^5$  beads/ml in a DI water solution containing 0.1% TWEEN 20 (Sigma-Aldrich).

## 2.8 Characterization of single cell trapping

Figure 2.9 illustrates the successful use of the four modes for the trapping and releasing of a Colo205 cell. While polystyrene beads are rigid and can withstand large pressures, special

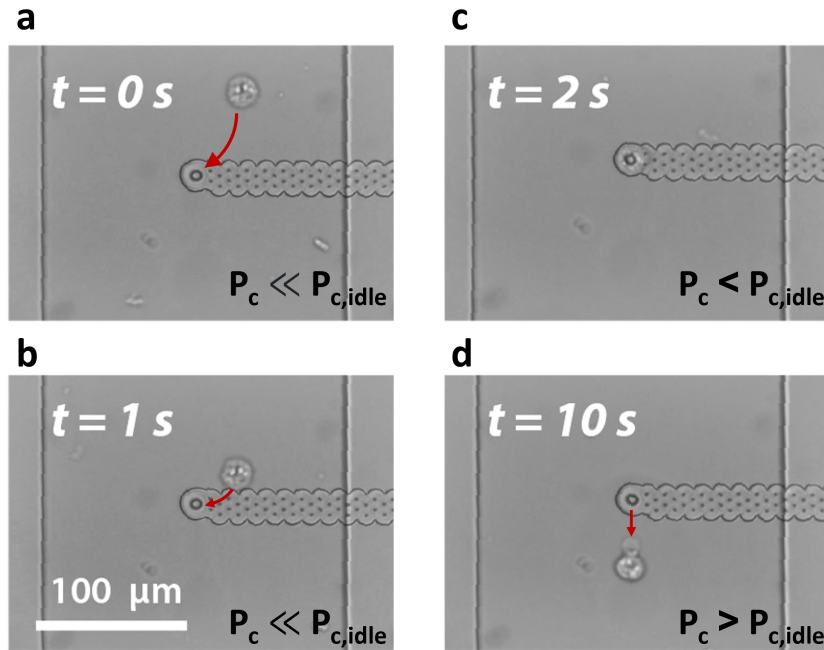


Figure 2.9: Brightfield pictures showing a sequence of trapping and releasing of a Colo205 cell in a single trap.

consideration must be taken when trapping cells with this novel kind of hydrodynamic traps. Indeed, cells are deformable bodies whose shapes are impacted by the difference of pressure built across them (Lim et al., 2006). When immobilizing cells in traps similar to the one presented in Figure 2.4, one must adapt the pressures and trap dimensions for the cells to stay intact.

In the frame of this thesis, we consider the cell membrane integrity as a gauge of success, such that the cells can be used for a subsequent assay on the cells membrane on chip such as probing receptor-ligand interaction. Cells were immobilized in traps of 3, 5, 7, and 9  $\mu\text{m}$  in diameter using a chip with a single trap and control pressure channel, to find the critical  $\Delta P_p$  where the membrane fails. For the visualization of membrane failure, cell cytosol was loaded with fluorescent calcein as it is a small molecule with no covalent binding to cell compounds that quickly diffuses in case of membrane rupture. To avoid fluorophore bleaching, cells were imaged every minute up to 15 minutes. This time threshold was chosen by overestimating the maximum time the filling of an array could take. Indeed once the cells trapped, the control pressure  $P_c$  can be increased to a value close to the idle pressure  $P_{idle}$  to reduce the stress on the cells while maintaining them in the traps.

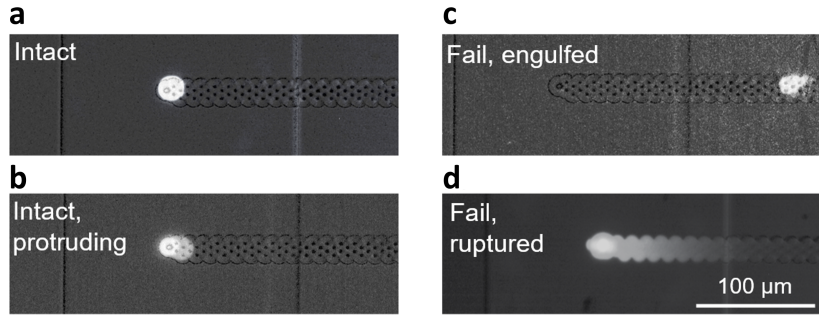


Figure 2.10: Fluorescent pictures of the different cells outcomes when trapped. **a** The cell is intact without any visible deformation **b** The cell is intact and a protrusion inside the buried channel is visible **c** The cell passed through the trap and is found inside the buried channel or in the PDMS control channel. **d** The membrane is ruptured and the fluorescent dye is diffusing in the buried channel.

$\Delta P_p$  was controlled by setting a negative value to  $P_c$  and setting  $P_{in}$  to zero, thus stopping the flow in the main channel. The different outcomes that could be observed after 15 minutes are shown in Figure 2.10. Intact cells could either have a round appearance and no visible deformation, or have a protrusion visible in the buried channel. Membrane failure was identified as dye leaking in the buried channel, or as an engulfed cell that could be found inside the buried channel or in the control PDMS channel.

The graph in Figure 2.11**a** shows the percentage of intact cells after 15 minutes, as a function of the trap diameter and the pressure difference across the trapped cells  $\Delta P_p$ . A pressure threshold under which cells did not suffer any membrane rupture or engulfment was found for each trap diameter. The minimum pressure with a percentage of intact cells lower than 50% is represented as a function of trap diameter in red in Figure 2.11**b**, indicating that cells resist to higher pressures in smaller traps. Previous studies on vesicle and cell deformation in pipettes indicate that the tension  $\tau$  of a spherical membrane of radius  $R_v$  can be determined via the difference of pressure  $\Delta P_p$  between the inside and outside of the pipette and the radius of curvature  $R_p$  in the pipette (Kwok & Evans, 1981; Sens & Plastino, 2015; S. C. W. Tan et al., 2011).

$$\tau = \frac{R_p \Delta P_p}{2(1 - \frac{R_p}{R_v})} \quad (2.3)$$

Since the vertical configuration of the planar traps makes the direct measurement of the radius of curvature  $R_p$  technically demanding, we used the radius of the trap as an estimate. We measured the distribution of cell radius using image analysis methods, which was found to be  $8.4 \mu m$  with standard deviation of  $1.5 \mu m$  as an estimate of  $R_v$ . We highlighted the region

resulting from the fitting of equation 2.3 to our experimental data using these estimates in blue in Figure 2.11: we observed a good agreement of the predicted trend with the measurement. Moreover, the range of tension at rupture resulting from the fitting is represented in the inset of Figure 2.11b. We obtain higher values for the fitted tension at rupture compared to values obtained for lipid vesicles (Alam Shibly et al., 2016; Kwok & Evans, 1981), which is coherent with the presence of cholesterol in the cell membrane and the presence of cytoskeleton inside the cell, which are both expected to contribute to increase the rupture tension of the cell membrane.

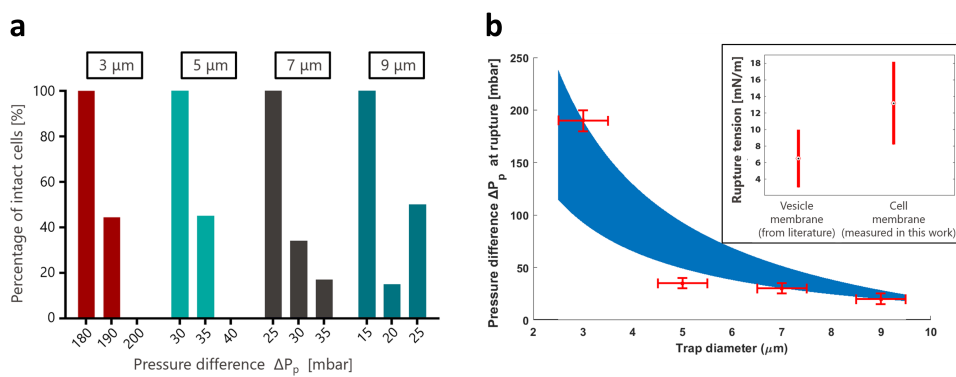


Figure 2.11: Characterization of single cell trapping in different hydrodynamic trap diameters and pressure conditions. **a** Graph representing the percentage of intact cells after 15 minutes for different trap diameters and gradients of pressure at the interface of the trapped cells  $\Delta P_p$ . The number of experiments is  $N \geq 5$  for each condition. **b** The minimum pressure with less than 50% intact cells after 15 minutes of trapping as a function of the trap diameter is represented in red. The blue area corresponds to the fit of equation 2.3 for a range of cell diameter of  $13.8 - 20 \mu\text{m}$ . The inset shows the range of membrane tension at rupture extracted from the fit measured in this work compared to the range of vesicle membrane tension at rupture from literature.

Intact cells are required for the goal application of controlled contact between two objects. This experiment defines the experimental frame in which planar hydrodynamic traps can be used for the safe trapping of cells. Measurement of membrane tension at rupture was found as a byproduct of the experiment, validating the experimental frame and model.

## 2.9 Hydrodynamic trapping of beads in large arrays

After showing the ability of the planar hydrodynamic traps to safely trap and release single cells, the next section shows its potential to trap polystyrene beads using a large number of traps arranged in an array.

The trapping of 5  $\mu\text{m}$  polystyrene beads in an array composed of 522 parallel traps arranged in an equilateral triangle tiling pattern spaced by 9  $\mu\text{m}$  is first demonstrated. Figure 2.12a shows a brightfield picture of an array of 522 traps used for this study, partially filled with beads and connected by a buried channel to a control PDMS channel on the right. The triangles visible on the membrane are the regions where no access holes or traps were designed to prevent the underetch and mechanically support the membrane. An orange filter is superimposed to the image where the PDMS is bonded to the substrate, and the inset shows a SEM picture of the 2  $\mu\text{m}$  diameter traps. We made the choice of operating the chip at constant pressure in order to avoid the need to use complex feedback control systems.

Figure 2.12b shows the experimentally measured fraction of lost beads, defined as  $LF = \frac{\text{Beads out}}{\text{Beads out} + \text{Beads trapped}}$ , as a function of the percentage of filled traps for different pressures  $P_{in}$  and pressure ratios  $P_c/P_{in}$ , measured while filling the arrays. Using these measurement, the trapping efficiency, here defined as  $\eta = 1 - LF$ , at 98% filling was measured and was found to be constant for experiments with same pressure ratio and different inlet pressures. The trapping efficiency at 98 % filling percentage and its standard deviation for a pressure ratio  $P_c/P_{in} = 0.2$  were respectively 70.4% and 1.1%, whereas for a pressure ratio  $P_c/P_{in} = 0$ , the trapping efficiency and its standard deviation were of 94.4% and 2.7%. By adapting the circuit in Figure 2.4 and replacing the resistance of a single trap of resistance  $R_h$  by  $n$  traps in parallel of total resistance  $R_h/n$ , the ratio of the inlet flow going in the buried channel is calculated as follows:

$$\frac{Q_{bc}}{Q_{in}} = \frac{R_{out} - \frac{P_c}{P_{in}}(R_{out} + R_{in})}{R_{bc} + R_h \frac{1}{n} + R_{out} - \frac{P_c}{P_{in}} R_{out}} \quad (2.4)$$

This equation indicates that the flow ratio decreases as the array is being filled with particles, explaining the increasing lost fraction as the filling percentage of the array increases in Figure 2.12b. It also shows that the flow ratio can be controlled dynamically by the pressure ratio only, decreasing when this latter increases. A constant trapping efficiency for equivalent pressure ratios hence indicates a dependency of the trapping efficiency on the ratio of the inlet flow going inside the traps, similarly to other trapping mechanisms (Kobel et al., 2010; Sohrabi Kashani & Packirisamy, 2019). The geometry also plays a role in the lost fraction as can be seen from the inset of Figure 2.12b: the center-top part is the first to be filled whereas the borders are last and most difficult to be filled, following the particle distribution in the



channel. We can also notice that the centerline of the trapped beads distribution is offset from the center of the channel towards the control channel. This comes from the increased resistance created by the channel under the membrane favoring the filling of the traps close to the control channel. An array geometry for improved efficiency would thus contain more traps in the center of the PDMS channel with a bias towards the control channel, following the curve shape formed by the trapped beads distribution shown in Figure 2.12b. The time needed to reach the 98% filling percentage increases with a reduction of the inlet pressure because of the lower flow rate, and increases with larger pressure ratio  $P_c/P_{in}$ , which indicates that for an efficient and fast filling, small pressure ratio and large inlet pressure should be used.

Furthermore, if the only criteria are fast and efficient filling, the resistances can be tailored for that application with a small inlet and buried channel resistances,  $R_{in}$  and  $R_{bc}$ , together with large outlet resistance  $R_{out}$ . This combination will increase the flow ratio  $Q_{bc}/Q_{in}$ , improve the trapping efficiency and reduce the filling time. In order to achieve 100% trapping efficiency, the downstream path should be of infinite resistance  $R_{out} = \infty$ . To that end, the downstream path could either not exist and be designed as a dead-end, which would remove the possibility of flowing subsequent analytes over the array and the releasing in a channel path different than the inlet, or be blocked by a valve that could be switched off once the array totally filled. 98% of the beads could be released from the array and brought to the outlet channel by increasing the control pressure together with the inlet pressure.

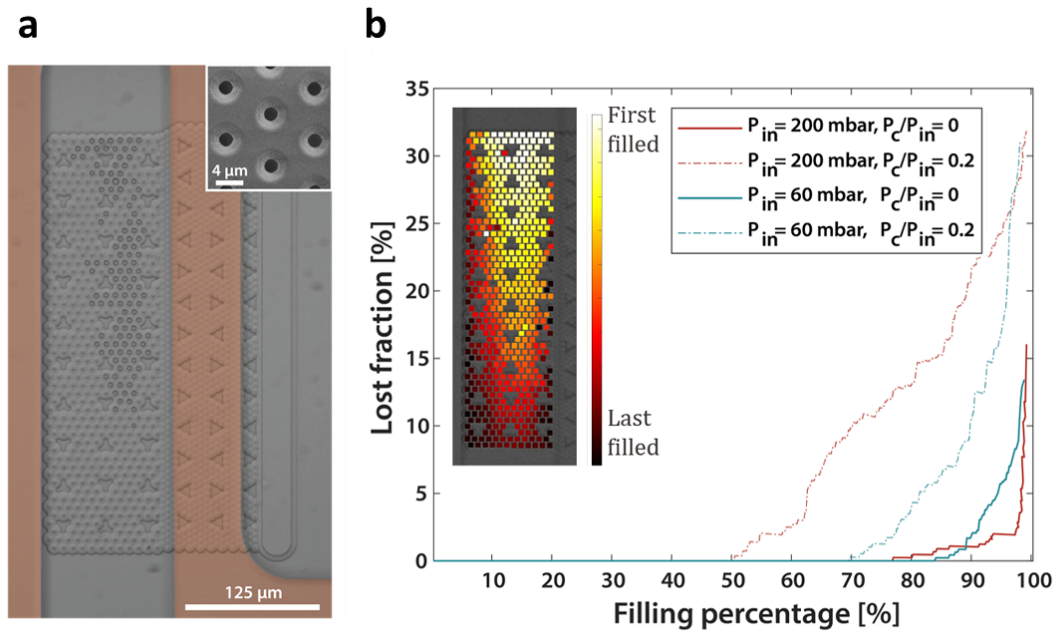


Figure 2.12: Characterization of bead trapping in large arrays of traps. **a** Bright-field picture of an array of 522 traps partially filled with polystyrene beads, connected by a buried channel to a control channel on the right. An orange filter highlights the regions where the PDMS is bonded to the substrate. The inset shows a SEM picture of the  $2 \mu\text{m}$  traps. **b** Graph representing the experimentally measured evolution of the fraction of lost beads as a function of the filling percentage of the array for different inlet pressures  $P_{in}$  and pressure ratios  $P_c/P_{in}$ . The inset shows a color map of the experimentally measured order of filling of the array.

## 2.10 Hydrodynamic trapping of cells in arrays

Based on the operation conditions observed with the trapping of beads in an array and the pressure condition determined for the safe trapping of cells, the buried channels technology was used to trap multiple cells, mammalian and algae, in arrays.

### 2.10.1 Mammalian cells

The design used for the trapping of cells in an array allows the passage of flowing cells around the immobilized ones but not on top. Indeed a channel height of  $20 \mu\text{m}$  is small enough to prevent the vertical stacking two cells. The traps are placed in a triangular tiling pattern to force the contact between the trapped and flowing cells and the distance between two traps was set to  $50 \mu\text{m}$ . During the filling of an array of traps with cells, the already immobilized cells are subject to a pressure gradient  $\Delta P_p$  that varies with  $1/n$ , with  $n$  the number of remaining

free traps as follows:

$$\Delta P_p = \frac{R_h[R_{out}P_{in} - (R_{in} + R_{out})P_c]}{n(R_{in}R_{bc} + R_{out}R_{in} + R_{bc}R_{out}) + R_h(R_{in} + R_{out})} \quad (2.5)$$

$\Delta P_p$  thus increases significantly as the last free traps are filled to reach the maximum pressure, defined by equation 2.2, once the array is totally filled. We determined the maximum pressure a cell can withstand during 15 minutes in Figure 2.11 and found that the maximum trapping efficiency happens for  $P_c/P_{in} = 0$ , which determines the working inlet pressure to fill an array of cells:  $P_{in} = \Delta P_{p,max} \frac{R_{in} + R_{out}}{R_{out}}$ . Once the array is totally filled, the control pressure  $P_c$  can be increased to minimize  $\Delta P_p$  while maintaining the trapped cells intact for long time duration and flowing additional material on top of the trapped cells.

Figure 2.13 shows a fluorescent picture of the successful trapping of 24 Colo205 cells stained with calcein AM in a compact array of 25 traps. Supplementary material S2 shows the trapping of Colo205 cells in the array using an inlet pressure  $P_{in} = 40$  mbar and a control pressure  $P_c = 0$  mbar. We chose traps with diameter of 5  $\mu\text{m}$  to allow working at reasonable pressures without compromising the successful filling of the array because of debris clogging the traps. The inlet pressure was set to 40 mbar in a chip with  $R_{in} = R_{out}$  such that the maximum pressure the cells were subjected to was 20 mbar, below the threshold pressure corresponding to that trap diameter, while working at a pressure ratio  $P_c/P_{in} = 0$  for a maximum trapping efficiency.

The observed trapping efficiency  $\eta$  was of 88.4% at 92% filling percentage and of  $\eta = 68.6\%$  at 96% filling percentage. 88% of the cells could be released from the array and brought to the outlet channel by increasing the control pressure together with the inlet pressure.

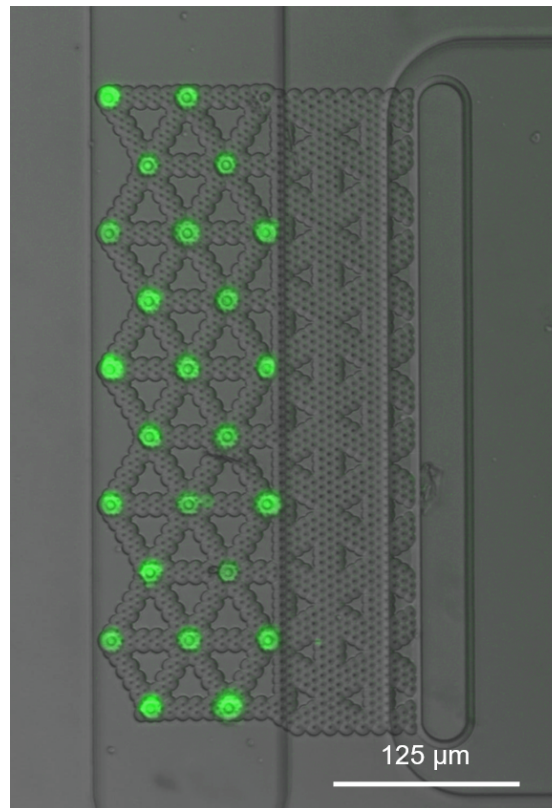


Figure 2.13: Fluorescent picture showing the successful trapping of 24 Colo205 cells stained with calcein AM in an array of 25 traps. The pressures are set so that the difference of pressure  $\Delta P_p$  endured by the cells is always under the pressure threshold for membrane rupture.

### 2.10.2 Algae cells

Chlorella is a unicellular microalgae whose diameter varies from 2 - 10  $\mu\text{m}$  during its maturation cycle. It is getting interest and studied among others for its capability to store large amounts of lipids for biofuel production (Safi et al., 2014). An interesting feature of these cells shared among plant cells is the presence of a wall around the cell's membrane, mainly composed of cellulose and other proteins that ensures mechanical rigidity. This rigidity and its size makes Chlorella cells a candidate of choice to demonstrate the trapping of cells in large arrays of planar traps.

Figure 2.14 shows a sequence of trapping and releasing of single algae cells in an array of 921 traps. As the cells are not easily identifiable in brightfield microscope pictures, the difference between a contrast enhanced version of the image shown and the image with empty traps is added in green colour on top of the original image. No algae were observed inside the control channel even for inlet pressures up to  $P_{in} = 500$  mbar indicating that there was no deformation and engulfment of the cells and demonstrating the high rigidity of these cells. All cells could

be released from the array by increasing the control pressure.

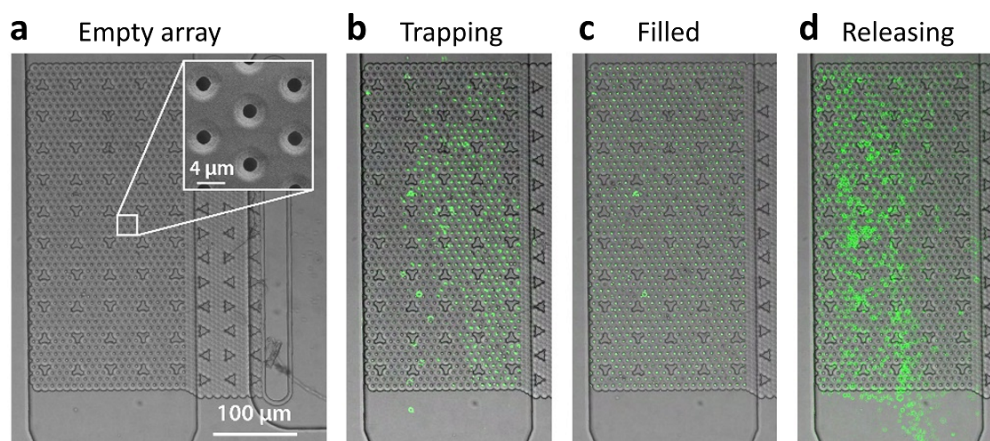


Figure 2.14: Sequence of brightfield pictures showing an empty array (a), the trapping of Chlorella cells (b), the array of traps filled with Chlorella cells (c) and the release of the cells (c). The array is composed of 921 traps.

## 2.11 Selective trapping

The trapping method proposed in this chapter offers the possibility of selectively trapping and releasing beads and cells using traps managed by independent control channels. A proof of concept demonstration of this possibility was done using a design illustrated in Figure 2.15a and comprising three lines of 18 interconnected traps connected to three control channels. The PDMS layer features two independent inlets with respective serpentine channels to create a fluidic resistance that merge before entering the chamber with buried channels and traps. These resistance channels are placed to avoid back-flow from an inlet channel to the other one when arriving at the intersection. The layout was originally designed with 36 interconnected traps but because of non uniform exposure in the direct laser writing of the buried channel layer most of the access holes were not etched and only half of the traps were connected to a common buried channel as can be seen in Figure 2.15b. Each of the lines has its own control channel with designated pressure control that can be independently operated in the different states described in section 2.5.

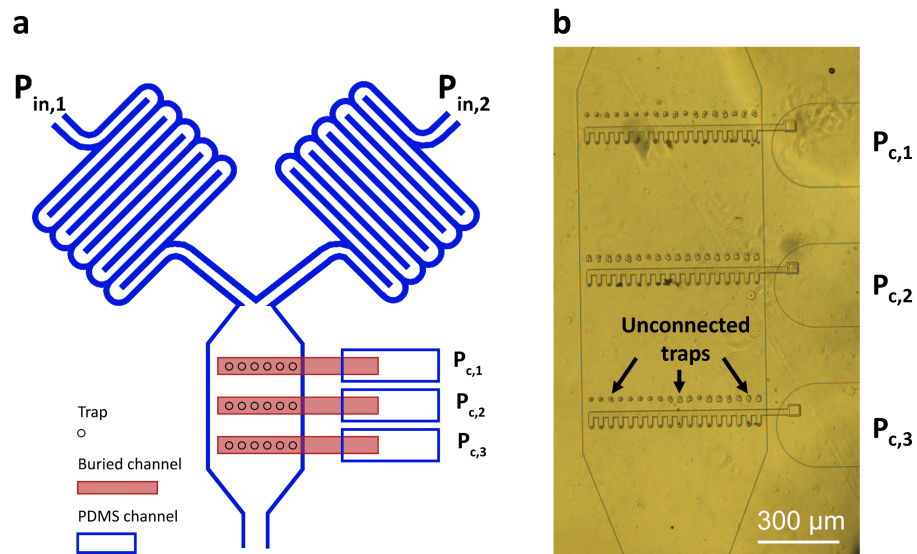


Figure 2.15: **a** Schematic representation of the device used for the selective trapping of beads with two inlets and three lines of interconnected traps controlled by individual control channels. **b** Brightfield picture of the trapping chamber.

The inlet channels were filled from both inlets respectively with a suspension of 8  $\mu\text{m}$  in diameter green and orange fluorescent polystyrene beads while the three lines of traps were in idle mode. The lines were sequentially filled with the desired beads following the sequence described in Table 2.1. The result of the filling at each step is represented in Figure 2.16.

Table 2.1: Description of the parameters for the sequential filling of three lines of traps with green and orange fluorescent beads using individual pressure control channels and two inlets. The pressures are in mbar.

Step	Figure 2.16	$P_{in,1}$	$P_{in,2}$	$P_{c,1}$	$P_{c,2}$	$P_{c,3}$
Channels filling	-	50	50	0	0	0
Line 3 filling with green beads	<b>a</b>	50	0	-20	0	0
Line 2 filling with orange beads	<b>b</b>	0	50	-5	-20	0
Line 1 filling with green beads	<b>c</b>	50	0	-5	-5	-20

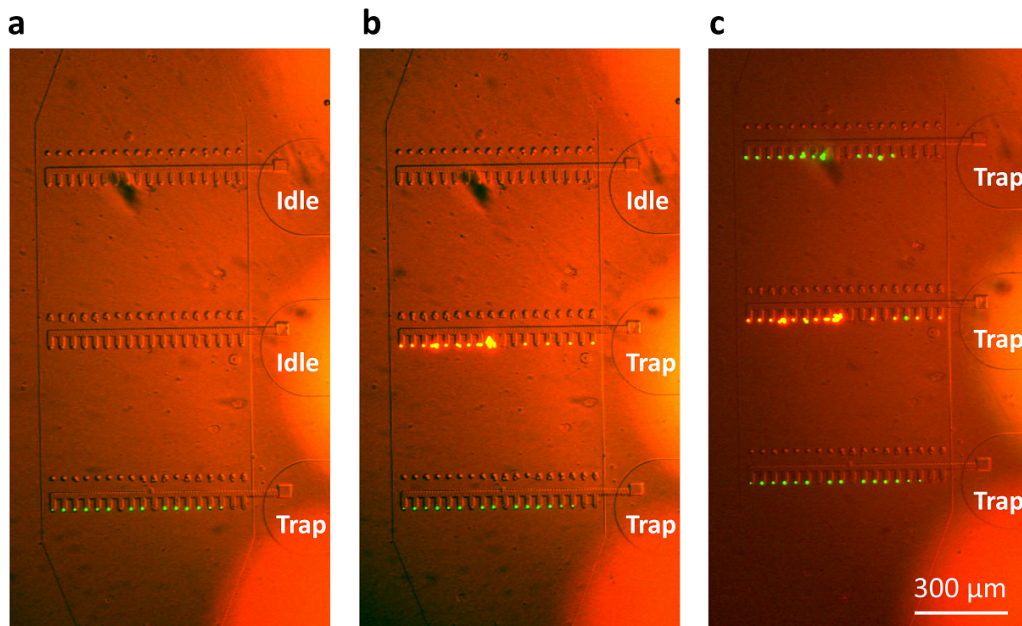


Figure 2.16: Superposition of fluorescent pictures taken in the orange and green channels showing the sequential loading of the traps and demonstrating the selective trapping capability of the planar hydrodynamic trapping approach.

## 2.12 Discussion

This novel type of hydrodynamic traps differs significantly from the typical traps found in the literature. It resolves the problem of space cluttering around the trapped object while allowing a dynamic control over the trapping state. We compare here different characteristics of the array of planar hydrodynamic traps with the two common types of hydrodynamic trapping arrays presented in the introduction in the case of particle trapping: the pachinko and the serpentine arrays shown in Figure 2.1.

### Scalability and density of traps

An interesting parameter to compare is the scalability of the array, or how many traps the system can handle. Each trap of the serpentine and pachinko trapping devices is independent from each other and relies on local flow lines. Once the geometry of one trap is optimized, they can theoretically be scaled infinitely. Both types can be optimized for density (Jin et al., 2015; X. Xu et al., 2013a), however the pachinko arrays are more dense and can accommodate more traps per unit surface because the serpentine arrays require the presence of a space-consuming bypass channel. In contrast the planar hydrodynamic traps proposed here are

interdependent when used in an array: equation 2.4 applied to a single trap shows that the flow passing in each trap depends on the percentage of filled traps of an array. It was also shown that the traps close to the border opposite to the control pressure channel were more difficult to fill due to the additional resistance under the membrane. To scale up the planar traps and limit interdependency, the array should be divided into separate parts controlled by independent control channels and filled sequentially following a sequence described in chapter 2.11: while the first part of the array is being filled, the other parts can be operated in idle mode and so forth until all parts are filled. This comes to the cost of increasing the complexity of the control. However the density of traps can be higher than for the other two mechanisms since there is no material around the trap and more particles can be observed in a defined field of view.

### **Addressability and multiplexing**

We demonstrated in chapter 2.11 the use of independent control channels for different lines of interconnected traps to selectively capture different species in the different parts of the main channel. The possibility of running the chip in the idle mode and the possibility of multiplexing are also available using both types of array only when coupled with pneumatic valve actuation (H. Kim & Kim, 2013; H. S. Kim et al., 2015; Pang et al., 2016).

### **Compliance with particle size**

A limitation of the serpentine and pachinko trapping methods comes from the fact that the single-particle trapping efficiency depends on the height of the channel. While the height has to be larger than the size of the particle to avoid clogging for any type of trapping, a height larger than twice that of the particle causes multiple particles to stack in a single trap in the pachinko and serpentine arrays. An exception to this is the pachinko type array proposed by Di Carlo et al. (2006) where the leaks maintaining the particles in the traps come from a thin horizontal slit. In both cases however the traps are designed for a specific range of particle sizes and are not compatible with a solution comprising a wide distribution of particle sizes. In contrast, the height of the main channel is not limited in the case of coplanar traps, as proved by the trapping of beads of 5  $\mu\text{m}$  diameter in a channel of 30  $\mu\text{m}$  height. Furthermore, a trap of defined diameter will be blocked by particles with a wide range of sizes larger than the trap as described in chapter 2.6, which implies that a wide range of particles can be successfully trapped using this technology.



**Trapping efficiency and filling percentage**

Due to its deterministic trapping property, the serpentine trapping can reach 100% trapping efficiency and filling percentage. The pachinko array was shown to have a filling percentage up to > 99% (X. Xu et al., 2013a) but no reported trapping efficiency was found for beads. However it is believed to be low because of its stochastic nature. In comparison, the planar hydrodynamic traps have both good trapping efficiency and filling percentage with respective values of 94% and 98%.

**Space available and complexity of fabrication**

The planar hydrodynamic traps have the advantage of having the space around the trapped particle completely available for the interaction with other particles, which can be manipulated with a different force, such as hydrodynamics, optical tweezers, dielectrophoresis, or other (Arnaud et al., 2020) as the microfabrication process with standard materials and processes allows to easily add an additional layer to fabricate micro-electrodes aligned to the buried and PDMS channels.

Figure 2.17 shows the frame superposition of subsequent cells flowing around the ones trapped in the array in a "roll-over" manner (M. Duchamp et al., 2019), demonstrating the potential of this technology to study in flow cell-cell interactions. This space could also be used to place electrodes for the impedance measurement of the particle for example. However these possibilities come to the cost of an increased complexity of fabrication: while the serpentine and pachinko devices can be fabricated by a single PDMS casting step, the planar hydrodynamic traps require an extra photolithography step for the fabrication of the buried channels.

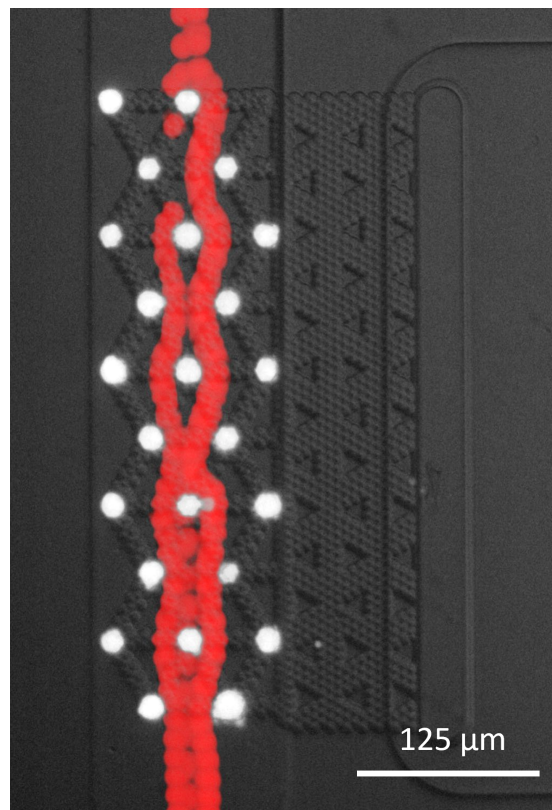


Figure 2.17: Timelapse image of three cells flowing around the ones immobilized in an array of traps in a "roll-over" manner showing the potential of the device to be used for interaction studies. The cells flowing in the channel are coloured in red by image processing for a better visualization.

### 2.13 Other applications

We discuss in this section the potential of the buried channel technology in microfluidics. Indeed this concept of two levels of channels interconnected by micro-sized vias has versatile functionalities with potential applications in different fields because, among others, of its three dimensional configuration, transparency and composition made of isolating materials. We list here some of these functionalities with some practical examples and the associated considerations.

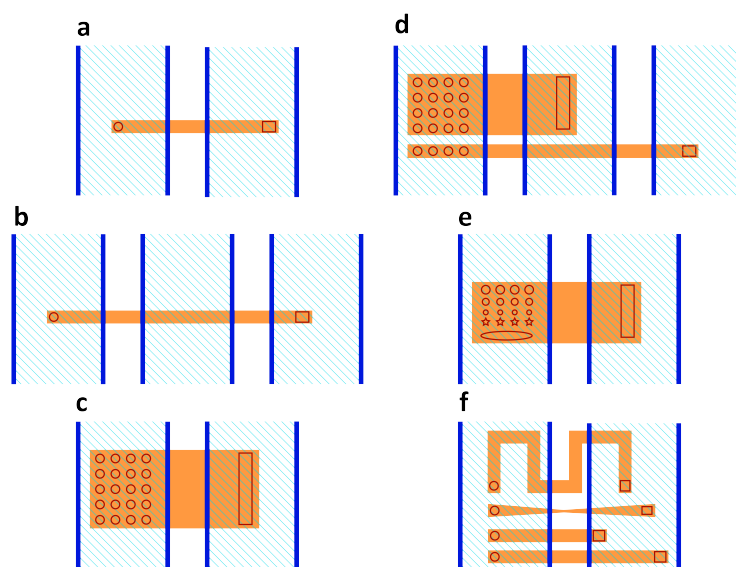


Figure 2.18: Examples of configuration modalities achievable with the buried channel process. **a** Flow connection **b** Flow connection with channel underpass **c** Arraying **d** Addressability **e** Microfluidic via shape modulability **f** Versatility in buried channel path and shape

### 2.13.1 Configuration modalities

The buried channels are capable of connecting two neighbouring channels (Figure 2.18a), but also of connecting two channels separated by another one without affecting this latter (Figure 2.18b). The microfluidic vias can be arranged in arrays and connected to a single channel as discussed in section 2.9 and represented in Figure 2.18c for the arrangement and trapping of micro-sized particles in a defined pattern which can be useful for particle assembly (Van Geite et al., 2022). Single microfluidic vias and arrays can be independently actuated in the different modes when connected to individual control channels (Figure 2.18d). Even though only round and rectangular microfluidic vias were presented in this chapter, the vias can be designed in any shape and arranged in any manner (Figure 2.18e). The limitations in via shape come from the resolution of the photolithography and etching methods chosen to pattern them together with the thin film deposition used to close the vias. These effects limit the sharpness of the edges as well as the minimum distance between two features. The shape of the buried channels can be tailored for specific functions such as resistance to flow, hydraulic diameter or path direction (Figure 2.18f).

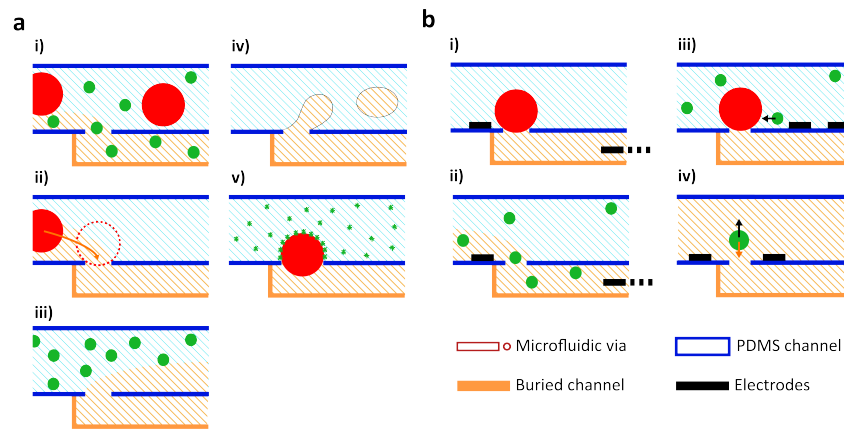


Figure 2.19: Example of applications using the buried channel technology **a** i) Particle filtering by size ii) Trapping iii) Focusing by flow perfusion iv) Droplet formation by perfusion of an oil phase v) Partial exposition of a trapped particle to molecules **b** Example of applications using electrode integration i) Counter-electrode placed at the outlet of the buried channel to force the electric current through the trapped particle ii) Electrical characterization of the passing particles iii) The counter electrode is placed in a coplanar configuration for the application a DEP force iv) Balance between DEP force and flow drag force for characterization or pick and place applications

### 2.13.2 Application

Controlling the flow inside the buried channels implies controlling the flow profile of the liquid coming in or going out from the buried channels. This feature can be used for different functionalities to manipulate objects. Considering the case of flow coming in the buried channel for example, particles with a radius larger than the height of the flow going inside the buried channels are not directed towards the buried channels whereas particles with a smaller radius do pass inside the buried channel and this latter acts as a particle filter (Yamada & Seki, 2005) as illustrated in Figure 2.19a i), as long as the microfluidic via and buried channel dimensions are large enough to let the smaller particles pass. When this is not the case, the particles whose center lie in the streamlines going in the buried channel are immobilized in the microfluidic via acts as a trap as illustrated in Figure 2.19a ii). Considering a trapped particle in this latter case, a flow containing reagent or coating chemicals can be flown in the top channel. Because the particle clogs the flow path to the buried channel, only the top part of the particle is exposed to the coating reagent, creating a Janus particle such as

represented in Figure 2.19a v) (Zhang et al., 2017). The ratio of microfluidic via diameter to particle diameter defines the portion of the particle that is coated. Considering the case where the flow is perfused from the buried channel to the top channel, the shape of the microfluidic via and value of the flows define the shape of the perfused flow lines, which can be used for focusing application (Figure 2.19a iii) ). Indeed, liquid can be injected from the buried channels directly in a large channel to create tailored stratified flow patterns and focus the incoming flow. The position of the stratum is defined by the position of the buried channels outlet whereas its width is controlled by the pressure applied to the control channel and its hydraulic resistance. A experimental example of this feature is detailed in appendix B.

Following the same concept, the buried channels could be used to create passive microfluidic mixers by taking advantage of the 3D structures to collect and inject the fluid passing in a PDMS channel similar to a 3D serpentine mixer for an efficient mixing (C.-Y. Lee et al., 2016). Oil could also be injected via the buried channel to create a membrane emulsion type with finely controlled spatial distribution and pore size (P. Zhu & Wang, 2017) as illustrated in Figure 2.19a iv).

One of the requirement for the process was the compatibility with electrode patterning. We discuss here the potential applications combining buried channels and electrodes. Considering a configuration where a particle is trapped as described in Figure 2.19b i) with an electrode patterned in the particle vicinity and the counter electrode placed at the outlet of the buried channel as illustrated in Figure 2.19b ii), one can use the electrodes for electrical characterization (Cheung et al., 2005), stimulation (C. Chen et al., 2019) or poration (Punjiya et al., 2019). The potential electrical characterization comprise impedance measurement at high frequency to characterize membrane capacitance and cytoplasm conductivity, with the advantage of this configuration to provide a single path for the current through the cell with limited contributions coming from current paths around the cells as in standard configurations. Using the same configuration, patch clamp technique could be performed on the cells for characterization, with the advantages of a small aspiration of the cell in the channel combined with the slanted profile of the trap to provide a large area of contact between the cell and the walls and ensure a good sealing (P. Chen et al., 2009). These characterizations can be performed on many cells in parallel thanks to the adressability feature of the method. Alternatively, the electrodes can be used to stimulate the trapped cell or electroporate them for transfection or insertion of cargo material inside the cell (Dong et al., 2020). With the same electrode configuration but considering buried channels and microfluidic via operating in the non-trapping regime with particles smaller than these latters dimension, the microfluidic via can be operated as a Coulter counter (Rodriguez-Trujillo et al., 2006) as illustrated in Figure 2.19b ii). Either the microfluidic via or a constriction of the buried channel (example illustrated in Figure 2.18f) can take the role of constriction to count and characterize the passing particles. The two electrodes can be patterned in the main channel as illustrated in Figure 2.19b iii). In

this configuration, the electrodes can be used to generate a force such as electrophoresis or dielectrophoresis on particles. These forces can be for example used to bring a second particle in contact with a particle previously trapped in the hydrodynamic trap such as the application proposed in this thesis. When patterned in the appropriate shape, the electrodes can generate a DEP force that balances the drag force exerted by the flow perfused from or aspirated to the buried channel for characterization or pick and place applications as shown in Figure 2.19b iv).

### 2.13.3 Flow control strategies

Flow and pressure control are necessary to obtain the different applications described above. Some proposition of flow control strategies are thus listed below. When a constant flow ratio is desired a simple passive approach such as the one proposed by W.-H. Tan and Takeuchi (2007) is preferred (Figure 2.20a iii)). The flow ratio is determined by design by the ratio of resistance between the buried channel and bypassing arm and is of special interest for the trapping of cells.

The flow control modality used in this chapter is an active method that controls the flow in the buried channel by controlling the inlet and buried path outlet pressures as illustrated in Figure 2.20a i). Syringe pumps connected to the same inlets/outlets can be used to control the flow instead of pressure. Flow control at the outlet of the buried channel is however not recommended when this latter is used to trap particles: since the particle clogs the path, the flow constraint will result in a virtually infinite difference of pressure at the interface of the particle. A mix of pressure and flow control can be used by controlling  $P_c$  and  $Q_{in}$ , but it is again not recommended to trap particles in this configuration. Indeed considering the same inlet flow before trapping, the value of  $\Delta P_p$  will be larger after trapping with flow control than with pressure control. Indeed  $\Delta P_p = R_2 Q - P_c$  after trapping with  $Q$  the total flow in the circuit after trapping. This latter decreases upon trapping of a particle using pressure control because of the increase in the total circuit resistance, but it remains constant using flow control.

Even for applications without particle trapping, the fine control of flow rates can be challenging using syringe pumps at very low flow rates because of the screw thread generating oscillations. We thus propose another circuit capable of finely controlling the flow in the buried channel using a flow control and a variable hydraulic resistance as illustrated in Figure 2.20a ii). The circuit is similar to a Wheatstone bridge and the expression of the flow in the buried channel is defined as (Tanyeri et al., 2011):

$$Q_{BC} = Q_{in} \frac{R_1 R_3 - R_2 R_{var}}{(R_1 + R_{var})(R_2 + R_3) + R_{BC}(R_1 + R_2 + R_3 + R_{var})} \quad (2.6)$$

and the difference of pressure at the interface of a trapped object is expressed as:

$$\Delta P_p = Q_{in} \frac{R_3(R_2 + R_3) - R_2(R_{var} + R_3)}{R_1 + R_2 + R_3 + R_{var}} \quad (2.7)$$

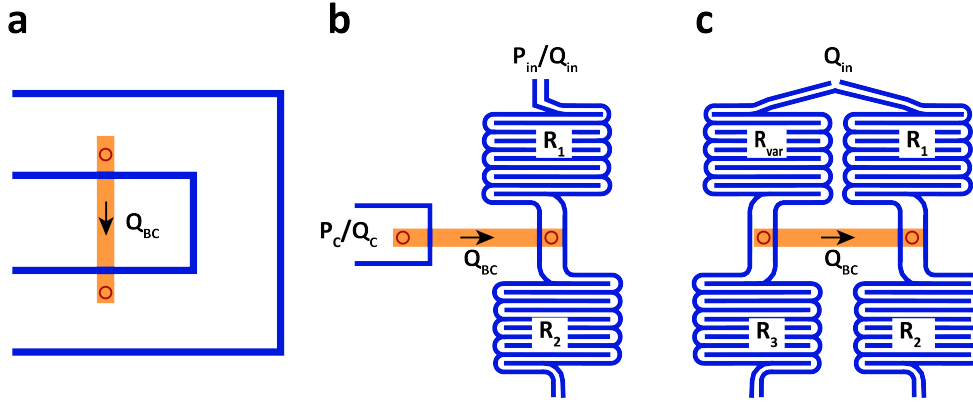


Figure 2.20: Example of flow control strategies **a** Passive **b** Active by direct control of the pressure or flow at the outlet of the buried channel **c** Active by a Wheatstone bridge configuration for a fine control over  $Q_{BC}$

## 2.14 Conclusion

This chapter detailed a process for the fabrication of a novel type of hydrodynamic traps based on a coplanar configuration that enables the trapping of beads and cells in flow with no material surrounding the trapped particles. The traps can be dynamically operated in different modes thanks to the presence of a pressure control channel and are able to trap and release particles, but also operate in idle mode. We studied the influence of flow shear and pressure induced forces on the bead using 2D finite element modeling and found that the main force maintaining the bead in the trap is due to the difference of pressure at its interface. The resistance to pressure difference of cells immobilized in traps of different diameters was assessed and the result fitted using a theoretical model from pipette assays to extract the tension at rupture of the cell membrane. We proposed a theoretical model to understand the trapping dynamics of object in arrays and showed that this technology can be used for the trapping and releasing of beads and cells in compact arrays. Furthermore, the presented fabrication method for multi-level microfluidic channels connected by vias compatible with electrodes fabrication opens up new possibilities in different fields of application presented in the last section of this chapter.

This novel trapping modality is a cornerstone of a device capable of performing cell-cell interaction. It fulfils all the requirements detailed in section 2.2 and is capable of dynamic switching between idle, trapping and releasing modes. The know-how for safe cell manipulation was

acquired and can be transferred to the application of cell-cell interaction. The second step towards the final device thus consists in the design and characterization of DEP traps capable of maintaining a second cell in contact to the objects immobilized in the planar hydrodynamic trap as illustrated in Figure 2.19b iii). This development is detailed in the next chapter.

The structures fabricated using the process described in the chapter were found to be nicely colorful. The characterization of these colors and its use for the creation of colorful images visible by eye are detailed in appendix D.





## 3 Array of dielectrophoretic traps

**This thesis chapter is adapted from the recently published article:** C. Lipp, L. Koebel, A. Bertsch, M. Gauthier, A. Bolopion and P. Renaud, “Dielectrophoretic Traps for Efficient Bead and Cell Trapping and Formation of Aggregates of Controlled Size and Composition”, *Frontiers in Bioengineering and Biotechnology*, vol. 10, 2022.

The development of dielectrophoretic traps in the context of single cell trapping is discussed in this chapter. The first cell is considered to be immobilized in the hydrodynamic traps presented in the previous chapter. The considerations and developments on electrodes configuration and geometry are presented to create a DEP force field that pushes the second type of cell towards the first one, *i.e.* a force field that directs towards a single point in three dimensions.

An original electrode design offering an efficient three-dimensional dielectrophoretic trap for single cells together with a distribution system is presented. Two easy to fabricate configurations are proposed and their trapping efficiency is compared and their heat generation assessed. The most efficient configuration is selected and the limits of voltage necessary to avoid cell membrane electroporation is determined. The design rules to accommodate more cells in higher channels is defined and the capability of the presented system to direct and arrange cells in a controlled manner demonstrated by forming multicellular assemblies of predetermined size and composition.

### 3.1 Motivation and literature

DEP is a method of choice when a non-contact, active and versatile manipulation of cells or particles suspended in a liquid medium is required and was thus naturally selected for the immobilization of the second type of cells. Dielectrophoretic force derives from the polarizability of a particle placed in a non-uniform electric field generated by a difference of electric potential applied to electrodes. The direction of the force on the particle arising from this polarization is defined by design, but its magnitude can be tuned by the voltage applied to the electrodes and its positive dielectrophoresis (pDEP) or negative dielectrophoresis (nDEP) effect can be tuned in particular cases by the frequency. The expression of the time averaged DEP force exerted on a spherical particle in a non uniform electric field is given as follows:

$$\mathbf{F}_{\text{DEP}} = 2\pi\epsilon_m R^3 \text{Re}[K(\omega)] \nabla \mathbf{E}_{\text{rms}}^2 \quad (3.1)$$

Where  $R$  is the radius of the particle,  $\epsilon_m$  is the fluid permittivity,  $\text{Re}[K(\omega)]$  is the real part of the Clausius-Mossotti factor and  $\mathbf{E}_{\text{rms}}$  is the root mean square (rms) of the electric field. Its magnitude thus mainly depends on the volume of the particle and on the gradient of the square of the electric field, while the Clausius-Mossotti factor determines its sign, positive or negative.

DEP has been widely used for separation of cells based on dielectric properties (Bisceglia et al., 2015; Piacentini et al., 2011), but has also often been used to direct, trap and position groups of cells (Frénéa et al., 2003) or single cells (Godino et al., 2019; Mittal et al., 2007; Punjiya et al., 2019). However, the presence of an electric field in a conductive medium can harm cells, and while many authors demonstrate the ability of their design to trap particles against a certain flow rate for a given voltage, very few assess the heat generation related to the traps (Seger-Sauli et al., 2005).

### 3.2 Requirements

The requirements for the DEP traps are listed hereafter.

1. The electrodes should generate a DEP force field that directs to a single point in three dimensions.
2. The fabrication process for the integration of the electrodes should be compatible with the planar hydrodynamic traps and buried channels.

3. The strategy for the generation of the non-uniform electric field should not influence the flow profile in the channel.
4. The DEP traps should generate a minimum Joule heating to avoid damaging the manipulated cells.
5. The number of DEP traps should be scalable.

### 3.3 Review of electrode configuration

The non uniform electric field used to create particle polarization can be generated by electrodes positioned in different configurations. The main electrodes configurations found in literature for the DEP manipulation of particles are described hereafter. Illustration of the different configurations is provided in Figure 3.1.

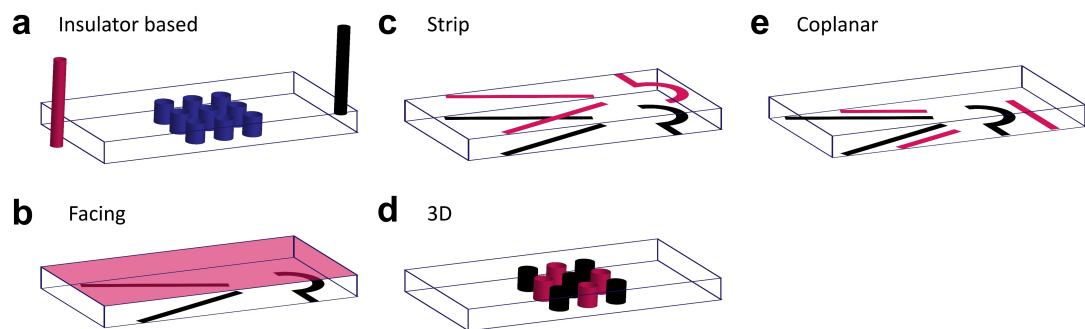


Figure 3.1: Different electrode configurations for generation of a non-uniform electric field used in DEP actuated particles manipulation. The voltage is applied to the electrodes colored in black and the counter electrode is colored in pink.

#### iDEP

In the insulator-based DEP (iDEP) configuration illustrated in Figure 3.1a, the electrodes used to generate the electric field are far away from the region of interest and often composed of macro-sized wires placed in specific reservoirs (Lapizco-Encinas, 2018). Insulator structures are used to deviate the electric field and yield the non-uniformity required for the DEP force. A notable advantage of this configuration is the distance between the electrodes and the particles which prevents any undesirable event such as bubble generation or electrode fouling to impact the trapping region. Additionally, the fabrication only requires a single mask for the structures and channels which lowers the fabrication costs and complexity. The distant

electrodes however require large voltages to generate the desired electric field magnitude. Additionally, the insulator structures impact the fluid flow field which is not desired in the current application.

### **Facing electrodes**

Facing electrodes is similar to strip electrodes, except one plane of electrodes is not patterned and consists in a large conducting and usually transparent layer that is also used for the fluidic capping function (Ho et al., 2013; Takahashi & Miyata, 2020) as illustrated in Figure 3.1b. The electric field is thus maximum close to the patterned electrodes and expands to the capping electrodes in a radial manner. The DEP force field is thus similar to the strip electrodes except it is non uniform in the vertical direction and particles will be directed towards the layer comprising the patterned electrodes in both nDEP and pDEP regimes.

### **Strip electrodes**

Strip electrodes are thin electrodes patterned on the cap and floor of a microfluidic channel and are represented in Figure 3.1c. They typically comprise pairs of electrodes of identical geometry facing each other. Each pair generate either a virtual wall or rail for particles upon application of a voltage difference across it. Walls are created in the case of negative DEP and rails for positive DEP. The force can be assumed uniform along the height of the channel and is directed perpendicular to the electrodes border. The relationship between the force direction and electrode geometries is thus direct, facilitating the design for a given function and funnels and traps are typical applications of this configuration (Fiedler et al., 1998; Kirschbaum et al., 2008; Seger et al., 2004). However the proper alignment between the top and bottom electrodes is critical and can be a fabrication challenge.

### **3D electrodes**

3D electrodes are conductive structures spanning the height of the channel and have the advantage of generating an electric field uniform along the vertical axis as illustrated in Figure 3.1d. This feature makes them a good candidate for applications requiring a tall channel for which the facing, strip and coplanar configurations do not perform well. They are also interesting in applications where their flow obstructing and electric field generation properties can be combined for unique functions, but require advanced fabrication methods such as electroplating (Voldman et al., 2002), pyrolysis (Martinez-Duarte et al., 2011) or non-directional metal coating of 3D structures (Kilchenmann et al., 2016).

### Coplanar electrodes

Coplanar electrodes are microfabricated electrodes with much thinner height than the characteristic height of the microchannel. The electrodes are placed on a plane that is parallel to the flow direction, either on the floor or cap of the microfluidic channel as illustrated in Figure 3.1e. Typical coplanar electrodes geometries for particle deviation and manipulation comprise interdigitated (H. Li, 2002), castellated (Morgan et al., 1999a), liquid (Demierre et al., 2007) and quadrupole electrodes (Jones, 2003) but none of these geometries is adapted to create parallel DEP traps. The simplicity of fabrication of this configuration is attractive but the force field generated by coplanar electrodes is more difficult to predict and often requires finite element modeling methods (Punjiya et al., 2019; Rosenthal & Voldman, 2005). Three dimensional traps in the nDEP regime are especially not straightforward to design since the maximum electric field will be present between two electrodes. This results in a vertical force pushing the particles to the cap where the component counteracting the flow is weaker.

The coplanar and facing configurations were selected based on their compatibility with the requirements for DEP traps generation but also on their compatibility with their fabrication on top of a substrate patterned with planar hydrodynamic traps.

## 3.4 Consideration for the manipulation of cells with DEP

Applying a voltage inside a conductive medium may have undesired consequences. In order to limit electrode polarization and electrochemical reactions at the electrodes the voltage applied is alternatively positive and negative. However the heating due to movement of charged molecules and ions under Coulomb force remains present and is directly proportional to the concentration of charged species. A workaround for this problem is to limit the conductivity of the working medium by dilution in de-ionized water. The change in osmolarity by dilution has nevertheless to be compensated by addition of non-charged molecules such as glucose or dextrose for the cells to keep a constant volume. While cells remains physically intact in such special medium, they cannot perform all their function properly and can only stay immersed for a limited time. It is thus necessary to develop DEP traps that generate the largest DEP force while limiting the heat generated.

Another consideration to take into account when exposing cells to electric fields is the potential drop across their membrane it induces. Pore formation occurs in the membrane when this potential drop exceeds a threshold value, which can be lethal to cells and must be avoided in this specific case.

### 3.5 Dielectrophoresis for the creation of multicellular aggregates

The formation of cell aggregates with controlled number and type of cells is crucial in the understanding of cancer invasion and development. For example the role of cancer associated fibroblasts in tumorigenicity is well known and the need for multicellular models based on co-culture to mimic the tumor environment was demonstrated (Labernadie et al., 2017; Lazzari et al., 2018), but there is a lack of tools to control the composition of multicellular assemblies down to the single cell level. In well plates, obtaining single cells using limiting dilution methods comes at the cost of a small portion only of usable wells due to Poisson distribution (Gross et al., 2015) and cell ratios are often determined based on volume and density to recreate heterogeneity (Bauleth-Ramos et al., 2020). Dielectrophoresis has already been used as a tool to form aggregates of cells (Altomare et al., 2003, Menad et al., 2015, Cottet et al., 2019) and to trap and pair single cells in a controlled manner (Yoshimura et al., 2014, Kirschbaum et al., 2008) but has not yet, to our knowledge, been used to create heterogeneous aggregates with controlled number and type of cells.

The hereafter proposed device is easy to fabricate and offers efficient three dimensional trapping capabilities with simple coplanar electrodes and is thus accessible to researchers with access to standard equipment. The distribution system allows a full control on the positioning of the arriving cell and enables for the first time the ability to form heterogeneous assemblies of cells with pre-determined number and type of cells using DEP. This feature is key in research domains focusing on cancer stem cells and the corresponding drug development strategies (Ishiguro et al., 2017), but finds also applications in studies of cellular aggregates that mimic the cancer micro-environment (Ham et al., 2016). While electroporation of the created assembly was avoided in this work, it can be exploited and is readily available in drug development or applications where cell transfection is desired (Chopin et al., 2012; Dalmay et al., 2011). These features were demonstrated here using an array of four traps, but this number can be easily scaled up by lateral repetitions of the trap units as well as repetitions of pairs of electrodes along the length of the channel.

## 3.6 Materials and methods

### 3.6.1 Microfabrication

#### Coplanar electrodes

The coplanar electrodes chips were fabricated using the following process: borofloat wafers were first cleaned using a piranha solution. The metal layer was deposited by sputtering 20 nm of titanium and 200 nm of platinum (SPIDER, Pfeiffer) (Figure 3.2 step 1a). Photoresist (AZ 1512 HS, MicroChemicals) was spincoated, exposed by direct laser writing (MLA150, Heidelberg Instruments) and developed (ACS200, Süss) (Figure 3.2 step 1b). Unprotected metal was etched using ion beam etching (IBE350, Veeco Nexus) and chips were diced (DAD321, Disco) (Figure 3.2 step 1c). The PDMS microfluidic channels were fabricated using a process described elsewhere (Cottet et al., 2017). Shortly, the PDMS master mold was fabricated by deep reactive ion etching of a silicon wafer (AMS200, Alcatel) (Figure 3.2 step 2a). PDMS was molded, cured, punched, precisely aligned and permanently bonded to the glass chips patterned with electrodes using a mask aligner (MJB4, Süss) (Figure 3.2 steps 2b-3).

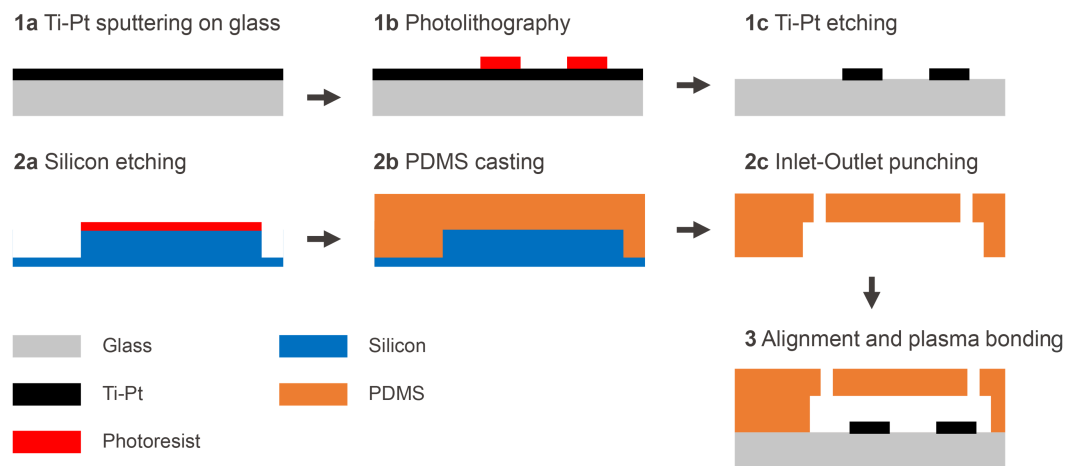


Figure 3.2: Process for the fabrication of the coplanar chip. that starts by the patterning of Ti-Pt electrodes on a glass substrate (wafer 1). PDMS is cast on a silicon mold, punched, aligned and permanently bonded to the glass chips (wafer 2).



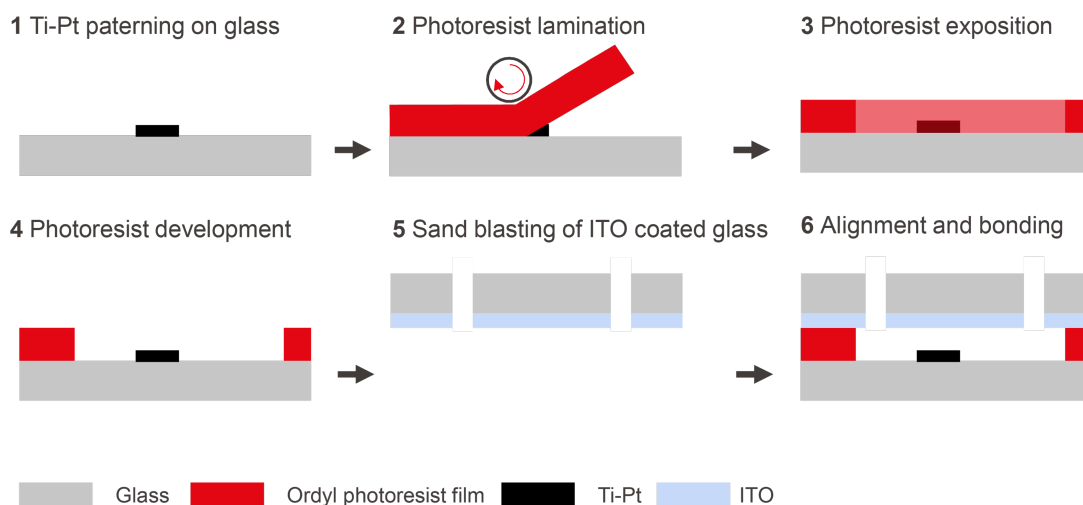


Figure 3.3: The fabrication of facing configuration chip starts by the patterning of electrodes on a glass wafer and is followed by the lamination and patterning of a photosensitive film to define the microfluidic channels (wafer 1). The cap wafer coated with ITO (wafer 2) is then aligned and bonded to the bottom chip.

### Facing electrode

The facing electrodes chips were fabricated following a process described previously (Vulto et al., 2005), by first patterning electrodes as described in the previous paragraph (Figure 3.3 steps 1a-1c). A photosensitive adhesive film was laminated (Ordyl SY320, 20  $\mu\text{m}$  thickness) (Figure 3.3 step 2), exposed through a mask using a mask aligner (MJB4, Süss) with a postbaking step of 1 min at 85°C, developed (Ordyl XFB) and rinsed (Ordyl Rinse) (Figure 3.3 step 3-4). The fluidic inlets and outlets of the capping borofloat wafer were fabricated by sandblasting (IcoFlex Sàrl, Switzerland) and 200 nm of ITO was then sputtered (SPIDER600, Pfeiffer) (Figure 3.3 step 5). Both wafers were then aligned (MA6/BA6, Süss) and bonded (SB6, Süss) by applying a pressure of 425 kPa for 30 min at 90°C followed by a curing step at 150°C for 2 hours (Figure 3.3 step 6). Connections between the top and bottom electrode were made by placing a chip on a heating plate at 90°C and introducing low temperature solder (The Indium Corporation of America) inside a microfluidic channel designed for this application and passing on top of the desired bottom electrode track.

### 3.6.2 Materials

5  $\mu\text{m}$  in diameter polystyrene beads were purchased from Sigma-Aldrich and suspended in a working solution composed of 10% in volume PBS (Gibco) and 90% DI water at a concentration of  $5 \cdot 10^5$  beads/ml. The surface of polystyrene beads was left uncoated and the particles are thus natively negatively charged in buffers with physiological pH. The use of AC electric fields however discards any net movement due to electrostatic forces.

### 3.6.3 Cell culture

Jurkat and Colo205 cell lines (ATCC) were cultured in RPMI 1640 supplemented with 10% of FBS and 1% Penicillin-Streptomycin at 37°C in 5% CO<sub>2</sub> atmosphere. Staining of Colo205 was performed by incubating the cells in PBS with 4  $\mu\text{M}$  Calcein UltraBlue AM (Cayman Chemical) for 1 h. Staining of Jurkat cells was done by incubation in PBS with 1  $\mu\text{M}$  Calcein AM (Invitrogen) for 1h. The working solution is composed of 40% RPMI and 60% DI water. The solution is compensated for osmolarity by the addition of dextrose (Sigma-Aldrich) and cleaned through a 0.22  $\mu\text{m}$  filter. Jurkat and Colo205 were both resuspended in the working solution and passed through a 40  $\mu\text{m}$  cell strainer before the experiment. All reagents are from Gibco unless specified.

### 3.6.4 Chip operation

Measurement of the current and phase was performed in a solution of 10% PBS and 90% DI water by applying an AC signal between 1 and 10 V amplitude to the trapping electrodes at a frequency of 100 kHz using an HF2TA current amplifier connected to a HF2LI Lock-In amplifier (Zurich Instruments).

The PDMS chip was primed with Pierce Protein-Free (PBS) Blocking Buffer during 1h to prevent cells from adhering to the surfaces. The cells or beads were placed in a chromatography vial connected to the punched PDMS by a 360  $\mu\text{m}$  outer diameter PEEK tubing (Idex). Pressure was applied to the vials using Fluigent Flow-EZ pressure controllers. The chip was mounted on and electrically connected to a custom PCB placed on the stage of a Leica DMI3000 B inverted microscope and observed using a uEye (IDS) camera. All the electric signals needed to control the positions of the particles are sent through a home made PCB creating the multiplication of an AC signal at 100 kHz and different DC signals whose amplitudes are controlled by the computer with a custom C++ program through an analog output generator (Mccdaq USB-3100).

### 3.6.5 COMSOL simulations

Modeling of the electric field and DEP force direction and magnitude was done using COMSOL Multiphysics 5.6 with the Electric Currents and Creeping Flow modules. The medium electrical conductivity and relative permittivity were set respectively to 0.16 S/m and 78. The fluid flow at the entrance of the channel was set to 700  $\mu\text{m/s}$ . A sinusoidal electric potential of 10 V amplitude and 100 kHz frequency was applied to the trapping electrode and the potential of the counter electrode was set to zero.

## 3.7 Concept

A microfluidic system capable of performing in-flow cell selection, sorting and trapping using non-contact DEP actuation is presented. The system is shown in Figure 3.4 i) and is composed of an upstream DEP actuated deviation system that laterally focuses the incoming particles or cells on specific flow lines so that they can be collected by the desired downstream DEP trap. The DEP traps are actuated by applying a potential across two electrodes: the upstream main electrode is designed with repetitions of funnel-shaped units and the counter electrode is either placed in a coplanar or facing configuration. Each trap unit is 60  $\mu\text{m}$  in width and capable of stopping a single cell or particle in flow by balancing the drag force and creating a single position of equilibrium upstream of the electrodes. The slanted parts of the trap unit finely focus the particles towards the center of the traps indicated by the focus line in Figure 3.4 i). The number of traps can be adjusted to the width of the channel by lateral repetitions of the funnel-shaped trap unit. A bypass area is also provided next to the trapping electrodes such that unwanted cells can be directed to bypass the traps and leave the chamber.

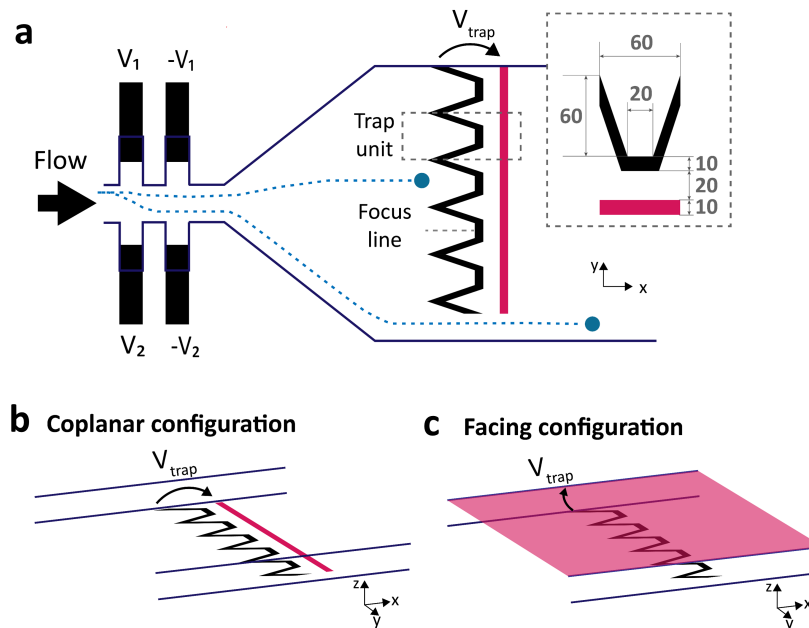


Figure 3.4: Deviation system, electrodes design and configuration. **a** Top view scheme of microfluidics and electrodes: the deviation system is based on liquid electrodes placed on each side of the channel, upstream of the trapping electrodes. The ratio of the voltages applied on each side ( $V_1/V_2$ ) defines the lateral position of the particles (Demierre et al., 2007), directing it towards a defined trap unit. Two examples of particles trajectories are illustrated in blue. The main electrode is composed of trap units placed next to each other and of a counter electrode highlighted in pink. The trapping electrodes are not covering the whole channel width so the unwanted cells can bypass the traps. The dimensions in  $\mu\text{m}$  of a trap unit are displayed in the inset. **b** In this coplanar configuration the counter electrode is a straight line placed downstream of the main electrode on the same plane. **c** The counter electrode of the facing configuration covers the cap of the microfluidic channel.

### 3.7.1 Deviation system

In order to control the trajectory of the incoming particles and guide them towards the desired trap unit, a deviation system using six pairs of liquid electrodes similar to the one presented by Demierre et al. (2007) was placed upstream of the trapping chamber. For the sake of simplicity, only two pairs of liquid electrodes are represented on the left of Figure 3.4a. Liquid electrodes are coplanar electrodes placed in a lateral recess from the main channel: this configuration guides the electric field and generate a vertical equipotential surface at the entrance of the main channel, hence their name. Two sets of liquid electrode combs are placed laterally on each side of the main channel and a voltage is applied to each set, with a phase shift of  $180^\circ$  to neighbouring electrodes. The electrodes width and clearance between them are both set to

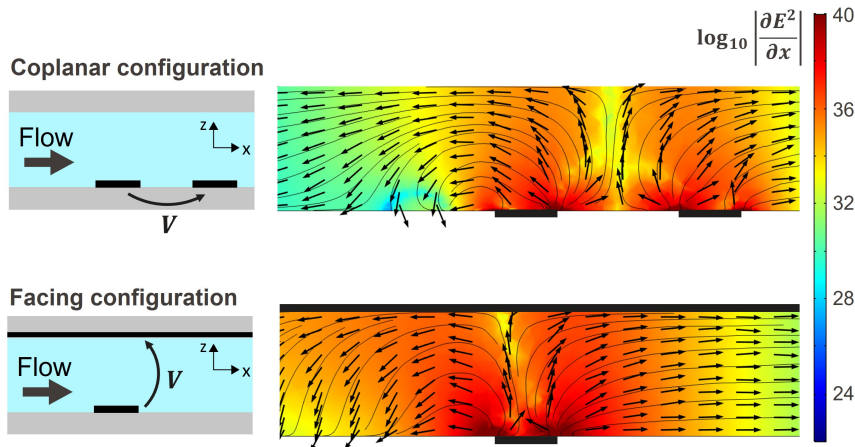


Figure 3.5: COMSOL simulation along a  $xz$  plane in the center of the trap as indicated by the focus line in Figure 3.4a for both configurations and for a voltage amplitude of 10 V. The colour indicates the magnitude of  $\frac{\partial E^2}{\partial x}$ , which is the electric field dependent factor that modulates the DEP force, while the arrows and streamlines indicate the direction of the nDEP force along the  $xz$  plane. The electrodes are drawn on top of the simulations for visualization. Both electrode configurations generate a force pushing against the flow and towards the bottom of the channel upstream of the main electrode.

the same value as the channel height. Each set of liquid electrodes generates a lateral DEP force uniform along the height of the channel pushing the particles away from them. The ratio of voltage applied to each side  $V_1 / V_2$  determines the equilibrium position along the  $y$  axis in the main channel, focusing the randomly distributed incoming particles towards a defined lateral position and deviating them towards the trap units, or to the bypass. As described by Demierre et al. (2007), the total force exerted on the particles is the sum of the forces exerted by each comb of electrodes and the particles are focused where these forces cancel each other: it is thus not dependent on the particle or cell size nor position before entering the deviation zone. At low fluid velocity, the limit in the focusing is due to particle collision and diffusion, which is compensated by the slanted part of the traps placed downstream, collecting particle streams covering  $60 \mu\text{m}$  in width. Nevertheless, the focusing has a size dependent limit on the channel sides: the particle center cannot be focused closer to the wall than the particle's radius due to straightforward reasons.

### 3.7.2 Counter electrode configuration and simulations

Two easy to fabricate configurations of counter electrode were implemented and studied. The coplanar counter electrode consists in a straight line electrode placed downstream of the trapping electrode as shown in Figure 3.4b. For the facing counter electrode, a conductive and transparent indium tin oxide (ITO) layer is provided on the glass plate used to close the channels on their upper part as illustrated in Figure 3.4c. Both configurations are popular and extensively used to manipulate cells using DEP in microfluidic chips (Ho et al., 2013, H. Li and Bashir, 2002, Morgan et al., 1999b, Takahashi and Miyata, 2020). In order to assess the three dimensional behaviour of the traps, both designs were simulated using COMSOL. Figure 3.5 illustrates the results of the simulation along the focus line indicated in Figure 3.4a: the colour indicates the magnitude of  $\frac{\partial E^2}{\partial x}$ , which is the electric field dependent factor that modulates the DEP force while the arrows of normalized size indicate the direction of the nDEP force along the  $x$  and  $z$  axis. Electrode locations are indicated on the results of simulations by black rectangles. Figure 3.6 represent the iso-surfaces of the electric field squared  $E^2$  and indicate that both configurations can be used for the trapping of particles in three dimensions: the nDEP force is perpendicular to these surfaces and directed towards the iso-surfaces of lower value. It is observed that the  $y$  component of the force directs the particles toward a single  $xz$  plane of equilibrium in the middle of each trapping unit while the  $z$  component pushes the particles towards the bottom of the channel. The  $x$  component of the DEP force counteracts the drag force. Its value, controlled by the applied voltage, determines the equilibrium position of the particles along the  $x$  direction. For the same applied voltage, the facing electrodes configuration generates a larger DEP force in the  $x$  direction compared to the coplanar configuration.

To test these two designs, chips with electrodes placed in both configurations and aligned to microfluidic channels with  $\mu\text{m}$  precision can be manufactured using standard cleanroom equipment with a few steps only. The fabrication process for both designs is detailed in the Materials and Methods section and illustrated in Figure 3.2 and 3.3. Experiments are presented in the next section.

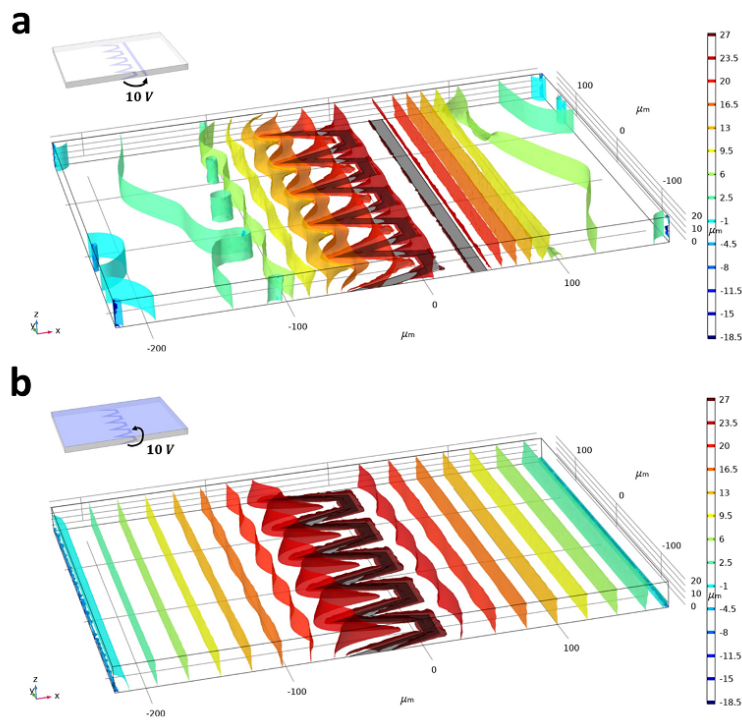


Figure 3.6: 3D COMSOL simulation representing the iso-surfaces of the electric field squared  $E^2$  for the coplanar (a) and facing (b) configurations: the nDEP force is perpendicular to the iso-surfaces and directed towards the iso-surfaces of lower value. The funnel shape of the iso-surface upstream of the electrodes indicate a three dimensional trapping behaviour: the  $y$  component of the force points towards the center of a trapping unit thanks to the slanted part of the electrodes, while the  $x$  component counter acts the flow. Both configurations thus generate a three dimensional trap against the flow. The inset shows the configuration and the electrode location are indicated in black.

## 3.8 Single object trapping

### 3.8.1 Bead trapping efficiency

DEP can damage cells as it can induce a local rise in temperature. Indeed the presence of an electric field in a conductive media induces Joule heating. This effect can be mitigated by reducing the conductivity of the medium and correcting for osmolarity with the addition of dextrose or sucrose, but prolonged exposition of cells to such diluted media can alter their function and health (Hylar et al., 2021). As both electrode configurations presented here create a three dimensional DEP trap against the flow, the most efficient configuration is selected by measuring the magnitude of the DEP force against the flow for both configurations and evaluating in both cases the induced temperature rise. As a reminder, the expression of the time averaged DEP force exerted on a spherical particle in a non uniform electric field is given by the following expression:

$$\mathbf{F}_{\text{DEP}} = 2\pi\epsilon_m R^3 \text{Re}[K(\omega)] \nabla \mathbf{E}_{\text{rms}}^2 \quad (3.2)$$

Where  $R$  is the radius of the particle,  $\epsilon_m$  is the fluid permittivity,  $\text{Re}[K(\omega)]$  is the real part of the Clausius-Mossotti factor and  $\mathbf{E}_{\text{rms}}$  is the root mean square (rms) of the electric field. For a homogeneous spherical particle, the Clausius-Mossotti factor is given by the following formula:

$$K(\omega) = \frac{\epsilon_p^* - \epsilon_m^*}{\epsilon_p^* + 2\epsilon_m^*} \quad (3.3)$$

With  $\epsilon_p^*$  the complex permittivity of the particle and  $\epsilon_m^*$  the complex permittivity of the medium, which are both frequency dependent. The sign of the Clausius-Mossotti defines the regime of the DEP force, negative or positive, resulting in particles being respectively repulsed from or attracted to the high electric field regions. In this work, the chip is operated at 100 kHz in the negative DEP regime and the real part of the Clausius-Mossotti factor has a value of  $-0.5$  for all medium and particle or cell conditions.

In order for a particle to be trapped, the projection of the DEP force on the axis of the flow direction ( $x$  in the present case) has to balance the viscous drag force exerted by the flow (Voldman et al., 2001, Rosenthal and Voldman, 2005):

$$6\pi\eta R \left(6\nu_{\text{mean}} \frac{F^* z_p}{h}\right) = 2\pi\epsilon_m R^3 \text{Re}[K(\omega)] \frac{\partial \mathbf{E}_{\text{rms}}^2}{\partial x} \quad (3.4)$$

Where  $\eta$  is the fluid viscosity,  $\nu_{\text{mean}}$  is the mean fluid velocity,  $h$  is the height of the channel,  $F^*$  is a factor accounting for the wall effect,  $z_p$  is the height of the particle.

The heat flow generated by electrodes matches the electrical power input in the system and the average temperature around the DEP electrodes was shown to depend on the real part of



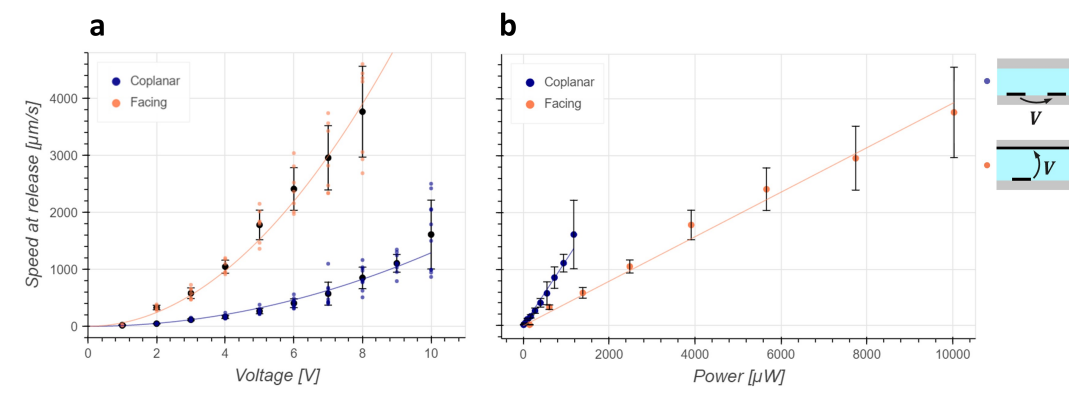


Figure 3.7: Characterization of the trapping efficiency: 5  $\mu\text{m}$  in diameter polystyrene beads are trapped for a given voltage and power and the flow is increased until the bead takes off and its speed is measured. The black dots and bars are the mean and standard deviation respectively and the continuous line is the fit. **a** The speed at release follows a squared dependency on the applied voltage as predicted by equation 3.14. As expected from simulations in Figure 3.5, the coplanar configuration develops a smaller force for a given applied voltage compared to the facing configuration. **b** The speed at release depends linearly on the developed power as expected from equation 3.15. It can be deduced that the coplanar design is more efficient at trapping in this case as it can develop a larger  $F_{\text{DEP},x}$  for a given power dissipated than the facing configuration.

the electrical power (Seger-Sauli et al., 2005, Ramos et al., 1998) which is defined as :

$$P = V_{\text{rms}} I_{\text{rms}} \cos(\theta) = \frac{V_{\text{rms}}^2}{Z} \cos(\theta) \quad (3.5)$$

With  $V_{\text{rms}}$  the rms voltage applied to the electrodes,  $I_{\text{rms}}$  the rms electrical current,  $\theta$  the phase shift between the current and voltage and  $Z$  the norm of the electrical impedance.

Since the temperature is directly proportional to the electrical power, this latter can be used as an indicator of electrode trapping efficiency when comparing designs of similar size. Following equation 3.4, the DEP force developed by a trap at steady state and at a defined position is directly proportional to the velocity of the fluid flow dragging the particle. Thus the maximum DEP force developed by each configuration is measured by immobilizing a polystyrene particle in a trap at low fluid flow and increasing the flow until the bead is released. The particle velocity at release is measured, which is directly proportional to the maximum DEP force the trap can develop in the  $x$  direction at the edge of the electrode as a function of applied voltage and generated power. The latter is obtained by multiplying the applied voltage by the measured current at each condition following Equation 3.5.

From Equation 3.4, the mean velocity of the fluid can be expressed as:

$$v_{\text{mean}} = \frac{h}{18\eta F^* z_p} \epsilon_m R^2 \text{Re}[K(\omega)] \frac{\partial \mathbf{E}_{\text{rms}}^2}{\partial x} \quad (3.6)$$

The potential distribution in space can be described as a direct function of the voltage  $V$  applied to the electrodes. Starting from the assumption that the expression of the potential  $\phi(\mathbf{r})$  in space is the factor of the voltage  $V$  applied to the electrodes and a function of space  $\gamma(\mathbf{r})$  describing its distribution:

$$\phi(\mathbf{r}) = V \cdot \gamma(\mathbf{r}) \quad (3.7)$$

with  $\mathbf{r}$  the position vector, the expression of the electric field  $\mathbf{E}(\mathbf{r})$  becomes:

$$\mathbf{E}(\mathbf{r}) = -\nabla\phi(\mathbf{r}) = -\nabla[V \cdot \gamma(\mathbf{r})] = -V \cdot \nabla[\gamma(\mathbf{r})] \quad (3.8)$$

Thus the gradient factor of equation 3.2 can be rewritten as:

$$\nabla \mathbf{E}^2 = \nabla[\mathbf{E} \cdot \mathbf{E}] \quad (3.9)$$

$$= \nabla[V \cdot \nabla[\gamma(\mathbf{r})] \cdot V \cdot \nabla[\gamma(\mathbf{r})]] \quad (3.10)$$

$$= V^2 \cdot \nabla[\nabla[\gamma(\mathbf{r})] \cdot \nabla[\gamma(\mathbf{r})]] \quad (3.11)$$

Defining  $\alpha(\mathbf{r})$ , a function of space:

$$\alpha(\mathbf{r}) = \nabla[\nabla[\gamma(\mathbf{r})] \cdot \nabla[\gamma(\mathbf{r})]] \quad (3.12)$$

The gradient factor of equation 3.2 becomes:

$$\nabla \mathbf{E}^2 = V^2 \cdot \alpha(\mathbf{r}) \quad (3.13)$$

With  $\alpha_x$  the  $x$  component of the vector  $\alpha(\mathbf{r})$ , equation 3.6 can thus be re-written as:

$$v_{\text{mean}} = \frac{h}{18\eta F^* z_p} \epsilon_m R^2 \text{Re}[K(\omega)] \alpha_x V^2 \quad (3.14)$$

Introducing the electrical power from Equation 3.5 into this equation:

$$v_{\text{mean}} = \frac{h}{9\eta F^* z_p \cos(\theta)} \epsilon_m R^2 \text{Re}[K(\omega)] \alpha_x ZP \quad (3.15)$$

With  $\alpha_x$  the  $x$  component of  $\alpha(x, y, z)$  described above and taken at the edge of the electrode, this equation indicates that the efficiency of trapping of a given design and configuration of electrodes depends on the multiplication of  $\alpha_x$  and  $Z$ .

The current and phase were measured for both configurations and for voltage amplitudes between 1 and 10 V. The real part of the electrical power, responsible for Joule heating, was calculated as of Equation 3.5. The mean and standard deviation phase was measured to be  $\theta = 11.2^\circ$  and  $1.4^\circ$  respectively for the coplanar configuration and  $\theta = 8.9^\circ$  and  $1.5^\circ$  respectively for the facing configuration, the real part of the power accounted for more than 97% of the apparent power thus indicating a mainly resistive load. Figure 3.7a is a plot of the measured speed at release for 5  $\mu\text{m}$  in diameter polystyrene particles as a function of applied voltage amplitude for both facing and coplanar configurations. The dependency of the velocity at release is quadratic on the voltage in accordance with Equation 3.14. As predicted by the simulations and Figure 3.5, the facing configuration generates a larger  $\frac{\partial E_{\text{rms}}^2}{\partial x}$  for a given voltage and the velocity of the particle at release is larger in this configuration. Figure 3.7b shows the velocity at release as a function of electric active power. It results that the velocity at release depends linearly on the power as predicted from Equation 3.15. It appears that the larger gradient factor  $\alpha_x$  of the facing design does not compensate the smaller impedance of this design, resulting in more heat dissipated for a given DEP force than the coplanar design and thus a larger increase in temperature. Furthermore, the temperature is not uniformly distributed and the active power only represents the average temperature increase. The larger temperatures are expected to be found where the electric field is larger, which is closer to the position of trapping for the facing configuration than for the coplanar configuration. The coplanar design was thus selected for the following study of cell trapping. However, the facing electrode configuration is suggested for applications where flow speed is the main criteria and heat generation is not a limitation since it generates a larger DEP force for a given voltage.

### 3.8.2 Single cell trapping

Electroporation can damage the cells when trapped using DEP. Electroporation takes place when the potential difference across the cell membrane exceeds a threshold value, inducing pores in the membrane. This phenomenon is not necessarily lethal for the cells and is widely exploited to introduce genetic material inside the cells. However electroporation is not desired in manipulation applications and to avoid any damage to the cells the applied voltage limit to avoid electroporation conditions was experimentally determined. Jurkat cells were loaded with Calcein AM to visualize pore formation: as calcein is a volatile fluorescent molecule, it quickly diffuses out of the cell in case of pore formation in the membrane. The maximum velocity for trapping without electroporation as a function of voltage amplitude is measured and reported in Figure 3.8a. In case of fluorescence loss, the voltage was immediately turned

off to release the cell and measure its speed. Events where a leak of calcein was observed are indicated by an orange circle, whereas events without fluorescence loss are indicated by a blue cross. A clear threshold under which no fluorescence loss is observed is found for a voltage amplitude of 5 V and determines the voltage operation limits to avoid cell damage. The large variation in speed at release can be explained by variations in cell size. Figure 3.8b is a picture of a cell arriving in the trap and Figure 3.8c shows the same cell after fluorescence loss.

Typical transmembrane potential threshold above which pores appear have been reported between 0.25 and 1 V (Escoffre et al., 2011). Schwan equation relates the transmembrane potential  $\Delta\Phi_m$  to the external alternating electric field  $E$  with angular frequency  $\omega$ :

$$\Delta\Phi_m = \frac{1.5RE\cos(\phi)}{[1 + (\omega\tau)^2]^{1/2}} \quad (3.16)$$

Given  $\tau = RC_{mem}(\rho_{int} + \rho_{ext}/2)$  with  $C_{mem}$  the membrane capacitance,  $\rho_{int}$  and  $\rho_{ext}$  the resistivity of respectively the internal and external fluid and  $\phi$  the angle between the electric field lines and a line drawn from the center of the cell to the considered point of interest on the cell membrane. The critical value for transmembrane potential corresponds to a range of electric field between  $2.8 \cdot 10^4$  and  $11.2 \cdot 10^4$  V/m using membrane properties values from Reichle et al. (2000). Such values of electric field are found at the edge of the electrode and for a height of 5  $\mu\text{m}$  in simulations for applied voltage amplitude ranging between 2.3 and 9.3 V and comprising the experimentally found threshold, consolidating the hypothesis of fluorescence leakage due to electroporation. The maximum voltage for cell manipulation without electroporation was thus set to 4 V amplitude. Larger voltages may be used without electroporating the cells as long as the flow drag force is limited and does not bring the cell in the critical electric field region close to the electrode edge.

### 3.9 Multiple cell trapping

The presented cell DEP traps with controlled deviation system can be used to co-localize multiple particles of different types in a single trap. Indeed the formation of aggregate of controlled composition and size can be of great interest to study the growth of tumors in their environment composed of different cell types. For applications that require to stop more than one cell, the trap and microfluidic channel need to be scaled up.

#### 3.9.1 Scaling rules

Different parameters were studied to understand their impact on the three-dimensional trapping property for an increased channel height. The following parameters are defined:  $d$  is the distance between the electrodes,  $l$  is the depth of the electrodes,  $h$  is the height of

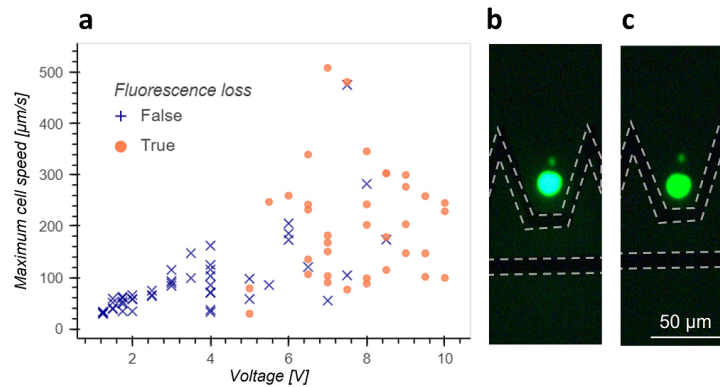


Figure 3.8: **a** Maximum cell speed at release without fluorescence loss as a function of voltage applied for Jurkat cells. Blue crosses indicate no fluorescence loss events whereas orange circles indicate a loss of fluorescence. A clear threshold under which cells never lose fluorescence is found at 5 V and determines the limit in voltage to avoid cell damage. The phenomenon behind the fluorescence loss is believed to be electroporation. **b** Fluorescence picture of a cell arriving in the trap before fluorescence loss. The position of electrodes is highlighted by a dotted line. **c** Fluorescent picture of the same cell after fluorescence loss.

the channel and  $e$  is the width of the parallel part of the main electrode as illustrated in the inset of Figure 3.9. The angle of the slanted part was kept constant as well as the trap depth. Figure 3.9 is the result of COMSOL simulations with the color indicating  $\log_{10}(\frac{\partial E^2}{\partial x})$ , the black streamlines indicate the direction of the DEP vectors for different geometries. The magenta line indicates the contour of a null  $z$  component of the DEP force and thus separates the regions with upwards and downwards DEP force. A vertical contour defines a stable trap for a wide range of sizes and positions in the channel (Rosenthal and Voldman, 2005). Indeed, particles with a center of mass in the region with upward DEP force will be pushed upwards where the DEP force counteracting the flow is weaker, and therefore leave the trap. This is a problem especially when trapping multiple objects where the chance of finding an object higher in the channel is larger. As shown in the previous discussion, the standard design has a vertical contour and all particles coming in the traps will be pushed down to the floor. However, Figure 3.9**b** shows that this property is lost when keeping the same electrode geometry and increasing the channels height  $h$ . The scaling of the electrodes depth  $l$  and distance between them  $d$  is not enough to recover the vertical contour as seen in Figure 3.9**c**. A homothetic scaling is necessary to obtain the property of DEP force pushing down to a single equilibrium position along the whole trap height and to create a compact aggregate, as shown in Figure 3.9**d**.

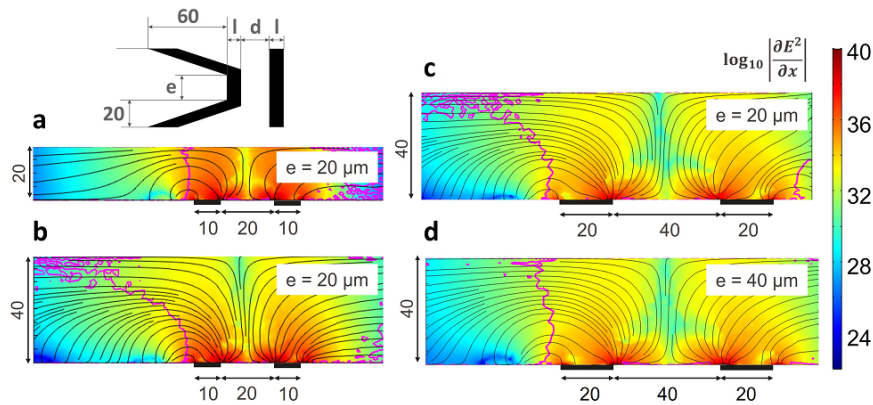


Figure 3.9: Effect of the geometry and channel height on the three dimensional trapping behaviour of coplanar electrodes. The colour indicates the magnitude of the  $x$  component of the gradient of the electric field squared, the black streamline indicate the direction of the DEP force and the magenta contour line separates regions with downward  $F_{DEP,z}$  on the left hand side, from upwards  $F_{DEP,z}$ . All dimensions are in  $\mu\text{m}$ . A vertical contour line is desirable to conserve a three dimensional trapping and avoid that particles found in the higher part of the channel flow over the trap without being stopped. **a** Original design as described in Figure 3.4 in a channel of  $20 \mu\text{m}$  height. **b** Original design in a higher channel: the three dimensional trapping behaviour is lost. **c** Distance between the electrodes and electrode width are scaled accordingly to the channel height. The contour line is still bent. **d** Homothetic scaling of the original design: the vertical trapping behaviour is recovered.

### 3.9.2 Formation of aggregates of controlled size and composition

Here the ability of the presented system to create cell aggregates of controlled size and composition is demonstrated. The single cell design was scaled up as in Figure 3.9d to accommodate more cells in a channel height of 40  $\mu\text{m}$ . Four parallel trapping units were placed next to each other and a bypass with no electrode was left next to the trapping units in order to discard unwanted cells. Two inlets were used sequentially to perfuse solutions with respectively Colo205 cells stained with blue calcein AM, and Jurkat cells stained with green calcein AM. The upstream deviation system was used to direct the incoming cells toward the desired trapping unit to create aggregates of four cells composed of three Colo205 and one Jurkat (Figure 3.10a-c) as well as two Colo205 and two Jurkat (Figure 3.10d-f). The calcein staining was used to both identify the cell type as well as to ensure cell viability. The aggregates could be held inside the traps up to five minutes without witnessing any leakage of the dye indicating membrane poration.

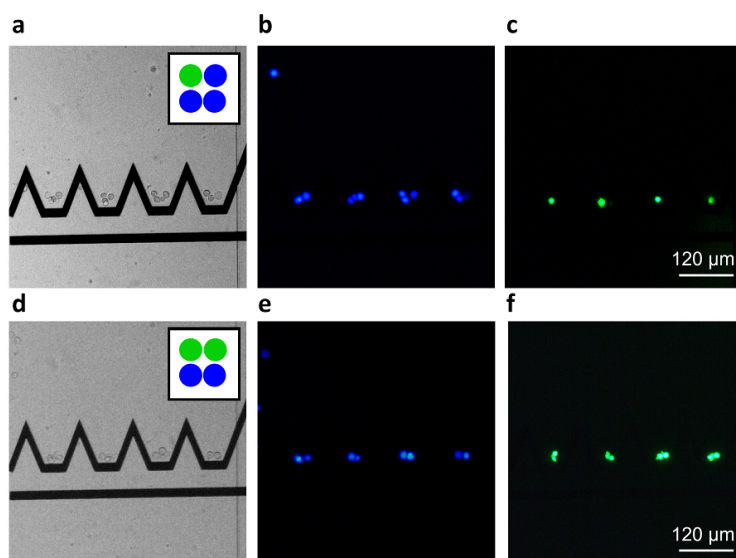


Figure 3.10: Proof of concept of the ability of the presented system to create aggregates of controlled size and composition. A homothetic scaling of the original design was done to accommodate more cells in the traps in a microfluidic channel of 40  $\mu\text{m}$  in height. Four trapping units are placed in parallel and a bypass is present on the left to discard unwanted cells. The left images are brightfield images with the inset corresponding to the content of each trapping unit, the middle images show Colo205 cells stained with blue calcein and the right images show Jurkat cells stained with green calcein. Top row: aggregate of four cells composed of three Colo205 (blue) and one Jurkat (green). Bottom row: aggregate composed of two Colo205 (blue) and two Jurkat (green). As the aggregates rotate under the effect of the flow, the pictures could not be superimposed.

### 3.10 Conclusion

This chapter first proposed a design of electrodes capable of generating three-dimensional single-object DEP traps in two different configurations of counter electrodes. This design offers the possibility of increasing the number of traps actuated simultaneously and the use of a DEP deviation system is demonstrated to direct the particles towards the desired trap in a controlled fashion. A simple method was proposed for the evaluation of DEP trap efficiency for designs comparison. The method evaluates the maximum DEP force the trap is capable of developing to counteract the drag force and assesses its relationship to the power, mainly dissipated in Joule heating, necessary to generate it. This method was used to compare the two types of electrodes configurations that are suitable with integration with planar hydrodynamic traps and the coplanar electrodes configuration was found to be more efficient than the facing electrodes configuration. The coplanar configuration was used to trap Jurkat cells and the voltage limit to avoid electroporation was experimentally assessed. The scaling rules were defined to follow changes in channel height and a scaled design was used to create aggregates of four cells with controlled number and type of cells as proof of concept.

The system of deviation and array of traps is readily usable in combination with planar hydrodynamic traps. Indeed the deviation system allows the control over the number of objects per trap which is necessary for the final device. The integration of coplanar electrodes to chip structured with planar hydrodynamic traps is detailed in the next chapter and the final device is then used for the controlled contact between two objects.





## 4 Combined trapping

**This thesis chapter is adapted from the submitted article:** C. Lipp, L. Koebel, R. Loyon, A. Bolopion, L. Spehner, M. Gauthier, C. Borg, A. Bertsch and P. Renaud, “Microfluidic device combining hydrodynamic and dielectrophoretic trapping for the controlled contact between single micro-sized objects and application to adhesion assays”.

This chapter reports the combination of the planar hydrodynamic traps introduced in chapter 2 with the DEP traps developed in chapter 3 to provide a bi-modal trapping device. The concept and workflow are first detailed, followed by the validation of the device with an adhesion frequency assay. Finally the measurement of pair lifetime after the controlled contact between cancer cells and T-cells is reported as a proof of concept for the use of the device in immunotherapy applications.

### 4.1 Concept

A microfluidic system combining fluidic and dielectrophoretic actuation and capable of performing in flow cell-particle interaction is presented. The device is illustrated in Figure 4.1a and comprises two inlets for medium perfusion controlled by the pressures  $P_{in,1}$  and  $P_{in,2}$  followed by serpentine channels to increase the inlets flow resistance. The two channels merge before entering the interaction chamber. The latter is composed of an upstream DEP actuated deviation system capable of steering the incoming particles to specific streamlines (Demierre et al., 2007), followed by an expansion of the channel and two lines of DEP traps. Each line is made of coplanar electrodes and comprises four distinct trapping units capable of focusing the particles to one point in three dimensions as described in chapter 3 as well as a bypass zone to which unwanted particles can be deviated to leave the chamber. The upstream

line is named the synchronization line because its role is to synchronize the arrival of particles to the second line once the amount of particle per trap is reached in the synchronization line. The second line is named the contact line and features hydrodynamic traps placed along the centers of each one of the DEP traps.

The hydrodynamic traps are precisely described in chapter 2 and feature holes, placed at the bottom of the the main PDMS channel and connected to a lower level of channels, named buried channels. The buried channels connect the traps to a pressure control channel, whose pressure  $P_c$  defines the flow direction in the buried channel. Particles of diameter larger than the trap and lying in the streamlines passing through the traps and buried channels clog the traps due to their larger dimensions, stopping the flow in the buried channels and immobilizing the particle thanks to the pressure difference built across them. Each of the hydrodynamic traps is connected by an individual buried channel to the control channel because this configuration of buried channels placed in parallel allows to provide sufficient pressure drop across the trapped cells to release them even after the release of one of the cells.

The interaction zone thus comprises DEP and planar hydrodynamic traps, whose roles are to exert independent effects on the particles. Once a particle is immobilized in the hydrodynamic trap, the DEP force does not affect it anymore because it is weaker than the force exerted by the difference of pressure across the hydrodynamic trap. This particle is hereafter named the Hydrodynamically Trapped Particle (HTP). A second particle however is affected by the DEP induced force when a difference of potential is applied across the contact electrodes. Because the hydrodynamic trap is placed at the equilibrium position of the DEP trap, its effect directs the second particle, hereafter named Dielectrophoretically Manipulated Particle (DMP), towards the HTP and immobilizes it in close contact with the HTP against the flow.

## 4.2 Workflow

The workflow steps for the controlled interaction are depicted in Figure 4.1b with emphasis on two traps of the contact line. The first step consists in the introduction of the first type of particles in the interaction chamber by increasing  $P_{in,1}$  and setting  $P_{in,2}$  to zero. The particles are then immobilized in the hydrodynamic traps by setting a negative value to  $P_c$  as illustrated in Figure 4.1b i). Once all the traps are filled with HTPs,  $P_c$  can be increased to a value close to zero to minimize the difference of pressure across them. The second type of particles is then introduced in the chamber by increasing  $P_{in,2}$  and setting  $P_{in,1}$  to zero. The arriving particles are first steered towards each of the trapping units of the synchronization line (not shown) using the deviation system and trapped against the flow drag force under the effect of the DEP force generated by  $V_{sync}$ . The destination of the particles is defined by the ratio of voltage applied to each side of the channel  $\frac{V_1}{V_2}$  (Demierre et al., 2007). Once the synchronization line is

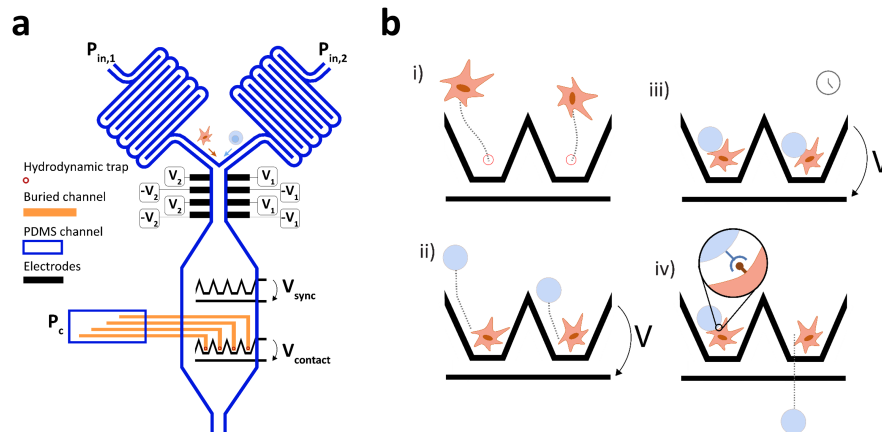


Figure 4.1: **a** Schematic representation of the microfluidic chip and electrodes with controlled voltages and pressures. The orange part represent the buried channel embedded in the glass substrate and running at a lower level under the PDMS channel. **b** Workflow steps for the controlled interaction between objects with emphasis on two traps of the synchronization line.

filled by one particle per trap,  $V_{sync}$  can be turned off and the DMPs are dragged downstream by the flow and immobilized in close contact with the HTP by turning on  $V_{contact}$  as shown in Figure 4.1b ii). The voltage is maintained for the desired contact duration as represented in Figure 4.1b iii). Once this duration is elapsed,  $V_{contact}$  is turned off and the DMPs are dragged away from the HTP by the flow. Adhesion events mediated through receptor-ligand bonds can be observed and related parameters such as state of adhesion or lifetime of the pairs can then be assessed and measured as illustrated in Figure 4.1b iv).

## 4.3 Materials and methods

### 4.3.1 Fabrication

Chips comprising buried channels were fabricated following the process described in section 2.4.1 featuring hydrodynamic traps having a diameter of  $3 \mu\text{m}$ . Electrodes were patterned on top of them using a lift-off process by spin coating (ACS200 GEN3, Süss), exposing (MLA150, Heidelberg Instruments) and developing a negative resist (AZ nLOF 2020, MicroChemicals) as illustrated in Figure 4.2a. The post-exposure bake step allows to control the undercut of the resist for a clean deposition. 20 nm of titanium followed by 200 nm of platinum were then evaporated (EVA 760, Alliance-Concept) and the extra metal was detached by lift-off process in a remover bath during 24 hours (Remover 1165, MICROPOSIT). A 5 min oxygen plasma

(GiGAbatch, Tepla) was performed to ensure no resist was left in the channels. A dicing step was finally done to separate the chips and the top PDMS channels layer was punched, aligned and bonded as described in section 2.4.1.

A first attempt for the structuring of electrodes on the substrate comprising buried channels was performed by deposition of metal followed by photolithography and etching by IBE technique as described in Figure 4.2**b**. The electrodes were well defined using this process, but a first disadvantage came from the fact that the metal deposited on the sloped, close to vertical profile of the LTO, such as the side of the traps or closed access holes, was not etched during IBE step as it can be seen in Figure 4.3**a**. This issue can be problematic for the fluorescent imaging of cells inside the traps because the metal blocks the light emitted by the fluorophore and prevents the assessment of the cell membrane integrity during the trapping. Furthermore, a clogging of the traps was observed after the IBE for traps diameters of 3  $\mu\text{m}$  and below. The clogging was due to a thin membrane covering the trap and Figure 4.3**b** shows a picture of an apparently broken membrane. The membrane seems to be deposited from inside the cavity and is due to redeposited material inside the high aspect ratio trap during the IBE. The lift-off process described above was thus found to be a more suitable option for the patterning of electrodes around the traps. The microfluidic circuit and electrodes arrangements were modified to accommodate two operational modules as described in Figure 4.1**a** on one single chip. The number of liquid electrodes was thus reduced to five instead of six on each side which did not modify their behaviour. Sixteen chips as shown in Figure 4.4 were fabricated on a 4" wafer.

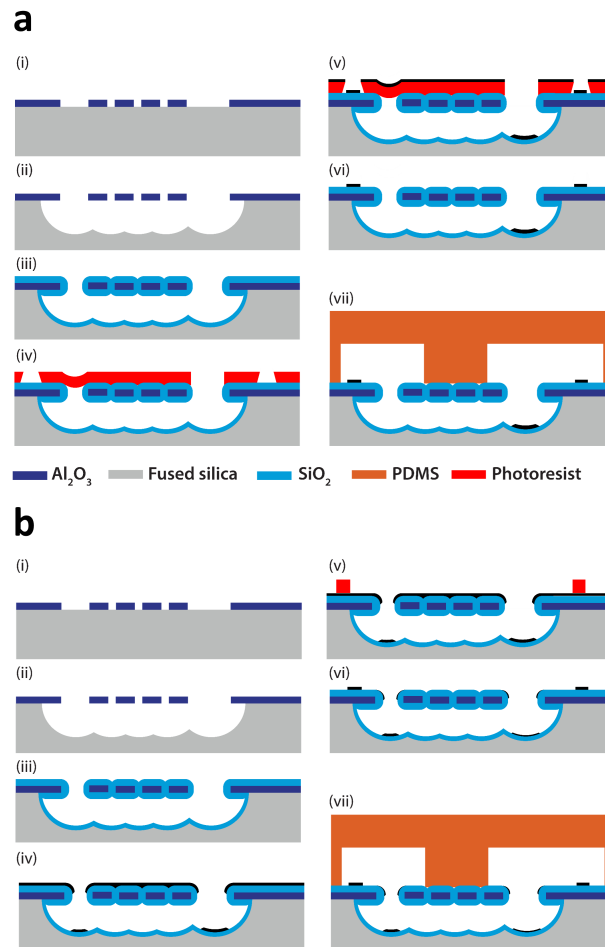


Figure 4.2: **a** Process for the fabrication of chips comprising buried channels and structured electrodes in their vicinity using a lift-off approach. Steps (i)-(iii) are precisely described in section 2.4.1. (iv) High topography adapted recipe for the spincoating of photoresist. (v) Photolithography and evaporation of metal. (vi) Metal lift-off. (vii) PDMS bonding. **b** Process for the fabrication of chips comprising buried channels and structured electrodes in their vicinity using a metal deposition followed by photolithography and etching step approach. Steps (i)-(iii) are precisely described in section 2.4.1. (iv) Metal deposition. (v) High topography adapted recipe for the spincoating of photoresist and photolithography. (vi) IBE of the metal. (vii) PDMS bonding.

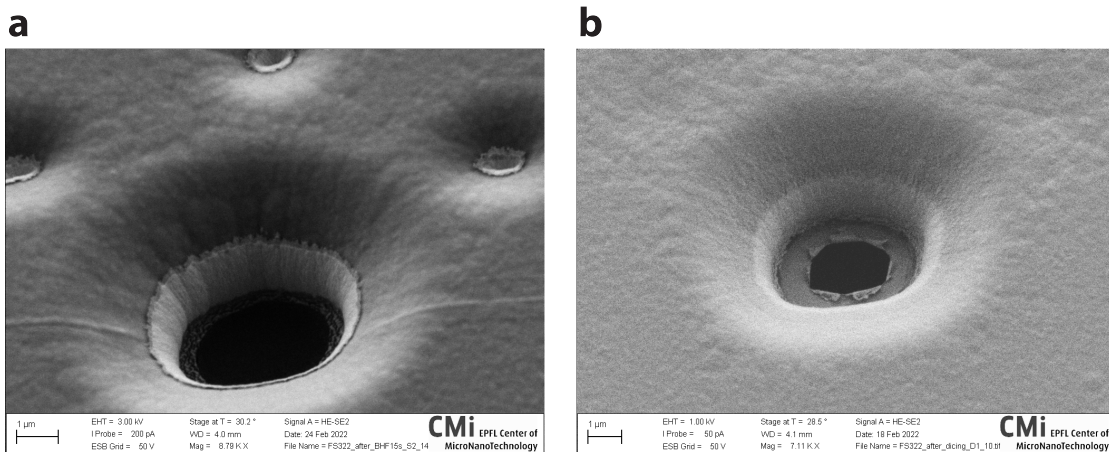


Figure 4.3: **a** SEM picture of the traps fabricated using a metal deposition and etching approach. Remaining metal can be seen on the vertical surfaces as the whiter material. **b** Small traps of chips fabricated using the a metal deposition and etching approach were found to be sealed by a small membrane. This membrane is here ruptured after application of high pressure.

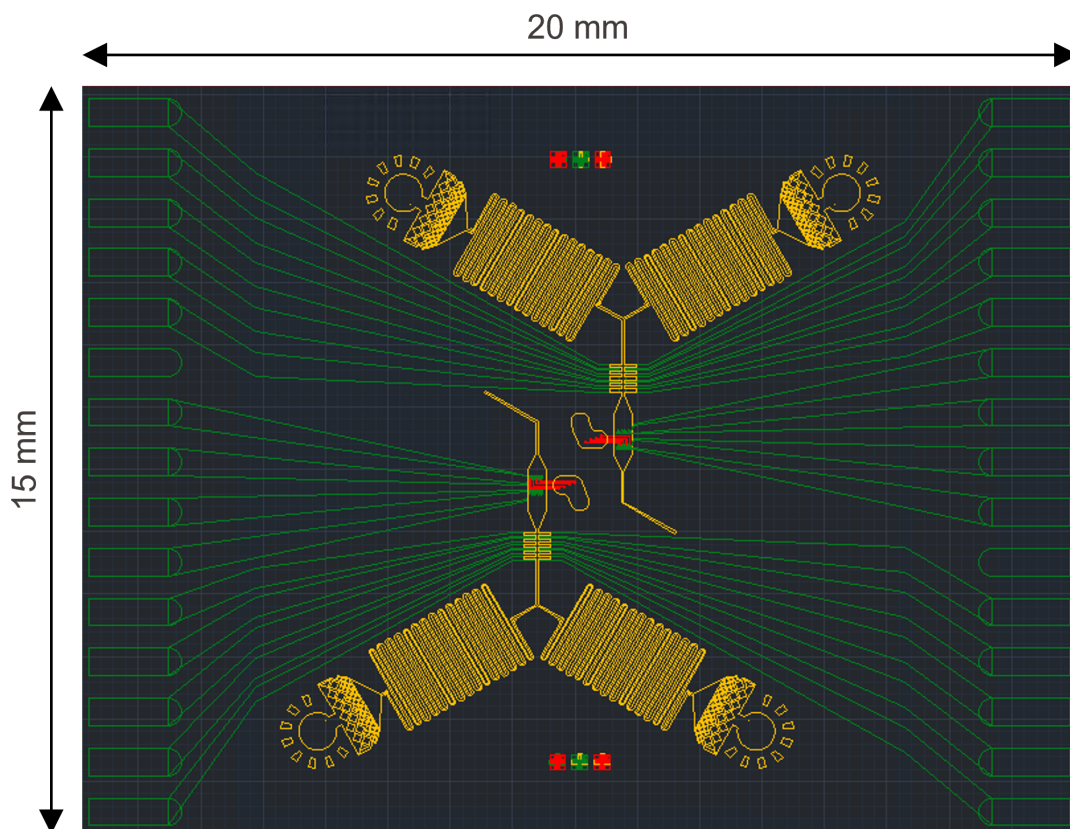


Figure 4.4: Layout for the chips comprising two functional modules on each chip. The PDMS layer is in yellow, the electrode in green and the buried channel in red. The entrance for the beads and cells comprise filters to avoid aggregates of particles to clog the chip.

### 4.3.2 Chip preparation and setup

The PDMS chip was degassed in a desiccator for 30 minutes prior to the experiment to avoid the formation of bubbles, and primed with Pierce protein-free (PBS) blocking buffer for 1 h to prevent proteins, beads and cells from adhering to the surfaces. The cells or beads were placed in a chromatography vial connected to the punched PDMS with 360  $\mu\text{m}$  outer diameter tubing for tight sealing. Pressure was applied to the vial using Fluigent Flow-EZ pressure controllers. The chip was mounted on a PCB for electrical connection placed on the stage of a Leica DMI3000 B inverted microscope and observed using a uEye (IDS) camera. All the electric signals needed to control the positions of the particles are sent through a home made PCB creating the multiplication of an AC signal at 100 kHz and different DC signals whose amplitudes are controlled by the computer with a custom C++ program through an analog output generator (Mccdaq USB-3100). The full setup is shown in Figure 4.5 and a picture of a chip and its mounting on the PCB are shown in Figure 4.6.

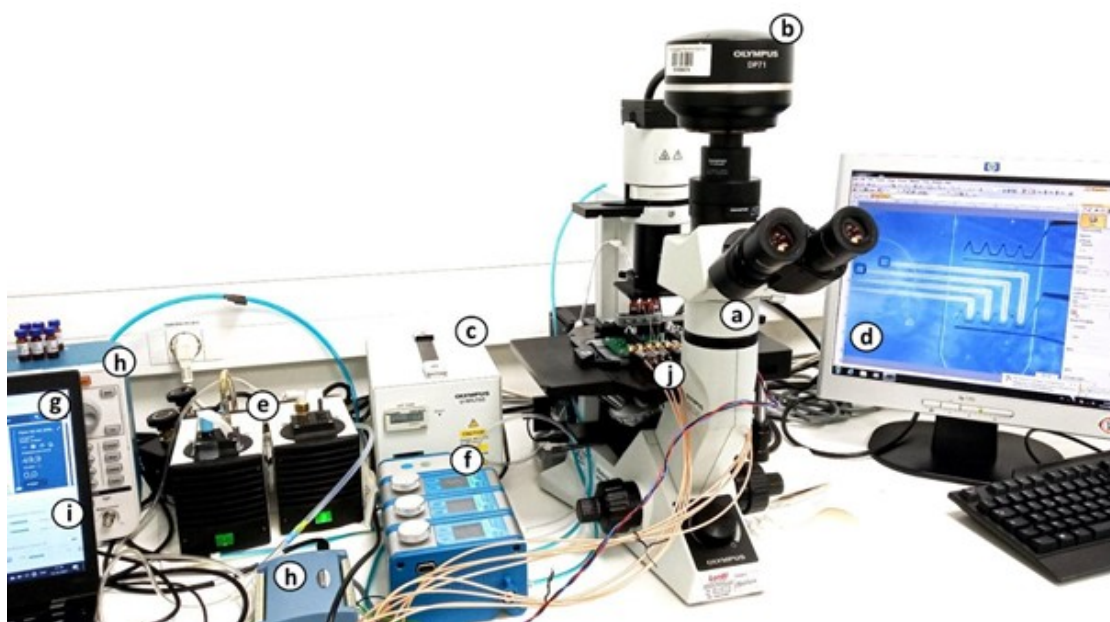


Figure 4.5: Picture of the experimental set-up, composed of the imaging system (a-d), the fluidic system (e-g) and the dielectrophoretic actuation system (h-j). The imaging system comprises a fluorescence microscope (a), a camera (b), a fluorescence light source (c) and the software to monitor the cells interacting in the device (d). The fluidic system consists in air pumps (e) generating negative and positive pressure outlets for the pressure controller (f) to deliver the right controlled pressures to the fluid tanks, sent via the pressure controller software (g). Finally, to generate the dielectrophoresis in the chip, electronic signals are produced by a custom PCB multiplying an AC signal from a signal generator with DC signals (h) whose different amplitudes are set on a custom C++ controlling software (i). The software enables the control of the trajectory of each single cell, and the duration of the interactions. All of the generated signals are then sent to another custom PCB on which the chip is mounted (j).



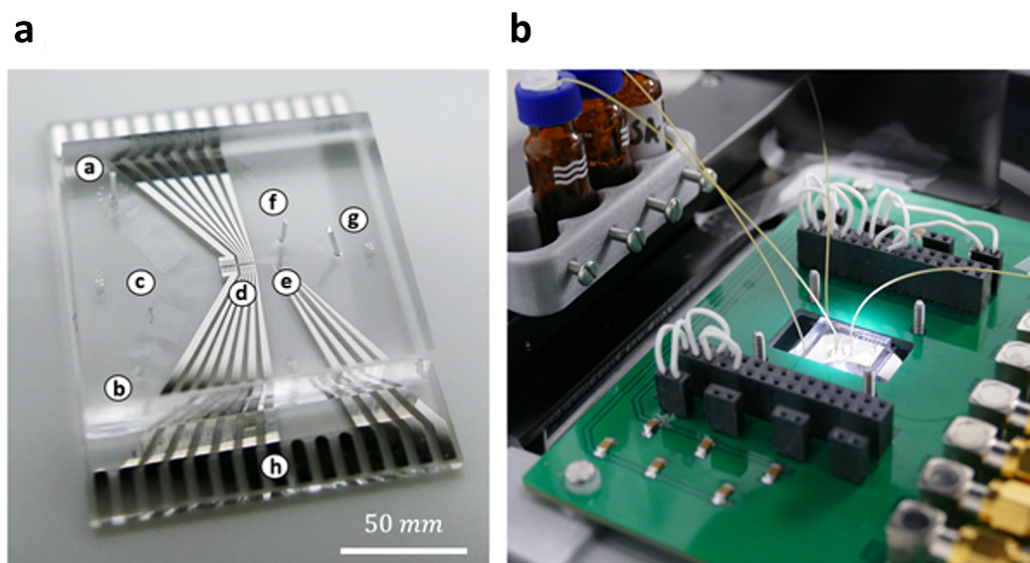


Figure 4.6: **a** Picture of a chip illustrated in Figure 1 a with two inlets (a-b) and corresponding serpentine channels (c) that merge before entering the deviation zone (d), followed by the interaction chamber (e), the hydrodynamic trapping in/outlet on its side (f) and the main outlet (g). The electrodes are also visible with respective connecting pads on the side (h). **b** Picture of the chip mounted on the PCB for electrical connection. The pressures in the vials are controlled via pressure pumps and a tubing plunged in the liquid conducts the fluid to the chip.

### 4.3.3 Cell culture and preparation

The adherent mouse fibroblast cell line NIH-3T3 was cultured in medium (DMEM, high glucose, GlutaMAX Supplement) supplemented with 10% FBS and 1% penicillin–streptomycin at 37 °C in a 5% CO<sub>2</sub> atmosphere. The semi-adherent cancer cell line Colo205 was cultured in medium (RPMI) supplemented with 10% FBS and 1% penicillin–streptomycin at 37 °C in a 5% CO<sub>2</sub> atmosphere. Colo205 tumor cell lines were pulsed with 10 µg/mL of specific or irrelevant peptide, and incubated for 1h at 37°C in 5% CO<sub>2</sub> in RPMI medium supplemented with 10% FBS and 1% penicillin-streptomycin. The specificity of CD8+ T-cells towards the peptide was previously assessed by co-culture of 5·10<sup>4</sup> T-cells with pulsed tumor cell lines in the presence of Golgi Plug (BD Biosciences) in 96-well plate at 1:1 E:T cell ratio.

Staining of the cells was performed by incubating the cells in PBS with 4 µm Calcein UltraBlue AM (Cayman Chemical) or with 1 µm Calcein AM (Invitrogen) for 1 h. The working solution is composed of 40% RPMI and 60% deionized water. The solution is compensated for osmolarity by the addition of dextrose (Sigma-Aldrich) and cleaned through a 0.22 µm filter. After staining, the cells were resuspended in the working solution and passed through a 40 µm cell strainer

before the experiment. All reagents are from Gibco unless specified.

#### 4.3.4 Medium compatibility

For viability assay, cells were immersed for 5 h in complete medium diluted in different percentage of DI water with corresponding amount of dextrose to compensate for osmolarity at 37 °C in a 5% CO<sub>2</sub> atmosphere. After 5 h, the cells were resuspended in standard complete medium and cultivated at 37 °C in a 5% CO<sub>2</sub> atmosphere for 48 h. Cell viability was assessed using trypan blue after the 5 h incubation in custom medium and 24 h and 48 h after resuspension in standard medium.

For cell activation assay, CD8+ T-cells were stimulated with specific or irrelevant peptides at 5 µg/mL (JPT Technologies) in the presence of Golgi Plug (BD Biosciences) in complete medium (RPMI medium supplemented with 10% FBS and 1% penicillin-streptomycin) or in complete medium diluted in different percentage of DI water with corresponding amount of dextrose to compensate for osmolarity. CD8+ T-cells were incubated at 37°C in 5% CO<sub>2</sub> for 5h for cell viability and cytokine production analysis. Cytokine production was analyzed by flow cytometry upon cell staining performed according to the manufacturer's instructions (BD). Briefly, cells were stained for 30 min with Live/Dead fixable dead cell stain (eBioscience Fixable Viability Dye eFluo 506 Invitrogen), anti-CD3 (PB, BD Pharmingen), anti-CD4 (APC-H7, BD Pharmingen) and anti-CD8 (PE, Diaclone). For intracellular staining, cells were incubated with Cytofix/Cytoperm (BD Biosciences) for 30 min then stained with anti interferon- $\gamma$  (IFN- $\gamma$ ) (APC, BD Pharmingen) and anti tumor necrosis factor- $\alpha$  (TNF- $\alpha$ ) (FITC, BD Pharmingen). Cells were acquired on a BD FACS- Canto II (BD Biosciences) flow cytometer and data analyzed using FlowJo Software.

### 4.4 Experimental validation of the concept

The concept was first tested using objects that are not expected to bind to each other such as cell-cell homotypic interactions. Figure 4.7a represents an optical microscope image of the synchronization (top) and contact (bottom) lines with transparent buried channels and hydrodynamic traps. Figure 4.7b is a scanning electron microscope image with two hydrodynamic traps surrounded by coplanar electrodes (highlighted in yellow for better visualization). Figure 4.7c is a timelapse image of the contact between two Colo205 cells held during 5 seconds demonstrating the device capability, the HTP is coloured in white and the DMP in green by image post-processing for clarity. Rotation of the DMPs was not observed contrary to cells trapped only with DEP only in chapter 3. The non rotation of the particles can be attributed to the compression of the DMP to the HTP generating a friction force preventing the rotation of the latter.

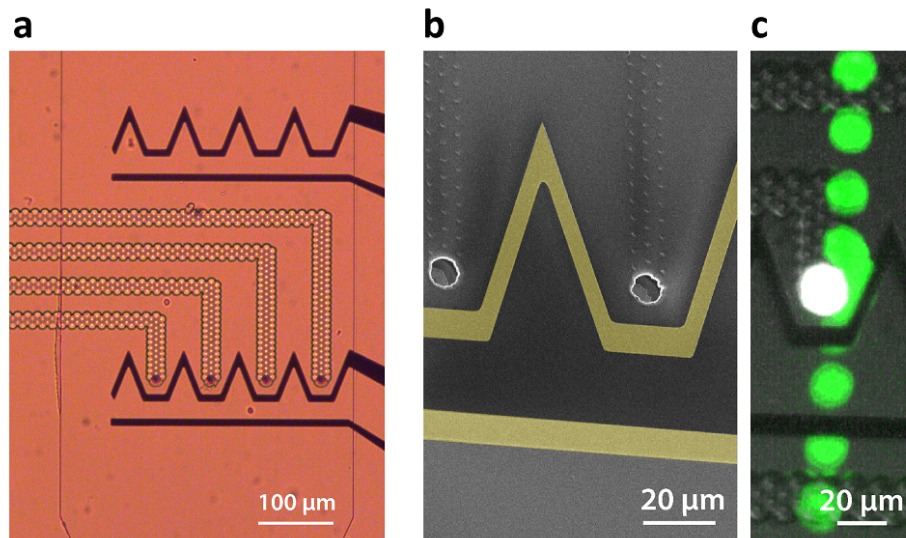


Figure 4.7: **a** Optical microscope picture of the interaction zone with the synchronization line (top) and contact line (bottom). Each funnel shaped electrode feature generates a DEP force field with single position of equilibrium against the flow at their center when a voltage is applied. The synchronization line comprises hydrodynamic traps at the center of the DEP traps. **b** SEM picture of two units of the synchronization line. The hydrodynamic trap is visible at the center of the funnel shaped electrodes. **c** Timelapse image of the controlled contact between two cells. The hydrodynamically trapped cell is coloured in white and the dielectrophoretically manipulated cell in green by image processing for clarity.

A binding interaction was first attempted using fibronectin coated beads as HTP and fibroblasts expressing integrins on their surfaces as DMP. These pairs are expected to bind via the integrin-fibronectin interaction. Figure 4.8 illustrates a timelapse image of an interaction between four NIH-3T3 cells (highlighted in green by image processing) and fibronectin coated beads (immobilized in the hydrodynamic traps) put in contact during 30 seconds. Half of the cells stayed attached to the beads after the forced contact and a cell arriving to the interaction chamber during the contact is deviated to the bypass zone (left) in such a manner that it does not interfere with the measurement. The measurements were however not pursued in this configuration because beads do not fully clog the planar hydrodynamic traps. Even if very small, flow leaks are still present and are susceptible of biasing the measurement of adhesion events. The roles were thus inverted to ensure a full clogging of the traps and the associated experiment is presented in the next section.

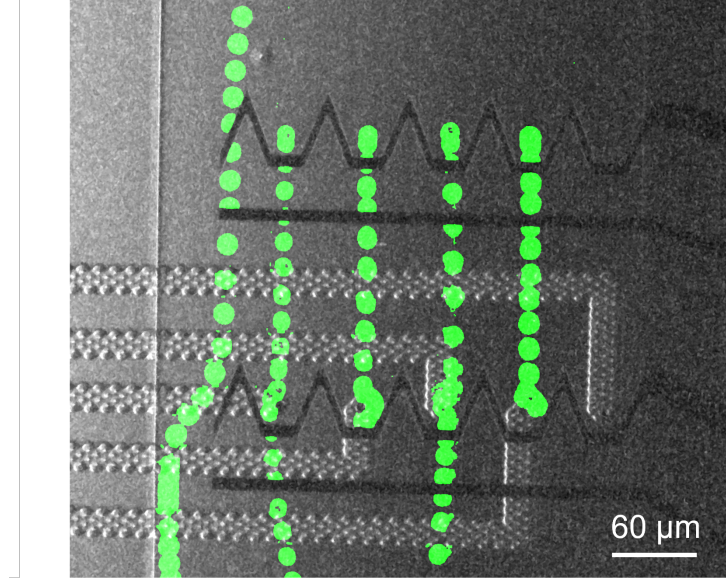


Figure 4.8: Timelapse image of an interaction between four NIH-3T3 cells (highlighted in green by image processing) as DMPs and fibronectin coated beads as HTPs put in contact during 30 seconds. Half of the cells stayed attached to the beads after the forced contact.

#### 4.5 Application to Fibronectin-Fibroblast interaction

In order to validate the device, a well known and characterized pair of receptor-ligand interaction was studied using the developed microfluidic chip. Integrins present on the surface of mouse fibroblasts were shown to bind specifically to fibronectin coated on a surface (Thoumine et al., 2000). For the specific case of a species outnumbering the other one, the mathematical expression describing the probability of adhesion of one bond after a contact time  $t$  was derived (Chesla et al., 1998):

$$p(t) = \frac{m_{max}k_{on}}{m_{max}k_{off} + k_{on}} [1 - \exp(-(m_{max}k_{on} + k_{off})t)] \quad (4.1)$$

With  $k_{on}$  and  $k_{off}$  the forward and reverse binding constant in  $\mu m^2 s^{-1}$  and  $s^{-1}$  respectively and  $m_{max}$  the surface density of the most abundant species out of the two in  $\mu m^{-2}$ . The probability  $p_n$  of forming  $n$  bonds after a time  $t$  is then given by the binomial distribution:

$$p_n = \binom{A_c m_{min}}{n} (p(t))^n [1 - p(t)]^{A_c m_{min} - n} \quad (4.2)$$

With  $A_c$  the surface of contact in  $\mu m^2$  and  $m_{min}$  the surface density of the less abundant

species in  $\mu m^{-2}$ . The probability of adhesion  $P_a$  mediated by minimum  $n_{min}$  bonds is then given by:

$$P_a = 1 - \sum_{C=0}^{n_{min}-1} P_C(t) \quad (4.3)$$

For cases where a single bond is sufficient to mediate an adhesion event, the last expression becomes:

$$P_a = 1 - [1 - p(t)]^{A_c m_{min}} \quad (4.4)$$

In this experiment, 5  $\mu m$  in diameter polystyrene beads coated with fibronectin were taken as DMPs and were put in contact during a controlled amount of time to mouse fibroblasts acting as HTPs. The adhesion state was assessed after the forced contact was released. The negative control consisted of 5  $\mu m$  in diameter polystyrene beads coated with bovine serum albumin (BSA) as DMPs. Figure 4.9a illustrates a controlled contact of 3 seconds between a fibronectin coated bead and a fibroblast that does not display any adhesion after the contact. The measure was taken for at least 20 events per contact time and the fraction of adhesion events is reported as a function of contact duration in Figure 4.9b. The contact time was measured from video analysis and taken as the time the bead was immobile in contact with the HTP. Disparities in contact duration were observed and its standard deviation is reported as the horizontal error bar. The large majority of beads had a position of equilibrium downstream of the HTP between this latter and the electrode, ensuring repeatable experimental conditions. The vertical error bar represents the 95% confidence interval on the percentage calculated from a binomial distribution of the adhesion events.

Integrins were taken as the less abundant species and one bond considered as sufficient to mediate a bond as deduced by the similar work performed by Thoumine et al. (2000). As expected from equation 4.4, the percentage of adhesion of fibronectin coated beads increases as a function of contact duration until reaching a plateau. The control data displays a significantly lower percentage of adhesion with no adhesion event reported for the lower range of contact duration. Experimentally, the strength of adhesion was significantly lower for BSA as the adhered beads would detach from the cell at very low flow rate, contrary to most fibronectin beads which remained attached even when increasing the flow rate until the maximum value allowed by the pump. Equation 4.4 was fitted to the data and is represented as the continuous line on the graph of Figure 4.9b. The parameters extracted from the best fit are  $k_r = 0.17 s^{-1}$  and  $A_c m_{min} m_{max} k_f = 0.76 s^{-1}$ . This latter parameter is constant for a given adhesion curve and was found to be in the range reported by the similar adhesion experiment by Thoumine et al. (2000).

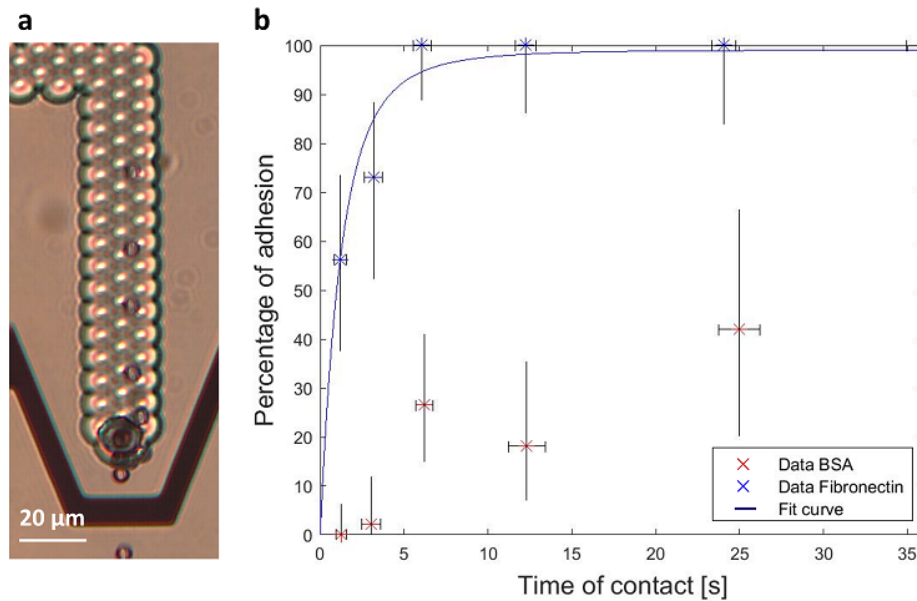


Figure 4.9: **a** Timelapse image of a fibronectin bead placed in contact with a mouse fibroblast during 3 seconds. No adhesion was observed after the contact and the bead is dragged downstream by the flow. **b** Percentage of adhesion events as a function of contact duration for fibronectin coated beads as DMPs and mouse fibroblasts as HTPs. BSA coated beads as DMPs are used as a control. The adhesion is mediated by integrin receptors at the surface of the fibroblasts binding specifically to fibronectin and the binding parameters from the fitting Equation 4.4 to the data are extracted.

## 4.6 Application to T-cell-cancer cell interaction

The proposed device was used to test more complex receptor-ligand pairs such as TCR-pMHC. An HLA-A2-restricted clone of human CD8+ T-cells was used as DMPs and cancer cells pulsed with the peptide to which the TCRs of the T-cells clone are specific were used as HTPs. The negative control consisted of the same cancer cells pulsed with an irrelevant peptide.

### 4.6.1 Medium compatibility

Because the presence of an electric field in a conductive medium induces movement of ions and ensuing Joule heating effect (Ramos et al., 1998), diluted media must be used to manipulate cells with DEP. Typical medium for DEP manipulation is composed of PBS diluted in deionized (DI) water and supplemented with dextrose or sucrose to correct for osmolarity (Piacentini et al., 2011). However T-cells need specific medium compounds to properly activate following a specific binding of their TCR (Hwang et al., 2020). Furthermore, prolonged exposition to modified media can compromise their viability, which is necessary for further culture after selection in cell based immunotherapies. The maximum time necessary for T-cell

selection in a chip was estimated to 5 h and the activation and viability of the T-cell clones in different medium diluted in DI water and corrected for osmolarity by the addition of dextrose after incubation with specific peptide was thus assessed using the protocol described in the Experimental section. The T-cell clones suspended in 10% PBS not only did not produce IFN- $\gamma$  and TNF- $\alpha$  after co-incubation with the specific peptide but only 8% of the initial cells remained alive after 5 h immersion in the specific medium and 48h re-culture in standard medium as seen in Figure 4.11. Activation and viability tests after a 5 h exposure to the medium were thus performed in different dilutions of RPMI supplemented with FBS and the results are represented in Figure 4.10 and Figure 4.12 indicating a minimum standard medium content of 40% to ensure proper activation of the clones as well as viability after immersion during 5 h. This concentration was thus selected to perform the on-chip interaction experiments.

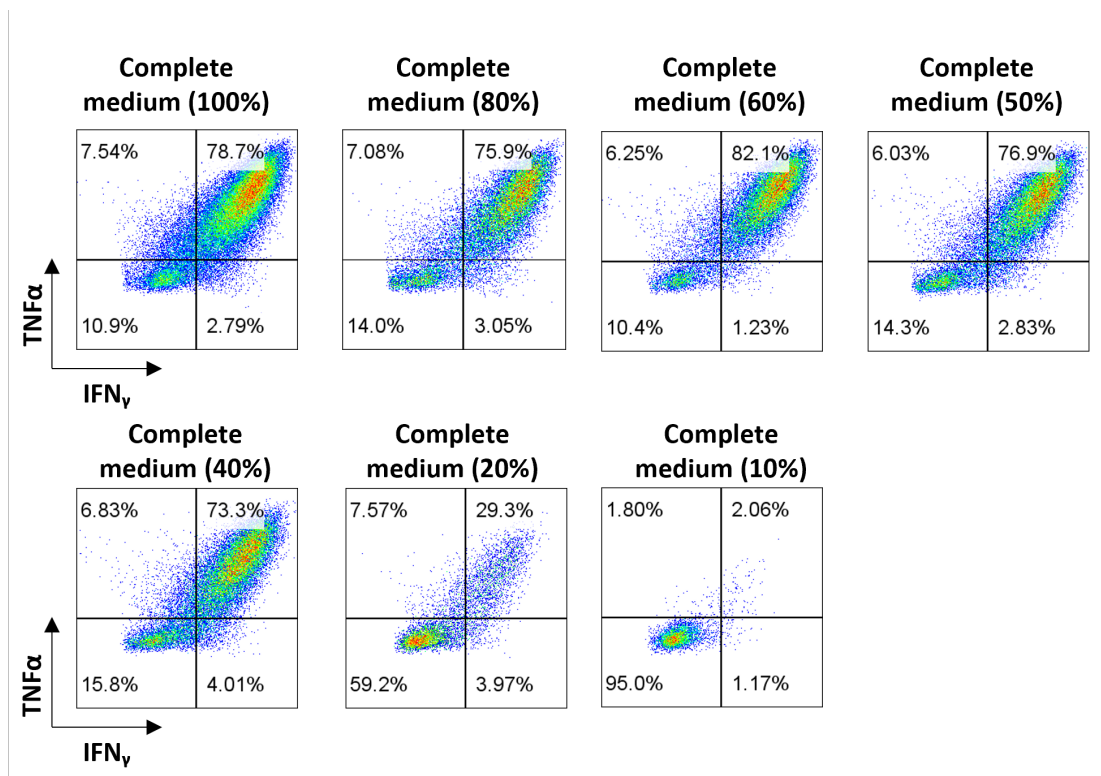


Figure 4.10: Intracellular IFN- $\gamma$  and TNF- $\alpha$  content after 5 h co-incubation of T-cell clones with specific peptide in medium composed of different percentage of RPMI supplemented with FBS and diluted in DI water with the adapted amount of dextrose to compensate for osmolarity. A minimum content of 40% complete medium was found to be necessary to ensure T-cell clones activation and viability.

		0 hours	5 hours	24 hours	48 hours
Colo205	Complete medium (all times)	50,000 cells	52,000 cells	132,000 cells	216,000 cells
	10% PBS medium (5h) then complete medium (24 and 48 h)	50,000 cells	10,000 cells	0 cells	0 cells
CD8 T cells	Complete medium (all times)	100,000 cells	96,000 cells	80,000 cells	52,000 cells
	10% PBS medium (5h) then complete medium (24 and 48 h)	100,000 cells	56,000 cells	8,000 cells	8,000 cells

Figure 4.11: Viability of Colo205 and CD8 T-cells at different stages after 5h immersion in 10% PBS diluted in DI water complemented in dextrose for osmolarity compared to complete medium (DMEM and RPMI respectively). After the 5 h incubation in the 10% PBS medium, cells were washed and cultured in standard medium. The 5 h in the 10% PBS medium is incompatible with the viability of both types of cells as it drops drastically in both cases even when the cells are put back into their original complete medium after the 5 h.

	0 hours	5 hours	24 hours	48 hours
<b>Complete medium (100%)</b>	500 000 cells (100% cell viability)	400 000 cells (100% cell viability)	500 000 cells (96% cell viability)	620 000 cells (98% cell viability)
<b>Complete medium (80%)</b>	500 000 cells (100% cell viability)	400 000 cells (100% cell viability)	340 000 cells (97% cell viability)	350 000 cells (96% cell viability)
<b>Complete medium (60%)</b>	500 000 cells (100% cell viability)	350 000 cells (100% cell viability)	300 000 cells (91% cell viability)	360 000 cells (92% cell viability)
<b>Complete medium (40%)</b>	500 000 cells (100% cell viability)	325 000 cells (97% cell viability)	330 000 cells (89% cell viability)	320 000 cells (87% cell viability)
<b>Complete medium (20%)</b>	500 000 cells (100% cell viability)	400 000 cells (96% cell viability)	230 000 cells (89% cell viability)	210 000 cells (84% cell viability)
<b>Complete medium (10%)</b>	500 000 cells (100% cell viability)	250 000 cells (93% cell viability)	170 000 cells (85% cell viability)	160 000 cells (89% cell viability)

Figure 4.12: T cell viability at different stages after 5 h immersion in different percentage of complete medium diluted in DI water with corresponding amount of dextrose to compensate for osmolarity. After the 5 h incubation in custom medium, cells were washed and cultured in standard medium.



### 4.6.2 Results

T cells and cancer cells were stained with calcein AM of distinct color (blue and green respectively) to be able to differentiate between cell types, but also to visualize any event of electroporation or membrane damage due to the difference of pressure applied by the hydrodynamic traps. Calcein is a small molecule without covalent binding to intracellular compounds that quickly diffuses out of the cell in case of membrane damage. Only events with intact cells displaying constant and bright fluorescence were considered for the analysis. The average duration of contact was measured as the time the cells were immobile and in contact with the HTPs and is of 22 seconds with standard deviation of 3 seconds. The large majority of T-cells had a position of equilibrium downstream of the the HTPs between this latter and the electrode, ensuring repeatable experimental conditions. Figure 4.13 is a microscopy image of a forced interaction with the T-cell placed downstream of the cancer cell. The pair lifetime was defined as the time a T-cell stays in a radius 20% larger than the cancer cell once the voltage of the interaction line  $V_{contact}$  is turned off. The results of the lifetime measurements are displayed in Figure 4.14. Adhesions were observed in both control and tested case, indicating that the expected TCR-pMHC bonds are not the only receptor-ligand pairs responsible for adhesion. Indeed T-cells have different receptors responsible for rolling on the endothelium, cell migration towards their targets and mediating the immune synapse such as LFA1-ICAM, CD28-CD80/CD86 or CD2-CD48/CD59 (Huppa & Davis, 2003).

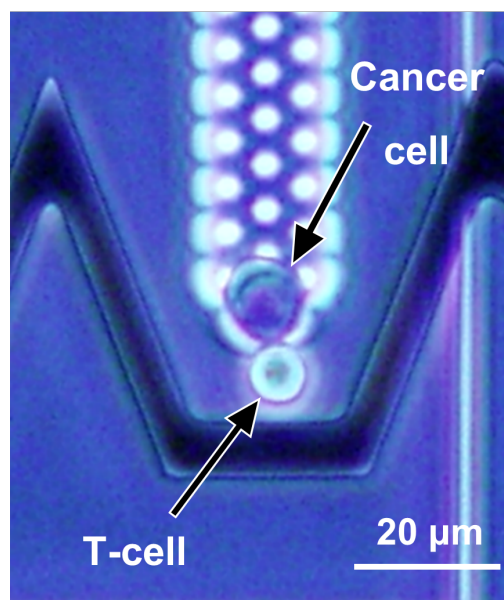


Figure 4.13: Optical microscope picture of a T-cell in contact with a cancer cell after the forced contact spontaneously adhering. The side of the PDMS channel is visible on the right and shows the good alignment between the top PDMS channel and the electrodes.

The sample distributions were tested for normality using a Kolmogorov-Smirnov test and the null hypothesis of a normal distribution was rejected in both cases. The samples were thus tested for equal median using Mann-Whitney U test and obtained a p-value of 0.03, rejecting at 95% confidence interval the null hypothesis and indicating a larger median lifetime in the presence of specific peptide on the cancer cells. The TCR-pMHC interaction thus tends to increase the pair lifetime. Observing the pair lifetime, one can first note that they are non null

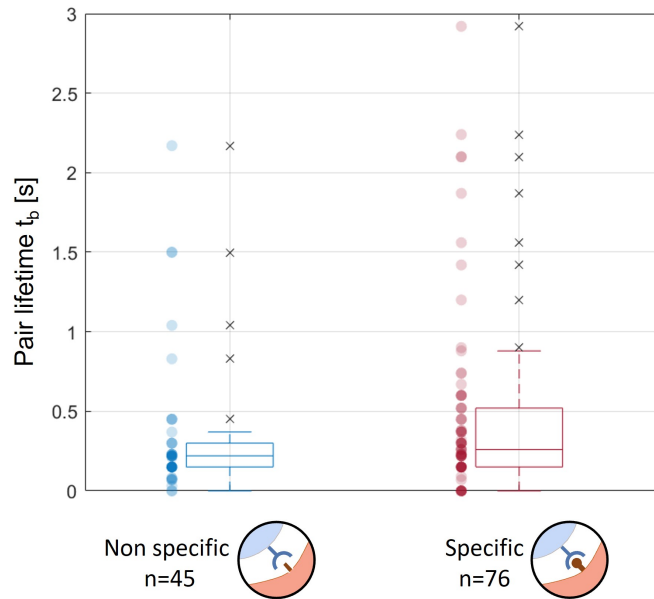


Figure 4.14: Pair lifetime measurements after 22 seconds of forced contact between Colo205 and T-cell clones in the case where the Colo205 cells were pulsed (specific) and non pulsed (non specific) with the TCRs cognate peptide.

in the case where the cancer cells were not pulsed with the specific peptide, indicating other receptor-ligand pairs mediated the adhesion. This is not surprising as T-cells have multiple types of receptors that, among others, allow them to roll on the endothelium (Rossiter et al., 1997) or mediate the immune synapse (Walling & Kim, 2018). While the median pair lifetime was found to be significantly different for the two distributions, the difference between the two populations is not large. In applications aiming at isolating rare cells with specific TCRs, a selection based on a lifetime criterion to ensure 100% specificity would miss 97.4% of the specific cells and have very low sensitivity. The best positive predictive value was found at 0.45 seconds with a value of 71%. This threshold value would imply that 72% of the specific T-cells would not be recognized. Hence it can be deduced that lifetime is not a good selection criteria for the selection of rare specific TCRs.

Lifetime of single bonds following first order dissociation kinetics can be described by an

exponential decay and the probability  $P_i$  of a bond formed at time  $t = 0$  to remain intact at time  $t_b$  follows the law:

$$P_i = \exp(-k_{off} t_b) \quad (4.5)$$

As discussed above, the pairs observed are not only not mediated by single bonds but also by different receptor-ligand pair types. Avidity represents the present situation better than affinity as it is defined as the strength of an interaction between cells mediated by multiple receptor-ligands such as the TCR, the co-receptor CD8, other adhesion molecules and activating/inhibitory molecules. Avidity is mainly measured via multimer binding assays and is believed to be a better predictor of T-cell effector function than simple TCR-pMHC affinity (Campillo-Davo et al., 2020; Yerbury, 2022). The cell-cell dissociation rate was thus approximated to a first order dissociation kinetics and the results were fitted to a linear equation to extract a lumped off-rate characterizing the avidity. Figure 4.15 represents the natural logarithm of the number of events with a lifetime longer than the  $x$  axis as a function of time and is thus a representation of  $\ln(P_i(t))$ . A linear dependency was fitted to the data and the slope taken as the effective off-rate, which was measured to be of  $1.4 \text{ s}^{-1}$  for the specific peptide and  $2.5 \text{ s}^{-1}$  in absence of specific peptide. As expected, the non randomly distributed residues indicate that the fit does not correspond to the physical reality. The lumped off-rate fit however allows to discriminate between two populations and evaluate their avidity.

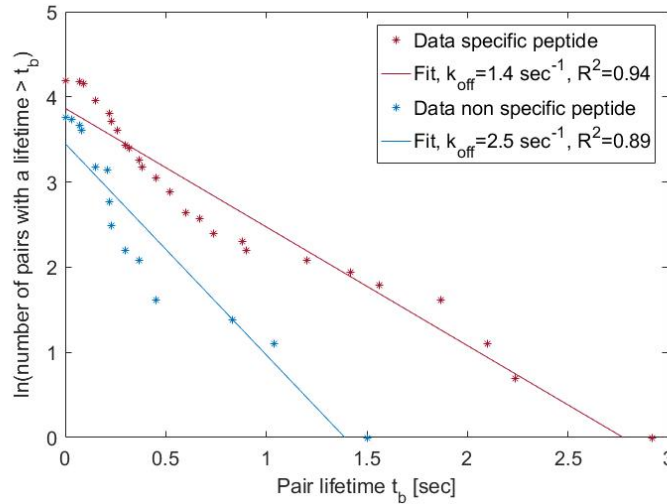


Figure 4.15: Experimental  $\ln(P_i(t))$  taken as the natural logarithm of the number of events with a lifetime longer than the  $x$  axis as a function of time. The slope of the linear fit represents the lumped off-rate of the pairs.

## 4.7 Application to CAR-T cell-cancer cell interaction

Chimeric antigen receptor T (CAR-T) cells are T-cells genetically modified to present an engineered receptor construct at their surfaces. This construct has similar peptide binding domains as the TCR and an intracellular signal transduction domain but does not need the binding of the co-receptor CD8 to trigger the T-cell activation. It can thus bind to antigens independent of the MHC presentation while keeping the effector function of a TCR T-cells which makes it a versatile tool. CAR cell therapy targeting the CD19 antigen present on B cells has been approved by the FDA and has been used effectively to treat some types of lymphoma (Huang et al., 2020).

In this experiment, the B3Z cell line was genetically modified to express CAR receptors specific to the human epidermal growth factor receptor-2 (HER2) and generously given by Leo Scheller from the LPDI laboratory at EPFL. HER2 is a receptor that can be over-expressed by certain types of breast cancers (Rimawi et al., 2015) and CAR-T cells therapies targeting this antigen are currently under clinical trials (“clinicaltrials.gov\_2022”, 2022). The SKOV-3 cell line expresses HER2 (Bjorkelund et al., 2011) and was used as a model cancer cell. The HER2 bearing SKOV-3 cells were stained with green calcein and used as HTPs, whereas the CAR-T bearing B3Z cells were stained with blue calcein and used as DMPs. The workflow described in Figure 4.1b was followed and the forced contact time was set to 30 seconds.

### 4.7.1 Results

Because of technical difficulties encountered with the B3Z cells, only three events satisfying the criteria for a valid interaction were observed. Their lifetime was measured and two of them exceeded two minutes, after which the flow was increased to detach them. The last event displayed a lifetime of 29 seconds and its sequence is illustrated in Figure 4.16 by a superposition of the green and blue fluorescent channels. In Figure 4.16a the DMP is placed in close contact with the HTP (green). In sequence **b** the DEP force is turned off and the DMP moves in response to the flow drag force but remains attached to the HTP. Finally sequence **c** shows a timelapse of the spontaneous detachment of the DMP from the HTP.

Despite the low number of events observed in this experiment, all of them displayed a lifetime an order of magnitude longer than the maximum lifetime observed in the same conditions with TCR T-cells. Because CAR-T receptors are known to have larger affinity than the TCRs and because the detachment of the DMPs happens in a single detachment step, the measured events seem to be mediated by CAR-T receptors, strengthening the confidence in its potential application to cell-based immunotherapies.

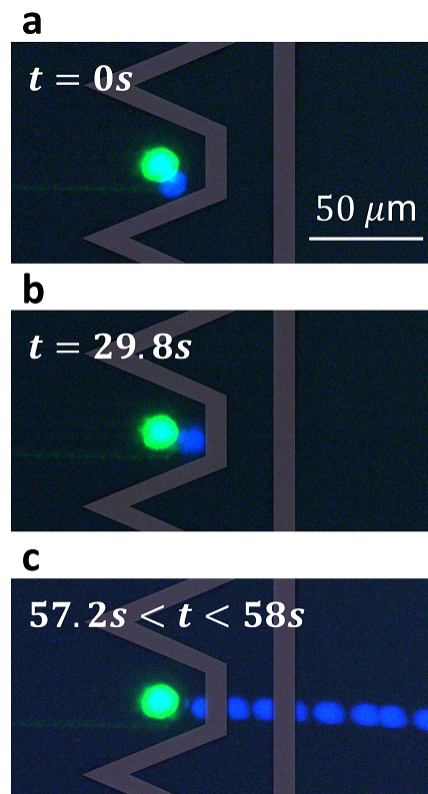


Figure 4.16: Sequence of the interaction between a HER2 expressing SKOV-3 cell immobilized in a hydrodynamic trap (green) and a CAR expressing B3Z cell manipulated with DEP (blue): **a** DEP is activated and the DMP is pushed against the HTP. **b** DEP is turned off and the DMP moves dragged by the flow but remains attached to the HTP. **c** The DMP spontaneously detaches and is dragged by the flow. The images from blue and green fluorescent channels are superimposed by image processing.

## 4.8 Analysis of forces

The order of magnitude of the forces applied to the DMPs during the pushing phase shown in Figure 4.1b iii) and the pulling phase shown in Figure 4.1b iv) are discussed in this section.

### Dielectrophoresis

A COMSOL Multiphysics model was simulated using the creeping flow and electric current modules. The model is composed of a channel with patterned coplanar electrodes of geometry and dimensions illustrated in Figure 3.4. For a first approximation, the DMP is assumed to be too small to alter the electric field and is not comprised in the model. The influence of the HTP is however taken into account and an electrical model of a spherical cell is placed at the  $x$  and  $y$  position where the hydrodynamic trap is placed considering a  $16\ \mu\text{m}$  diameter HTP cell. Its center is located at a vertical position half that of its radius to include the deformation of the

cell inside the trap and its domain is not part of the fluidic simulation, but its influence on the local electric field is considered in the electric current module. Because the cell membrane is much thinner than the rest of the elements and might induce errors in the simulation, a single homogeneous sphere of equivalent electrical property  $\epsilon_{eff}^*$  is modeled using the formula derived by Kaler and Jones (1990):

$$\epsilon_{eff}^* = \epsilon'_{eff}(\omega) - j\epsilon''_{eff}(\omega) \quad (4.6)$$

where

$$\epsilon'_{eff}(\omega) = \epsilon_{cp} + \frac{c_m R - \epsilon_{cp}}{(\omega \tau_m)^2 + 1} \quad (4.7)$$

and

$$\epsilon''_{eff}(\omega) = \frac{(c_m R - \epsilon_{cp}) \omega \tau_m}{(\omega \tau_m)^2 + 1} \quad (4.8)$$

with  $\tau_m = \frac{c_m R}{\sigma_{cp}}$ ,  $c_m = \epsilon_{mb} / \delta_{mb}$ ,  $\epsilon_{cp}$  and  $\sigma_{cp}$  respectively the cytoplasm permittivity and conductivity,  $R$  the cell radius,  $\delta_{mb}$  and  $\epsilon_{mb}$  respectively the membrane thickness and permittivity. A first simulation is performed in this configuration and the value of the DEP force as of equation 3.2 calculated across the volume of the DMP. This latter is considered downstream of and in contact with the HTP. The diameter of the DMP are 5  $\mu\text{m}$  for the polystyrene beads and 7  $\mu\text{m}$  for the T-cells. The  $\nabla E^2$  value was observed to vary considerably across the volume of the DMP (data not shown), which indicates that the dipole approximation to estimate the DEP force as of equation 3.2 is not valid and another strategy must be used to estimate this force. The value of the force calculated following equation 3.2 with the gradient value taken at the center of the DMPs is reported in table 4.1.

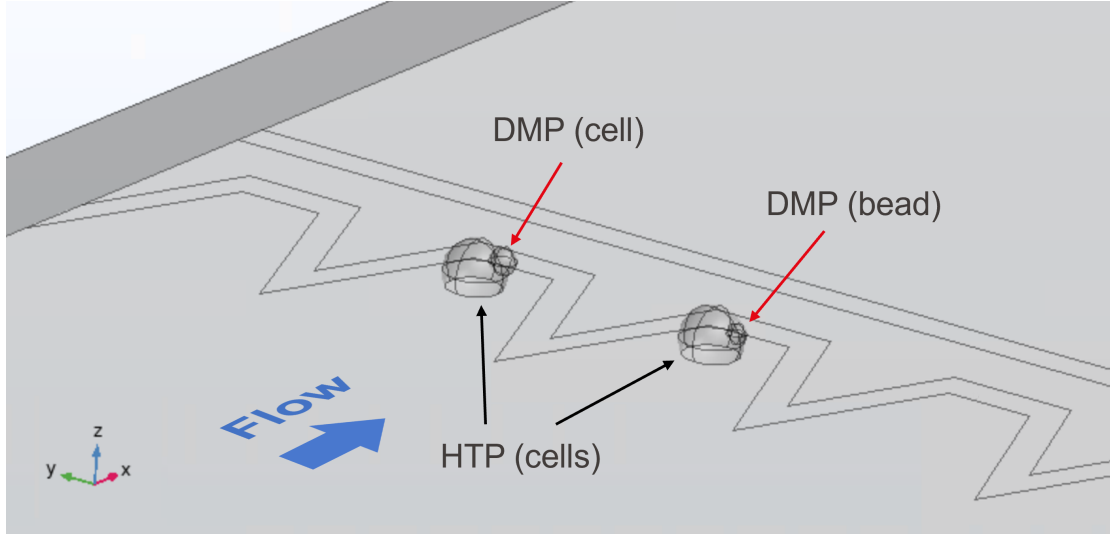


Figure 4.17: Simulation used to estimate the drag and dielectrophoresis force acting on the DMPs. The HTPs are included in the electrical model to take into account their impact on the electric field. The two DMPs considered in this chapter are modeled: a cell of 7  $\mu\text{m}$  diameter and a bead of 5  $\mu\text{m}$  diameter. The drag force is obtained by integration of the shear stress on their surface and the DEP force by integration of the Maxwell stress tensor.

The Maxwell stress tensor (MST) method in opposition to the dipole approximation takes into account the influence of the affected particle for the calculation of the electric field. It is considered to give an exact value of the DEP force (X. Wang et al., 1997) and is often taken as reference value for approximations (Michálek & Zemánek, 2017). The expression of the time averaged DEP force on a particle is given by a surface integral on the particle:

$$\langle \mathbf{F}_{\text{DEP}} \rangle = \frac{\text{Re}[\epsilon_m^*]}{4} \oint_S [(\mathbf{E}_1 \mathbf{E}_1^* + \mathbf{E}_1^* \mathbf{E}_1) - |\mathbf{E}_1|^2 \mathbf{U}] \cdot \mathbf{n} dS \quad (4.9)$$

with  $\epsilon_m^*$  the complex permittivity of the medium,  $\mathbf{E}_1$  the electric field at the external surface of the particle, the \* symbol indicating the complex conjugate of  $\mathbf{E}_1$ ,  $\mathbf{U}$  the unit tensor and  $\mathbf{n}$  the surface normal vector.

The developed expression is given by:

$$\langle \mathbf{F}_{\text{DEP}} \rangle = \frac{\text{Re}[\epsilon_m^*]}{4} \begin{bmatrix} E_x^* E_x - E_y E_y^* & E_x E_y^* + E_x^* E_y & E_x E_z^* + E_x^* E_z \\ -E_z E_z^* & E_y^* E_y - E_x E_x^* & E_y E_z^* + E_y^* E_z \\ E_z E_x^* + E_z^* E_x & E_z E_y^* + E_z^* E_y & E_z^* E_z - E_x E_x^* \\ & & -E_y E_y^* \end{bmatrix} \cdot \begin{bmatrix} n_x \\ n_y \\ n_z \end{bmatrix} dS \quad (4.10)$$

The DMPs were thus added in contact and downstream of the HTP in the simulation with corresponding dimensions and material permittivities and comprised in the electric current module domain as illustrated in Figure 4.17. The T-cell was also approximated by a single homogeneous sphere using the equivalent electrical properties described in equation 4.7. The values of the ensuing DEP force are reported in table 4.1.

### Drag force

The drag force was estimated by simulating the same finite element model as described above with the DMP walls set as a boundary with no slip condition in the creeping flow module. The shear stress exerted by the flow was integrated over its surface and its  $x$  component taken as the value of drag force. The results of these calculation are reported in Table 4.1.

Table 4.1: Forces acting on the DMPs for polystyrene bead and the T-cell with respective radius

	$R$ [ $\mu\text{m}$ ]	$F_{drag,x}$	$F_{DEP,x}$ dipole method	$F_{DEP,x}$ MST method
T cell	3.5	1.8 pN	-57.1 pN	-19.9 pN
Bead	2.5	0.7 pN	-9.4 pN	-2.9 pN

### Discussion

The sign of the forces corresponds to the direction of the respective forces along the  $x$  axis represented in Figure 4.17 and it is negative for the DEP force and positive for the drag force as expected. It can first be observed that the dipole method yields larger DEP forces than the MST method. Indeed in similar trap geometries, multipole consideration was found to decrease the magnitude of the DEP force (Rosenthal & Voldman, 2005). The drag force corresponds to the disruptive force used to detach the pair in step iv) of Figure 4.1b. The calculated force is small compared to typical forces used in literature to detach pairs using the OT method (Thoumine et al., 2000), DPA (Ju et al., 2013) and AFM methods (Kong et al., 2009) and is in the same range as the force experienced by integrins during adhesion to the substrate (Chang et al., 2016). The flow rate could thus easily be increased, provided the control method allows faster reaction for cells and beads manipulation. This would also allow minimization of the contribution of non-specific adhesions.

During the pushing phase, the compression force is given by  $|F_{DEP}| - |F_{drag}|$  and is in the tens of piconewton range, comparable to other studies (Y. Chen et al., 2019; Fiore et al., 2014; Thoumine et al., 2000).



## 4.9 Discussion

The development of a novel microfluidic chip capable of performing in flow interaction assays based on two distinct phenomena was demonstrated for the independent manipulation of two micro-sized objects. The orthogonal manipulation of the two objects allows a spatial and time control over the contact, which enables for the first time different adhesion assays on chip. Two different assays were performed as proof of concept to demonstrate the possibilities achievable with this method. First a biophysical experiment was performed in which fibroblasts were put in contact with fibronectin coated beads during different contact times. The adhesion mediated by the binding of integrin receptors on the surface of the fibroblasts to fibronectin was assessed and the binding kinetics of the receptor ligand pair were extracted by fitting the theoretical curve to the data. Second, human T-cell clones were put in contact with cancer cells pulsed with a peptide to which the TCRs are specific. The pair lifetime was measured after a contact time of 22 seconds, indicating a longer adhesion of T-cells to cancer cells pulsed with the specific peptide than to the cancer cells not pulsed with the specific peptide. The data were approximated by a single bond dissociation to extract a pair lumped off-rate describing the avidity of the interaction. Third, CAR-T cells were put in contact with cancer cells expressing their cognate ligand HER2 and three events of adhesion were measured with lifetime larger than 29 seconds, which is significantly larger than for TCR-pMHC in the same conditions. These last assay opens the door to application in cancer immunotherapy for specific (CAR) T-cell selection via avidity evaluation (Ashby et al., 2022; Yerbury, 2022). Combination of lifetime measurement together with intracellular calcium increase indicating a specific activation of the (CAR) T-cells for example could allow a precise assay for specific T-cell recognition (Ashby et al., 2022; Dura et al., 2016). Future development will comprise the addition of a dielectrophoresis actuated cell sorter (DACS) downstream of the contact chamber to sort and retrieve cells of interest (D. Lee et al., 2016). However, the largest improvement will come from computer vision automation of the actuation for the reasons described below.

Reverse binding constants are known to be dependent on the force applied to disrupt the bonds. First order forward and backward kinetics were described by a single energy barrier in the potential landscape along the distance between the receptor and the ligand. The effect of a force applied on the complex can be understood as a lowering in the energy barrier and an increase in the off-rate, as described by the Bell model (Bell, 1978):

$$k_{off} = k_{off}^0 \exp(F/F_b) \quad (4.11)$$

with  $k_{off}^0$  the reverse binding constant under zero force and  $F_b$  the force necessary to lower the energy barrier by one unit of thermal energy  $k_b T$  with  $k_b$  the Boltzmann constant and  $T$  the absolute temperature. This was later described as a slip bond, which was verified for numerous receptor-ligand complexes (B. Liu et al., 2015). Integrins however were shown to

display a minimum in reverse binding constant as a function of disruptive force, also known as catch bond (Kong et al., 2009). In the present case, the disruptive force is generated by the flow drag force exerted on the DMPs after the dielectrophoretic force of the contact line is turned off. Repeatable flow rates are thus of prime importance for comparable results. This is ensured by designing the serpentine that act as large hydraulic flow resistance to minimize flow variation with pressure variation or clogs. However, feedback activated controlled particle image velocimetry (PIV) (Kobel et al., 2010) would allow a dynamic and more precise control on the flow and thus on forces acting on the DMPs.

Variation of the compressive force pushing the two objects together changes the area of contact between them and has an impact on the parameter  $A_c m_{min} m_{max} k_f$ . The compressive force is defined by the difference between drag and DEP force and this latter is dependent on both volume of the DMPs, but also on the position of the HTPs surface. Large variations on both HTPs and DMPs size thus have an impact on both the compressive force and disruptive force experienced by the DMPs and alter the extracted binding kinetics, which should be taken into account when working with samples of large size distribution. Using computer vision control, the voltage used to compress the DMPs in contact with the HTPs could be dynamically adapted to both sizes to reach a constant compressive force.

Precise control on the time of contact is not possible when defining the time of contact as  $t_{V_{sync}=0} - t_{V_{contact}=0}$ , indeed particles have a distribution in velocity due to differences in size and position along the channel height and do not stabilize in contact simultaneously. Control on the time of contact for less than 6 seconds was thus made a single trap at a time, but resolution in contact time could not be controlled to values lower than 1 second due to human limitation in reactivity. This aspect would also be solved using automated control of the interaction, together with identification and sorting of events of interest.

## 4.10 Conclusion

In summary, a new microfluidic chip combining two types of actuation for the controlled contact and separation of two micro-sized objects was proposed and developed, in particular for single-cells, and their independent controlled motions. Hydrodynamic traps were designed to first trap and arrange single-cells in the chip, and the dielectrophoresis phenomenon is used on the second type of particles, either beads or cells, to bring them towards the first cells and create a forced monitored interaction. This developed tool is specially designed to guarantee manipulation methods that preserve cell integrity and receptor functions. While not yet capable of generating interaction in parallel and at high throughput, it paves the way to a second generation of larger throughput devices using automation methods for its actuation and event detection. Two different assays were performed to demonstrate the

capability of the device to generate repeatable cell-bead and cell-cell interactions, first on the fibronectin-integrin bond to fit the experimental data to the well-known binding kinetic model and validate the device. Finally, the challenge of TCR-pMHC bond was tackled and the discrimination between specific and non-specific interactions was successful, leading to an advance in cell-based cancer immunotherapy development with potential for faster and cheaper T-cell screening and sorting. This novel method opens many new perspectives for applications in biophysical experiments and adoptive cell therapy developments.

## 5 Perspective and conclusions

We conclude in this chapter with a summary of the main achievements of this thesis, followed by a discussion about their impact on the field. Finally, future development directions are proposed to meet the requirements of a the tool that can be used to obtain even more significant biological results.

### 5.1 Summary

The current tools for the controlled contact between micro-sized objects are currently very slow and require skilled people to perform the assay. Such assays are capable of determining the adhesion state of two objects after a forced contact of fixed duration and are highly attractive for the characterization of receptor-ligand pairs. The development of tools capable of performing such assays at larger throughput would benefit fields studying the biophysics of receptor-ligand interactions, but also immunotherapy applications where the fast identification and isolation of cancer antigen specific T-cells would accelerate the development of cell based therapies. In this context, technological innovations were done to provide a microfluidic tool capable of performing such a controlled interaction following three main axis, each corresponding to a chapter summarized below.

### Planar hydrodynamic traps

The interaction device requires the independent and bi-modal trapping of two objects to put them in contact and separate them in a controlled fashion. A novel type of hydrodynamic traps was thus developed to provide these necessary features to the interaction device:

- No impact of the trap on other objects than the trapped particle, obtained by the absence of flow leaks around the trapped object.
- Free space around the trapped object for the second particle to come in contact without encountering another surface.
- Fabrication process compatible with the structuring of electrodes.
- Compatibility with an inverted microscope (transparency).

A process was thus developed for the fabrication of two levels of microfluidic channels interconnected by micron-sized microfluidic vias and used to fabricate a device capable of immobilizing a particle flowing in the top channel, cell or bead, by holding it from below through the microfluidic via. The trapping principle based on a difference of pressure rather than shear stress was characterized to minimize damage and ensure the cells physical integrity. The new hydrodynamic traps also give access to the dynamic control over the state of a trap, which can be operated in *idle*, *trapping* or *releasing* mode via the pressure at the outlets of the traps. The possibilities of this method were further explored by arranging the traps in an array for the assembly of particles in a defined pattern and by controlling their trapping and releasing state. This feature was demonstrated experimentally using polystyrene beads, mammalian and algae cells.

A critical comparison of this trapping method with regards to more standard circuits was proposed and the different modalities and usage in other fields discussed in the conclusion.

### Array of dielectrophoretic traps

The second modality of trapping is provided by the dielectrophoretic manipulation of the second object and allows to place it in contact with the object immobilized in the hydrodynamic traps. We thus developed a shape of electrodes, arranged in either a coplanar or facing configuration, capable of generating a DEP force field directing the incoming objects to a single stable position and in three dimensions against the fluid drag flow. A method for the characterization of the trapping efficiency was proposed, using the electrical power generated for a given trapping force. This method was used to select the configuration that generates the minimum electrical power for a given DEP force, minimising the heat generation for safe cell manipulation. For the same purpose, the voltage limit to avoid electroporation during cell trapping was defined.

Next, a deviation system based on DEP force generated by liquid electrodes was proposed to steer the incoming particles to the desired trap for a control over the immobilized objects. Using this feature, four aggregates of cells with controlled size and composition were created to demonstrate the advantage of this system.

### **Combination of hydrodynamic and dielectrophoretic traps for the contact between micro-sized objects**

The two trapping systems developed in the previous chapters were put together to provide bi-modal trapping features. More precisely, the electrodes were patterned in order to direct the DEP force field towards the hydrodynamic trap. In that way, the Hydrodynamically Trapped Particle (HTP) is first trapped and the Dielectrophoretically Manipulated Particle (DMP) is directed and held in contact with the HTP against the fluid flow using DEP. The adhesion state is visually probed once the DEP force is turned off and the DMP dragged away by the fluid. The device was first validated using the well-characterized pair of receptor and ligand fibronectin (coated on a polystyrene bead used as DMP) and integrin (naturally present on mouse fibroblast used as HTP). An adhesion frequency assay was performed and compared to the literature, displaying similar adhesion curves than what was previously reported. Then, the potential of the device to be used in immunotherapy application was challenged by using human T-cell clones as DMPs and cancer cells as HTPs. The lifetime of the adhesion after the forced contact was measured and the difference between specific and non specific interactions was found to be significant. Finally, a lumped pair off-rate was assigned for different populations and was found to be the best way to discriminate between populations.

## **5.2 Perspective**

New tools are emerging both in research and in industry for the avidity measurement of homogeneous populations of T-cells (Ashby et al., 2022; Yerbury, 2022). There is high interest in these technologies for their capability to accelerate adoptive cell therapies and bring new drugs on the market. So far however no tool is able to screen an inhomogeneous population of T-cells for specific T-cell identification and selection. This feature is of highly attractive when the analysis of the nature of the cancer associated antigens and TCR is not required, but when the identification of matching pairs is necessary. This scenario would fit the case where patient derived cancer cells and T-cells are used for specific and rare T-cells isolation. The demand for a device with such capability is pressing and the the developed device has the potential to meet these criteria. Indeed the preliminary results are promising and allows to understand what are the requirement to follow with the development. We thus hereafter propose technological developments to bring the presented prototype to a stage better suited for applications with larger throughput.

### 5.2.1 Future technological developments

#### First generation device

Keeping in mind the perspective of device for specific T-cell selection for immunotherapy applications, some developments could already be done using minor modifications of the device as presented here. The early tests that should be performed at this stage should be the evaluation of the possibility to detect the specificity of a TCR-pMHC binding event through the fluorescently reported increase of intracellular calcium content. Indeed as discussed in chapter 4, the measurement of pair lifetime as it is done so far allows to evaluate the specificity of a population of genetically identical cells, but does not allow to identify single specific events. Increasing the complexity of the stimulation and using the DEP only chip, the first tests should be performed by perfusion of ionomycin on dielectrophoretically trapped T-cells to evaluate the increase in fluorescence. If visible, the T-cells should then be paired with anti-CD8 anti-CD28 coated beads, until reaching physiological stimulation using APC. Next, the viability of the cells after passage in the chip and manipulation by dielectrophoresis should be assessed. Large outlets acting as reservoir will be punched in the PDMS to allow the pipetting of the outlet's content and reculture of cells in standard conditions. With minimal modification, a deviation system based on liquid electrodes will be added at the outlets of the system for specific cells isolation and collection.

As discussed in chapter 4 the device used was manually operated and only a few proof of concept experiments were done. In order to gain confidence in the reliability of the device, more experiments should be performed to allow statistical analysis and evaluate repeatability. In particular, the dependency of the binding kinetic on the pushing and pulling forces, which are themselves dependent on the particle size, should be evaluated. The main gain will thus come from image recognition-based automation of the voltage and pressure actuation. If the field of view cannot be extended to the deviation system, the detection of incoming particle could be done via impedance cytometry.

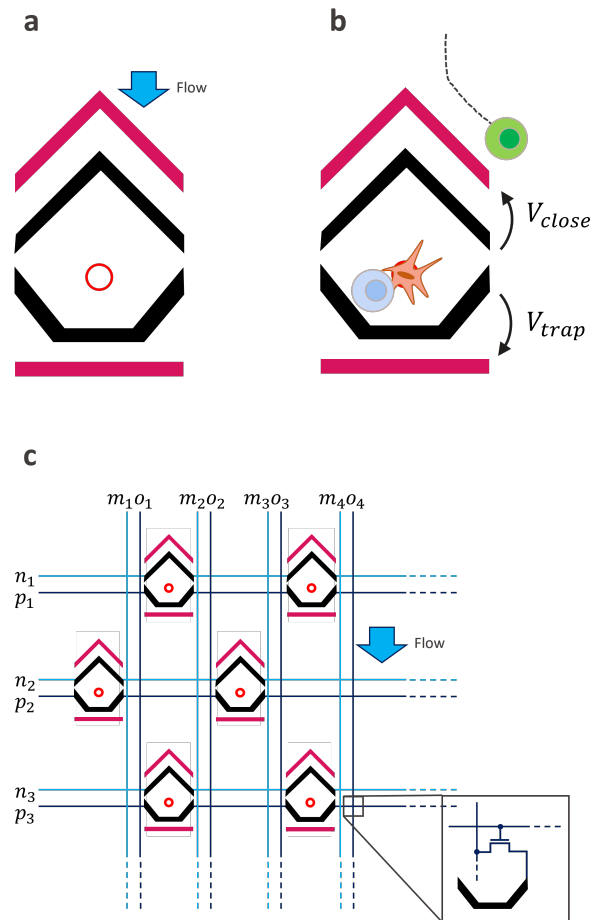


Figure 5.1: Proposition of a 2nd generation device free from the need for a deviation system to ensure a single cell per interaction zone. Ground electrodes are represented in pink and hydrodynamic traps by a red circle. **a** Representation of an interaction unit featuring similar hydrodynamic trap and buried channel as presented in chapter 4, but also comprises closing electrodes upstream of the hydrodynamic traps. **b** The closing electrodes are used to prevent unwanted additional cells to come in contact with the HTP once an interaction is occurring. **c** The interaction units can be arranged in an array to allow simultaneous interactions to occur. The device is fabricated using CMOS technology and the activation of the electrodes are made using a switch matrix.



### Second generation device

The technological developments presented in this thesis set the first stone of a more complete device capable of performing cell-cell interaction at larger throughput. We foresee that the latter will mainly be limited by the use of the deviation system to control the arrival of the particles to the interaction zone. Indeed only one particle can be affected by the DEP at a time to ensure reliable deviation. We thus propose an alternative device that does not require the use of a deviation system. The device is illustrated in Figure 5.1 and comprises only a single large inlet that lets the cells flow on random streamlines in the interaction zone. This latter comprises an array of interaction units. These are composed of a single hydrodynamic traps and DEP trap as presented in chapter 4, but they also feature an additional electrode pair upstream of the hydrodynamic trap as illustrated in Figure 5.1a. This pair of electrodes is responsible for "closing" the interaction zone by deviating unwanted incoming cells to the side as illustrated in Figure 5.1b. Because the traps are arranged in an array, a cell deviated in this manner will have another chance for interaction downstream and the perfusion of randomly distributed cells can be done continuously.

The actuation of a large number of electrodes and counter electrodes arranged in an array requires the use of multiple layers of wiring. The fabrication of buried channels is easily feasible on silicon substrate and we thus foresee the use of CMOS technology for the addressing of the active electrodes using an active matrix as shown in Figure 5.1c, the counter electrodes being always connected to the ground.

Transparency would be lost using silicon technologies and the validation of the second generation device would be done based on image feedback using an upright microscope. But in order to avoid the intrinsic limitation of field of view and image resolution, the electrodes can be used for impedance detection of cell passage through application of a small voltage and current monitoring. While in idle mode, the closing electrodes of the interaction unit can sense the passage of a cell through a current variation across them, triggering the activation of the unit DEP trapping. Similarly, the adhesion state of a pair can be sensed by the impedance monitoring by the trapping electrodes.

#### 5.2.2 Other applications

The device was developed in the frame of cell-cell interaction for immunotherapy applications, but it can find applications in other domains. In particular, it is capable of disrupting the membrane of the HTP using electric pulses. This feature makes it a device of choice for electro-fusion of two cells (Lu et al., 2015). Such possibility could be used for the *in vitro* fertilization of plant female gametes and be exploited for genetic manipulation, plants hybridization as well as study of embryogenesis in plants (F. & Bozhkov, 2008; PENG et al., 2005).

The hydrodynamic traps are capable of handling any object of sufficient size and surface

tension, such as droplets in oil phase or vesicles. Using this feature, controlled droplet pairing and coalescence for cell doublets or cell-bead encapsulation could be achieved with the device. More importantly, this feature could be use for the synthesis of artificial cells or cargo containing membrane defined objects by introduction of specific elements (Lussier et al., 2021; C. Xu et al., 2016).

Given the broad nature of the potential applications and the pressing need for faster T-cell screening tools for adoptive cell therapies, the novel microfluidic device holds the potential to revolutionize cell analysis.



# A Transition pressure

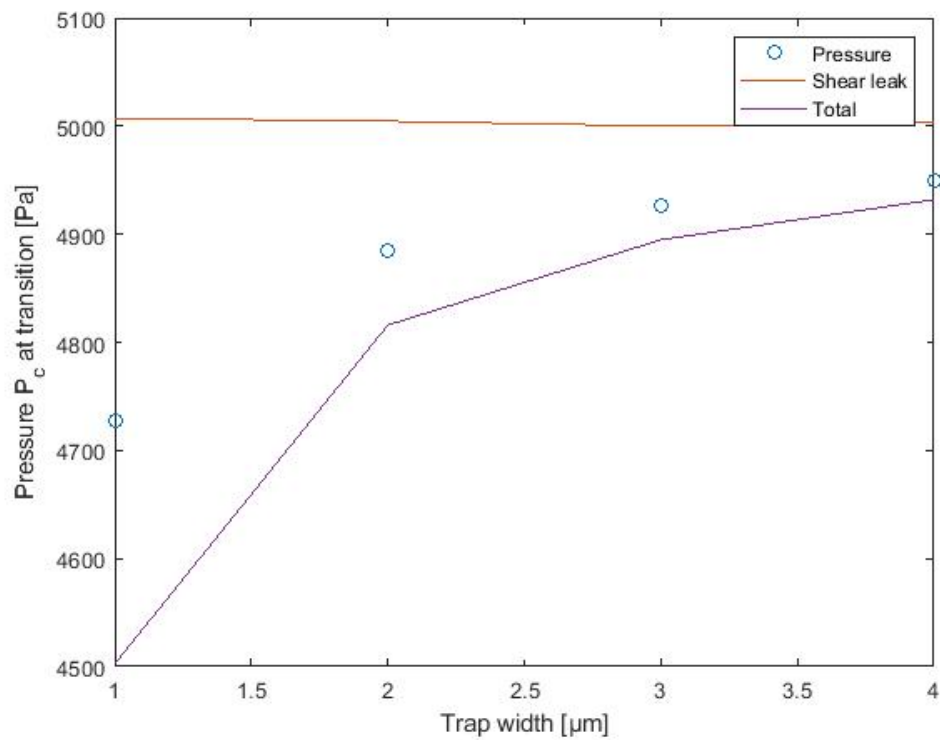


Figure A.1: Pressure  $P_c$  at which the moments of different sources are null, called transition pressure, as a function of trap width for an inlet pressure of 10000 Pa, a bead diameter of 8  $\mu\text{m}$ .



## B Flow perfusion

To demonstrate the capability of flow focusing using perfusion, we used only the fluidic part of a chip with a configuration similar to the one presented in 2.4 with  $R_{out} = 0$  and four parallel buried channels of equal length and connected to the same control channel. Since the hydraulic resistance of each buried channel is equal, the flow should thus be equal in each of the four branches. A configuration with different lengths for each channel would tailor the relationship between the flow ratio coming out of the channels. A solution with a mixture of 5  $\mu\text{m}$  and 500 nm diameter polystyrene beads was flown from the main inlet kept to a value  $P_{in}$  of 200 mbar. The control pressure  $P_c$  was varied and the flow coming out of the buried channels could be observed and its width measured after superposition of images taken during 20 seconds as illustrated in Figure B.1. The flow ratio  $\frac{Q_{BC}}{Q_{BC}+Q_{in}}$  was approximated by the width ratio of the region without beads over total width of the channel and plotted as a function of pressure ratio, demonstrating the possibility to control the focusing of the bead suspension flowing from the top using buried channels. Note that this measurement of the flow ratio does not take into account the three dimensionality of the flow and is only an approximation. PDMS structures in the shape of a half circle concentric to and upstream of the buried channels outlets would allow the flow to span the entire height of the channel directly when injected and generate a better vertical distribution of the flow. This feature can also be used in applications where a flow of liquid needs to be sandwiched in between another one to create stratified layers such as the device presented by Cooksey et al. (2009). These devices require as many inlets as the number of strata, which is space consuming and complicates the operation of the device. With the buried channel technology and its associated three dimensionality, only one inlet per reagent is necessary.

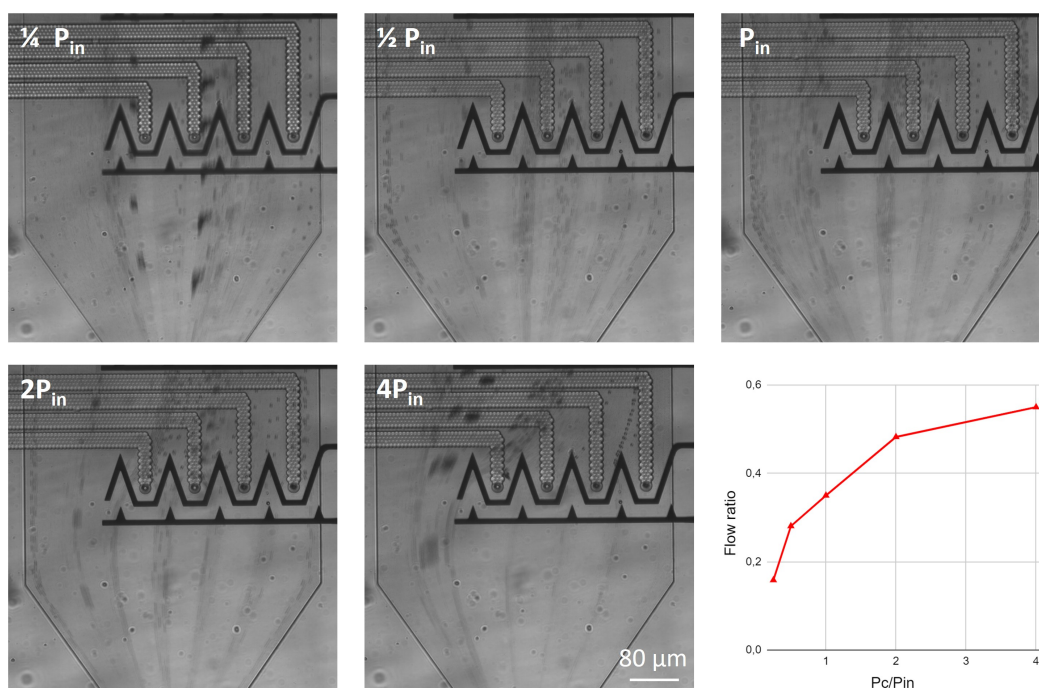


Figure B.1: Timelapse images of a liquid containing a suspension of a mixture of  $5 \mu m$  and  $500 \text{ nm}$  polystyrene beads focused using four parallel buried channels. The electrodes are not used for this experiment. The control pressure  $P_c$  is indicated on the top left of the images and varied to generate different flow ratio and focusing widths. The flow ratio  $\frac{Q_{BC}}{Q_{BC}+Q_{in}}$  was approximated by the width ratio of the region without beads over total width of the channel.

## C Contact between two cells using standard hydrodynamic traps

While the device combining hydrodynamic and dielectrophoretic traps for the controlled contact between cells fills the required functionalities, the fabrication and operation of the planar hydrodynamic traps remain the more complicated parts. We thus explored the possibility of building a device capable of performing the same interaction functionalities using standard hydrodynamic traps as described in section 2. The hydrodynamic traps were inspired from the work of Yesilkoy et al. (2016) and X. Xu et al. (2013b) and are depicted in Figure C.1. The layout also comprises two inlets with respective hydraulic resistance to ensure the pressure controlled independent perfusion of two types of particles. The main area features hydrodynamic traps fabricated in PDMS shaped in half moon with a trapezoidal shaped opening in the middle. The semi-circular shape of the obstacle was supposed to avoid hydrodynamic trapping of multiple objects after the forced contact. The main and counter electrodes are parallel and designed in a chevron-shape aligned with the center of the half-moon.

A COMSOL simulation was performed to understand the direction of the DEP force in this configuration and a result of this simulation with an isosurface represented in grey is shown in Figure C.2. The isosurface indicates a main component of the force directed in  $x$  and  $y$  directions, but comprises also a smaller  $z$  component. The orientation of the nDEP force in the  $z$  direction is indicated in the figure. The simulation validates that this configuration of electrodes and dielectrics pushes the particles from the side to the center of the hydrodynamic trap where the first particle is held.

A device was fabricated following the same process as described in chapter 4 and the alignment of the PDMS layer on top of the electrodes could not be optimal across the whole region of traps which constituted a first limitation. The device was used to perfuse NIH-3T3 cells stained with green calcein AM and a second limitation was observed because of the arrangement of the hydrodynamic traps structures: the traps collect only a small fraction of the streamline and deviate the particles that are not in these streamline to the side, preventing the collection of the particle by downstream traps as illustrated in Figure C.3a. In order to avoid



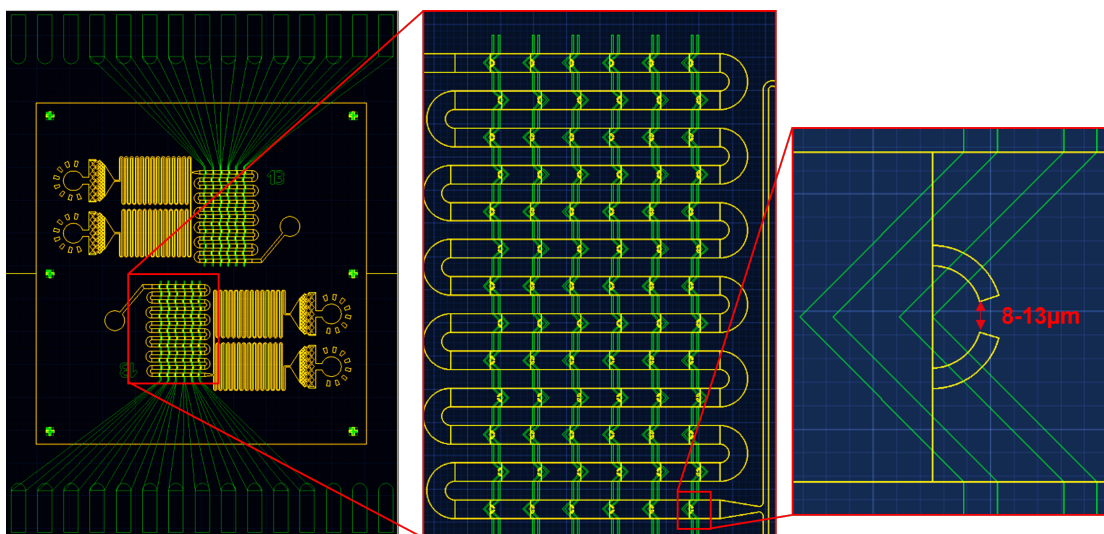


Figure C.1: Layout of the device for the controlled contact between two objects using DEP and standard hydrodynamic traps made from PDMS. The electrode layer is displayed in green and the PDMS layer in yellow.

the first limitation, the microfluidics should be defined by structural photosensitive resist such as SU-8 (Ren et al., 2015) to ensure reliable alignment across the sensitive area. Secondly, the hydrodynamic traps should either feature guiding structures such as the ones proposed by Yesilkoy et al. (2016), or the traps should be placed alternatively on different streamlines.

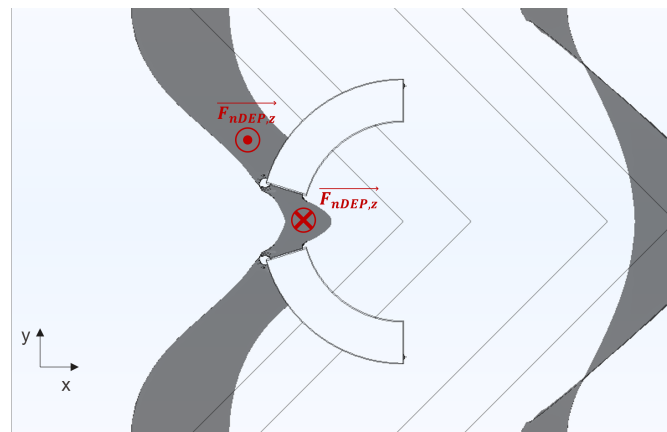


Figure C.2: Result of the 3D simulation of the device with isosurface of the electric field displayed in grey. The direction of the z component of the nDEP force is shown in red for the external and internal part of the structure.

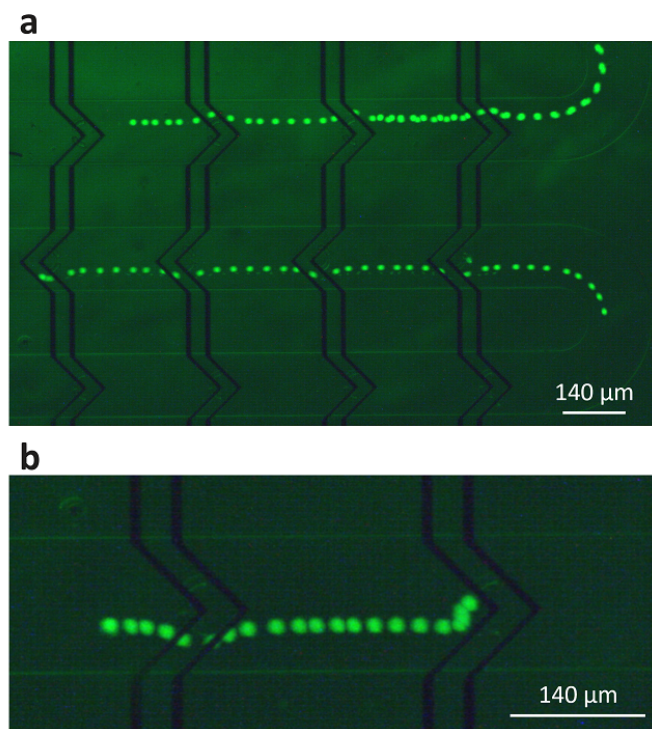


Figure C.3: **a** Timelapse image of the trajectory of cells flowing in the device. The arrangement of the hydrodynamic traps makes it impossible for the particles to be trapped if they are not placed on a specific streamline region. **b** DEP actuated hydrodynamic trapping: the activation of the electrodes directs the cells towards the hydrodynamic trap and the cells remains in the hydrodynamic trap after the DEP is turned off.

However, activating the electrodes was shown to exert a DEP force pushing the cells inside the traps as shown in Figure C.3b, demonstrating the possibility to dynamically activate the hydrodynamic trapping. This was possible for features where the electrodes were close enough from the traps and for large cells. Figure C.4 shows the activation of the electrodes to bring in contact two incoming cells with the previously hydrodynamically trapped cell. The inset shows a close up picture of the contact, demonstrating the sensitivity to the alignment between the PDMS layer and the electrodes to obtain a contact. Indeed the top cell is in contact with the HTP on this image whereas the bottom cell is stopped but is not in contact with the HTP as shown by the clearance between them and the fact that it was rotating on itself, contrary to the top cell and despite its larger size. Furthermore, some HTPs were observed to adhere to the DMP after the release of the DEP force, despite the fact that no adhesion was expected for this homotypic interaction. As discussed in chapter 2, the adhesion could be due to the flow leaks that maintains the HTP, validating the planar hydrodynamic traps approach.

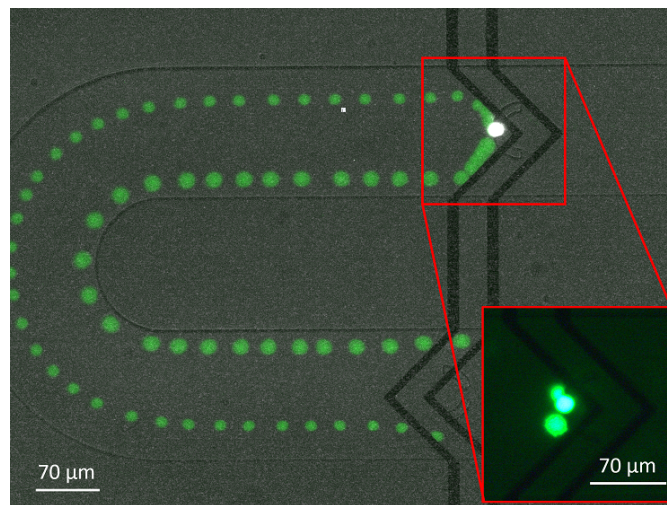


Figure C.4: Timelapse image of the forced contact between a HTP (white) and two DMPs (green). The inset shows a zoom in image of the contact revealing that the top DMP is in contact with the HTP whereas the bottom DMP is not. The contact is thus very sensitive to the placement of the electrodes with respect to the microfluidic layer.

To conclude, the controlled contact was possible between the DMPs and HTPs using this device, but the contact was very sensitive to the alignment between the electrodes and the fluidic layer as well as to the cell size. Future development could be done using a similar device given that large particles with homogeneous size distribution are used.



# D Aperture-controlled fabrication of all-dielectric structural color pixels

**This thesis appendix is adapted from the article in preparation:** C. Lipp, A. Jacquillat, D. Migliozi, H. Wang, A. Bertsch, E. Glushkov, O. Martin and P. Renaud, “Aperture-controlled fabrication of all-dielectric structural color pixels”.

Colors emerge from the structures fabricated using the process described in chapter 2. Interestingly, the colors observed depend on the size of the aperture in the  $\text{Al}_2\text{O}_3$  mask. This appendix describes the study performed to understand the nature of these colors as well as their characterization in the format of a journal paper.

## D.1 Abstract

Structural colors are widespread in nature giving rise to a plethora of bright, iridescently-looking creatures. Humans only recently discovered the physical principles behind structural coloration, which has during the last decade become a rapidly developing field thanks to the availability of micro- and nanoscale fabrication and inspection methods. A multitude of physical systems have been identified as promising platforms for structural colors, however most of them rely either on electron-beam lithography (EBL) or focused ion beam (FIB) approach to define color pixels. This comes with high manufacturing costs and poses a high implementation barrier preventing the wider use of structural coloration in industrial applications. To overcome this, we report a simple yet elegant interference-based method of creating bright structural colors using a single UV photolithography on an all-dielectric substrate, making use of the varied aperture-controlled physical deposition rate of low-temperature silicon dioxide. Being fully CMOS-compatible, such a method paves the way towards large scale usage of structural colors in commercial products.

## D.2 Introduction

Color is a surprisingly rich source of information abundantly enriching our perception of the world. No wonder that since ancient times people tried to reproduce the colors they saw in nature by using, first, natural pigments and, later, synthetic dyes (Pastoureau, 2017). The color of these materials is produced thanks to the absorption of specific wavelengths of incident white light and the reflection of others. The physical origin of such pigmentary colors is results from the exchange of energy between photons and electrons in the materials, being excited into the higher energy states (Kinoshita et al., 2008). A different mechanism of color generation comes in play when incident light is not absorbed, but rather deflected by a material in a certain way due to the presence of an internal structure with dimensions of the same order as the light wavelength. Such structural, typically iridescent, colors have been first described in the scientific literature by Hooke and Newton in the 17th century, based on their observations of the iridescent peacock feathers (Hooke, 1665; Newton, 1704). The first visual evidence of the complex microscopic structure of these feathers came two and a half centuries later with the invention of the scanning electron microscope (Frank & Ruska, 1939), which became the main tool for studying structural coloration in nature (Fox & Vevers, 1960; Zi et al., 2003). The theoretical description of such systems was first developed in the beginning of the 20th century in terms of thin-film interference (Rayleigh, 1919; Strutt, 1917), later generalized through a transfer matrix method (Kinoshita & Yoshioka, 2005), and photonic crystal structures (Sakoda, 2001; Zi et al., 2003).

Bio-inspired potential of structural colors featuring higher stability and lower photodegradation, while being more environmentally-friendly, compared to traditional dyes, was clear. However, fully harnessing this potential in man-made materials only became possible with the advent of micro- and nanostructuring tools (Duan et al., 2011; T. Xu et al., 2011). One of the first platforms to demonstrate the generation of artificial structural colors were metallic nanoantennas utilizing localized surface plasmon resonances (Kumar et al., 2012). Fabricated either using electron beam lithography (EBL) or pulsed femtosecond lasers, they were able to provide an unprecedented printing resolution of structural color pixels up to  $> 10^5$  dots per inch (DPI) (Kristensen et al., 2017; X. Zhu et al., 2016) on various materials (Clausen et al., 2014; Goh et al., 2016; Z. Li et al., 2016). Such structural colors have found numerous applications in several areas, ranging from solar energy harvesting (F. Chen et al., 2015) to displays (Song et al., 2018), security and anti-counterfeiting (Cui et al., 2014; Hong et al., 2020; Lapidis et al., 2022; Z. Li et al., 2021).

The downside of using metals for the implementation of structural colors is not only their high cost, but also inherent optical losses, which prevent from generating saturated colors

from a wide gamut available for traditional dyes. In contrast to plasmonic nanostructures, dielectric metasurfaces have much lower optical losses and, therefore, provide an efficient way of generating bright structural colors (Flauraud et al., 2017; H. Li et al., 2022; Proust et al., 2016; Sun et al., 2017; J. H. Yang et al., 2020; W. Yang et al., 2020), but still rely on FIB or EBL techniques to define the individual color pixels. The inherent dependence on these tools leads to high manufacturing costs and severely limits the scalability and industrial applications of such structural colors (Rezaei et al., 2020; Xuan et al., 2021).

In this context, we propose a novel method to locally control the color, produced by a stack of thin dielectric films using only a photolithography-based fabrication process, which is conceptually shown in Figure D.1a. The local color is produced by light interfering at the interface of a thin film stack, whose thickness is controlled by a non conformal deposition of a dielectric inside a cavity (Cheng et al., 1991; Wille et al., 1992). A cavity itself is etched isotropically in the substrate underneath a transparent mask featuring an opening of a designed diameter, defining a circular region with suspended mask. After the cavity is formed, a second type of dielectric, different than that constituting the mask, is deposited in conditions tailored to lead to a non-conformal coating of the surfaces. In particular, its thickness inside the cavity underneath the mask is limited and controlled by the diameter of the hole in the mask. The fabricated structure seen from the top represents a circle and is composed by a suspended stack of three layers with two constant thicknesses, the top and middle layers, and a variable bottom one. This stack of thin films creates interference patterns with the incoming light and the spectrum of the reflected light is specific to the stack, creating visible colors as illustrated in Figure D.1b. The holes in the mask with surrounding cavities and thin film stacks creating defined colors can be arranged in a specific pattern to create a colored image, similar to pixels arranged to form an image. An example of an image formed by these structures is shown in Figure D.1d with the inset image Figure D.1c showing the detailed pixels.

This method has the advantage of creating a structural color pixel in a thin film stack utilizing a single UV photolithography step used to define the openings in the mask. The rest of the process comprises only etching and deposition steps, which are described in detail in the following section.

## D.3 Results

### D.3.1 Fabrication

The fabrication process to create structural color pixels is illustrated in Figure D.2a and starts from the deposition of the mask material onto a substrate wafer. The choice of the mask material is dictated by its optical properties (transparency to light of a chosen wavelength) and etch rate selectivity relative to the substrate material to ensure the efficient cavity etching



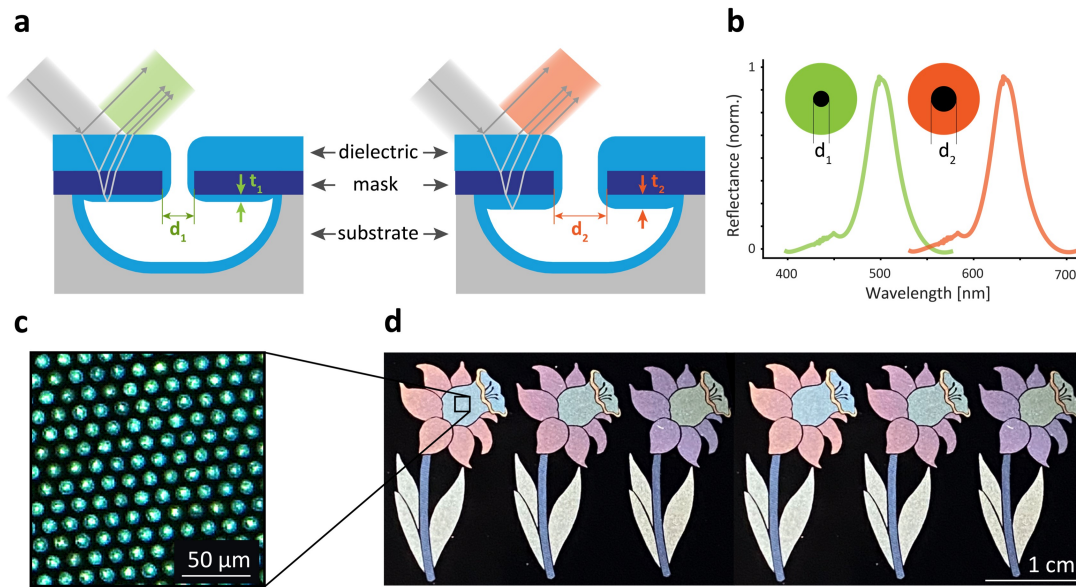


Figure D.1: Concept of the aperture-controlled thin film stack for interference-based colors **a** Side view: a cavity is formed via uniform etching of the substrate through a circular aperture of respective diameter ( $d_1$  and  $d_2$ ). A subsequent deposition of another dielectric leads to an aperture-controlled thickness of the film deposited inside of the cavity ( $t_1$  and  $t_2$ ), creating a three-film stack. The thickness of the top two layers stays the same irrespective of the size of the aperture, while the bottom layer has a variable thickness. This leads to a difference in the spectra of reflected light. **b** Top view: the reflectance spectrum and, therefore, the perceived color of the cavity are thus controlled by the aperture. **c** Each cavity can be used as a pixel of controlled color **d** which can be arranged in patterns to form structurally-colored images.

process (e.g. plasma, gas or wet etch). The openings of diameter  $d_{mask}$  are then defined by UV photolithography and transferred onto the mask using an adapted etching process. The spacing between the openings can be set to achieve two different outcomes: if the spacing is smaller than the diameter of the cavity, the cavities will merge due to the underetch and form a larger area of suspended mask material. This option can be interesting to increase the fill factor, but can be problematic because of the stress in the thin film and will not be explored in detail here. However, if the spacing is chosen to be larger than the diameter of the cavities the mask layer is regularly anchored to the substrate which avoids stress issues. Therefore, this regime will be primarily used for the purpose of the work presented here (Figure D.2b).

The next fabrication step is the controlled deposition of a second dielectric with a refractive index different from that of the mask material. The deposited film has to be non-conformal to the shape of the cavity, so that its thickness at the backside of the underetched mask depends on the size of the opening. One well known method for such non-conformal deposition of a dielectric is the low-pressure chemical vapor deposition (LPCVD) of LTO. LTO is deposited at low pressure (150 mTorr here) and low temperature compared to other LPCVD processes (425

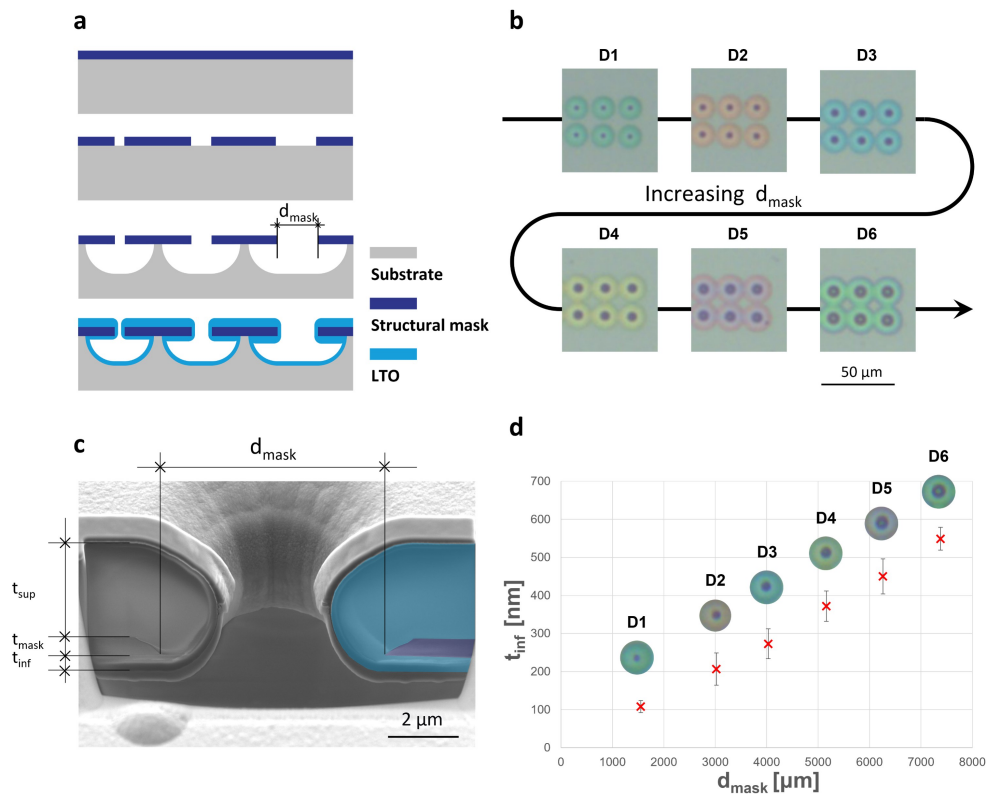


Figure D.2: **a** Side view of the process for the fabrication of the structure: i) a thin transparent mask is deposited on a substrate and ii) patterned with circular apertures of different diameters  $d_{mask}$ . iii) The substrate is selectively and isotropically etched, producing cavities with overhanging mask. iv) A deposition of LTO is then performed, which has the property of depositing non conformally. The thickness of LTO under the overhanging mask is thus defined by the value of  $d_{mask}$ . **b** Top view of the 6 test structures fabricated using the proposed process with fused silica as substrate and  $\text{Al}_2\text{O}_3$  as mask.  $d_{mask}$  ranges between 1 and 8  $\mu\text{m}$  creating different colors. **c** FIB cut of a structure revealing the overhanging thin film stack. The different measured parameters are indicated and the LTO is colored in blue and the  $\text{Al}_2\text{O}_3$  in purple for better visualization. **d** Measured bottom LTO layer  $t_{inf}$  as a function of the aperture in the mask for the same 6 test structures. The dependency seems to be linear.

°C). The surface coverage of LTO on similar structures was studied by Cheng *et al.* (Cheng et al., 1991) who deduced that the material deposited inside the cavity underneath the overhang is due to re-emission of the precursor owing to its low sticking coefficient and not to surface diffusion. The generally accepted mechanism is that precursors with mean free path much larger than the structure size, deposit at the bottom of the cavity under the opening and re-emits under the overhang. Thus the larger  $d_{mask}$  is, the larger is the amount of re-emitted material. Another parameter affecting the deposition under the overhang is the aspect ratio of the cavity: as the center-bottom part of the cavity acts as a point source, the larger the cavity width/height ratio, the more tapered is the resulting film profile. In our case this aspect ratio is constant thanks to the isotropic nature of the etching process, so compared the test structures from Cheng *et al.* (Cheng et al., 1991) we estimate the variation in thin film thickness under the overhang to be less than 15%. Specifically, the structures fabricated for this work were made on fused silica and Si substrates, using  $\text{Al}_2\text{O}_3$  and  $\text{Si}_x\text{N}_y$  as mask materials (the detailed fabrications process is provided in D.5 Materials and Methods). LTO was chosen as a second dielectric with a nominal film thickness over the mask layer set to  $2.5\mu\text{m}$ . The choice of materials was not only supported by their optical properties, but also by their ease of integration into CMOS-oriented industrial microfabrication processes.

### D.3.2 Cross-section characterization

In order to validate the described concept, test structures were fabricated on a fused silica substrate with 480 nm-thick  $\text{Al}_2\text{O}_3$  film as a mask. Color pixels with  $d_{mask}$  between 1 and 8  $\mu\text{m}$  were fabricated and are shown in Figure D.2b: the black dot in the center of the pixel is the empty opening in the mask through which the etching was performed and the colored part indicates the presence of the overhanging thin-film stack causing the interference of the reflected light. Focused ion beam cuts were performed on the six test structures to observe the cross section along their center. Figure D.2c shows a scanning electron microscopy image of such cut along with parameters extracted from it. The diameter of the opening in the mask is referred to as  $d_{mask}$ , the top LTO thickness as  $t_{sup}$ , the middle  $\text{Al}_2\text{O}_3$  thickness as  $t_{mask}$  and the bottom LTO thickness as  $t_{inf}$ . The different materials are false-colored for an easier visual perception on the right part of the cut with the LTO layer in blue and the  $\text{Al}_2\text{O}_3$  mask in purple. The non-conformal deposition is clearly visible with a  $t_{sup}$  being much larger than the  $t_{inf}$  value. A plot of the bottom thickness  $t_{inf}$  as a function of the hole diameter  $d_{mask}$  extracted from SEM images is shown in Figure D.2d, indicating a linear dependence of the bottom layer as a function of  $d_{mask}$  and validating the concept of an aperture-controlled thin film stack.

### D.3.3 Physical modeling

To validate the physical phenomenon responsible for the appearance of colors in the surroundings of the micro-apertures, we first used the transfer matrix method (Pedrotti & Pedrotti, 1996) to calculate the reflectance spectrum of the stack of the thin layers close to the hole, and then converted it to the CIE-1931 XYZ color space.

For the first step, we considered p-polarized light at normal incidence on the stack, and modelled the  $j^{th}$  layer as a matrix:

$$M_j = \begin{bmatrix} \cos(\delta_j) & i \frac{c \sin(\delta_j)}{n_j} \\ i \frac{n_j \sin(\delta_j)}{c} & \cos(\delta_j) \end{bmatrix} \quad (D.1)$$

where  $i$  is the imaginary unit,  $c$  the speed of light and  $\delta_j$  the phase shift induced on a plane wave of wavelength  $\lambda$  by the layer having refractive index  $n_j$  and thickness  $t_j$  defined as:

$$\delta_j = \left(\frac{2\pi}{\lambda}\right) n_j t_j \quad (D.2)$$

The total transfer matrix is then given by the product of the transfer matrices of the  $L$  layers in the order in which the light encounters the layers:

$$M = \prod_1^L M_j = \begin{bmatrix} m_{11} & m_{12} \\ m_{21} & m_{22} \end{bmatrix} \quad (D.3)$$

Finally, the reflectance spectrum is given by

$$R(\lambda) = \left| \frac{n_0 m_{11} c + n_0 n_{L+1} m_{12} - m_{21} c^2 - n_{L+1} m_{22} c}{n_0 m_{11} c + n_0 n_{L+1} m_{12} + m_{21} c^2 + n_{L+1} m_{22} c} \right|^2 \quad (D.4)$$

Where  $n_0$  and  $n_{L+1}$  are the refractive indices of the media preceding and following the stack, respectively.

To convert the reflectance spectrum into the color appearance under an illuminant with spectrum  $I(\lambda)$ , we used the color matching functions  $x(\lambda)$ ,  $y(\lambda)$  and  $z(\lambda)$  to obtain the CIE-1931 XYZ color space as:

$$X = \frac{1}{N} \int_{380}^{780} R(\lambda) I(\lambda) \bar{x}(\lambda) d\lambda \quad (\text{D.5})$$

$$Y = \frac{1}{N} \int_{380}^{780} R(\lambda) I(\lambda) \bar{y}(\lambda) d\lambda \quad (\text{D.6})$$

$$Z = \frac{1}{N} \int_{380}^{780} R(\lambda) I(\lambda) \bar{z}(\lambda) d\lambda \quad (\text{D.7})$$

with

$$N = \int_{380}^{780} I(\lambda) \bar{y}(\lambda) d\lambda \quad (\text{D.8})$$

The spectrum of the incident light was measured from a halogen lamp source, while the colors of the reflected light were simulated by sweeping over the thicknesses of the three layers,  $t_{sup}$ ,  $t_{mask}$  and  $t_{inf}$ , to generate a 3D volume with a corresponding color. As a result of such parameter sweep, the top  $\text{SiO}_2$  layer thickness was found to play an insignificant role in the generated color and was thus fixed to its measured value of 2700 nm. The simulated color palette for a sweep of two remaining parameters ( $t_{mask}$  and  $t_{inf}$ ) is represented in Figure D.3a with  $\text{Al}_2\text{O}_3$  as mask material. Here we observe a periodicity in both directions with more well-defined colors in the lower range of  $t_{inf}$  and  $t_{mask}$ . The colors of the test samples represented in Figure D.1b seem to match the color found on the color palette at the corresponding dimensions reported in Figure D.1d. Figure D.3b represents the color palette modeled in the same conditions for a mask made of a higher refractive index material - silicon nitride. The resulting shorter period in the  $x$  direction shows the expected influence of the larger refractive index of  $\text{Si}_x\text{N}_y$  ( $n \approx 2.4$ ) versus  $\text{Al}_2\text{O}_3$  ( $n \approx 1.9$ ). The simulated colors with the  $\text{Si}_x\text{N}_y$  as the mask material are also more saturated than for  $\text{Al}_2\text{O}_3$  and are thus more interesting for obtaining wide-gamut color palettes.

### D.3.4 Validation of reflectance spectra and color appearance

A relevant aspect of the current model is its ability to make predictions on the expected color appearance depending on the diameter of the hole. By using the SEM measurements of D.2d, we compared the predicted color appearance with the observed colors of the microfabricated holes D.3c. To account for reflectance and illuminance variations due to real measurement conditions, we normalized the simulated reflectance spectra to have maximum brightness: this exalts the tone and make the colors very visible while preserving the ratios of the contribution for each wavelength. Remarkably, we found that the accordance between the predicted and the

observed color is very high for all the apertures tested. By using the raw spectra, the outcomes are not qualitatively different (Figure D.4): the predicted spectra follow the measured ones, and colors remain the same (*i.e.* a red shade is red-ish, a green one, green-ish, etc.), but their brightness is much lower, making it difficult to quantitatively compare with the colors obtained on the very shiny wafers.

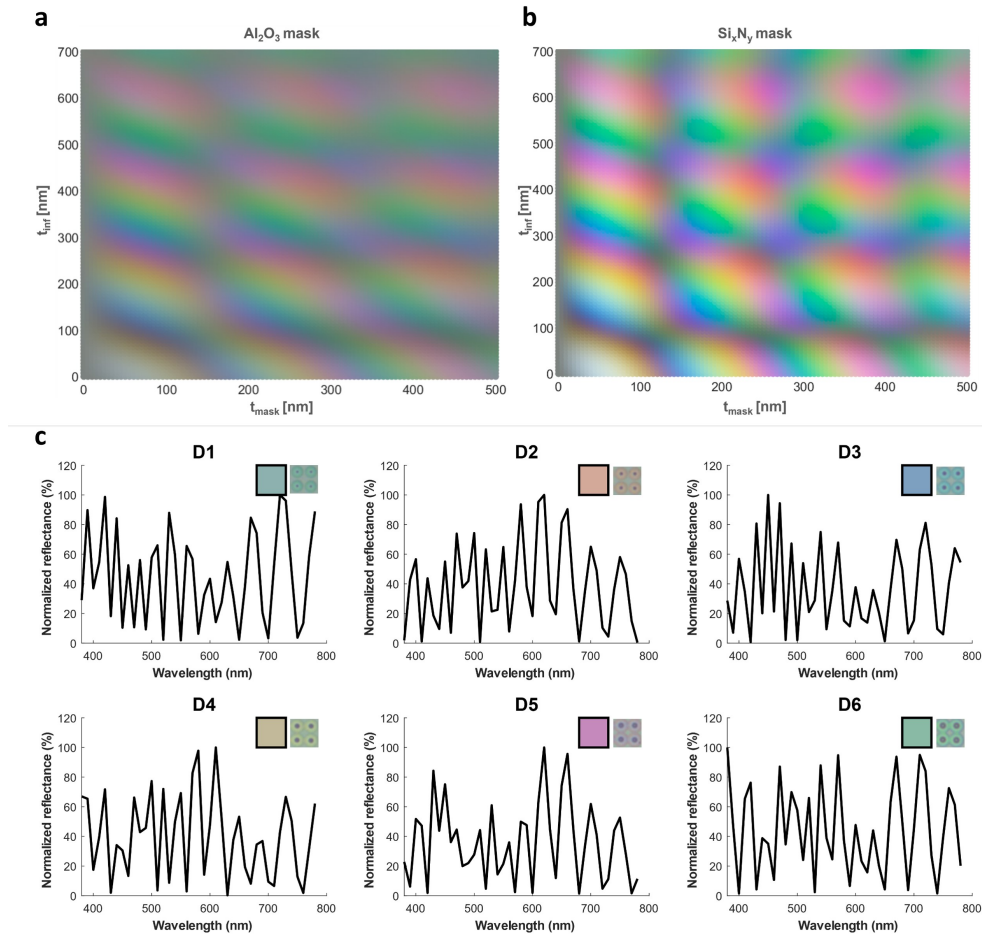


Figure D.3: **a-b** Color appearance modelled with the transfer matrix method and the CIE 1931 XYZ color space for  $t_{\text{sup}} = 2700$  nm and varying  $t_{\text{mask}}$  and  $t_{\text{inf}}$ , for two different materials for the mask layer. **b** Predicted normalized reflectance spectra of the micro-apertures tested. Square insets display the predicted (rigid outline) and observed (dashed outline) color appearance. The theoretical spectrum was calculated for the values measured:  $t_{\text{sup}} = 2700$  nm,  $t_{\text{mask}} = 460$  nm and  $t_{\text{inf}} = 95, 205, 310, 370, 440, 520$  nm.

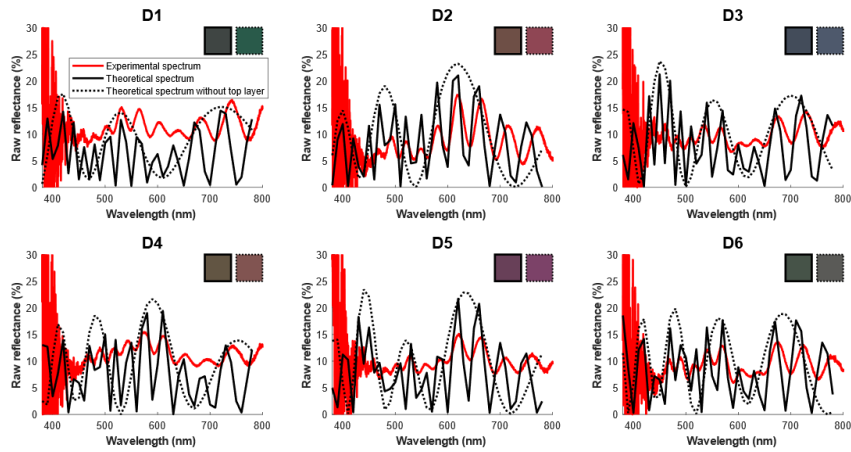


Figure D.4: Simulated and measured reflectance spectra with corresponding colors without scaling for clarity. The simulated spectra of the stack without top layer is represented as well to illustrate the role of envelope the two last layers have on the spectra.

### D.3.5 Color palette

Given the robustness of our methodology to predict and create different colors on the same wafer by adjusting micro-aperture sizes, we explored the potential to apply it to other substrates and different illumination modalities. Thus, we fabricated structures on silicon and fused silica substrates and with  $\text{Al}_2\text{O}_3$  and  $\text{Si}_x\text{N}_y$  as mask with all the combinations of mask and substrate materials (four wafers in total). Since Figure D.3a and b revealed that colors are more defined and saturated in the lower thickness range, mask thickness was set to 80 nm for  $\text{Al}_2\text{O}_3$  and 200 nm for  $\text{Si}_x\text{N}_y$ . The color palette simulated for both thicknesses and materials is shown in Figure D.6b, showing that the created structural colors should be better defined and more saturated than the test samples. The fabrication process was optimized for each combination of materials, as described in detail in Materials and Methods. Briefly, the 80 nm  $\text{Al}_2\text{O}_3$  was deposited using atomic layer deposition (ALD) because this technique deposits films with a better thickness uniformity across the wafer than sputtering and  $\text{Si}_x\text{N}_y$  was deposited using the LPCVD technique. The masks were etched using ion beam etching in all material combinations. The underetching of silicon substrates was performed in a vapor phase of  $\text{XeF}_2$  whose selectivity is infinite towards  $\text{Al}_2\text{O}_3$  and very high towards  $\text{Si}_x\text{N}_y$ . The underetching of fused silica covered by an  $\text{Al}_2\text{O}_3$  mask was performed using a vapor phase of HF with infinite selectivity, while the fused silica covered by  $\text{Si}_x\text{N}_y$  was etched using a solution of 49 % HF. The last step of LTO deposition was common for all four wafers.

The layout of each wafer is shown in Figure D.5 and comprises test structure units with nominal dimensions ranging from 1 to 8  $\mu\text{m}$  swept with an increment of 0.2  $\mu\text{m}$  to obtain the full color range. Each unit is depicted in Figure D.5 and comprises an array of holes of nominal diameter and spaced in such a way that the underetched parts of the cavities do not merge



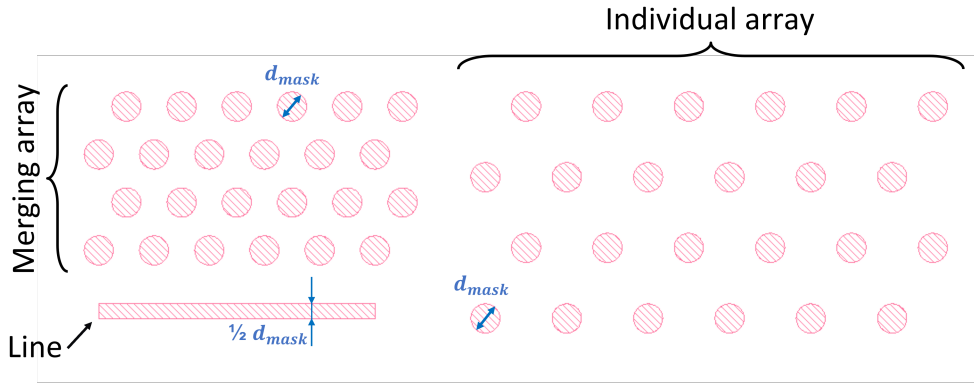


Figure D.5: Layout for the colour palette structures. The value of  $d_{mask}$  ranges from 1 to 8  $\mu\text{m}$  in step of 0.2  $\mu\text{m}$  to obtain the full color range.

(individual arrays), an array of holes of nominal diameter and spaced so that the underetched parts do merge (merging arrays) and a straight line with constant height and width of half nominal dimension. The layout also contains visually-appealing images of flowers, composed of six different parts, each made of an array of individual pixels with different diameters. Flowers of different sizes (height ranging from 0.6 to 20 mm) and diameter combinations were patterned on the wafer.

The result of fabricating all the aforementioned structures is shown in Figure D.6a with the units arranged along their measured  $d_{mask}$  to display the full color progression. The pictures were taken in identical conditions, varying only the intensity of the illumination and without using image or color correction. Images of silicon substrates were set to saturate the background and leave the colorful units on a white background. This was not possible while imaging the fused silica substrates as the color pixels would saturate before the background. The colors were found to follow the same progression as shown in simulations, proving that the created structural colors can be controlled and predicted from the simulated parameters. However, the colors emerging from structures with  $\text{Si}_x\text{N}_y$  masks were not found to be more saturated or defined than the other ones made from  $\text{Al}_2\text{O}_3$  contrary to what was predicted by simulations.

Cracks in the suspended film originating from the edge of the line and on the suspended structure created by the merging arrays were observed in all cases, but these cracks were more pronounced in the cases with  $\text{Si}_x\text{N}_y$  mask.  $\text{XeF}_2$  etch rate was found to be limited by the opening in the mask and the lower range of  $d_{mask}$  had smaller underetch than the larger ones. Merging arrays had brighter color thanks to the larger fill factor but did not have the same color as the individual arrays. The color in the middle of the array matched the color of individual arrays of larger diameter, indicating a larger  $t_{inf}$  for merging arrays than individual arrays. This can be explained by the fact that the bottom LTO layer benefits from multiple point sources for merging arrays. This explanation is supported by the observation of a different

color on the edges of the merging arrays, especially visible in the larger range of  $d_{mask}$ .

Finally, to demonstrate the large-scale capabilities of the proposed method of creating structural colors, we show in Figure D.7 stitched images of colored flowers. The insets on each image indicate the substrate and mask materials, and whether the picture was taken in bright field (BF) or dark field (DF) conditions. The first observation is that the bright field and dark field colors do not match. Indeed the light in the dark field mode mainly comes from the substrate at a large angle that considerably changes the interference spectrum. Secondly, the bright field image also comprises the reflection from the substrate at the bottom of the cavity which adds to the interfering light. The flowers made on fused silica substrates however did not display any color in the dark field mode (we attribute it to the fact that the light incident at a large angle was evenly diffused in the transparent substrate) and are thus not represented. To further prove the real-world attractiveness of the proposed method, we show in Figure D.7b a picture of the microfabricated flowers on the silicon wafer (with  $\text{Al}_2\text{O}_3$  mask) taken with a standard smartphone camera using a white-light illumination from the side. The different structural colors are clearly visible by eye showing the potential of the method to pattern arbitrary images from micrometer to centimeter scale. Notably, the first flower of each row on the left consist of merging arrays where the suspended membrane cracked and detached during fabrication, explaining the absence of colors. Moreover, the colors observed by eye (or by the smartphone camera) closely match the ones observed in the dark field mode under the microscope, which can be qualitatively seen from the microscope image of the flower shown in Figure D.7a i) and its image taken with a smartphone highlighted by the dashed red line in Figure D.7b.

## D.4 Conclusion

In conclusion, we designed, tested and optimized an interference-based method for creating structural color pixels from a stack of thin-film dielectrics. The method uses only a single UV photolithography step to define openings with desired diameters in the etch mask, which then define the reflected light wavelength via the varied aperture-controlled thickness of silicon dioxide layer deposited at the backside of the mask. The choice of both the substrate and the mask materials can be made such as to optimize the desired parameters of the reflected light. Being fully compatible with existing CMOS-oriented microfabrication facilities, such method paves the way towards large scale applications of structural colors in industry, ranging from security features for anti-counterfeiting to surface decoration in high-end watches and jewelry.

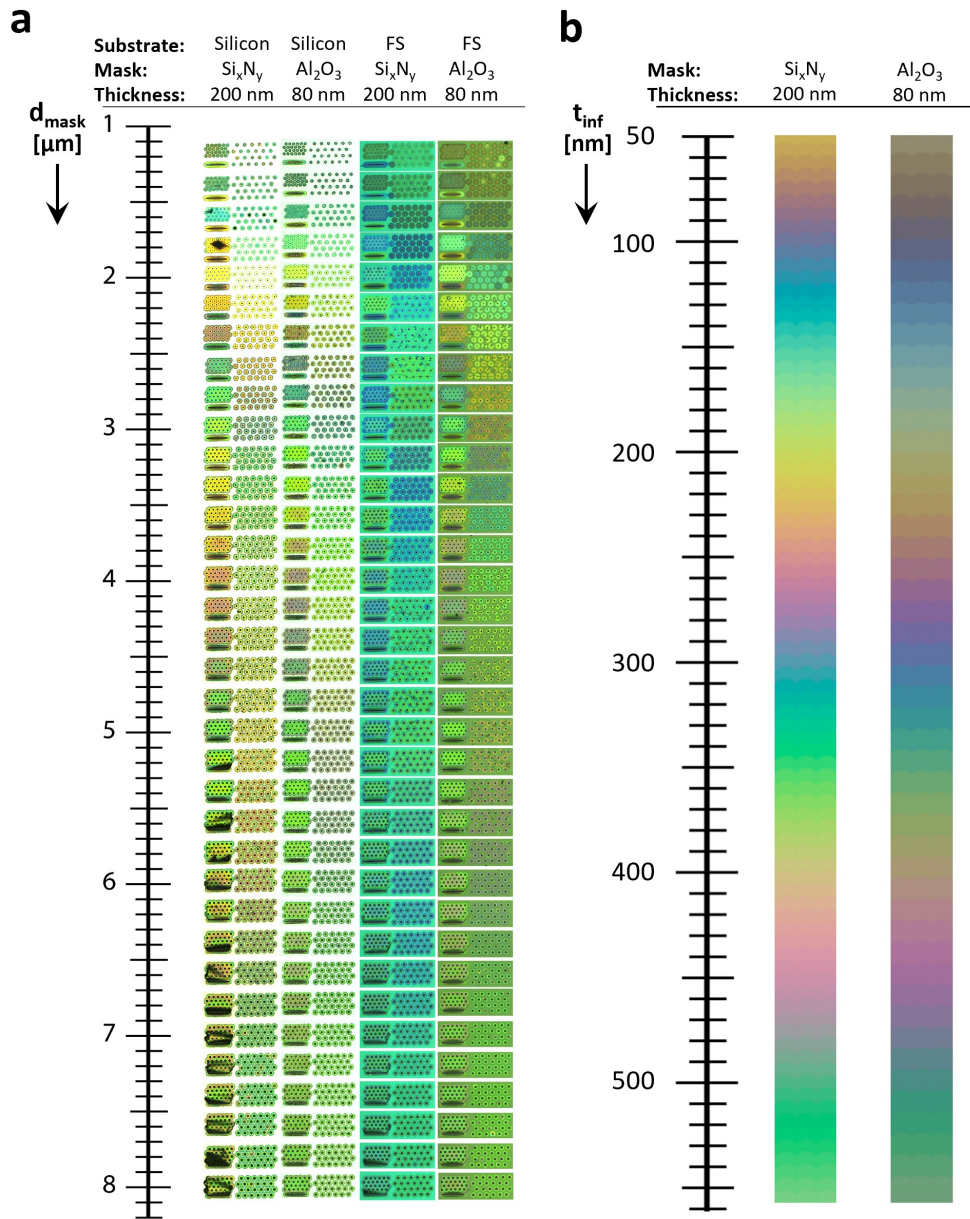


Figure D.6: **a** Test structures comprising individual and merging arrays of holes of varying diameter  $d_{mask}$  and straight line of constant height and width of nominal dimension. The structures were fabricated in all combinations of  $\text{Al}_2\text{O}_3$  and  $\text{Si}_x\text{N}_y$  as mask material on silicon and fused silica (FS) substrates. **b** Color generated by the spectra modeled as of the transfer matrix method for  $t_{sup} = 2700$  nm, fixed  $t_{mask}$  indicated on the figure and varying  $t_{inf}$  for masks made of  $\text{Al}_2\text{O}_3$  and  $\text{Si}_x\text{N}_y$ . The color progression matches the experimentally observed colors.

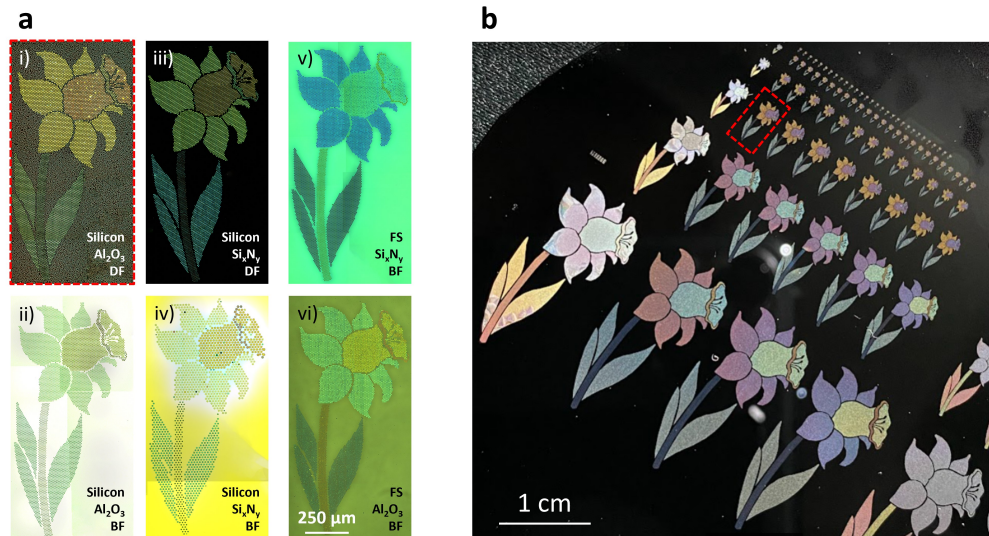


Figure D.7: **a** Stitched microscopy images of colorful flowers fabricated in all combinations of  $\text{Al}_2\text{O}_3$  (80 nm) and  $\text{Si}_x\text{N}_y$  (200 nm) as mask material on silicon and fused silica (FS) substrates. Flowers fabricated on silicon substrates observed under dark field illumination (DF) revealed different colors than in bright field illumination (BF) **b** Picture of a silicon wafer with structures fabricated using 80 nm of  $\text{Al}_2\text{O}_3$  as mask taken with a smartphone camera. The flower highlighted in red corresponds to the flower shown in **a** i) revealing that the colors visible by eye match the colors observed in the dark field mode.

## D.5 Materials and methods

### D.5.1 Fabrication

All substrates were prepared for deposition by first performing the standard RCA cleaning (Kern, 1990).

#### Fused silica with $\text{Al}_2\text{O}_3$ mask

The test structures used for cross section characterization and reflectance measurements were fabricated by depositing a 500 nm thick  $\text{Al}_2\text{O}_3$  layer using sputtering method (SPIDER 600, Pfeiffer). The structures fabricated for the color palette in Figure D.6 start by depositing 80 nm of  $\text{Al}_2\text{O}_3$  using atomic layer deposition (ALD) (TFS 200, Beneq). A 750 nm thick photoresist layer (AZ ECI 3007, MicroChemicals) was spincoated and developed using an automated coater and developer (ACS200 GEN3, Süss) and exposed using direct writing methods (MLA150, Heidelberg Instruments). The pattern was transferred to the mask using ion beam etching (Nexus IBE350, Veeco) and the underetch performed by a vapor phase of HF (uEtch, SPTS) to lead to 5  $\mu\text{m}$  lateral etching. Finally, a deposition of 2.5  $\mu\text{m}$  of low temperature oxide (Centrotherm furnace) is performed to create the thin film stack.

#### Fused silica substrate with $\text{Si}_x\text{N}_y$ mask

200 nm of low stress  $\text{Si}_x\text{N}_y$  was deposited using LPCVD method (Centrotherm furnace). A 750 nm thick photoresist layer (AZ ECI 3007, MicroChemicals) was spincoated and developed using an automated coater and developer (ACS200 GEN3, Süss) and exposed using direct writing methods (MLA150, Heidelberg Instruments). The pattern was transferred to the mask using ion beam etching (Nexus IBE350, Veeco). The underetch was then performed in a 49% solution of HF to lead to 5  $\mu\text{m}$  lateral etching. Finally, a deposition of 2.5  $\mu\text{m}$  of low temperature oxide (Centrotherm furnace) is performed to create the thin film stack.

#### **Silicon substrate with $\text{Al}_2\text{O}_3$ mask**

80 nm of  $\text{Al}_2\text{O}_3$  were deposited using atomic layer deposition (ALD) (TFS 200, Beneq). A 750 nm thick photoresist layer (AZ ECI 3007, MicroChemicals) was spincoated and developed using an automated coater and developer (ACS200 GEN3, Süss) and exposed using direct writing methods (MLA150, Heidelberg Instruments). The pattern was transferred to the mask using ion beam etching (Nexus IBE350, Veeco) and the underetch performed by a vapor phase of  $\text{XeF}_2$  (Xactix, SPTS) to lead to 5  $\mu\text{m}$  lateral etching for the largest dimensions. The etch rate was found to be aperture dependent and the smaller structures had a smaller underetch. Finally, a deposition of 2.5  $\mu\text{m}$  of low temperature oxide (Centrotherm furnace) is performed to create the thin film stack.

#### **Silicon substrate with $\text{Si}_x\text{N}_y$ mask**

200 nm of low stress  $\text{Si}_x\text{N}_y$  was deposited using LPCVD method (Centrotherm furnace). A 750 nm thick photoresist layer (AZ ECI 3007, MicroChemicals) was spincoated and developed using an automated coater and developer (ACS200 GEN3, Süss) and exposed using direct writing methods (MLA150, Heidelberg Instruments). The pattern was transferred to the mask using ion beam etching (Nexus IBE350, Veeco) and the underetch performed by a vapor phase of  $\text{XeF}_2$  (Xactix, SPTS) to lead to 5  $\mu\text{m}$  lateral etching for the largest dimensions. The etch rate was found to be aperture dependent and the smaller structures had a smaller underetch. Finally, a deposition of 2.5  $\mu\text{m}$  of low temperature oxide (Centrotherm furnace) is performed to create the thin film stack.

### **D.5.2 Reflectance spectrum measurements**

The experimental setup used for the spectra measurements comprises an Olympus microscope used to focus a spot light to less than 5  $\mu\text{m}$  diameter on the sample. The spectral detection occurs in the Fourier space thanks to a series of lenses. The background spectrum (i.e. no illumination) was recorded and subtracted from every measure, see equation D.9. The illuminant spectrum (i.e. the light source), used as a reference, was measured by placing a mirror at the sample's place, see equation D.10. Each measurement on the samples was taken five times under the same conditions and the measures were averaged, see equation D.11. Overall, the reflectance spectrum of a sample is obtained as described by equation D.12.

$$I_{corrected}(\lambda) = I_{measured}(\lambda) - I_{background}(\lambda) \quad (D.9)$$

$$R(\lambda) = \frac{I_{reflected}(\lambda)}{I_{source}(\lambda)} \quad (D.10)$$

$$I_{averaged}(\lambda) = \sum_{i=1}^N \frac{I_i(\lambda)}{N} \quad (D.11)$$

$$R(\lambda) = \frac{\frac{1}{N} \sum_{i=1}^N (I_{reflected,i}(\lambda) - I_{background}(\lambda))}{I_{source}(\lambda) - I_{background}(\lambda)} \quad (D.12)$$

### D.5.3 Miscellaneous

The images of the samples were taken using a Leica DM8000 microscope, the DMC2900 camera and acquired using the LAS X software set to provide no color correction. The layout was prepared using the AutoCAD software. The flower image was taken from the website [reussiralecole.fr](http://reussiralecole.fr) and used upon agreement of the owner. The flower layout was created by applying the AND logical operation between an array of holes of fixed diameter and a part of the flower. The calculation and modeling of spectra and colors were made on MATLAB 2022 a.



## Bibliography

- (2022). <https://www.femtoprint.ch/>
- Abonnenc, M., Borgatti, M., Fabbri, E., Gavioli, R., Fortini, C., Destro, F., Altomare, L., Manaresi, N., Medoro, G., & Romani, A. e. a. (2013). Lysis-on-chip of single target cells following forced interaction with CTLs or NK cells on a dielectrophoresis-based array. *The Journal of Immunology*, *191*(7), 3545–3552. <https://doi.org/10.4049/jimmunol.1300890>
- Alam Shibly, S. U., Ghatak, C., Sayem Karal, M. A., Moniruzzaman, M., & Yamazaki, M. (2016). Experimental estimation of membrane tension induced by osmotic pressure. *Biophysical Journal*, *111*(10), 2190–2201. <https://doi.org/10.1016/j.bpj.2016.09.043>
- Alberts, B. (2010). *Essential cell biology*. Garland Science.
- Altomare, L., Borgatti, M., Medoro, G., Manaresi, N., Tartagni, M., Guerrieri, R., & Gambari, R. (2003). Levitation and movement of human tumor cells using a printed circuit board device based on software-controlled dielectrophoresis. *Biotechnology and Bioengineering*, *82*(4), 474–479. <https://doi.org/10.1002/bit.10590>
- Angres, B., Barth, A., & Nelson, W. J. (1996). Mechanism for transition from initial to stable cell-cell adhesion: kinetic analysis of E-cadherin-mediated adhesion using a quantitative adhesion assay. *Journal of Cell Biology*, *134*(2), 549–557. <https://doi.org/10.1083/jcb.134.2.549>
- Antona, S., Platzman, I., & Spatz, J. P. (2020). Droplet-based cytotoxicity assay: implementation of time-efficient screening of antitumor activity of natural killer cells. *ACS Omega*, *5*(38), 24674–24683. <https://doi.org/10.1021/acsomega.0c03264>
- Aplin, A., Howe, A., Alahari, S., & Juliano, R. (1998). Signal transduction and signal modulation by cell adhesion receptors: the role of integrins, cadherins, immunoglobulin-cell adhesion molecules, and selectins. *Pharmacological reviews*, *50*(2), 197–264.
- Arnaud, M., Duchamp, M., Bobisse, S., Renaud, P., Coukos, G., & Harari, A. (2020). Biotechnologies to tackle the challenge of neoantigen identification. *Current Opinion in Biotechnology*, *65*, 52–59. <https://doi.org/10.1016/j.copbio.2019.12.014>



- Ashby, J. F., Schmidt, J., KC, N., Kurum, A., Koch, C., Harari, A., Tang, L., & Au, S. H. (2022). Microfluidic T-cell selection by cellular avidity. *Advanced Healthcare Materials*, 11(16), 2200169. <https://doi.org/10.1002/adhm.202200169>
- Bakke, T., Schmidt, J., Friedrichs, M., & Volker, B. (2005). Etch stop materials for release by vapor HF etching. *Micromechanics Europe*, 122, 68.
- Barlian, A. A., Park, W.-T., Mallon, J. R., Rastegar, A. J., & Pruitt, B. L. (2009). Review: semiconductor piezoresistance for microsystems. *Proceedings of the IEEE*, 97(3), 513–552. <https://doi.org/10.1109/JPROC.2009.2013612>
- Bauleth-Ramos, T., Feijao, T., Goncalves, A., Shahbazi, M.-A., Liu, Z., Barrias, C., Oliveira, M. J., Granja, P., Santos, H. A., & Sarmiento, B. (2020). Colorectal cancer triple co-culture spheroid model to assess the biocompatibility and anticancer properties of polymeric nanoparticles. *Journal of Controlled Release*, 323, 398–411. <https://doi.org/10.1016/j.jconrel.2020.04.025>
- Bell, G. I. (1978). Models for the specific adhesion of cells to cells. *Science*, 200(4342), 618–627. <https://doi.org/10.1126/science.347575>
- Bellouard, Y., Champion, A., Lenssen, B., Matteucci, M., Schaap, A., Beresna, M., Corbari, C., Gecevičius, M., Kazansky, P., Chappuis, O., Kral, M., Clavel, R., Barrot, F., Breguet, J.-M., Mabillard, Y., Bottinelli, S., Hopper, M., Hoenninger, C., Mottay, E., & Lopez, J. (2012). The femtoprint project. *Journal of Laser Micro/Nanoengineering*, 7(1), 1–10. <https://doi.org/10.2961/jlmn.2012.01.0001>
- Bellouard, Y., Said, A., Dugan, M., & Bado, P. (2004). Fabrication of high-aspect ratio, microfluidic channels and tunnels using femtosecond laser pulses and chemical etching. *Optics Express*, 12(10), 2120. <https://doi.org/10.1364/opex.12.002120>
- Bisceglia, E., Cubizolles, M., Trainito, C. I., Berthier, J., Pudda, C., François, O., Mallard, F., & Le Pioufle, B. (2015). A generic and label free method based on dielectrophoresis for the continuous separation of microorganism from whole blood samples. *Sensors and Actuators B: Chemical*, 212, 335–343. <https://doi.org/https://doi.org/10.1016/j.snb.2015.02.024>
- Bjorkelund, H., Gedda, L., Barta, P., Malmqvist, M., & Andersson, K. (2011). Gefitinib induces epidermal growth factor receptor dimers which alters the interaction characteristics with 125I-EGF. *PLoS ONE*, 6(9), e24739. <https://doi.org/10.1371/journal.pone.0024739>
- Bruus, H. (2011). *Theoretical microfluidics*. Oxford Univ. Press.
- Cai, L., Dalal, C. K., & Elowitz, M. B. (2008). Frequency-modulated nuclear localization bursts coordinate gene regulation. *Nature*, 455(7212), 485–490. <https://doi.org/10.1038/nature07292>
- Campillo-Davo, D., Flumens, D., & Lion, E. (2020). The quest for the best: how TCR affinity, avidity, and functional avidity affect TCR-engineered T-cell antitumor responses. *Cells*, 9(7), 1720. <https://doi.org/10.3390/cells9071720>

- Cao, Y., Floehr, J., Ingebrandt, S., & Schnakenberg, U. (2021). Dry film resist laminated microfluidic system for electrical impedance measurements. *Micromachines*, *12*(6), 632. <https://doi.org/10.3390/mi12060632>
- Carmona-Fontaine, C., Theveneau, E., Tzekou, A., Tada, M., Woods, M., Page, K. M., Parsons, M., Lambris, J. D., & Mayor, R. (2011). Complement fragment c3a controls mutual cell attraction during collective cell migration. *Developmental Cell*, *21*(6), 1026–1037. <https://doi.org/10.1016/j.devcel.2011.10.012>
- Chang, A. C., Mekhdjian, A. H., Morimatsu, M., Denisin, A. K., Pruitt, B. L., & Dunn, A. R. (2016). Single molecule force measurements in living cells reveal a minimally tensioned integrin state. *ACS Nano*, *10*(12), 10745–10752. <https://doi.org/10.1021/acsnano.6b03314>
- Chen, C., Bai, X., Ding, Y., & Lee, I.-S. (2019). Electrical stimulation as a novel tool for regulating cell behavior in tissue engineering. *Biomaterials Research*, *23*(1), 1–12. <https://doi.org/10.1186/s40824-019-0176-8>
- Chen, F., Wang, S.-W., Liu, X., Ji, R., Yu, L., Chen, X., & Lu, W. (2015). High performance colored selective absorbers for architecturally integrated solar applications. *Journal of Materials Chemistry A*, *3*(14), 7353–7360. <https://doi.org/10.1039/C5TA00694E>
- Chen, J., & Wise, K. (1997). A high-resolution silicon monolithic nozzle array for inkjet printing. *IEEE Transactions on Electron Devices*, *44*(9), 1401–1409. <https://doi.org/10.1109/16.622594>
- Chen, P., Zhang, W., Zhou, J., Wang, P., Xiao, L., & Yang, M. (2009). Development of planar patch clamp technology and its application in the analysis of cellular electrophysiology. *Progress in Natural Science*, *19*(2), 153–160. <https://doi.org/https://doi.org/10.1016/j.pnsc.2008.06.012>
- Chen, W., Evans, E. A., McEver, R. P., & Zhu, C. (2008). Monitoring receptor-ligand interactions between surfaces by thermal fluctuations. *Biophysical Journal*, *94*(2), 694–701. <https://doi.org/10.1529/biophysj.107.117895>
- Chen, Y., Ju, L. A., Zhou, F., Liao, J., Xue, L., Su, Q. P., Jin, D., Yuan, Y., Lu, H., Jackson, S. P., & et al. (2019). An integrin  $\alpha_{IIb}\beta_3$  intermediate affinity state mediates biomechanical platelet aggregation. *Nature Materials*, *18*(7), 760–769. <https://doi.org/10.1038/s41563-019-0323-6>
- Cheng, L.-Y., McVittie, J. P., & Saraswat, K. C. (1991). New test structure to identify step coverage mechanisms in chemical vapor deposition of silicon dioxide. *Applied Physics Letters*, *58*(19), 2147–2149. <https://doi.org/10.1063/1.104988>
- Chesla, S. E., Selvaraj, P., & Zhu, C. (1998). Measuring two-dimensional receptor-ligand binding kinetics by micropipette. *Biophysical Journal*, *75*(3), 1553–1572. [https://doi.org/10.1016/s0006-3495\(98\)74074-3](https://doi.org/10.1016/s0006-3495(98)74074-3)

- Cheung, K., Gawad, S., & Renaud, P. (2005). Impedance spectroscopy flow cytometry: on-chip label-free cell differentiation. *Cytometry Part A*, *65A*(2), 124–132. <https://doi.org/https://doi.org/10.1002/cyto.a.20141>
- Chopinnet, L., Wasungu, L., & Rols, M.-P. (2012). First explanations for differences in electrotransfection efficiency in vitro and in vivo using spheroid model. *International Journal of Pharmaceutics*, *423*(1), 7–15. <https://doi.org/10.1016/j.ijpharm.2011.04.054>
- Clausen, J. S., Højlund-Nielsen, E., Christiansen, A. B., Yazdi, S., Grajower, M., Taha, H., Levy, U., Kristensen, A., & Mortensen, N. A. (2014). Plasmonic metasurfaces for coloration of plastic consumer products. *Nano letters*, *14*(8), 4499–4504. <https://doi.org/10.1021/nl5014986>
- Clinicaltrials.gov\_2022. (2022). <https://clinicaltrials.gov/ct2/show/NCT04995003>
- Cooksey, G. A., Sip, C. G., & Folch, A. (2009). A multi-purpose microfluidic perfusion system with combinatorial choice of inputs, mixtures, gradient patterns, and flow rates. *Lab Chip*, *9*(3), 417–426. <https://doi.org/10.1039/b806803h>
- Cottet, J., Kehren, A., Lasli, S., Lintel, H., Buret, F., Frénea-Robin, M., & Renaud, P. (2019). Dielectrophoresis-assisted creation of cell aggregates under flow conditions using planar electrodes. *Electrophoresis*, *40*(10), 1498–1509. <https://doi.org/10.1002/elps.201800435>
- Cottet, J., Vaillier, C., Buret, F., Frénea-Robin, M., & Renaud, P. (2017). A reproducible method for  $\mu\text{m}$  precision alignment of pdms microchannels with on-chip electrodes using a mask aligner. *Biomicrofluidics*, *11*(6), 064111. <https://doi.org/10.1063/1.5001145>
- Cui, Y., Hegde, R. S., Phang, I. Y., Lee, H. K., & Ling, X. Y. (2014). Encoding molecular information in plasmonic nanostructures for anti-counterfeiting applications. *Nanoscale*, *6*(1), 282–288. <https://doi.org/10.1039/C3NR04375D>
- Dalmay, C., Villemejeane, J., Joubert, V., Silve, A., Arnaud-Cormos, D., Français, O., Mir, L. M., Leveque, P., & Le Pioufle, B. (2011). A microfluidic biochip for the nanoporation of living cells. *Biosensors and Bioelectronics*, *26*(12), 4649–4655. <https://doi.org/https://doi.org/10.1016/j.bios.2011.03.020>
- Demierre, N., Braschler, T., Linderholm, P., Seger, U., van Lintel, H., & Renaud, P. (2007). Characterization and optimization of liquid electrodes for lateral dielectrophoresis. *Lab Chip*, *7*(3), 355–365. <https://doi.org/10.1039/b612866a>
- Di Carlo, D., Aghdam, N., & Lee, L. P. (2006). Single-cell enzyme concentrations, kinetics, and inhibition analysis using high-density hydrodynamic cell isolation arrays. *Analytical Chemistry*, *78*(14), 4925–4930. <https://doi.org/10.1021/ac060541s>
- Dijkstra, M., de Boer, M., Berenschot, J., Lammerink, T., Wiegerink, R., & Elwenspoek, M. (2008). Miniaturized thermal flow sensor with planar-integrated sensor structures on semicircular surface channels. *Sensors and Actuators A: Physical*, *143*(1), 1–6. <https://doi.org/10.1016/j.sna.2007.12.005>

- Dong, Z., Jiao, Y., Xie, B., Hao, Y., Wang, P., Liu, Y., Shi, J., Chitrakar, C., Black, S., & Wang, Y.-C. (2020). On-chip multiplexed single-cell patterning and controllable intracellular delivery. *Microsystems & Nanoengineering*, 6(1), 1–11. <https://doi.org/10.1038/s41378-019-0112-z>
- Duan, H., Hu, H., Kumar, K., Shen, Z., & Yang, J. K. (2011). Direct and reliable patterning of plasmonic nanostructures with sub-10-nm gaps. *ACS nano*, 5(9), 7593–7600. <https://doi.org/10.1021/nn2025868>
- Duchamp, M., Dahoun, T., Vaillier, C., Arnaud, M., Bobisse, S., Coukos, G., Harari, A., & Renaud, P. (2019). Microfluidic device performing on flow study of serial cell-cell interactions of two cell populations. *RSC Advances*, 9(70), 41066–41073. <https://doi.org/10.1039/c9ra09504g>
- Duchamp, M. C. M. (2020). *Microfluidic devices for the study of cell-cell, cell-particle and particle-particle interactions* (Doctoral dissertation).
- Dura, B., Dougan, S. K., Barisa, M., Hoehl, M. M., Lo, C. T., Ploegh, H. L., & Voldman, J. (2015). Profiling lymphocyte interactions at the single-cell level by microfluidic cell pairing. *Nature Communications*, 6(1), 1–13. <https://doi.org/10.1038/ncomms6940>
- Dura, B., Servos, M. M., Barry, R. M., Ploegh, H. L., Dougan, S. K., & Voldman, J. (2016). Longitudinal multiparameter assay of lymphocyte interactions from onset by microfluidic cell pairing and culture. *Proceedings of the National Academy of Sciences*, 113(26), E3599–E3608. <https://doi.org/10.1073/pnas.1515364113>
- Escoffre, J.-M., Portet, T., Favard, C., Teissié, J., Dean, D. S., & Rols, M.-P. (2011). Electromediated formation of dna complexes with cell membranes and its consequences for gene delivery. *Biochimica et Biophysica Acta (BBA) - Biomembranes*, 1808(6), 1538–1543. <https://doi.org/10.1016/j.bbamem.2010.10.009>
- F, S. M., & Bozhkov, P. V. (2008). *Plant embryogenesis*. Humana Press.
- Fan, L., Guan, Z., Luo, T., Ren, J., Lam, R. H. W., & Sun, D. (2021). High-throughput deterministic pairing and coculturing of single cells in a microwell array using combined hydrodynamic and recirculation flow captures. *Biomicrofluidics*, 15(5), 054103. <https://doi.org/10.1063/5.0066668>
- Fiedler, S., Shirley, S. G., Schnelle, T., & Fuhr, G. (1998). Dielectrophoretic sorting of particles and cells in a microsystem. *Analytical Chemistry*, 70(9), 1909–1915. <https://doi.org/10.1021/ac971063b>
- Fiore, V. F., Ju, L., Chen, Y., Zhu, C., & Barker, T. H. (2014). Dynamic catch of a thy-1  $\alpha_5\beta_1$ +syndecan-4 trimolecular complex. *Nature Communications*, 5(1), 4886. <https://doi.org/10.1038/ncomms5886>
- Flauraud, V., Reyes, M., Reyes, M., Paniagua-DomÁnguez, R., Kuznetsov, A. I., Brugger, J., Brugger, J., & Brugger, J. (2017). Silicon nanostructures for bright field full color prints. *ACS Photonics*, 4(8), 1913–1919. <https://doi.org/10.1021/acsp Photonics.6b01021>
- Fox, H. M., & Vevers, G. (1960). *The nature of animal colours*. Sidgwick; Jackson.

- Frank, F., & Ruska, H. (1939). Übermikroskopische untersuchung der blaustuktur der vogelfeder. *Naturwissenschaften*, 27(14), 229–230. <https://doi.org/10.1007/BF02716495>
- Frénéa, M., Faure, S., Le Pioufle, B., Coquet, P., & Fujita, H. (2003). Positioning living cells on a high-density electrode array by negative dielectrophoresis. *Materials Science and Engineering: C*, 23(5), 597–603. [https://doi.org/10.1016/S0928-4931\(03\)00055-9](https://doi.org/10.1016/S0928-4931(03)00055-9)
- Garber, K. (2018). Driving T-cell immunotherapy to solid tumors. *Nature Biotechnology*, 36(3), 215–219. <https://doi.org/10.1038/nbt.4090>
- Gee, K., Brown, K., Chen, W.-N., Bishop-Stewart, J., Gray, D., & Johnson, I. (2000). Chemical and physiological characterization of Fluo-4 ca<sup>2+</sup>-indicator dyes. *Cell Calcium*, 27(2), 97–106. <https://doi.org/10.1054/ceca.1999.0095>
- Godino, N., Pfisterer, F., Gerling, T., Guernth-Marschner, C., Duschl, C., & Kirschbaum, M. (2019). Combining dielectrophoresis and computer vision for precise and fully automated single-cell handling and analysis. *Lab on a Chip*, 19(24), 4016–4020. <https://doi.org/10.1039/c9lc00800d>
- Goh, X. M., Ng, R. J. H., Wang, S., Tan, S. J., & Yang, J. K. (2016). Comparative study of plasmonic colors from all-metal structures of posts and pits. *ACS photonics*, 3(6), 1000–1009. <https://doi.org/10.1021/acsp Photonics.6b00099>
- Grosberg, R. K., & Strathmann, R. R. (2007). The evolution of multicellularity: a minor major transition? *Annual Review of Ecology, Evolution, and Systematics*, 38(1), 621–654. <https://doi.org/10.1146/annurev.ecolsys.36.102403.114735>
- Gross, A., Schoendube, J., Zimmermann, S., Steeb, M., Zengerle, R., & Koltay, P. (2015). Technologies for single-cell isolation. *International Journal of Molecular Sciences*, 16(8), 16897–16919. <https://doi.org/10.3390/ijms160816897>
- Guo, F., Li, P., French, J. B., Mao, Z., Zhao, H., Li, S., Nama, N., Fick, J. R., Benkovic, S. J., & Huang, T. J. (2014). Controlling cell-cell interactions using surface acoustic waves. *Proceedings of the National Academy of Sciences*, 112(1), 43–48. <https://doi.org/10.1073/pnas.1422068112>
- Ham, S. L., Joshi, R., Thakuri, P. S., & Tavana, H. (2016). Liquid-based three-dimensional tumor models for cancer research and drug discovery. *Experimental Biology and Medicine*, 241(9), 939–954. <https://doi.org/10.1177/1535370216643772>
- He, C.-K., & Hsu, C.-H. (2021). Microfluidic technology for multiple single-cell capture. *Biomechanics*, 15(6), 061501. <https://doi.org/10.1063/5.0057685>
- Heathman, T. R., Nienow, A. W., McCall, M. J., Coopman, K., Kara, B., & Hewitt, C. J. (2015). The translation of cell-based therapies: clinical landscape and manufacturing challenges. *Regenerative Medicine*, 10(1), 49–64. <https://doi.org/10.2217/rme.14.73>
- Helenius, J., Heisenberg, C.-P., Gaub, H. E., & Muller, D. J. (2008). Single-cell force spectroscopy. *Journal of Cell Science*, 121(11), 1785–1791. <https://doi.org/10.1242/jcs.030999>

- Hellwig, C. T., Kohler, B. F., Lehtivarjo, A.-K., Dussmann, H., Courtney, M. J., Prehn, J. H., & Rehm, M. (2008). Real time analysis of tumor necrosis factor-related apoptosis-inducing ligand/cycloheximide-induced caspase activities during apoptosis initiation. *Journal of Biological Chemistry*, *283*(31), 21676–21685. <https://doi.org/10.1074/jbc.m802889200>
- Hideharu, H., & Haruo, M. (1994). Fluorescence imaging of intracellular Ca<sup>2+</sup>. *Journal of Pharmacological and Toxicological Methods*, *31*(1), 1–10. [https://doi.org/10.1016/1056-8719\(94\)90023-x](https://doi.org/10.1016/1056-8719(94)90023-x)
- Ho, C.-T., Lin, R.-Z., Chen, R.-J., Chin, C.-K., Gong, S.-E., Chang, H.-Y., Peng, H.-L., Hsu, L., Yew, T.-R., & Chang, S.-F. e. a. (2013). Liver-cell patterning lab chip: mimicking the morphology of liver lobule tissue. *Lab on a Chip*, *13*(18), 3578. <https://doi.org/10.1039/c3lc50402f>
- Holm, J., Elderstig, H., Kristensen, O., & Rigler, R. (1997). A fluorescence detection and selection device for dna-molecules bound to microspheres. *Nucleosides and Nucleotides*, *16*(5-6), 557–562. <https://doi.org/10.1080/07328319708002916>
- Hong, W., Hong, W., Yuan, Z., & Chen, X. (2020). Structural color materials for optical anticounterfeiting. *Small*, *16*(16), 1907626. <https://doi.org/10.1002/sml.201907626>
- Hooke, R. (1665). *Micrographia: or some physiological descriptions of minute bodies made by magnifying glasses with observations and inquiries thereupon*. London: Jo. Martyn; J. Allestry. <https://doi.org/10.5962/bhl.title.904>
- Huang, R., Li, X., He, Y., Zhu, W., Gao, L., Liu, Y., Gao, L., Wen, Q., Zhong, J. F., & Zhang, C. e. a. (2020). Recent advances in CAR-T cell engineering. *Journal of Hematology & Oncology*, *13*(1), 1–19. <https://doi.org/10.1186/s13045-020-00910-5>
- Huppa, J. B., & Davis, M. M. (2003). T-cell-antigen recognition and the immunological synapse. *Nature Reviews Immunology*, *3*(12), 973–983. <https://doi.org/10.1038/nri1245>
- Hwang, J.-R., Byeon, Y., Kim, D., & Park, S.-G. (2020). Recent insights of T cell receptor-mediated signaling pathways for T cell activation and development. *Experimental & Molecular Medicine*, *52*(5), 750–761. <https://doi.org/10.1038/s12276-020-0435-8>
- Hyer, A. R., Hong, D., Davalos, R. V., Swami, N. S., & Schmelz, E. M. (2021). A novel ultralow conductivity electromanipulation buffer improves cell viability and enhances dielectrophoretic consistency. *Electrophoresis*, *42*(12-13), 1366–1377. <https://doi.org/10.1002/elps.202000324>
- Ide, H., Espulgar, W. V., Saito, M., Aoshi, T., Koyama, S., Takamatsu, H., & Tamiya, E. (2020). Profiling T-cell interaction and activation through microfluidics-assisted serial encounter with APCs. *Sensors and Actuators B: Chemical*, *330*, 129306. <https://doi.org/10.1016/j.snb.2020.129306>
- Ishiguro, T., Ohata, H., Sato, A., Yamawaki, K., Enomoto, T., & Okamoto, K. (2017). Tumor-derived spheroids: relevance to cancer stem cells and clinical applications. *Cancer Science*, *108*(3), 283–289. <https://doi.org/10.1111/cas.13155>

- Jang, J. H., Huang, Y., Zheng, P., Jo, M. C., Bertolet, G., Zhu, M. X., Qin, L., & Liu, D. (2015). Imaging of cell-cell communication in a vertical orientation reveals high-resolution structure of immunological synapse and novel PD-1 dynamics. *The Journal of Immunology*, *195*(3), 1320–1330. <https://doi.org/10.4049/jimmunol.1403143>
- Jeknic, S., Kudo, T., & Covert, M. W. (2019). Techniques for studying decoding of single cell dynamics. *Frontiers in Immunology*, *10*, 755. <https://doi.org/10.3389/fimmu.2019.00755>
- Jiang, Y., Li, Y., & Zhu, B. (2015). T-cell exhaustion in the tumor microenvironment. *Cell Death & Disease*, *6*(6), e1792–e1792. <https://doi.org/10.1038/cddis.2015.162>
- Jin, D., Deng, B., Li, J. X., Cai, W., Tu, L., Chen, J., Wu, Q., & Wang, W. H. (2015). A microfluidic device enabling high-efficiency single cell trapping. *Biomicrofluidics*, *9*(1), 014101. <https://doi.org/10.1063/1.4905428>
- Johnson, A. W., & Harley, B. A. (2011). *Mechanobiology of cell-cell and cell-matrix interactions*. Springer Science + Business Media.
- Jones, T. (2003). Basic theory of dielectrophoresis and electrorotation. *IEEE Engineering in Medicine and Biology Magazine*, *22*(6), 33–42. <https://doi.org/10.1109/memb.2003.1304999>
- Ju, L., Dong, J.-f., Cruz, M. A., & Zhu, C. (2013). The n-terminal flanking region of the  $\alpha 1$  domain regulates the force-dependent binding of von willebrand factor to platelet glycoprotein  $\text{Ib}\alpha$ . *Journal of Biological Chemistry*, *288*(45), 32289–32301. <https://doi.org/10.1074/jbc.m113.504001>
- Kaiser, D. (2001). Building a multicellular organism. *Annual Review of Genetics*, *35*(1), 103–123. <https://doi.org/10.1146/annurev.genet.35.102401.090145>
- Kaler, K., & Jones, T. (1990). Dielectrophoretic spectra of single cells determined by feedback-controlled levitation. *Biophysical Journal*, *57*(2), 173–182. [https://doi.org/10.1016/s0006-3495\(90\)82520-0](https://doi.org/10.1016/s0006-3495(90)82520-0)
- Kalyuzhny, A. E., & Kalyuzhny, A. E. (2005). *Handbook of elispot: methods and protocols*. Humana Press.
- Kaplan, W., Elderstig, H., & Veider, C. (1994). A novel fabrication method of capillary tubes on quartz for chemical analysis applications. *Proceedings IEEE Micro Electro Mechanical Systems An Investigation of Micro Structures, Sensors, Actuators, Machines and Robotic Systems*, 63–68. <https://doi.org/10.1109/memsys.1994.555599>
- Kashef, J., & Franz, C. M. (2015). Quantitative methods for analyzing cell-cell adhesion in development. *Developmental Biology*, *401*(1), 165–174. <https://doi.org/10.1016/j.ydbio.2014.11.002>
- Kern, W. (1990). The evolution of silicon wafer cleaning technology. *Journal of the Electrochemical Society*, *137*(6), 1887. <https://doi.org/10.1149/1.2086825>

- Kilchenmann, S. C., Rollo, E., Maoddi, P., & Guiducci, C. (2016). Metal-coated SU-8 structures for high-density 3-d microelectrode arrays. *Journal of Microelectromechanical Systems*, 25(3), 425–431. <https://doi.org/10.1109/jmems.2016.2539000>
- Kim, H., & Kim, J. (2013). A microfluidic-based dynamic microarray system with single-layer pneumatic valves for immobilization and selective retrieval of single microbeads. *Microfluidics and Nanofluidics*, 16(4), 623–633. <https://doi.org/10.1007/s10404-013-1267-9>
- Kim, H. S., Devarenne, T. P., & Han, A. (2015). A high-throughput microfluidic single-cell screening platform capable of selective cell extraction. *Lab on a Chip*, 15(11), 2467–2475. <https://doi.org/10.1039/c4lc01316f>
- Kimura, Y., Gel, M., Techaumnat, B., Oana, H., Kotera, H., & Washizu, M. (2011). Dielectrophoresis-assisted massively parallel cell pairing and fusion based on field constriction created by a micro-orifice array sheet. *ELECTROPHORESIS*, 32(18), 2496–2501. <https://doi.org/10.1002/elps.201100129>
- Kinoshita, S., & Yoshioka, S. (2005). Structural colors in nature: the role of regularity and irregularity in the structure. *ChemPhysChem*, 6(8), 1442–1459. <https://doi.org/10.1002/cphc.200500007>
- Kinoshita, S., Yoshioka, S., & Miyazaki, J. (2008). Physics of structural colors. *Reports on Progress in Physics*, 71(7), 076401. <https://doi.org/10.1088/0034-4885/71/7/076401>
- Kirschbaum, M., Jaeger, M. S., Schenkel, T., Breinig, T., Meyerhans, A., & Duschl, C. (2008). T cell activation on a single-cell level in dielectrophoresis-based microfluidic devices. *Journal of Chromatography A*, 1202(1), 83–89. <https://doi.org/10.1016/j.chroma.2008.06.036>
- Ko, K. S., Arora, P. D., & McCulloch, C. A. (2001). Cadherins mediate intercellular mechanical signaling in fibroblasts by activation of stretch-sensitive calcium-permeable channels. *Journal of Biological Chemistry*, 276(38), 35967–35977. <https://doi.org/10.1074/jbc.M104106200>
- Kobel, S., Valero, A., Latt, J., Renaud, P., & Lutolf, M. (2010). Optimization of microfluidic single cell trapping for long-term on-chip culture. *Lab on a Chip*, 10(7), 857. <https://doi.org/10.1039/b918055a>
- Kong, F., García, A. J., Mould, A. P., Humphries, M. J., & Zhu, C. (2009). Demonstration of catch bonds between an integrin and its ligand. *Journal of Cell Biology*, 185(7), 1275–1284. <https://doi.org/10.1083/jcb.200810002>
- Kristensen, A., Yang, J. K. W., Bozhevolnyi, S. I., Link, S., Nordlander, P., Halas, N. J., & Mortensen, N. A. (2017). Plasmonic colour generation. *Nature Reviews Materials*, 2(1), 1–14. <https://doi.org/10.1038/natrevmats.2016.88>
- Kudo, T., Jeknic, S., Macklin, D. N., Akhter, S., Hughey, J. J., Regot, S., & Covert, M. W. (2017). Live-cell measurements of kinase activity in single cells using translocation reporters. *Nature Protocols*, 13(1), 155–169. <https://doi.org/10.1038/nprot.2017.128>



- Kulkarni, A., Anderson, A. G., Merullo, D. P., & Konopka, G. (2019). Beyond bulk: a review of single cell transcriptomics methodologies and applications. *Current Opinion in Biotechnology*, 58, 129–136. <https://doi.org/10.1016/j.copbio.2019.03.001>
- Kumar, K., Duan, H., Hegde, R. S., Koh, S. C. W., Wei, J. N., & Yang, J. K. W. (2012). Printing colour at the optical diffraction limit. *Nature Nanotechnology*, 7(9), 557–561. <https://doi.org/10.1038/nnano.2012.128>
- Kwok, R., & Evans, E. (1981). Thermoelasticity of large lecithin bilayer vesicles. *Biophysical Journal*, 35(3), 637–652. [https://doi.org/10.1016/s0006-3495\(81\)84817-5](https://doi.org/10.1016/s0006-3495(81)84817-5)
- Labernadie, A., Kato, T., Brugues, A., Serra-Picamal, X., Derzsi, S., Arwert, E., Weston, A., Gonzalez-Tarrago, V., Elosegui-Artola, A., & Albertazzi, L. e. a. (2017). A mechanically active heterotypic E-cadherin/N-cadherin adhesion enables fibroblasts to drive cancer cell invasion. *Nature Cell Biology*, 19(3), 224–237. <https://doi.org/10.1038/ncb3478>
- Lapidas, V., Zhizhchenko, A., Pustovalov, E., Storozhenko, D., & Kuchmizhak, A. A. (2022). Direct laser printing of high-resolution physically unclonable function anti-counterfeit labels. *Applied Physics Letters*, 120(26), 261104. <https://doi.org/10.1063/5.0091213>
- Lapizco-Encinas, B. H. (2018). On the recent developments of insulator-based dielectrophoresis: a review. *Electrophoresis*, 40(3), 358–375. <https://doi.org/10.1002/elps.201800285>
- Lazzari, G., Nicolas, V., Matsusaki, M., Akashi, M., Couvreur, P., & Mura, S. (2018). Multicellular spheroid based on a triple co-culture: a novel 3d model to mimic pancreatic tumor complexity. *Acta Biomaterialia*, 78, 296–307. <https://doi.org/10.1016/j.actbio.2018.08.008>
- Lee, C.-Y., Wang, W.-T., Liu, C.-C., & Fu, L.-M. (2016). Passive mixers in microfluidic systems: a review. *Chemical Engineering Journal*, 288, 146–160. <https://doi.org/10.1016/j.cej.2015.10.122>
- Lee, D., Hwang, B., & Kim, B. (2016). The potential of a dielectrophoresis activated cell sorter (DACs) as a next generation cell sorter. *Micro and Nano Systems Letters*, 4(1), 1–10. <https://doi.org/10.1186/s40486-016-0028-4>
- Li, H. (2002). Dielectrophoretic separation and manipulation of live and heat-treated cells of listeria on microfabricated devices with interdigitated electrodes. *Sensors and Actuators B: Chemical*, 86(2-3), 215–221. [https://doi.org/10.1016/s0925-4005\(02\)00172-7](https://doi.org/10.1016/s0925-4005(02)00172-7)
- Li, H., & Bashir, R. (2002). Dielectrophoretic orientation, manipulation and separation of live and heat-treated cells of listeria on microfabricated devices with interdigitated electrodes. *MRS Proceedings*, 729. <https://doi.org/10.1557/proc-729-u4.7>
- Li, H., Xu, Y., Zhang, X., Xiao, X., Zhou, F., & Zhang, Z. (2022). All-dielectric high saturation structural colors enhanced by multipolar modulated metasurfaces. *Optics Express*, 30(16), 28954–28965. <https://doi.org/10.1364/OE.464782>

- Li, Y., Jang, J. H., Wang, C., He, B., Zhang, K., Zhang, P., Vu, T., & Qin, L. (2017). Microfluidics cell loading-dock system: ordered cellular array for dynamic lymphocyte-communication study. *Advanced Biosystems*, *1*(10), 1700085. <https://doi.org/10.1002/adbi.201700085>
- Li, Z., Clark, A. W., & Cooper, J. M. (2016). Dual color plasmonic pixels create a polarization controlled nano color palette. *Acs Nano*, *10*(1), 492–498. <https://doi.org/10.1021/acsnano.5b05411>
- Li, Z., Qi, D., Liangui, D., Zheng, G., & Li, G. (2021). Structural-color nanoprinting with hidden watermarks. *Optics Letters*, *46*(3), 480–483. <https://doi.org/10.1364/ol.417026>
- Lim, C., Zhou, E., & Quek, S. (2006). Mechanical models for living cells—a review. *Journal of Biomechanics*, *39*(2), 195–216. <https://doi.org/10.1016/j.jbiomech.2004.12.008>
- Limozin, L., Bridge, M., Bongrand, P., Dushek, O., van der Merwe, P. A., & Robert, P. (2019). TCR–pMHC kinetics under force in a cell-free system show no intrinsic catch bond, but a minimal encounter duration before binding. *Proceedings of the National Academy of Sciences*, *116*(34), 16943–16948. <https://doi.org/10.1073/pnas.1902141116>
- Liu, B., Chen, W., & Zhu, C. (2015). Molecular force spectroscopy on cells. *Annual Review of Physical Chemistry*, *66*(1), 427–451. <https://doi.org/10.1146/annurev-physchem-040214-121742>
- Liu, X., Jia, Y., Han, Z., Hou, Q., Zhang, W., Zheng, W., & Jiang, X. (2021). Integrating a concentration gradient generator and a single-cell trapper array for high-throughput screening the bioeffects of nanomaterials. *Angewandte Chemie*, *133*(22), 12427–12430. <https://doi.org/10.1002/ange.202101293>
- Lu, Y.-T., Pendharkar, G. P., Lu, C.-H., Chang, C.-M., & Liu, C.-H. (2015). A microfluidic approach towards hybridoma generation for cancer immunotherapy. *Oncotarget*, *6*(36), 38764–38776. <https://doi.org/10.18632/oncotarget.5550>
- Lussier, F., Stauffer, O., Platzman, I., & Spatz, J. P. (2021). Can bottom-up synthetic biology generate advanced drug-delivery systems? *Trends in Biotechnology*, *39*(5), 445–459. <https://doi.org/10.1016/j.tibtech.2020.08.002>
- Maillard, D., De Pastina, A., Abazari, A. M., & Villanueva, L. G. (2021). Avoiding transduction-induced heating in suspended microchannel resonators using piezoelectricity. *Microsystems and Nanoengineering*, *7*(1), 1–7. <https://doi.org/10.1038/s41378-021-00254-1>
- Martinez-Duarte, R., Renaud, P., & Madou, M. J. (2011). A novel approach to dielectrophoresis using carbon electrodes. *Electrophoresis*, *32*(17), 2385–2392. <https://doi.org/10.1002/elps.201100059>
- Menad, S., Franqueville, L., Haddour, N., Buret, F., & Frenea-Robin, M. (2015). Ndep-driven cell patterning and bottom-up construction of cell aggregates using a new bioelectronic chip. *Acta Biomaterialia*, *17*, 107–114. <https://doi.org/10.1016/j.actbio.2015.01.011>

- Michálek, T., & Zemánek, J. (2017). Dipole and multipole models of dielectrophoresis for a non-negligible particle size: simulations and experiments. *Electrophoresis*, *38*(11), 1419–1426. <https://doi.org/10.1002/elps.201600466>
- Mittal, N., Rosenthal, A., & Voldman, J. (2007). Ndep microwells for single-cell patterning in physiological media. *Lab on a Chip*, *7*(9), 1146. <https://doi.org/10.1039/b706342c>
- Mollick, E. (2006). Establishing moore's law. *IEEE Annals of the History of Computing*, *28*(3), 62–75. <https://doi.org/10.1109/mahc.2006.45>
- Morgan, H., Hughes, M. P., & Green, N. G. (1999a). Separation of submicron bioparticles by dielectrophoresis. *Biophysical Journal*, *77*(1), 516–525. [https://doi.org/10.1016/s0006-3495\(99\)76908-0](https://doi.org/10.1016/s0006-3495(99)76908-0)
- Morgan, H., Hughes, M. P., & Green, N. G. (1999b). Separation of submicron bioparticles by dielectrophoresis. *Biophysical Journal*, *77*(1), 516–525. [https://doi.org/10.1016/s0006-3495\(99\)76908-0](https://doi.org/10.1016/s0006-3495(99)76908-0)
- Moura Rosa, P., Gopalakrishnan, N., Ibrahim, H., Haug, M., & Halaas, O. (2016). The intercell dynamics of T cells and dendritic cells in a lymph node-on-a-chip flow device. *Lab on a Chip*, *16*(19), 3728–3740. <https://doi.org/10.1039/c6lc00702c>
- Nagai, M., Oohara, K., Kato, K., Kawashima, T., & Shibata, T. (2015). Development and characterization of hollow microprobe array as a potential tool for versatile and massively parallel manipulation of single cells. *Biomedical Microdevices*, *17*(2), 1–11. <https://doi.org/10.1007/s10544-015-9943-z>
- Newton, I. (1704). *Red: the history of a color*. London: S. Smith; B. Walford. <https://doi.org/10.5479/sil.302475.39088000644674>
- Oh, K. W., Lee, K., Ahn, B., & Furlani, E. P. (2012). Design of pressure-driven microfluidic networks using electric circuit analogy. *Lab Chip*, *12*(3), 515–545. <https://doi.org/10.1039/c2lc20799k>
- Ounkomol, C., Yamada, S., & Heinrich, V. (2010). Single-cell adhesion tests against functionalized microspheres arrayed on afm cantilevers confirm heterophilic e- and n-cadherin binding. *Biophysical Journal*, *99*(12), L100–L102. <https://doi.org/10.1016/j.bpj.2010.11.013>
- Paek, A. L., Liu, J. C., Loewer, A., Forrester, W. C., & Lahav, G. (2016). Cell-to-cell variation in p53 dynamics leads to fractional killing. *Cell*, *165*(3), 631–642. <https://doi.org/10.1016/j.cell.2016.03.025>
- Pang, L., Ding, J., Liu, X.-X., Kou, Z., Guo, L., Xu, X., & Fan, S.-K. (2021). Microfluidics-based single-cell research for intercellular interaction. *Frontiers in Cell and Developmental Biology*, *9*. <https://doi.org/10.3389/fcell.2021.680307>
- Pang, L., Liu, W., Tian, C., Xu, J., Li, T., Chen, S.-W., & Wang, J. (2016). Construction of single-cell arrays and assay of cell drug resistance in an integrated microfluidic platform. *Lab on a Chip*, *16*(23), 4612–4620. <https://doi.org/10.1039/c6lc01000h>
- Pastoureau, M. (2017). *Red: the history of a color*. Princeton University Press.

- Pattnaik, P. (2005). Surface plasmon resonance: applications in understanding receptor-ligand interaction. *Applied Biochemistry and Biotechnology*, 126(2), 079–092. <https://doi.org/10.1385/abab:126:2:079>
- Pedrotti, F. L., & Pedrotti, L. S. (1996). *Introduction to optics*. Prentice Hall.
- PENG, X. B., SUN, M. X., & YANG, H. Y. (2005). A novel in vitro system for gamete fusion in maize. *Cell Research*, 15(9), 734–738. <https://doi.org/10.1038/sj.cr.7290343>
- Pennisi, E. (2018). Is cancer a breakdown of multicellularity? *Science*, 360(6396), 1391–1391. <https://doi.org/10.1126/science.360.6396.1391>
- Piacentini, N., Mernier, G., Tornay, R., & Renaud, P. (2011). Separation of platelets from other blood cells in continuous-flow by dielectrophoresis field-flow-fractionation. *Biomicrofluidics*, 5(3), 034122. <https://doi.org/10.1063/1.3640045>
- Potthoff, E., Guillaume-Gentil, O., Ossola, D., Polesel-Maris, J., LeibundGut-Landmann, S., Zambelli, T., & Vorholt, J. A. (2012). Rapid and serial quantification of adhesion forces of yeast and mammalian cells. *PLoS ONE*, 7(12), e52712. <https://doi.org/10.1371/journal.pone.0052712>
- Prezhdo, O. V., & Pereverzev, Y. V. (2009). Theoretical aspects of the biological catch bond. *Accounts of Chemical Research*, 42(6), 693–703. <https://doi.org/10.1021/ar800202z>
- Proust, J., Bedu, F., Gallas, B., Ozerov, I., & Bonod, N. (2016). All-dielectric colored metasurfaces with silicon Mie resonators. *ACS Nano*, 10(8), 7761–7767. <https://doi.org/10.1021/acsnano.6b03207>
- Punjiya, M., Nejad, H. R., Mathews, J., Levin, M., & Sonkusale, S. (2019). A flow through device for simultaneous dielectrophoretic cell trapping and AC electroporation. *Scientific Reports*, 9(1), 1–11. <https://doi.org/10.1038/s41598-019-48198-x>
- Qian, F., Ermilov, S., Murdock, D., Brownell, W. E., & Anvari, B. (2004). Combining optical tweezers and patch clamp for studies of cell membrane electromechanics. *Review of Scientific Instruments*, 75(9), 2937–2942. <https://doi.org/10.1063/1.1781382>
- Ramos, A., Morgan, H., Green, N. G., & Castellanos, A. (1998). AC electrokinetics: a review of forces in microelectrode structures. *Journal of Physics D: Applied Physics*, 31(18), 2338–2353. <https://doi.org/10.1088/0022-3727/31/18/021>
- Rasmussen, A., Gaitan, M., Locascio, L., & Zaghloul, M. (2001). Fabrication techniques to realize cmos-compatible microfluidic microchannels. *Journal of Microelectromechanical Systems*, 10(2), 286–297. <https://doi.org/10.1109/84.925785>
- Rayleigh, L. (1919). On the optical character of some brilliant animal colours. *The London, Edinburgh, and Dublin Philosophical Magazine and Journal of Science*, 37(217), 98–111. <https://doi.org/10.1080/14786440108635867>
- Reichle, C., Schnelle, T., Muller, T., Leya, T., & Fuhr, G. (2000). A new microsystem for automated electrorotation measurements using laser tweezers. *Biochimica et Biophysica Acta (BBA) - Bioenergetics*, 1459(1), 218–229. [https://doi.org/10.1016/s0005-2728\(00\)00150-x](https://doi.org/10.1016/s0005-2728(00)00150-x)

- Ren, Y., Huang, S.-H., Mosser, S., Heuschkel, M., Bertsch, A., Fraering, P., Chen, J.-J., & Renaud, P. (2015). A simple and reliable pdms and SU-8 irreversible bonding method and its application on a microfluidic-MEA device for neuroscience research. *Micromachines*, 6(12), 1923–1934. <https://doi.org/10.3390/mi6121465>
- Rettig, J. R., & Folch, A. (2005). Large-scale single-cell trapping and imaging using microwell arrays. *Analytical Chemistry*, 77(17), 5628–5634. <https://doi.org/10.1021/ac0505977>
- Rezaei, S. D., Dong, Z., Chan, J. Y. E., Trisno, J., Ng, R. J. H., Ruan, Q., Qiu, C.-W., Mortensen, N. A., Mortensen, N. A., & Yang, J. K. W. (2020). Nanophotonic structural colors. *ACS Photonics*, 8(1), 18–33. <https://doi.org/10.1021/acsp Photonics.0c00947>
- Rimawi, M. F., Schiff, R., & Osborne, C. K. (2015). Targeting HER2 for the treatment of breast cancer. *Annual Review of Medicine*, 66(1), 111–128. <https://doi.org/10.1146/annurev-med-042513-015127>
- Rodriguez-Trujillo, R., Mills, C. A., Samitier, J., & Gomila, G. (2006). Low cost micro-coulter counter with hydrodynamic focusing. *Microfluidics and Nanofluidics*, 3(2), 171–176. <https://doi.org/10.1007/s10404-006-0113-8>
- Rosenberg, S. A., & Restifo, N. P. (2015). Adoptive cell transfer as personalized immunotherapy for human cancer. *Science*, 348(6230), 62–68. <https://doi.org/10.1126/science.aaa4967>
- Rosenthal, A., & Voldman, J. (2005). Dielectrophoretic traps for single-particle patterning. *Biophysical Journal*, 88(3), 2193–2205. <https://doi.org/10.1529/biophysj.104.049684>
- Rossiter, H., Alon, R., & Kupper, T. S. (1997). Selectins, T-cell rolling and inflammation. *Molecular Medicine Today*, 3(5), 214–222. [https://doi.org/10.1016/s1357-4310\(97\)01040-x](https://doi.org/10.1016/s1357-4310(97)01040-x)
- Safi, C., Zebib, B., Merah, O., Pontalier, P.-Y., & Vaca-Garcia, C. (2014). Morphology, composition, production, processing and applications of chlorella vulgaris: a review. *Renewable and Sustainable Energy Reviews*, 35, 265–278. <https://doi.org/10.1016/j.rser.2014.04.007>
- Sakoda, K. (2001). *Optical properties of photonic crystals*. Springer Berlin, Heidelberg. <https://doi.org/10.1007/978-3-662-14324-7>
- Sarkar, S. (2015). T cell dynamic activation and functional analysis in nanoliter droplet microarray. *Journal of Clinical & Cellular Immunology*, 06(03). <https://doi.org/10.4172/2155-9899.1000334>
- Segaliny, A. I., Li, G., Kong, L., Ren, C., Chen, X., Wang, J. K., Baltimore, D., Wu, G., & Zhao, W. (2018). Functional TCR T-cell screening using single-cell droplet microfluidics. *Lab on a Chip*, 18(24), 3733–3749. <https://doi.org/10.1039/c8lc00818c>
- Seger, U., Gawad, S., Johann, R., Bertsch, A., & Renaud, P. (2004). Cell immersion and cell dipping in microfluidic devices. *Lab on a Chip*, 4(2), 148. <https://doi.org/10.1039/b311210a>
- Seger-Sauli, U., Panayiotou, M., Schnydrig, S., Jordan, M., & Renaud, P. (2005). Temperature measurements in microfluidic systems: heat dissipation of negative dielectrophoresis barriers. *Electrophoresis*, 26(11), 2239–2246. <https://doi.org/10.1002/elps.200410358>

- Sens, P., & Plastino, J. (2015). Membrane tension and cytoskeleton organization in cell motility. *Journal of Physics: Condensed Matter*, 27(27), 273103. <https://doi.org/10.1088/0953-8984/27/27/273103>
- Sohrabi Kashani, A., & Packirisamy, M. (2019). Efficient low shear flow-based trapping of biological entities. *Scientific Reports*, 9(1). <https://doi.org/10.1038/s41598-019-41938-z>
- Song, M., Li, X., Pu, M., Guo, Y., Liu, K., Yu, H., Ma, X., & Luo, X. (2018). Color display and encryption with a plasmonic polarizing metamirror. *Nanophotonics*, 7(1), 323–331. <https://doi.org/10.1515/nanoph-2017-0062>
- Stockslager, M. A., Bagnall, J. S., Hecht, V. C., Hu, K., Aranda-Michel, E., Payer, K., Kimmerling, R. J., & Manalis, S. R. (2017). Microfluidic platform for characterizing TCR-pMHC interactions. *Biomicrofluidics*, 11(6), 064103. <https://doi.org/10.1063/1.5002116>
- Strutt, J. W. (1917). On the reflection of light from a regularly stratified medium. *Proceedings of the Royal Society of London. Series A, Containing Papers of a Mathematical and Physical Character*, 93(655), 565–577.
- Sun, S., Zhou, Z., Zhang, C., Gao, Y., Duan, Z., Xiao, S., & Song, Q. (2017). All-dielectric full-color printing with TiO<sub>2</sub> metasurfaces. *ACS Nano*, 11(5), 4445–4452. <https://doi.org/10.1021/acsnano.7b00415>
- Takahashi, Y., & Miyata, S. (2020). Continuous es/feeder cell-sorting device using dielectrophoresis and controlled fluid flow. *Micromachines*, 11(8), 734. <https://doi.org/10.3390/mi11080734>
- Tan, S. C. W., Yang, T., Gong, Y., & Liao, K. (2011). Rupture of plasma membrane under tension. *Journal of Biomechanics*, 44(7), 1361–1366. <https://doi.org/10.1016/j.jbiomech.2011.01.010>
- Tan, W.-H., & Takeuchi, S. (2007). A trap-and-release integrated microfluidic system for dynamic microarray applications. *Proceedings of the National Academy of Sciences*, 104(4), 1146–1151. <https://doi.org/10.1073/pnas.0606625104>
- Tanyeri, M., Ranka, M., Sittipolkul, N., & Schroeder, C. M. (2011). Microfluidic wheatstone bridge for rapid sample analysis. *Lab on a Chip*, 11(24), 4181. <https://doi.org/10.1039/c1lc20604d>
- Thoumine, O., Kocian, P., Kottelat, A., & Meister, J.-J. (2000). Short-term binding of fibroblasts to fibronectin: optical tweezers experiments and probabilistic analysis. *European Biophysics Journal*, 29(6), 398–408. <https://doi.org/10.1007/s002490000087>
- Tighe, P. J., Ryder, R. R., Todd, I., & Fairclough, L. C. (2015). Elisa in the multiplex era: potentials and pitfalls. *PROTEOMICS – Clinical Applications*, 9(3-4), 406–422. <https://doi.org/10.1002/prca.201400130>
- Ungai-Salanki, R., Peter, B., Gerecsei, T., Orgovan, N., Horvath, R., & Szabo, B. (2019). A practical review on the measurement tools for cellular adhesion force. *Advances in Colloid and Interface Science*, 269, 309–333. <https://doi.org/10.1016/j.cis.2019.05.005>

- Van Geite, W., Jimidar, I. S., Sotthewes, K., Gardeniers, H., & Desmet, G. (2022). Vacuum-driven assembly of electrostatically levitated microspheres on perforated surfaces. *Materials & Design*, 216, 110573. <https://doi.org/10.1016/j.matdes.2022.110573>
- Vieider, C., Holm, J., Forssen, L., Elderstig, H., Lindgren, S., & Ahlfeldt, H. (1997). A new process for combining anisotropic bulk etching with subsequent precision lithography. *Proceedings of International Solid State Sensors and Actuators Conference (Transducers '97)*, 1, 679–682. <https://doi.org/10.1109/sensor.1997.613743>
- Vigolo, D., Rusconi, R., Stone, H. A., & Piazza, R. (2010). Thermophoresis: microfluidics characterization and separation. *Soft Matter*, 6(15), 3489–3493. <https://doi.org/10.1039/C002057E>
- Voldman, J., Braff, R. A., Toner, M., Gray, M. L., & Schmidt, M. A. (2001). Holding forces of single-particle dielectrophoretic traps. *Biophysical Journal*, 80(1), 531–542. [https://doi.org/10.1016/s0006-3495\(01\)76035-3](https://doi.org/10.1016/s0006-3495(01)76035-3)
- Voldman, J., Gray, M. L., Toner, M., & Schmidt, M. A. (2002). A microfabrication-based dynamic array cytometer. *Analytical Chemistry*, 74(16), 3984–3990. <https://doi.org/10.1021/ac0256235>
- Vulto, P., Glade, N., Altomare, L., Bablet, J., Tin, L. D., Medoro, G., Chartier, I., Manaresi, N., Tartagni, M., & Guerrieri, R. (2005). Microfluidic channel fabrication in dry film resist for production and prototyping of hybrid chips. *Lab on a Chip*, 5(2), 158. <https://doi.org/10.1039/b411885e>
- Walling, B. L., & Kim, M. (2018). LFA-1 in T cell migration and differentiation. *Frontiers in Immunology*, 9, 952. <https://doi.org/10.3389/fimmu.2018.00952>
- Wang, H., Zhou, F., Guo, Y., & Ju, L. A. (2022). Micropipette-based biomechanical nanotools on living cells. *European Biophysics Journal*, 51(2), 119–133. <https://doi.org/10.1007/s00249-021-01587-5>
- Wang, X., Wang, X.-B., & Gascoyne, P. R. (1997). General expressions for dielectrophoretic force and electrorotational torque derived using the Maxwell stress tensor method. *Journal of Electrostatics*, 39(4), 277–295. [https://doi.org/10.1016/s0304-3886\(97\)00126-5](https://doi.org/10.1016/s0304-3886(97)00126-5)
- Wille, H., Burte, E., Burte, E. P., & Ryssel, H. (1992). Simulation of the step coverage for chemical vapor deposited silicon dioxide. *Journal of Applied Physics*, 71(7), 3532–3537. <https://doi.org/10.1063/1.350908>
- Williams, K., Gupta, K., & Wasilik, M. (2003). Etch rates for micromachining processing-part ii. *Journal of Microelectromechanical Systems*, 12(6), 761–778. <https://doi.org/10.1109/jmems.2003.820936>
- Wlodkowic, D., Faley, S., Zagnoni, M., Wikswo, J. P., & Cooper, J. M. (2009). Microfluidic single-cell array cytometry for the analysis of tumor apoptosis [PMID: 19514700]. *Analytical Chemistry*, 81(13), 5517–5523. <https://doi.org/10.1021/ac9008463>

- Wu, A. H. (2006). A selected history and future of immunoassay development and applications in clinical chemistry. *Clinica Chimica Acta*, 369(2), 119–124. <https://doi.org/10.1016/j.cca.2006.02.045>
- Xu, C., Hu, S., & Chen, X. (2016). Artificial cells: from basic science to applications. *Materials Today*, 19(9), 516–532. <https://doi.org/10.1016/j.mattod.2016.02.020>
- Xu, T., Shi, H., Wu, Y.-K., Kaplan, A. E., Ok, J. G., & Guo, L. J. (2011). Structural colors: from plasmonic to carbon nanostructures. *Small*, 7(22), 3128–3136. <https://doi.org/10.1002/smll.201101068>
- Xu, X., Sarder, P., Li, Z., & Nehorai, A. (2013a). Optimization of microfluidic microsphere-trap arrays. *Biomicrofluidics*, 7(1), 014112. <https://doi.org/10.1063/1.4793713>
- Xu, X., Sarder, P., Li, Z., & Nehorai, A. (2013b). Optimization of microfluidic microsphere-trap arrays. *Biomicrofluidics*, 7(1), 014112. <https://doi.org/10.1063/1.4793713>
- Xuan, Z., Xuan, Z., Xuan, Z., Li, J., Qingquan, L., Yi, F., Wang, S.-W., & Lu, W. (2021). Artificial structural colors and applications. *Innovation-the European Journal of Social Science Research*, 2(1), 100081. <https://doi.org/10.1016/j.xinn.2021.100081>
- Yamada, M., & Seki, M. (2005). Hydrodynamic filtration for on-chip particle concentration and classification utilizing microfluidics. *Lab on a Chip*, 5(11), 1233. <https://doi.org/10.1039/b509386d>
- Yang, J. H., Babicheva, V. E., Yu, M. W., Lu, T.-C., Lin, T.-R., & Chen, K.-P. (2020). Structural colors enabled by lattice resonance on silicon nitride metasurfaces. *ACS Nano*, 14(5), 5678–5685. <https://doi.org/10.1021/acsnano.0c00185>
- Yang, W., Xiao, S., Song, Q., Liu, Y., Wu, Y., Wang, S., Wang, S., Wang, S., Yu, J., Yu, J., Han, J., Han, J., Han, J., & Tsai, D. P. (2020). All-dielectric metasurface for high-performance structural color. *Nature Communications*, 11(1), 1–8. <https://doi.org/10.1038/s41467-020-15773-0>
- Yerbury, T. (2022). Z-movi cell avidity analyzer - lumicks. <https://lumicks.com/products/z-movi-cell-avidity-analyzer/>
- Yesilkoy, F., Ueno, R., Desbiolles, B. X. E., Grisi, M., Sakai, Y., Kim, B. J., & Brugger, J. (2016). Highly efficient and gentle trapping of single cells in large microfluidic arrays for time-lapse experiments. *Biomicrofluidics*, 10(1), 014120. <https://doi.org/10.1063/1.4942457>
- Yoshimura, Y., Tomita, M., Mizutani, F., & Yasukawa, T. (2014). Cell pairing using microwell array electrodes based on dielectrophoresis. *Analytical Chemistry*, 86(14), 6818–6822. <https://doi.org/10.1021/ac5015996>
- Zhang, J., Grzybowski, B. A., & Granick, S. (2017). Janus particle synthesis, assembly, and application. *Langmuir*, 33(28), 6964–6977. <https://doi.org/10.1021/acs.langmuir.7b01123>
- Zhang, J., Ma, Y., Taylor, S. S., & Tsien, R. Y. (2001). Genetically encoded reporters of protein kinase activity reveal impact of substrate tethering. *Proceedings of the National Academy of Sciences*, 98(26), 14997–15002. <https://doi.org/10.1073/pnas.211566798>



- Zhou, B., & Ramirez, W. F. (1996). Kinetics and modeling of wet etching of aluminum oxide by warm phosphoric acid. *Journal of The Electrochemical Society*, 143(2), 619–623. <https://doi.org/10.1149/1.1836489>
- Zhou, Y., Shao, N., Bessa de Castro, R., Zhang, P., Ma, Y., Liu, X., Huang, F., Wang, R.-F., & Qin, L. (2020). Evaluation of single-cell cytokine secretion and cell-cell interactions with a hierarchical loading microwell chip. *Cell Reports*, 31(4), 107574. <https://doi.org/10.1016/j.celrep.2020.107574>
- Zhu, P., & Wang, L. (2017). Passive and active droplet generation with microfluidics: a review. *Lab on a Chip*, 17(1), 34–75. <https://doi.org/10.1039/c6lc01018k>
- Zhu, X., Vannahme, C., Hojlund-Nielsen, E., Mortensen, N. A., & Kristensen, A. (2016). Plasmonic colour laser printing. *Nature Nanotechnology*, 11(4), 325–329. <https://doi.org/10.1038/nnano.2015.285>
- Zi, J., Yu, X., Li, Y., Hu, X., Xu, C., Xu, C., Wang, X. J., Liu, X., & Fu, R. (2003). Coloration strategies in peacock feathers. *Proceedings of the National Academy of Sciences of the United States of America*, 100(22), 12576–12578. <https://doi.org/10.1073/pnas.2133313100>

# Acronyms

<b>ACT</b>	adoptive cell transfer
<b>AFM</b>	atomic force microscopy
<b>APC</b>	antigen presenting cell
<b>BSA</b>	bovine serum albumin
<b>CAR</b>	chimeric antigen receptor
<b>CAR-T</b>	chimeric antigen receptor T
<b>DEP</b>	dielectrophoresis
<b>DI</b>	deionized
<b>DMP</b>	Dielectrophoretically Manipulated Particle
<b>DPA</b>	dual pipette assay
<b>DRIE</b>	deep reactive ion etching
<b>ELISA</b>	enzyme linked immunosorbent assay
<b>FBS</b>	fetal bovine serum
<b>FRET</b>	Förster resonance energy transfer
<b>HER2</b>	human epidermal growth factor receptor-2
<b>HF</b>	hydrofluoric acid
<b>HTP</b>	Hydrodynamically Trapped Particle
<b>IBE</b>	ion beam etching
<b>IFN-<math>\gamma</math></b>	interferon- $\gamma$
<b>KTR</b>	kinase transcription reporter

---

<b>LPCVD</b>	low pressure chemical vapor deposition
<b>LTO</b>	low temperature oxide
<b>MHC</b>	major histocompatibility complex
<b>MST</b>	Maxwell stress tensor
<b>nDEP</b>	negative dielectrophoresis
<b>OT</b>	optical tweezers
<b>PBS</b>	phosphate-buffered saline
<b>pDEP</b>	positive dielectrophoresis
<b>PDMS</b>	polydimethylsiloxane
<b>pMHC</b>	peptide major histocompatibility complex
<b>RNA</b>	ribonucleic acid
<b>SPR</b>	surface plasmon resonance
<b>TCR</b>	T-cell receptor
<b>TIL</b>	tumor infiltrated lymphocyte
<b>TNF-<math>\alpha</math></b>	tumor necrosis factor- $\alpha$

# Clémentine Lipp

PhD in Microsystems and microelectronics.  
EPFL Microtechnologies Engineer.  
Swiss nationality

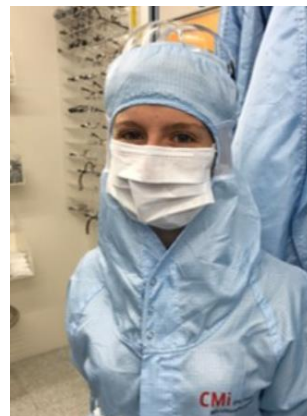
Allée des Cèdres 4  
1022 Chavannes-près-Renens  
Switzerland  
+41 77 422 87 19

[clementine.lipp@alumni.epfl.ch](mailto:clementine.lipp@alumni.epfl.ch)

Expertise in microfabrication processes  
and microsystems for biomedical  
applications

Versatile and resourceful, I thrive in  
multidisciplinary projects

Passionate about teamwork, mentoring  
and knowledge transfer



## PROFESSIONAL EXPERIENCE

---

<b>Doctoral assistant, École Polytechnique Fédérale de Lausanne (EPFL), Lausanne, Switzerland</b> PhD on the development of hydrodynamic and dielectrophoretic traps for the controlled interaction between single cells and application to immunotherapies. Work achieved in the Laboratory for Microsystems 4 led by Prof. Philippe Renaud. <ul style="list-style-type: none"><li>Multidisciplinary project in microtechnology (from design and fabrication processes development to microfluidics) and life sciences (from cell culture to on-chip biological assays)</li><li>Project in collaboration with femto-ST institute and the Etablissement Français du Sang (EFS), Besançon, France</li><li>Work in close collaboration with biology and automation experts for the assay of cell-cell interaction between tumor cells and human immune cells using the developed technology</li><li>Side-project on the study of aperture controlled structural colors</li><li>Design and supervision of 13 successful students (MSc level) projects</li><li>In charge of 2 practicals for classes MEMS practicals I and II for master students: characterization of an electrothermal microactuators, characterization of a MEMS accelerometer.</li></ul>	2018-2022 (4 y, 3 mo)
<b>Research Engineer, Mursla, Cambridge, UK</b> Development of a fabrication process in the local facilities, design and microfabrication of the chips, experiments design, measurements, data analysis and stock management for an early startup in liquid biopsy	2018 (6 mo)
<b>R&amp;D Engineer, Xsensio, Ecublens, Switzerland</b> Design and tests of microfluidic SU8 devices aiming at collecting and transporting sweat for lab-on-skin analysis.	2018 (3 mo)

## SKILLS

---

**Engineering** Control and design of microfluidic systems, Dielectrophoresis, Microfabrication technologies, Scanning electron microscopy

**Biomedical technologies** Mammalian cell culture, Cell preparation, Fluorescent assay, Fluorescence microscopy

**Informatics** C, MATLAB, Python, CAD Design (AutoCAD, SolidWorks), COMSOL Multiphysics, Adobe Illustrator, Microsoft Office, ImageJ.

**Certifications** Agile PM

**Soft skills** Creative problem-solving, out-of-the-box thinking, active listening, teamwork, knowledge transfer, mentoring.

## LANGUAGES

---

**French:** native  
**English:** C1

**German:** B1  
**Italian:** basic

**Spanish:** basic understanding

## EDUCATION

---

<b>PhD in Microsystems and Microelectronics, EPFL, Lausanne, Switzerland</b>	2018-2022
<ul style="list-style-type: none"><li>• Publications in scientific journals, presentation international conferences, seminars in laboratories at Stanford, UC Berkeley, UC Santa Barbara, UC Los Angeles.</li><li>• PhD classes on biology fundamentals for engineers, medical implantable devices, electron microscopy techniques and Python coding.</li></ul>	
<b>MSc in Microengineering, EPFL, Lausanne, Switzerland</b>	2015-2017
<ul style="list-style-type: none"><li>• Internship and master thesis at CERN, Geneva: development of a microfabrication process and characterization of a microfluidic cooling device for detectors in high-energy physics experiments</li><li>• Major in Micro- and nanosystems</li><li>• Average grade of 5.53/6.</li></ul>	
<b>BSc in Microengineering, EPFL, Lausanne</b>	2012-2015
<ul style="list-style-type: none"><li>• Exchange year in University of Waterloo, Canada</li></ul>	

## SCIENTIFIC PUBLICATIONS

---

- C. Lipp, K. Uning, J. Cottet, D. Migliozi, A. Bertsch and P. Renaud, "Planar hydrodynamic traps and buried channels for bead and cell trapping and releasing", Lab on a Chip, vol. 21 p. 3686-3694, 2021
- C. Lipp, L. Koebel, A. Bertsch, M. Gauthier, A. Bolopion and P. Renaud, "Dielectrophoretic Traps for Efficient Bead and Cell Trapping and Formation of Aggregates of Controlled Size and Composition", Frontiers in Bioengineering and Biotechnology, vol. 10, 2022
- C. Lipp, L. Koebel, R. Loyon, A. Bolopion, L. Spehner, M. Gauthier, C. Borg, A. Bertsch and P. Renaud, "Microfluidic device combining hydrodynamic and dielectrophoretic trapping for the controlled contact between single micro-sized objects and application to adhesion assays", manuscript submitted, 2022
- C. Lipp, A. Jacquillat, D. Migliozi, H. Wang, A. Bertsch, E. Glushkov, O. Martin and P. Renaud, "Aperture-controlled fabrication of all-dielectric structural color pixels", manuscript submitted, 2022
  
- C. Lipp, J. Cottet, A. Berstch, P. Renaud "Hydrodynamic and dielectrophoretic trapping for the controlled interaction between beads and cells", DEP2020.1 conference, Flagstaff, Arizona, USA, 2021
- C. Lipp, K. Uning, J. Cottet, D. Migliozi, A. Bertsch and Philippe Renaud, "Planar hydrodynamic traps connected to buried channels for beads and cells trapping and releasing", uTAS conference, Palmsprings, California, USA, 2021
- C. Lipp, K. Uning, J. Cottet, D. Migliozi, A. Bertsch and P. Renaud, "Large arrays of vertical hydrodynamic traps for beads and cells trapping", Nanobiotech Montreux conference, Switzerland, 2021
- C. Lipp, L. Koebel, L. Spehner, A. Bolopion, R. Loyon, M. Gauthier, C. Borg, A. Bertsch and P. Renaud "Combining hydrodynamic and dielectrophoretic trapping for the controlled interaction between cells", EICSE retreat, Lausanne, Switzerland, 2022

## PERSONAL INTERESTS

---

- Violoncello player for 12 years, played in international festivals with a youth orchestra, attended scholarship program for talented musicians
- Outdoor lover, hiking, skiing and running
- Indoor bouldering addict
- Certified yoga teacher
- Cat person